The Search for High Energy Neutrinos from Gamma-Ray Bursts with the AMANDA Detector

by

Rellen Hardtke

A dissertation submitted in partial fulfillment of the

requirements for the degree of

Doctor of Philosophy

(Physics)

at the

University of Wisconsin – Madison

2002

Abstract

Gamma-ray bursts (GRBs) are brief, intense, isotropically distributed explosions of extremely high energy electromagnetic radiation. GRBs are located at cosmological distances, some up to half way across the observable universe. According to the relativistic fireball model of GRBs, they are likely to be astrophysical sources of high energy neutrinos. These neutrinos are chargeless and nearly massless; therefore, they can reach the earth, undeflected and unabsorbed, from the furthest reaches of the universe. Occasionally, one of these neutrinos will interact in the ice or rock near the Antarctic Muon and Neutrino Detector Array (AMANDA). AMANDA uses the ice shelf near the geographic South Pole as a Cherenkov medium for detecting high energy muons. When a neutrino interact near the detector, it produces a relativistic muon that emits Cerenkov radiation as it hurtles through the transparent ice. Muons are also produced by cosmic rays hitting the atmosphere. Since only neutrinos can pass through the entire earth, AMANDA uses the earth as a filter, tagging upgoing events as authentic neutrino-induced muons and rejecting downgoing cosmic ray muons. Data recorded by AMANDA from 1997 through May of 2000 were searched for high energy neutrinos coincident with GRBs detected by the Burst and Transient Satellite Experiment (BATSE). Because both the time and position of the bursts are provided by the BATSE satellite, the cosmic ray muon background level from which the neutrinos must be separated is greatly reduced. The analysis – including data handling, Monte Carlo simulations, optimization cuts, background studies, and calculation of upper limits – is decribed here. The search result is currently consistent with no signal.

Sponsor

This work was supported by the Computational Science Graduate Fellowship Program of the Office of Scientific Computing in the Department of Energy under contract W-7405-Eng-82.

Acknowledgements

My boundless appreciation goes to:

My advisor Francis Halzen and the Wisconsin AMANDA group for their patience, understanding, guidance, assistance and sociability.

My fellow graduate students, especially Tyce DeYoung and Katherine Rawlins.

Gilles Barouch, for raising the GRB analysis to a new level of sophistication during his time at Wisconsin.

Gary Hill, teacher and confidante.

John Jacobsen, Jodi Lamoureux, Leilah Ma, Peter Steffen and Tonio Hauschildt who filtered the raw AMANDA data and produced GRB data sets.

Ryan Bay, who extracted the 1997 AMANDA data for GRB studies, and performed the first complete AMANDA GRB analysis.

All those who spent those first years of AMANDA conceiving, designing, constructing, calibrating, simulating and improving the detector. I was lucky enough to join the AMANDA collaboration as it was seeing its first light and proving its ability to detect neutrinos. I am lucky enough to depart as AMANDA analyzes and studies several years of good data, offering scientific insight into several areas of research.

Randy Durand, for being my first year advisor and encouraging me to look into the AMANDA group.

Brian Schwartz, for explaining to me the way the department really operates, and for a 4,000 mile road trip I'll talk about the rest of my life.

My much-needed and much-loved supportive friends: Nelle, Indy, Jean and Jen.

Jan Miller, for challenging me, for helping me find clarity, and for a future of unadulterated happiness.

Joanne, Carol and Phyllis who trained me early to be strong, and who taught me that a woman's value is determined by her character and intellect.

My brother Dan, for being a much needed, sometimes brutal, reality check and for giving me my very cool sister-in-law Vicki.

Mom and Dad, for their unconditional love and support. I hope to be half the person and parents you are.

Todd, the love of my life, the best part of my life. I look forward to a lifetime of continued joy, laughter, understanding, and happiness.

This thesis is dedicated to the hardest working people I have ever known, people who handed down the authentic "family values" of love, acceptance, perseverance, caring, and kindness: Harold Hardtke, Grace Hardtke-Milchner, Walter "Cocky" Tisch and Magdalen Tisch.

Contents

Abstract **i**

1 Gamma-Ray Bursts **1**

1.1 Discovery 1

1.2 Revolution: BATSE 2

1.3 GRB Characteristics 4

2 GRBs and Neutrinos **9**

2.1 Fireball Model 9

2.2 Hadrons and Cosmic Rays 10

2.3 Other Implications 12

3 Neutrino Astronomy and AMANDA **13**

3.1 Neutrino Astronomy 13

3.2 AMANDA: Antarctic Muon and Neutrino Detector Array 14

3.3 Detection and Path Reconstruction 16

4 Analysis of AMANDA-B10 Data (1997-1999) **21**

4.1 Signal Simulation and Monte Carlo Generation 21

4.2 Effective Area 29

4.3 Background Studies 30

4.4 Blindness 33

4.5 Data Handling 34

4.6 Merging of BATSE and AMANDA Data . . . 34
4.7 Reconstruction . . . 35
4.8 Quality Cuts . . . 35
4.9 Significance Calculations . . . 36
4.10 Additional Notes for 1998 and 1999 . . . 38

5 Analysis of AMANDA-II GRB Data (2000) 39

5.1 AMANDA-II . . . 39
5.2 Data Filtering and Stability . . . 39
5.3 Signal Simulation and Monte Carlo Generation . . . 41
5.4 Model Rejection Factor . . . 43
5.5 Quality Cuts . . . 46
5.6 Evolution of "Waxman-Bahcall" and "Halzen-Hooper" Fluxes . . . 49
5.7 Search . . . 61
5.8 Note on Setting Upper Limit . . . 63
5.9 Summary . . . 64

6 Results 65

6.1 Comment on Neutrino Oscillations . . . 65
6.2 Results . . . 65
6.3 Theoretical Impact . . . 67

7 Future 68

7.1 Other Satellite Detectors . . . 68
7.2 Current Data Extraction . . . 69
7.3 Other Types of Searches . . . 70
7.4 IceCube . . . 70

A Non-Triggered Bursts 76

A.1 BATSE Archived Data . . . 76

B Computation and Data Processing **80**

B.1 1997-1999 80

B.2 2000 83

C Soft Gamma Repeater 1900+14 **84**

C.1 Soft Gamma Repeaters 84

C.2 Neutrino Search 84

D Atmospheric Neutrino Overlap Analysis **85**

D.1 Atmospheric Neutrinos 85

D.2 GRB Search 85

E GRBs Studied in Analysis **86**

E.1 1997 BATSE GRBs 86

E.2 1998 BATSE GRBs 88

E.3 1999 BATSE GRBs 91

E.4 2000 BATSE GRBs 93

F Blinded Event Rates for 1999 **95**

G Unblinded Event Rates for 1999 **101**

H Distribution of Background Events in 10-Second Windows **126**

I Some δ-t Plots for 2000 **130**

J Blinded Event Rates for 2000 **134**

K Unblinded Event Rates for 2000 **139**

List of Tables

1.1 The general characteristics of GRBs. 4

3.1 Evolution of the AMANDA detector. AMANDA-A was deployed between 800 and 1000 meters [46]. AMANDA-II strings have generally been deployed between 1.5 and 2 km. 16

4.1 Number of events expected in the AMANDA-B10 array for different values of the GRB boost factor, Γ. The parameter A and E_B in Equation 4.1 are choosen to reproduce the results of reference [47]. The last two columns are the actual number of events expected for 78 GRBs (the number in the 1997 AMANDA data set) before and after the angular and quality cuts. 22

4.2 The well-known redshifts of some GRBs, in increasing distance. 23

4.3 The values of the normalization constant, A, for 3 values of Γ and 3 assumptions of GRB evolution. The units are TeV / cm^2 sec sr. 23

4.4 Sky binning for determining zenith-dependent cuts. 25

4.5 Expected number of events in AMANDA-B10 from Monte Carlo simulations. Here, the cuts are independent of zenith and burst durations. Results are shown for comparison purposes. 28

4.6 The number of triggered BATSE bursts analyzed in each year of AMANDA data. . . . 32

4.7 Data gaps found in 96 GRB files. 33

4.8 Final cut results for AMANDA-B10. (See Table 4.4 for details on the sky binning procedure.) 37

5.1 Data gaps found in 70 GRB files. 40

5.2 Stages of event selection. 41

5.3 Calculation of the Model Rejection Factor (MRF) for two sets of cuts. The signal and background rates are for 44 GRBs, the number of triggered bursts examined in this analysis. See text for more details. 45

5.4 Final quality cuts for AMANDA-II GRB data. 49

6.1 The expected number of signal events in 2π sr for three fluxes: Waxman-Bahcall [24], Alvarez-Muñiz, Halzen and Hooper [47] with and without fluctuations in energy and distance. 66

6.2 Summary of search results. 67

B.1 Monte Carlo production statistics. The number of events, time required, and file sizes are per file per CPU for $E_\nu < 10$ PeV. *Line fit results are piped directly to muff and then to recoos again for the full reconstruction. 82

List of Figures

1.1 Compton Gamma Ray Observatory. 2
1.2 One of eight detectors that constituted the Burst and Transient Satellite Experiment. 3
1.3 This map shows the locations of 2704 gamma-ray bursts recorded by BATSE during its nine-year mission. The distribution is isotropic. 4
1.4 Sample time profiles of GRB photon emission. Note the unique, often complicated structure. Also note the smaller time scale for the last sample burst. 5
1.5 BATSE's angular resolution for GRBs detected 1997-2000. 6
1.6 Distribution of GRB durations measured by BATSE. 6
1.7 BeppoSAX observation of GRB970228. The left side shows a region of sky on February 28, 1997, during the gamma-ray burst. The right side shows the same region of sky three days later. 7

2.1 The cosmic ray spectrum with the breaks in the spectrum at the "knee" and "ankle" highlighted. 11

3.1 Optical modules. 14
3.2 The AMANDA detector. 15
3.3 Detection of Cerenkov light by PMTs. 17
3.4 A neutrino candidate event in the AMANDA-B10 detector. The time profile of this event indicates that the muon is traveling upwards. 18

3.5 AMANDA coordinate system. "Upgoing" neutrinos originate in the northern hemisphere, enter the detector from below, and exit through the top. "Downgoing" events originate in the atmosphere of the southern hemisphere and enter the top of the detector first. θ is the local zenith coordinate and ϕ is local azimuth. 19

3.6 The energy of muons at the center of the AMANDA-B10 detector, from background cosmic rays and from GRB neutrinos. 20

4.1 The Alvarez-Muñiz, Halzen and Hooper fluxes for 5 values of Γ [47]. 24

4.2 GRB spectrum at AMANDA-B10 trigger level. The plot is a convolution of the neutrino flux and the probability of conversion to a muon within the range of the detector. The integral of this curve gives the expected event rate for AMANDA-B10. The result is about 0.1 events for 78 bursts with Γ=300. 26

4.3 Number of events expected at trigger level as a function of zenith angle for $\Gamma = 300$ and a 30^o search bin. Cos(zenith)=1 denotes upgoing events and cos(zenith)=0 denotes horizontal events. 27

4.4 Effective area of detector before and after cuts. 30

4.5 Two hours of data are used to characterize the background. 31

4.6 P_C is the probability that the observed number of events is due to background. It is the area under the curve greater than the number of events observed. 37

5.1 The zenith dependence of the GRB signal at trigger level in AMANDA-II. 42

5.2 Offset between the reconstructed zenith angle and the true zenith angle in AMA-II without any quality cut. 43

5.3 There is almost no offset between the reconstructed zenith angle and the true zenith angle in AMA-II when a soft quality cut of nch>8 is applied. 44

5.4 The number of ndird direct hits for background data and signal Monte Carlo. 47

5.5 The smoothness of the distribution of hits along the reconstructed muon track. Background data is the solid line; signal Monte Carlo is dotted. A high-quality event has a small absolute value of smoothness. 48

5.6 The number of channels involved in background and signal events. 50

5.7 The MRF as a function of nch. 51

5.8 The MRF as a function of ndird. 52

5.9 The background and signal distribution of nch with all cuts except nch>25 applied. . 53

5.10 The background and signal distribution of ndird with all cuts except ndird>14 applied. 54

5.11 The background and signal distribution of smootallphit with all cuts except smoothness applied. 55

5.12 The Waxman-Bahcall flux [24] before and after the final quality cuts. 56

5.13 The Waxman-Bahcall flux [24] as a function of cosine(zenith) before and after the final quality cuts. Horizontal events have a cos(zenith)=0.0 and vertical upgoing events have a cos(zenith)=-1.0. 57

5.14 The Waxman-Bahcall flux of [24]. 59

5.15 The Alvarez-Muñiz, Halzen and Hooper fluxes for 5 values of Γ [47]. 60

5.16 The Waxman-Bahcall flux of [wax-bah2] and the Alvarez-Muñiz, Halzen and Hooper flux, with and without fluctuations in energy and distance, for Γ=300. 62

A.1 Light curve from non-triggered burst 970914.91 found by Kommers [82]. 77

A.2 Distribution of peak fluxes for bursts triggered on-board BATSE and for non-triggered bursts found in archived data by [70]. 77

A.3 Distribution of 1σ error boxes for triggered and non-triggered bursts. 78

F.1 The background distribution of events for grb7379, except for the 10 minute blind spot around the trigger time, before (top) and after (bottom) cuts. 96

F.2 The background distribution of events for grb7387, except for the 10 minute blind spot around the trigger time, before (top) and after (bottom) cuts. 96

F.3 The background distribution of events for grb7403, except for the 10 minute blind spot around the trigger time, before (top) and after (bottom) cuts. 96

F.4 The background distribution of events for grb7429, except for the 10 minute blind spot around the trigger time, before (top) and after (bottom) cuts. 96

F.5 The background distribution of events for grb7434, except for the 10 minute blind spot around the trigger time, before (top) and after (bottom) cuts. 97

F.6 The background distribution of events for grb7448, except for the 10 minute blind spot around the trigger time, before (top) and after (bottom) cuts. 97

F.7 The background distribution of events for grb7451, except for the 10 minute blind spot around the trigger time, before (top) and after (bottom) cuts. 97

F.8 The background distribution of events for grb7452, except for the 10 minute blind spot around the trigger time, before (top) and after (bottom) cuts. 97

F.9 The background distribution of events for grb7455, except for the 10 minute blind spot around the trigger time, before (top) and after (bottom) cuts. 98

F.10 The background distribution of events for grb7456, except for the 10 minute blind spot around the trigger time, before (top) and after (bottom) cuts. 98

F.11 The background distribution of events for grb7457, except for the 10 minute blind spot around the trigger time, before (top) and after (bottom) cuts. 98

F.12 The background distribution of events for grb7460, except for the 10 minute blind spot around the trigger time, before (top) and after (bottom) cuts. 98

F.13 The background distribution of events for grb7464, except for the 10 minute blind spot around the trigger time, before (top) and after (bottom) cuts. 99

F.14 The background distribution of events for grb7481, except for the 10 minute blind spot around the trigger time, before (top) and after (bottom) cuts. 99

F.15 The background distribution of events for grb7484, except for the 10 minute blind spot around the trigger time, before (top) and after (bottom) cuts. 99

F.16 The background distribution of events for grb7485, except for the 10 minute blind spot around the trigger time, before (top) and after (bottom) cuts. 99

F.17 The background distribution of events for grb7486, except for the 10 minute blind spot around the trigger time, before (top) and after (bottom) cuts. 100

F.18 The background distribution of events for grb7487, except for the 10 minute blind spot around the trigger time, before (top) and after (bottom) cuts. 100

G.1 The number of events for grb7379 during the burst, before (top) and after (bottom) cuts. . . 102

G.2 The number of events for grb7387 during the burst, before (top) and after (bottom) cuts. . . 102

G.3 The number of events for grb7403 during the burst, before (top) and after (bottom) cuts. . . 102
G.4 The number of events for grb7429 during the burst, before (top) and after (bottom) cuts. . . 102
G.5 The number of events for grb7434 during the burst, before (top) and after (bottom) cuts. . . 103
G.6 The number of events for grb7448 during the burst, before (top) and after (bottom) cuts. . . 103
G.7 The number of events for grb7451 during the burst, before (top) and after (bottom) cuts. . . 103
G.8 The number of events for grb7452 during the burst, before (top) and after (bottom) cuts. . . 103
G.9 The number of events for grb7455 during the burst, before (top) and after (bottom) cuts. . . 104
G.10 The number of events for grb7456 during the burst, before (top) and after (bottom) cuts. . . 104
G.11 The number of events for grb7457 during the burst, before (top) and after (bottom) cuts. . . 104
G.12 The number of events for grb7460 during the burst, before (top) and after (bottom) cuts. . . 104
G.13 The number of events for grb7464 during the burst, before (top) and after (bottom) cuts. . . 105
G.14 The number of events for grb7481 during the burst, before (top) and after (bottom) cuts. . . 105
G.15 The number of events for grb7484 during the burst, before (top) and after (bottom) cuts. . . 105
G.16 The number of events for grb7485 during the burst, before (top) and after (bottom) cuts. . . 105
G.17 The number of events for grb7486 during the burst, before (top) and after (bottom) cuts. . . 106
G.18 The number of events for grb7487 during the burst, before (top) and after (bottom) cuts. . . 106
G.19 The number of events for grb7489 during the burst, before (top) and after (bottom) cuts. . . 106
G.20 The number of events for grb7494 during the burst, before (top) and after (bottom) cuts. . . 106
G.21 The number of events for grb7495 during the burst, before (top) and after (bottom) cuts. . . 107
G.22 The number of events for grb7497 during the burst, before (top) and after (bottom) cuts. . . 107
G.23 The number of events for grb7498 during the burst, before (top) and after (bottom) cuts. . . 107
G.24 The number of events for grb7504 during the burst, before (top) and after (bottom) cuts. . . 107
G.25 The number of events for grb7513 during the burst, before (top) and after (bottom) cuts. . . 108
G.26 The number of events for grb7514 during the burst, before (top) and after (bottom) cuts. . . 108
G.27 The number of events for grb7523 during the burst, before (top) and after (bottom) cuts. . . 108
G.28 The number of events for grb7528 during the burst, before (top) and after (bottom) cuts. . . 108
G.29 The number of events for grb7529 during the burst, before (top) and after (bottom) cuts. . . 109
G.30 The number of events for grb7539 during the burst, before (top) and after (bottom) cuts. . . 109

G.31 The number of events for grb7541 during the burst, before (top) and after (bottom) cuts. . . 109
G.32 The number of events for grb7550 during the burst, before (top) and after (bottom) cuts. . . 109
G.33 The number of events for grb7552 during the burst, before (top) and after (bottom) cuts. . . 110
G.34 The number of events for grb7554 during the burst, before (top) and after (bottom) cuts. . . 110
G.35 The number of events for grb7561 during the burst, before (top) and after (bottom) cuts. . . 110
G.36 The number of events for grb7567 during the burst, before (top) and after (bottom) cuts. . . 110
G.37 The number of events for grb7573 during the burst, before (top) and after (bottom) cuts. . . 111
G.38 The number of events for grb7578 during the burst, before (top) and after (bottom) cuts. . . 111
G.39 The number of events for grb7581 during the burst, before (top) and after (bottom) cuts. . . 111
G.40 The number of events for grb7582 during the burst, before (top) and after (bottom) cuts. . . 111
G.41 The number of events for grb7587 during the burst, before (top) and after (bottom) cuts. . . 112
G.42 The number of events for grb7594 during the burst, before (top) and after (bottom) cuts. . . 112
G.43 The number of events for grb7598 during the burst, before (top) and after (bottom) cuts. . . 112
G.44 The number of events for grb7599 during the burst, before (top) and after (bottom) cuts. . . 112
G.45 The number of events for grb7602 during the burst, before (top) and after (bottom) cuts. . . 113
G.46 The number of events for grb7604 during the burst, before (top) and after (bottom) cuts. . . 113
G.47 The number of events for grb7608 during the burst, before (top) and after (bottom) cuts. . . 113
G.48 The number of events for grb7615 during the burst, before (top) and after (bottom) cuts. . . 113
G.49 The number of events for grb7625 during the burst, before (top) and after (bottom) cuts. . . 114
G.50 The number of events for grb7626 during the burst, before (top) and after (bottom) cuts. . . 114
G.51 The number of events for grb7630 during the burst, before (top) and after (bottom) cuts. . . 114
G.52 The number of events for grb7632 during the burst, before (top) and after (bottom) cuts. . . 114
G.53 The number of events for grb7633 during the burst, before (top) and after (bottom) cuts. . . 115
G.54 The number of events for grb7648 during the burst, before (top) and after (bottom) cuts. . . 115
G.55 The number of events for grb7652 during the burst, before (top) and after (bottom) cuts. . . 115
G.56 The number of events for grb7654 during the burst, before (top) and after (bottom) cuts. . . 115
G.57 The number of events for grb7655 during the burst, before (top) and after (bottom) cuts. . . 116
G.58 The number of events for grb7660 during the burst, before (top) and after (bottom) cuts. . . 116

G.59 The number of events for grb7662 during the burst, before (top) and after (bottom) cuts. . . 116
G.60 The number of events for grb7665 during the burst, before (top) and after (bottom) cuts. . . 116
G.61 The number of events for grb7671 during the burst, before (top) and after (bottom) cuts. . . 117
G.62 The number of events for grb7674 during the burst, before (top) and after (bottom) cuts. . . 117
G.63 The number of events for grb7683 during the burst, before (top) and after (bottom) cuts. . . 117
G.64 The number of events for grb7688 during the burst, before (top) and after (bottom) cuts. . . 117
G.65 The number of events for grb7693 during the burst, before (top) and after (bottom) cuts. . . 118
G.66 The number of events for grb7703 during the burst, before (top) and after (bottom) cuts. . . 118
G.67 The number of events for grb7705 during the burst, before (top) and after (bottom) cuts. . . 118
G.68 The number of events for grb7706 during the burst, before (top) and after (bottom) cuts. . . 118
G.69 The number of events for grb7707 during the burst, before (top) and after (bottom) cuts. . . 119
G.70 The number of events for grb7735 during the burst, before (top) and after (bottom) cuts. . . 119
G.71 The number of events for grb7737 during the burst, before (top) and after (bottom) cuts. . . 119
G.72 The number of events for grb7749 during the burst, before (top) and after (bottom) cuts. . . 119
G.73 The number of events for grb7750 during the burst, before (top) and after (bottom) cuts. . . 120
G.74 The number of events for grb7753 during the burst, before (top) and after (bottom) cuts. . . 120
G.75 The number of events for grb7754 during the burst, before (top) and after (bottom) cuts. . . 120
G.76 The number of events for grb7764 during the burst, before (top) and after (bottom) cuts. . . 120
G.77 The number of events for grb7766 during the burst, before (top) and after (bottom) cuts. . . 121
G.78 The number of events for grb7769 during the burst, before (top) and after (bottom) cuts. . . 121
G.79 The number of events for grb7770 during the burst, before (top) and after (bottom) cuts. . . 121
G.80 The number of events for grb7774 during the burst, before (top) and after (bottom) cuts. . . 121
G.81 The number of events for grb7775 during the burst, before (top) and after (bottom) cuts. . . 122
G.82 The number of events for grb7776 during the burst, before (top) and after (bottom) cuts. . . 122
G.83 The number of events for grb7781 during the burst, before (top) and after (bottom) cuts. . . 122
G.84 The number of events for grb7784 during the burst, before (top) and after (bottom) cuts. . . 122
G.85 The number of events for grb7790 during the burst, before (top) and after (bottom) cuts. . . 123
G.86 The number of events for grb7791 during the burst, before (top) and after (bottom) cuts. . . 123

G.87 The number of events for grb7792 during the burst, before (top) and after (bottom) cuts. . . 123
G.88 The number of events for grb7800 during the burst, before (top) and after (bottom) cuts. . . 123
G.89 The number of events for grb7802 during the burst, before (top) and after (bottom) cuts. . . 124
G.90 The number of events for grb7811 during the burst, before (top) and after (bottom) cuts. . . 124
G.91 The number of events for grb7822 during the burst, before (top) and after (bottom) cuts. . . 124
G.92 The number of events for grb7835 during the burst, before (top) and after (bottom) cuts. . . 124
G.93 The number of events for grb7838 during the burst, before (top) and after (bottom) cuts. . . 125
G.94 The number of events for grb7840 during the burst, before (top) and after (bottom) cuts. . . 125

H.1 Number of background events in 10-second intervals for GRB 7988, 7989, 7991 and 7992. 127
H.2 Number of background events in 10-second intervals for GRB 7994, 7995, 7997 and 7998.127
H.3 Number of background events in 10-second intervals for GRB 7999, 8002, 8004 and 8005.127
H.4 Number of background events in 10-second intervals for GRB 8008, 8009 and 8012. . . 127
H.5 Number of background events in 10-second intervals for GRB 8022, 8030, 8031 and 8035.128
H.6 Number of background events in 10-second intervals for GRB 8036, 8039, 8045, 8047. . 128
H.7 Number of background events in 10-second intervals for GRB 8049, 8056, 8057 and 8061.128
H.8 Number of background events in 10-second intervals for GRB 8063, 8064, 8069 and 8071.128
H.9 Number of background events in 10-second intervals for GRB 8074. 8075, 8077 and 8079. 129
H.10 Number of background events in 10-second intervals for GRB 8084, 8085, 8086 and 8097.129
H.11 Number of background events in 10-second intervals for GRB 8099, 8109, 8110 and 8111.129

I.1 Time between consecutive events, δt, plots for GRB 7988, 7989, 7991 and 7992. 131
I.2 Time between consecutive events, δt, plots for GRB 7994, 7995, 7997 and7998. 131
I.3 Time between consecutive events, δt, plots for GRB 7999, 8002, 8004 and 8005. . . . 131
I.4 Time between consecutive events, δt, plots for GRB 8008, 8009, 8012 and 8022. . . . 131
I.5 Time between consecutive events, δt, plots for GRB 8030, 8031, 8035 and 8036. . . . 132
I.6 Time between consecutive events, δt, plots for GRB 8039, 8045, 8047 and 8049. . . . 132
I.7 Time between consecutive events, δt, plots for GRB 8056, 8057, 8061 and 8063. . . . 132

I.8 Time between consecutive events, δt, plots for GRB 8064, 8069, 8071 and 8074. . . . 132

I.9 Time between consecutive events, δt, plots for GRB 8075, 8077, 8079 and 8084. . . . 133

I.10 Time between consecutive events, δt, plots for GRB 8085, 8086, 8097 and 8099. . . . 133

I.11 Time between consecutive events, δt, plots for GRB 8109, 8110 and 8111. 133

J.1 The background distribution of events for grb11591c, except for the 10 minute blind spot around the trigger time, before (top) and after (bottom) cuts. 135

J.2 The background distribution of events for grb11597b, except for the 10 minute blind spot around the trigger time, before (top) and after (bottom) cuts. 135

J.3 The background distribution of events for grb11599b, except for the 10 minute blind spot around the trigger time, before (top) and after (bottom) cuts. 135

J.4 The background distribution of events for grb11600b, except for the 10 minute blind spot around the trigger time, before (top) and after (bottom) cuts. 135

J.5 The background distribution of events for grb11602b, except for the 10 minute blind spot around the trigger time, before (top) and after (bottom) cuts. 136

J.6 The background distribution of events for grb11608a, except for the 10 minute blind spot around the trigger time, before (top) and after (bottom) cuts. 136

J.7 The background distribution of events for grb11609b, except for the 10 minute blind spot around the trigger time, before (top) and after (bottom) cuts. 136

J.8 The background distribution of events for grb11625b, except for the 10 minute blind spot around the trigger time, before (top) and after (bottom) cuts. 136

J.9 The background distribution of events for grb11633b, except for the 10 minute blind spot around the trigger time, before (top) and after (bottom) cuts. 137

J.10 The background distribution of events for grb11633f, except for the 10 minute blind spot around the trigger time, before (top) and after (bottom) cuts. 137

J.11 The background distribution of events for grb11634g, except for the 10 minute blind spot around the trigger time, before (top) and after (bottom) cuts. 137

J.12 The background distribution of events for grb11637c, except for the 10 minute blind spot around the trigger time, before (top) and after (bottom) cuts. 137

J.13 The background distribution of events for grb11637e, except for the 10 minute blind spot around the trigger time, before (top) and after (bottom) cuts. 138

J.14 The background distribution of events for grb11638b, except for the 10 minute blind spot around the trigger time, before (top) and after (bottom) cuts. 138

J.15 The background distribution of events for grb11642d, except for the 10 minute blind spot around the trigger time, before (top) and after (bottom) cuts. 138

J.16 The background distribution of events for grb11644b, except for the 10 minute blind spot around the trigger time, before (top) and after (bottom) cuts. 138

K.1 The number of events for grb11591c during the burst, before (top) and after (bottom) cuts. . 140

K.2 The number of events for grb11597b during the burst, before (top) and after (bottom) cuts. . 140

K.3 The number of events for grb11599b during the burst, before (top) and after (bottom) cuts. . 140

K.4 The number of events for grb11599b during the burst, before (top) and after (bottom) cuts. . 140

K.5 The number of events for grb11602b during the burst, before (top) and after (bottom) cuts. . 141

K.6 The number of events for grb11608a during the burst, before (top) and after (bottom) cuts. . 141

K.7 The number of events for grb11609b during the burst, before (top) and after (bottom) cuts. . 141

K.8 The number of events for grb11625b during the burst, before (top) and after (bottom) cuts. . 141

K.9 The number of events for grb11633b during the burst, before (top) and after (bottom) cuts. . 142

K.10 The number of events for grb11633f during the burst, before (top) and after (bottom) cuts. . 142

K.11 The number of events for grb11634g during the burst, before (top) and after (bottom) cuts. . 142

K.12 The number of events for grb11637c during the burst, before (top) and after (bottom) cuts. . 142

K.13 The number of events for grb11637e during the burst, before (top) and after (bottom) cuts. . 143

K.14 The number of events for grb11638b during the burst, before (top) and after (bottom) cuts. . 143

K.15 The number of events for grb11642d during the burst, before (top) and after (bottom) cuts. . 143

K.16 The number of events for grb11644b during the burst, before (top) and after (bottom) cuts. . 143

K.17 The number of events for grb11644f during the burst, before (top) and after (bottom) cuts. . 144

K.18 The number of events for grb11646c during the burst, before (top) and after (bottom) cuts. . 144

K.19 The number of events for grb11650a during the burst, before (top) and after (bottom) cuts. . 145

K.20 The number of events for grb11652g during the burst, before (top) and after (bottom) cuts. . 145

K.21 The number of events for grb11654b during the burst, before (top) and after (bottom) cuts. . 145

K.22 The number of events for grb11663b during the burst, before (top) and after (bottom) cuts. . 145

K.23 The number of events for grb11663f during the burst, before (top) and after (bottom) cuts. . 146

K.24 The number of events for grb11668c during the burst, before (top) and after (bottom) cuts. . 146

K.25 The number of events for grb11672h during the burst, before (top) and after (bottom) cuts. . 146

K.26 The number of events for grb11675e during the burst, before (top) and after (bottom) cuts. . 146

K.27 The number of events for grb7988 during the burst, before (top) and after (bottom) cuts. . . 147

K.28 The number of events for grb7989 during the burst, before (top) and after (bottom) cuts. . . 147

K.29 The number of events for grb7991 during the burst, before (top) and after (bottom) cuts. . . 147

K.30 The number of events for grb7992 during the burst, before (top) and after (bottom) cuts. . . 147

K.31 The number of events for grb7994 during the burst, before (top) and after (bottom) cuts. . . 148

K.32 The number of events for grb7995 during the burst, before (top) and after (bottom) cuts. . . 148

K.33 The number of events for grb7997 during the burst, before (top) and after (bottom) cuts. . . 148

K.34 The number of events for grb7998 during the burst, before (top) and after (bottom) cuts. . . 148

K.35 The number of events for grb7999 during the burst, before (top) and after (bottom) cuts. . . 149

K.36 The number of events for grb8002 during the burst, before (top) and after (bottom) cuts. . . 149

K.37 The number of events for grb8004 during the burst, before (top) and after (bottom) cuts. . . 150

K.38 The number of events for grb8005 during the burst, before (top) and after (bottom) cuts. . . 150

K.39 The number of events for grb8008 during the burst, before (top) and after (bottom) cuts. . . 150

K.40 The number of events for grb8009 during the burst, before (top) and after (bottom) cuts. . . 150

K.41 The number of events for grb8012 during the burst, before (top) and after (bottom) cuts. . . 151

K.42 The number of events for grb8019 during the burst, before (top) and after (bottom) cuts. . . 151

K.43 The number of events for grb8022 during the burst, before (top) and after (bottom) cuts. . . 151

K.44 The number of events for grb8030 during the burst, before (top) and after (bottom) cuts. . . 151

K.45 The number of events for grb8031 during the burst, before (top) and after (bottom) cuts. . . 152

K.46 The number of events for grb8035 during the burst, before (top) and after (bottom) cuts. . . 152

K.47 The number of events for grb8036 during the burst, before (top) and after (bottom) cuts. . . 152

K.48 The number of events for grb8039 during the burst, before (top) and after (bottom) cuts. . . 152

K.49 The number of events for grb8045 during the burst, before (top) and after (bottom) cuts. . . 153
K.50 The number of events for grb8047 during the burst, before (top) and after (bottom) cuts. . . 153
K.51 The number of events for grb8049 during the burst, before (top) and after (bottom) cuts. . . 153
K.52 The number of events for grb8056 during the burst, before (top) and after (bottom) cuts. . . 153
K.53 The number of events for grb8057 during the burst, before (top) and after (bottom) cuts. . . 154
K.54 The number of events for grb8061 during the burst, before (top) and after (bottom) cuts. . . 154
K.55 The number of events for grb8063 during the burst, before (top) and after (bottom) cuts. . . 154
K.56 The number of events for grb8064 during the burst, before (top) and after (bottom) cuts. . . 154
K.57 The number of events for grb8069 during the burst, before (top) and after (bottom) cuts. . . 155
K.58 The number of events for grb8071 during the burst, before (top) and after (bottom) cuts. . . 155
K.59 The number of events for grb8074 during the burst, before (top) and after (bottom) cuts. . . 155
K.60 The number of events for grb8075 during the burst, before (top) and after (bottom) cuts. . . 155
K.61 The number of events for grb8077 during the burst, before (top) and after (bottom) cuts. . . 156
K.62 The number of events for grb8079 during the burst, before (top) and after (bottom) cuts. . . 156
K.63 The number of events for grb8084 during the burst, before (top) and after (bottom) cuts. . . 156
K.64 The number of events for grb8085 during the burst, before (top) and after (bottom) cuts. . . 156
K.65 The number of events for grb8086 during the burst, before (top) and after (bottom) cuts. . . 157
K.66 The number of events for grb8097 during the burst, before (top) and after (bottom) cuts. . . 157
K.67 The number of events for grb8099 during the burst, before (top) and after (bottom) cuts. . . 157
K.68 The number of events for grb8109 during the burst, before (top) and after (bottom) cuts. . . 157
K.69 The number of events for grb8110 during the burst, before (top) and after (bottom) cuts. . . 158
K.70 The number of events for grb8111 during the burst, before (top) and after (bottom) cuts. . . 158

Chapter 1

Gamma-Ray Bursts

1.1 Discovery

In the 1960s, the United States government deployed a network of satellites to monitor the earth for clandestine nuclear explosions that would violate the Partial Test Ban treaty. This network, called Vela, was administered by the Department of Defense and the Atomic Energy Commission (the precursor of today's Department of Energy). Vela did not detect terrestrial explosions. Perhaps more surprisingly, Vela did detect gamma-ray explosions from space. The intense explosions lasted a few seconds, did not repeat, and were seemingly random in time and location. Gamma-ray bursts (GRBs) were classified until their discovery was announced and published in 1973 [1].

In the 1970s and 1980s, the field suffered from a lack of observational data, and few constraints could be placed on the phenomenon. Dozens of widely varying theories regarding the sources of the high energy eruptions were proposed. One proposed origin was the collision of comets in the Oort cloud that surrounds our solar system [2, 3]. This hypothesis could not reproduce the high energies that had been observed. Another proposal was that the bursts were erupting from neutron stars in our galactic disk [4, 5] or galactic halo [6]. This hypothesis was initially supported by reports of emission lines in the bursts, but the lines were not confirmed by later experiments. This idea produced too few sources.

The overarching difficulty of explaining the origins of GRBs was the production of such large energies. Most scientists believed that whatever was producing such energies must originate in our

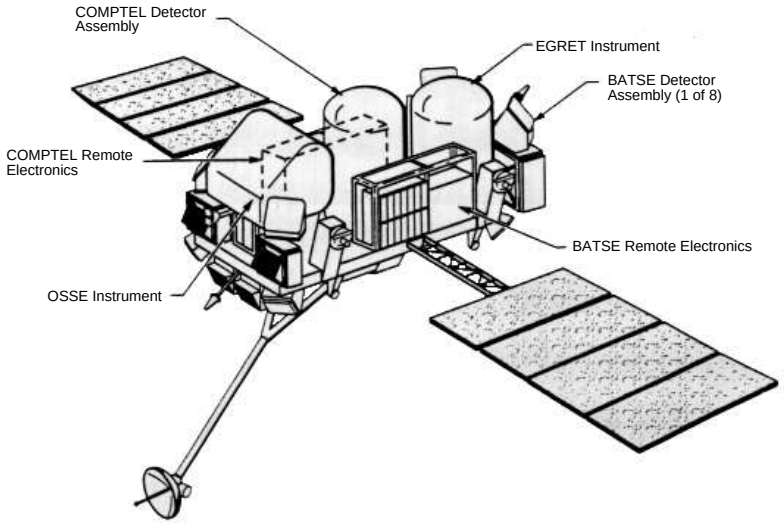

Figure 1.1: Compton Gamma Ray Observatory.

galaxy. If the bursts were at cosmological distances, the energy requirements would be enormous.

Gamma-rays interact in the earth's atmosphere, producing a shower of particles and energy. These cascades can be detected by air shower experiments on the ground, but must be separated from showers produced by cosmic rays (atomic nuclei). Gamma-rays can be directly detected above the earth's atmosphere using scintillation methods. This was the method used by Vela and by future satellite detectors.

1.2 Revolution: BATSE

The study of GRBs changed dramatically with the deployment of the Burst and Transient Satellite Experiment (BATSE). BATSE, one experiment aboard the Compton Gamma-Ray Observatory (CGRO)[1], was launched from the Atlantis space shuttle in April of 1991. See Figure 1.1.

BATSE consisted of eight detector modules located at the corners of the CRGO. Each detector weighed about 100kg and operated on 3 Watts of power. See Figure 1.2. The GRB photon flux was

[1]The CGRO housed three other high energy gamma-ray experiments: OSSE, COMPTEL and EGRET.

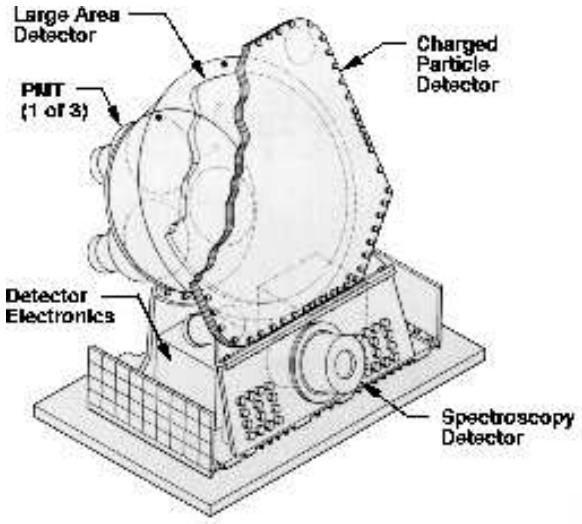

Figure 1.2: One of eight detectors that constituted the Burst and Transient Satellite Experiment.

determined by the number of counts recorded, and the direction of a GRB was determined by the relative counts in the 8 detectors.

With $\sim 1/3$ sky coverage, BATSE detected about one burst per day. BATSE confirmed that the distribution of GRBs was isotropic and uniform [7]. See Figure 1.3. This eliminated several theories of GRB origin, namely those predicting non-isotropic distributions, such as neutron stars in the galactic disk. The isotropy of the bursts hinted that they may indeed be located at cosmological distances.

BATSE recorded fluxes in 4 energy bands: 20-50keV, 50-100 keV, 100-300keV, and $\geq$300keV. The on-board trigger operated on 3 timescales: 64ms, 256 ms, and 1.024 seconds. On-board trigger conditions and further details can be found at [8].

Though still operational, BATSE's mission was ended to ensure safe re-entry of the spacecraft. BATSE recorded its last gamma-ray burst on May 26, 2000 and CGRO was plunged into the Pacific Ocean on June 4, 2001.

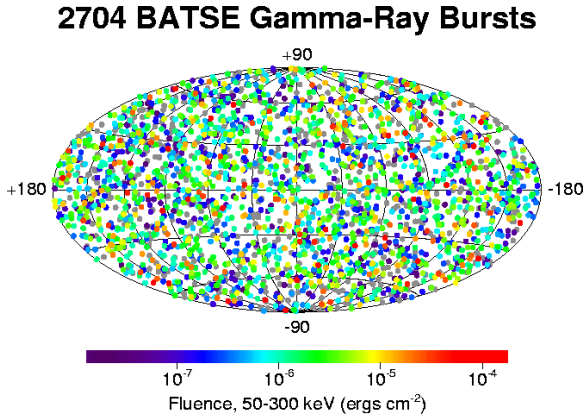

Figure 1.3: This map shows the locations of 2704 gamma-ray bursts recorded by BATSE during its nine-year mission. The distribution is isotropic.

1.3 GRB Characteristics

Table 1.1 outlines the general characteristics of GRBs, but no GRB is exactly like another.

Duration	fraction of a second to many minutes
Flux	100-10^6 photons/m^2/sec
γ energy	0.01 - 100 Mev
γ frequency	10^{15}-10^{24} Hz
Wavelength	μm - fm
Rate	10^{-6}/galaxy/year (without beaming)
Total energy	10^{51}-10^{54} ergs

Table 1.1: The general characteristics of GRBs.

Indeed, BATSE quickly demonstrated that there is no such thing as a "typical" GRB. Temporal structure is noted even on the shortest time scales resolved – milliseconds. Figure 1.4 demonstrates the widely varying nature of GRB photon emission. Some bursts are singularly bright. Some exhibit very complicated temporal structure. Some include afterpulsing. The physical mechanism that emits such enormous amounts of energy must also account for the variety, complexity, and fine structure of the emission.

BATSE's angular resolution depended strongly on the strength of the burst, with strong bursts being localized to one or two degrees and weak bursts having error ellipses on the order of 10 degrees

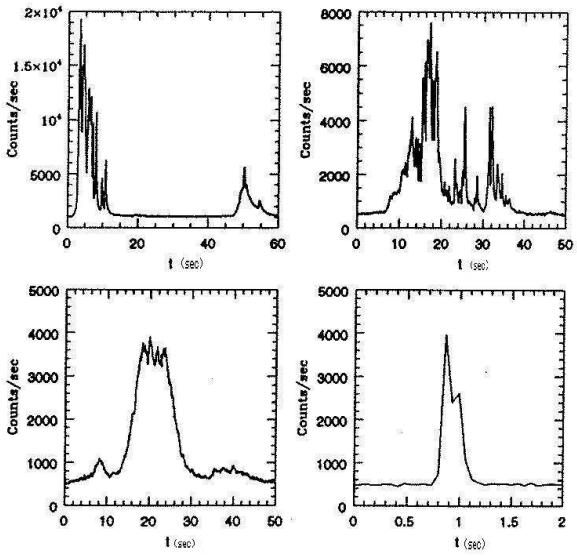

Figure 1.4: Sample time profiles of GRB photon emission. Note the unique, often complicated structure. Also note the smaller time scale for the last sample burst.

or more. See Figure 1.5.

Figure 1.6 shows the durations of GRBs recorded by BATSE. The duration is described by the T90 parameter which is the time over which a burst emits from 5% to 95% of its total measured counts. Lightcurves used for the calculation of T90 are integrated over all 4 channels (E>20 keV). The bimodal distribution of GRB durations, with peaks at 0.3 seconds and at ∼50 seconds, may indicate that there are two classes of GRBs. The short GRBs, those less than 2 seconds long, exhibit the hardest energy spectra [9].

BeppoSAX (see Figure 1.7), an Italian-Dutch X-ray satellite, was the first experiment to accurately localize a GRB in real-time. This led to breakthrough follow-up observations: the longer wavelength afterglows of GRBs; the first redshifts that conclusively showed GRBs to be at cosmological distances; and detection of host galaxies by the Hubble Space Telescope (HST) that resolved the "missing host" problem.

A successful theory of GRB emission must account for the longer wavelength afterglows observed for days and weeks after the initial gamma-ray emission. GRBs have been observed at X-rays, optical and radio frequencies.

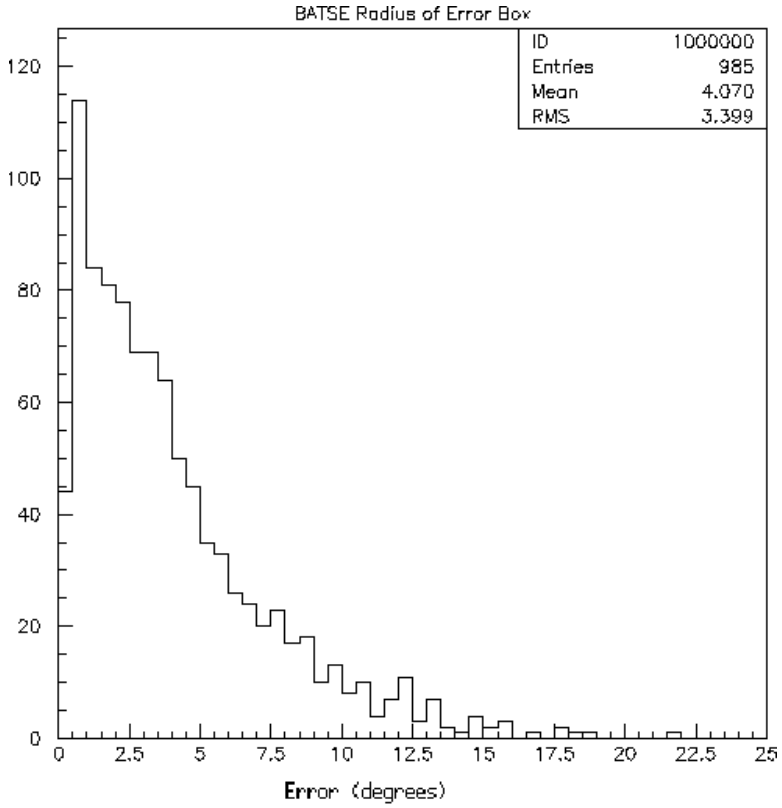

Figure 1.5: BATSE's angular resolution for GRBs detected 1997-2000.

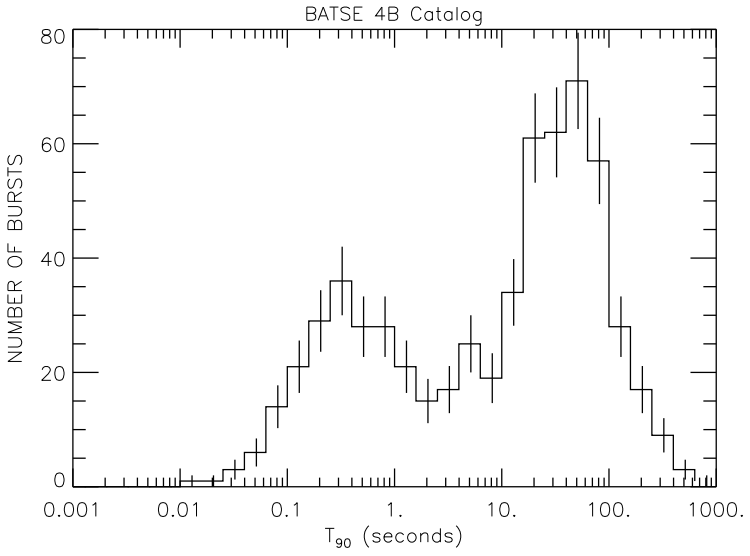

Figure 1.6: Distribution of GRB durations measured by BATSE.

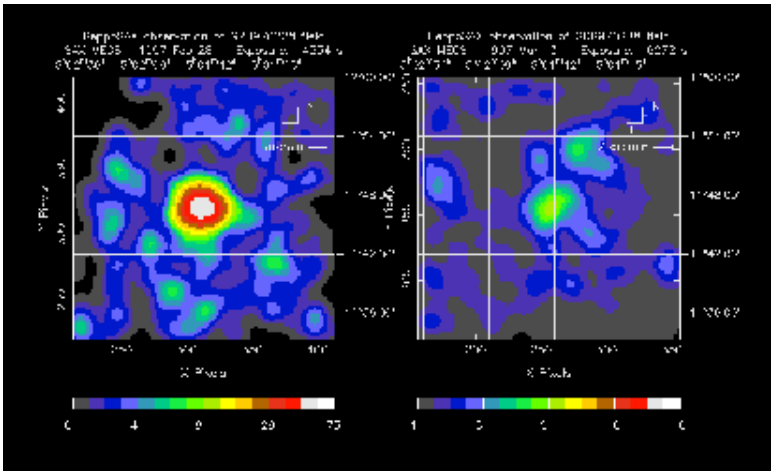

Figure 1.7: BeppoSAX observation of GRB970228. The left side shows a region of sky on February 28, 1997, during the gamma-ray burst. The right side shows the same region of sky three days later.

We now know that these phenomena, the largest explosions in the universe since the Big Bang, are comoslogical in origin. Redshifts of afterglows have been measured via spectroscopy for about 20 GRBs. The largest measured redshift of $z = 4.5$ (GRB000131) implies an isotropic energy release of 10^{54} ergs.

There is evidence, however, for beaming in GRBs. The evidence is found in afterglow studies. The afterglow light curves of GRB990123 and GRB990510 decay gradually and then noticeably "break" to a steeper decay rate [10, 11, 12]. Beaming reduces the total energy requirements of the system, but also increases the total number of GRBs that must be occurring, as we will only observe those which have emission beams along our line of sight. The fraction of GRBs with an opening beam half-angle of θ that we can potentially observe is $2\pi(1 - cos\theta)/4\pi$, or twice that if there are two jets.

The size of the GRB is restricted by its very short temporal variability, δt. Therefore the size of the source is approximately c(δt)$\approx$30km. However, so many energetic photons in such a small space would render the source optically opaque due to the constant pair production of electrons and positrons. Relativistic motion was proposed as a solution to this "compactness" problem. (See next

chapter for further details.) Observations have confirmed relativistic motion in GRBs. Reeves, et al. [13], recently announced the first direct measurement of outflowing matter in a gamma-ray burst at $v/c = 0.086 \pm 0.004$.

Resolution of some GRB host galaxies by HST has shown that these objects are not located in the center of galaxies, and are therefore not correlated with supermassive black holes or AGN. There does seem to be a correlation between hot, energetic star-forming regions and GRBs.

Many ideas regarding the nature of the initial compact object have been offered. Currently, the leading candidates are (1) the mergers of massive objects, like two neutron stars or a neutron star and a black hole, and (2) the collapse of a super-massive star. The merger of massive objects converts the gravitational energy and angular momentum of a decaying binary system to the fireball energy of the GRB. These mergers should emit gravitational waves that would be observed by advanced versions of LIGO and VIRGO. The collapse of a massive star could lead to a GRB in the relativistc analog of a supernova. In fact, there may be an explicit connection between supernovae and GRBs. A Type Ic supernova, 1998bw, occurred at the same time and within the location error box of GRB980425 [14, 15, 16]. Although this was an otherwise unremarkable GRB, this coincidence and the new discovery of heavy element emission lines in GRB011211 [13], indicate that there may indeed be a connection between supernovae and the long duration GRBs[2].

Sadly, whatever they are, the inner engines of GRBs are hidden from direct detection. We are left, for now, to study the life of a GRB after its birth. Its properties and development should tell us, at least indirectly, about its origins. Unlike photons and charged particles, neutrinos can carry information to us from the depths of a GRB, from the earliest stages after its creation.

[2]The study of GRBs has, in fact, come full circle. The very first GRB paper [1] in 1973 searched for an explicit correlation between GRBs and supernovae, but failed to find such a connection within the astronomical capabilities of the day.

Chapter 2

GRBs and Neutrinos

2.1 Fireball Model

The likely process for achieving the extraordinary energies produced by GRBs is the conversion to radiation of the kinetic energy of particles that have been accelerated in a relativistically expanding fireball. This leading, and successful, explanation for the mechanics of a GRB explosion is called the "fireball model". The gamma-ray burst initially consists of a relativistically expanding fireball plasma of electrons, positrons and photons. Protons and neutrons may also be accelerated [17, 18]. Gamma-rays are produced by the synchrotron radiation and inverse Compton scattering of accelerated electrons.

As mentioned previously, the rapid variability of the GRB light curves imply that the source is compact. In these conditions, pair production would make the fireball optically thick if $\sqrt{E_1 E_2} > m_{\mathrm{electron}}c^2$. We know the fireball is not optically thick as the radiation is non-thermal. One way to resolve this difficulty is to assume that the fireball is expanding at relativistic speeds. In this case, the energy at the source is really $E = h\nu_{\mathrm{observed}}/\Gamma$. Thus fewer photons would pair produce electrons and positrons. Also, the radius of the source would be larger by two factors of Γ, $R_{\mathrm{source}} < \Gamma^2 c(\delta \mathrm{T})$, further solving the compactness problem.

So the radiation is initially trapped by the production of $e^- e^+$ pairs. Radiation will finally escape when its energy has fallen below the pair production threshold of 20 keV. At this point, the fireball becomes optically thin and photons will escape, much like the photons of the cosmic

microwave background at last scattering.

In the explosion, shells of matter and energy move away from the source. These shells have different Lorentz factors, and faster shells will collide with slower shells. These shocks convert kinetic energy to internal energy. The rapid variability of GRBs, which is observed on the smallest time scales (ms) that can be resolved by current detectors, is an immediate consequence of these relativistically shocked shells.

Not all the energy of the fireball can be dissipated internally though. External shocks will collide with surrounding or interstellar material as the fireball expands. These external shocks are likely responsible for the afterglow observations of GRBs observed in longer wavelengths.

Rapid variability and afterglows are two of the fundamental successes of the fireball model.

2.2 Hadrons and Cosmic Rays

We know that electrons are accelerated in GRBs as the gamma rays exhibit a synchrotron spectrum. Protons and neutrons may also be accelerated in the fireball. In fact, depending on the object that initiates the explosion, it would be surprising if hadrons were not present. If protons are accelerated in the fireball, they will initiate the production of neutrinos. Neutrinos are the decay products of pions produced when accelerated protons interact with the intense radiation field of the burst:

$$p + \gamma \rightarrow \pi^+ \rightarrow \mu^+ + \nu_\mu \rightarrow e^+ + \nu_e + \overline{\nu}_\mu + \nu_\mu$$

The π^+ receives $\sim 20\%$ of the energy of the interacting proton. Each of the four leptons carries approximately equal energy. Therefore, each neutrino will have $\sim 5\%$ of the energy of the initiating proton.

The neutrino flux can be calculated as a function of the relative ratio of protons and electrons in the fireball. It can, for instance, be fixed by the assumption that GRBs are the source of the observed highest energy cosmic ray flux. In this case, energy should be approximately equally transferred to electrons and protons in the fireball [20].

GRBs have indeed been postulated as the sources of the highest energy cosmic rays [21, 22, 23, 30, 31]. It has been noted that the rate at which energy is injected into the universe by GRBs, $\sim 10^{-10}$ TeV/cm^2 s sr, is closely matched to the energy of the highest energy cosmic rays. Some [32] have

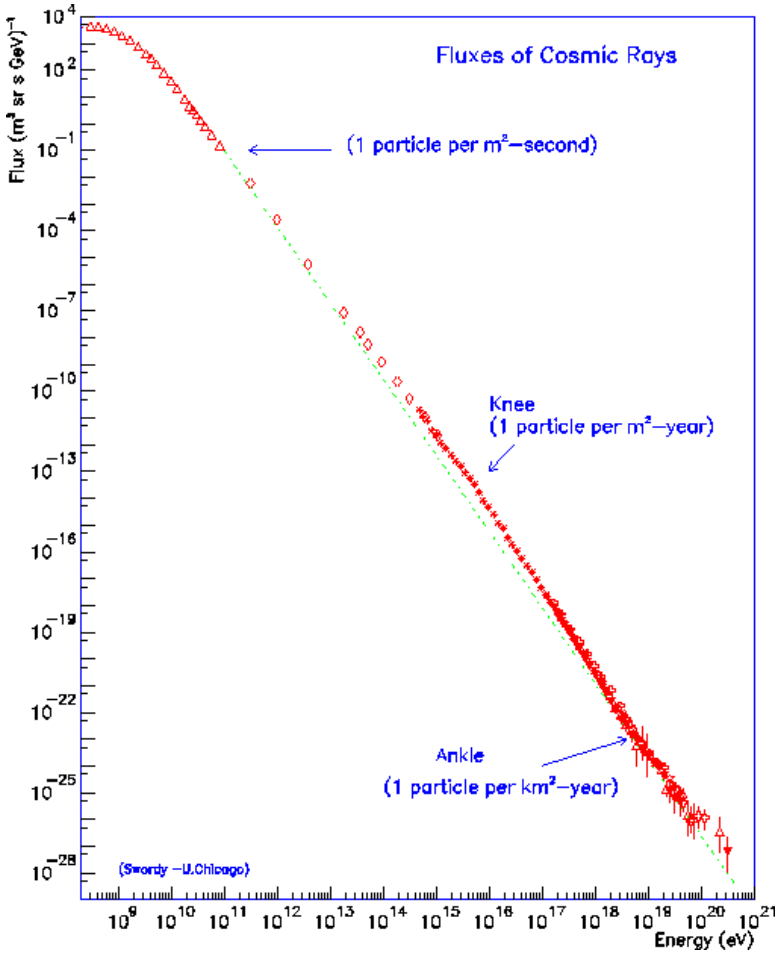

Figure 2.1: The cosmic ray spectrum with the breaks in the spectrum at the "knee" and "ankle" highlighted.

even suggested that GRBs produce the cosmic rays above the "knee" of the cosmic ray spectrum. See Figure 2.1. The discovery of neutrinos from gamma-ray bursts would confirm hadronic acceleration in the fireball.

The GRB neutrino flux predicted by Waxman and Bahcall [23] follows a broken power law spectrum where the flux is given by

$$\frac{dN_\nu}{dE_\nu} = \frac{A}{E_b E_\nu} \text{ for } \mathrm{E}_\nu < \mathrm{E}_\mathrm{b} \tag{2.1}$$

and

$$\frac{dN_\nu}{dE_\nu} = \frac{A}{E_\nu^2} \text{ for } \mathrm{E}_\nu > \mathrm{E}_\mathrm{b}. \tag{2.2}$$

A, with units of $\frac{\mathrm{TeV}}{\mathrm{cm}^2 \text{ sec sr}}$, is the normalization constant. E_b is the energy at which the differential flux spectrum breaks from power $\alpha = -1$ to $\alpha = -2$.

An alternative to the fireball model has been proposed by Dar and De Rujula [33]. In this model, the neutrino beam is much more tightly collimated than the gamma ray beam. The neutrino beam is so small that we would have to examine about 10,000 GRBs before having a chance of finding one in which the neutrino beam was directed at us. At this point, the GRB sample is not large enough for AMANDA to comment on this scenario.

2.3 Other Implications

Detection of neutrinos from GRBs would verify the fireball scenario. Studying GRB neutrinos may also permit these fundamental tests [23, 34]:

- According to special relativity, photons and neutrinos should have the same limiting speed.
- According to the weak equivalence principle, photons and neutrinos should undergo the same time delay in a gravitational potential, like that of our galaxy.
- ν_τ are unlikely to be produced in the GRB fireball. Therefore, detecting ν_τ's from GRBs would be a ν_τ appearance experiment with a cosmological length scale and would verify such oscillations.

Chapter 3

Neutrino Astronomy and AMANDA

3.1 Neutrino Astronomy

Traditionally, astronomy has been conducted by observing light from the universe. Initially, the universe was studied in visible light. Later, the universe was observed in radio waves, X-rays, and eventually gamma-rays. Neutrino astronomy constitutes an entirely new way of studying the universe. By searching for and mapping the sky in neutrinos, we create the first particle picture of the universe.

Neutrinos are stable, neutral and weakly interacting particles. Unlike charged particles that are deflected in magnetic fields, neutrinos will always point back to their source. Unlike photons that interact with the background microwave or infrared light, neutrinos can travel to us from the farthest reaches of the universe. They are unimpeded by ambient matter or radiation. They more easily escape from their sources than photons or other matter.

In transparent media such as water and ice, relativistic neutrino-induced muons produce the electromagnetic equivalent of a sonic boom. This blue light is called Cerenkov radiation [35]. Cherenkov light can be detected by photomultiplier tubes (PMTs). The path of the muon can be reconstructed using the timing and topology of PMT detections. At TeV energies, the direction of the muon is aligned with that of the parent neutrino to $\sim 1^o$. This pointing accuracy allows for the science of neutrino astronomy.

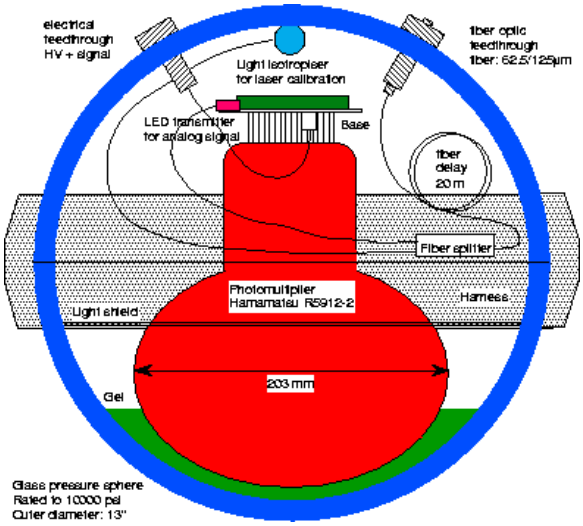

Figure 3.1: Optical modules.

3.2 AMANDA: Antarctic Muon and Neutrino Detector Array

In 1997, the AMANDA-B10 detector consisted of 302 optical modules (OMs) with 8-inch PMTs enclosed inside spherical glass pressure vessels [36]. See Figure 3.1. The OMs are deployed on 10 strings forming two concentric circles. The outer ring of 6 strings has a radius of 60m. The cables are instrumented with OMs between 1.5 and 2 km deep in the ice. See Figure 3.2. At these depths, the pressure of the ice above 1.5 km has forced out air bubbles, resulting in better (less) scattering conditions. Most scattering at these depths result from dust layers in the ice, volcanic activity that occurred between 100,000 and 15,000 years ago [37, 38].

Electrical signals are sent to the surface electronics and data acquisition system via coaxial and twisted pair cables. Fiber optic technology is also employed, achieving less distortion of the PMT signal as it travels the length of the cables. The optical fibers are also used for laser calibrations.

Deploying a neutrino detector in Antarctic ice has several advantages over water detectors. We suffer no background from potassium decay or bioluminescence. The ice surface provides a stable platform for electronics and data acquisition equipment. The South Pole infrastructure, remote as it may be, has been supporting scientific endeavors for several decades. The deep ice is also very transparent. The absorption length of light in this ice is 72m for blue light [39], much longer than

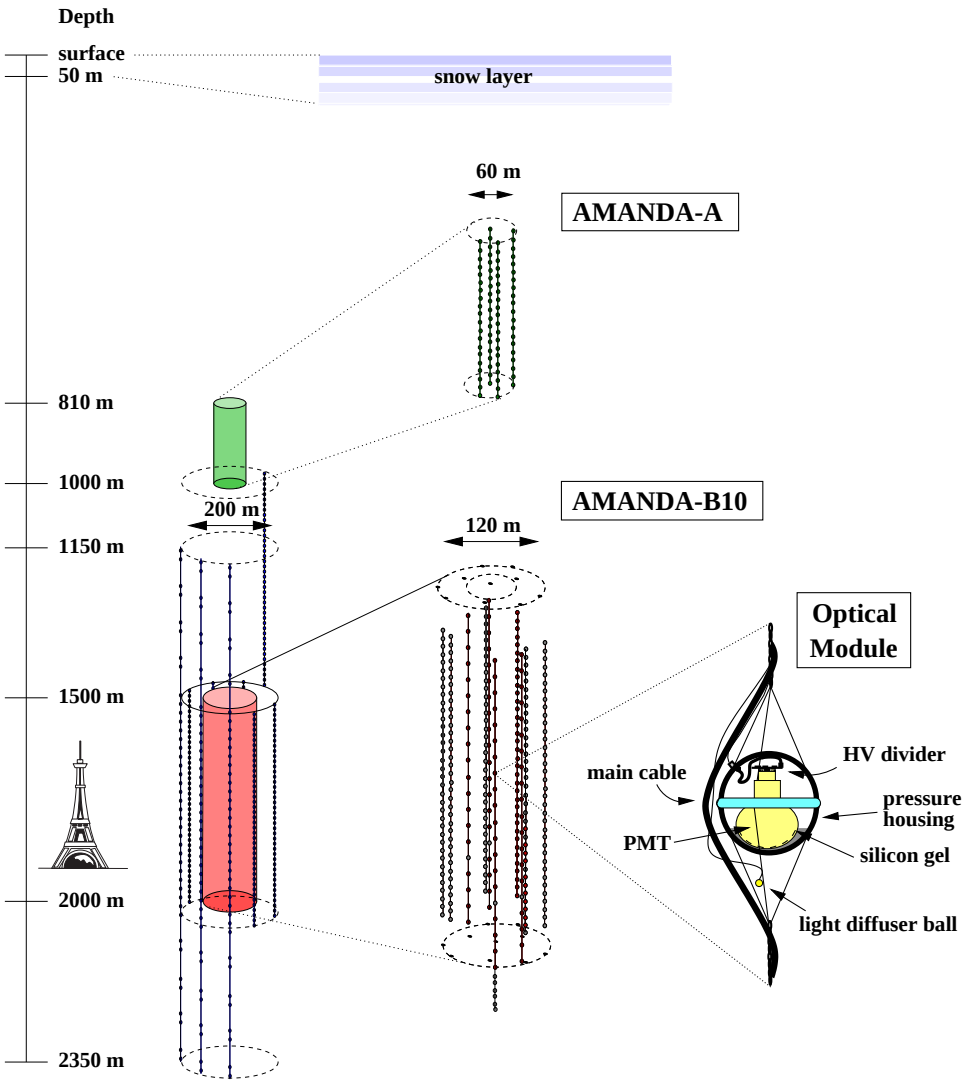

Figure 3.2: The AMANDA detector.

Austral Summer	Strings Deployed	OMs Deployed	Number of Strings in Place	Number of OMs in Place	Reference Name
1993-94	4	80	4	80	AMANDA-A
1995-96	4	80	4	80	AMANDA-B4
1996-97	6	222	10	302	AMANDA-B10
1997-98	3	126	13	428	AMANDA-B13
1999-2000	6	252	19	680	AMANDA-II (B19)

Table 3.1: Evolution of the AMANDA detector. AMANDA-A was deployed between 800 and 1000 meters [46]. AMANDA-II strings have generally been deployed between 1.5 and 2 km.

the aborption length of water experiments. The Antarctic ice shelf also provides the experiment with plenty of room to grow. Enlarging the detector only requires deploying more strings. (See the IceCube section in the last chapter.)

AMANDA-B10 was built using lessons learned from the deployment of AMANDA-A at shallower depths and was a larger version of the four-string AMANDA-B4 array. During the austral summer of 1997-98, AMANDA-B10 was upgraded with three additional strings. That arrangement is referred to as AMANDA-B13. During the austral summer of 1999-2000, six additional strings were added, completing the AMANDA-II (or AMANDA-B19) array. See Table 3.1 for a construction history of AMANDA.

3.3 Detection and Path Reconstruction

Neutrinos interact with nucleons via the charged current process and the exchange of a W boson:

$$\nu_\mu + N \rightarrow \mu^\pm + X \tag{3.1}$$

At TeV energies, the directions of the neutrino and muon are aligned to $\sim 1^o$.

When the muon is traveling faster than the speed of light in ice, i.e., faster than $v > c/n$ where n_{ice}=1.33, it emits Cerenkov radiation. The Cerenkov light is detected by the AMANDA array of OMs. See Figure 3.3. The timing and topology of the struck OMs is used to reconstruct the path of the muon. Figure 3.3 shows a reconstructed neutrino candidate in AMANDA-B10. The muon enters the detector in the lower left corner and exits through the upper right.

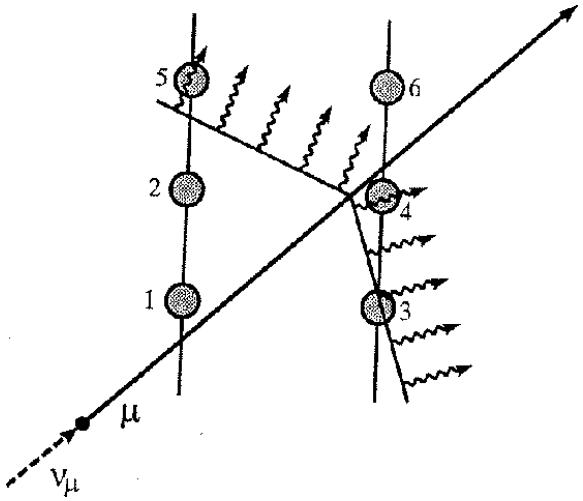

Figure 3.3: Detection of Cerenkov light by PMTs.

Only neutrinos can pass through the entire earth, so AMANDA uses the earth as a filter, seeking upgoing neutrino-induced muons from the northern hemisphere. This method allows us to eliminate the large background of downgoing, cosmic ray-induced muons from the southern hemisphere. See Figure 3.3.

The size of the AMANDA detector and OM spacing sets the energy threshold of muon detection at about 50GeV. This energy is much higher than that of water tank detectors. With a higher energy threshold, we operate in the energy regime where astrophysical sources begin to dominate the atmospheric background muons. See Figure 3.6.

It should be noted that searching for GRB neutrinos is far from the only scientific pursuit of AMANDA and its successor, IceCube. Analyses have been published or are in preparation for: WIMPs [40], supernovae [41], monopoles, point sources [42], diffuse sources like AGNs, cascades [43], atmospheric neutrinos [44], EeV events, coincidences with an air shower array and cosmic ray composition [45].

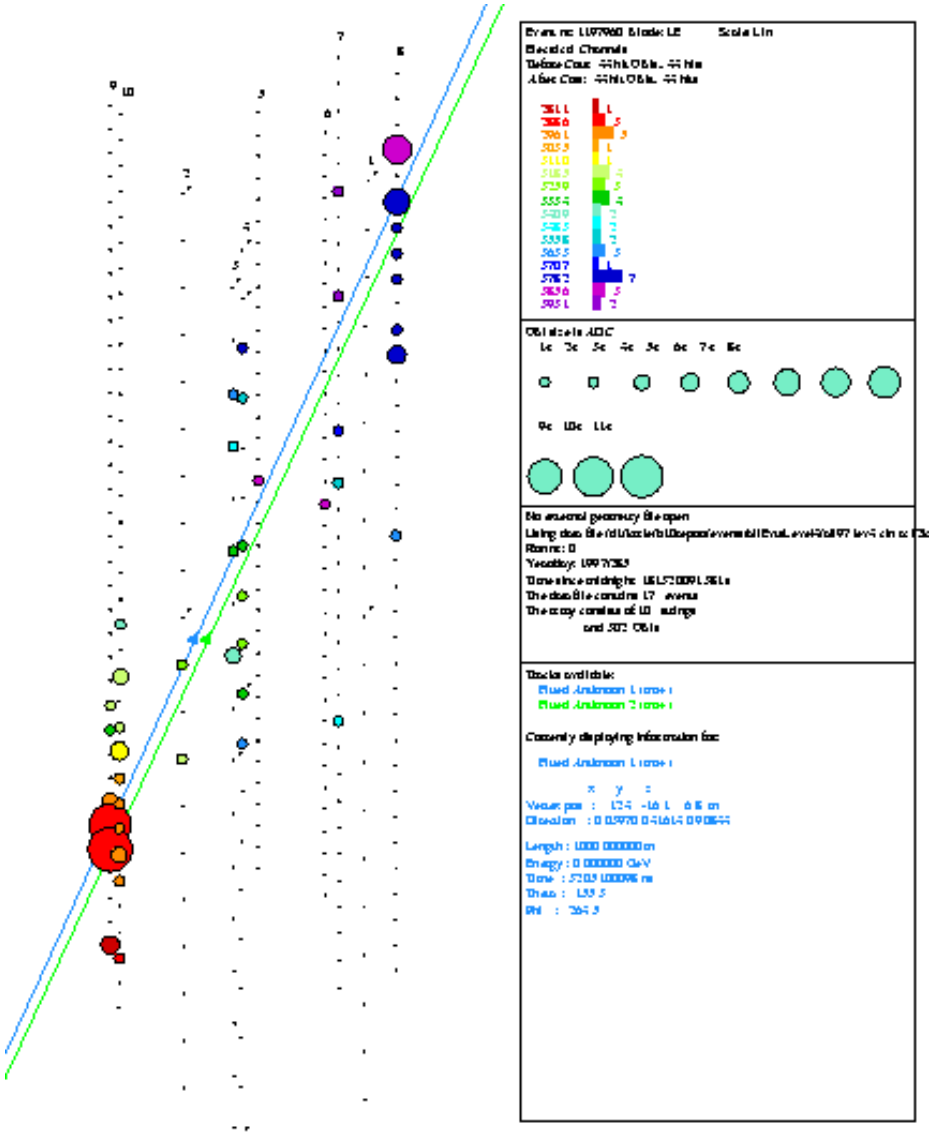

Figure 3.4: A neutrino candidate event in the AMANDA-B10 detector. The time profile of this event indicates that the muon is traveling upwards.

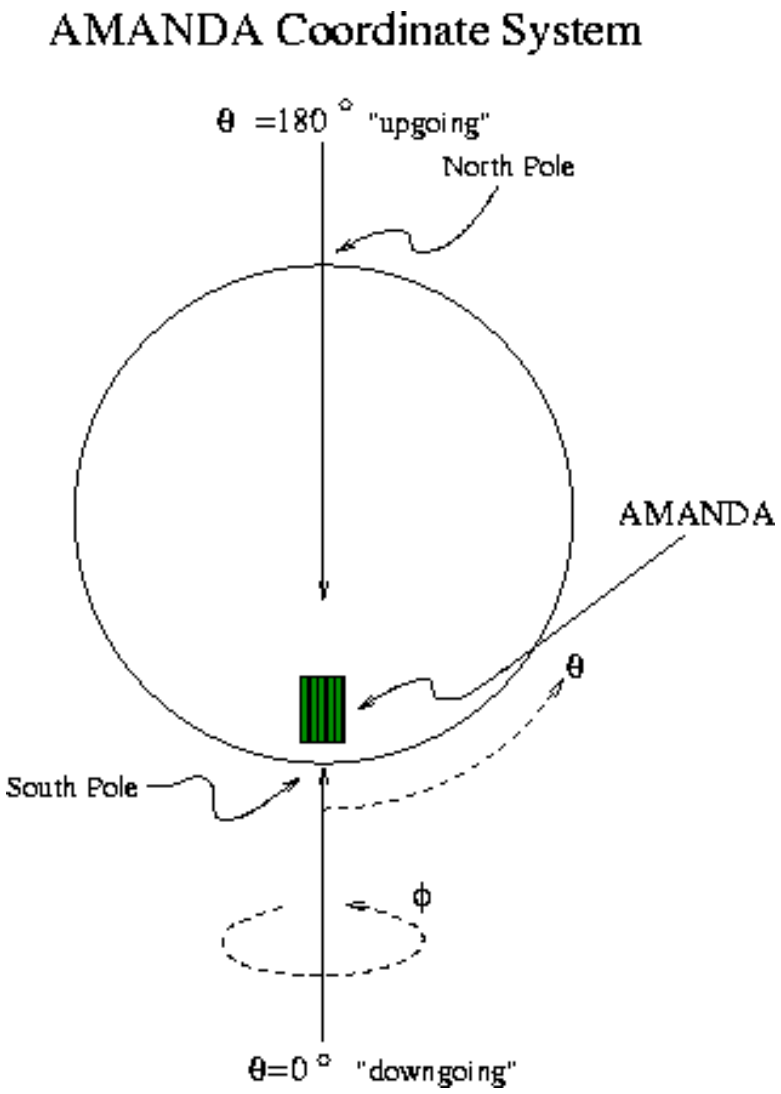

Figure 3.5: AMANDA coordinate system. "Upgoing" neutrinos originate in the northern hemisphere, enter the detector from below, and exit through the top. "Downgoing" events originate in the atmosphere of the southern hemisphere and enter the top of the detector first. θ is the local zenith coordinate and ϕ is local azimuth.

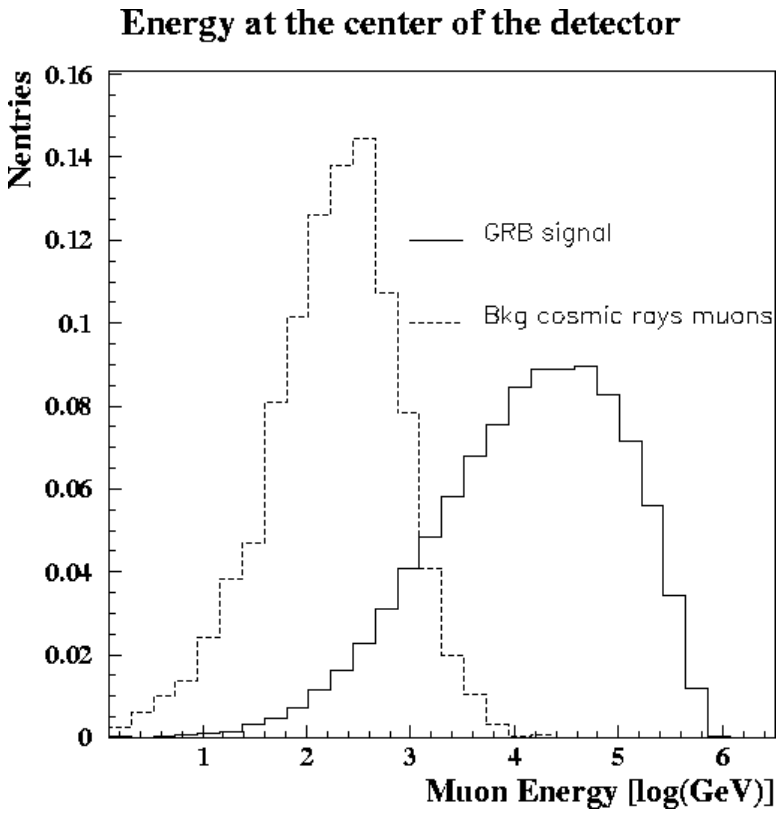

Figure 3.6: The energy of muons at the center of the AMANDA-B10 detector, from background cosmic rays and from GRB neutrinos.

Chapter 4

Analysis of AMANDA-B10 Data (1997-1999)

4.1 Signal Simulation and Monte Carlo Generation

The expected neutrino event rate in AMANDA-B10 was determined from a full Monte Carlo simulation of the GRB signal and the detector. GRB neutrinos were generated following a broken power law energy-spectrum [23]:

$$\frac{d\phi}{dE_\nu} = \frac{A}{E_B E} \text{ for } \mathrm{E} < \mathrm{E_B}; \frac{\mathrm{d}\phi}{\mathrm{dE}_\nu} = \frac{\mathrm{A}}{\mathrm{E}^2} \text{ for } \mathrm{E} > \mathrm{E_B} \tag{4.1}$$

where E_B is the energy of the break in the typical GRB two power law spectrum. Its value depends on the boost factor of the fireball. We used Γ=300 and E_b=700 TeV. See Table 4.1.

The normalization constant A is determined from the assumption that GRBs are the source of the highest energy cosmic rays – those with energies above 10^{19}eV (10 EeV). In this case, energy is shared about equally by the electrons and protons in the GRB fireball [21]. The magnitude of A[1] is calculated for three redshift distributions and for three values of Γ in Table 4.3.

The neutrino event rate is determined by convolving:

i. the flux described in Equation 4.1,

ii. the distance distribution of GRBs,

iii. the energy distribution of GRBs, and

[1] A does not reflect absorption in the earth of high energy neutrinos or the efficiency of the detector. It is the GRB neutrino flux when it reaches the earth. Absorption in the earth and detector characteristcs are modeled in later components of the Monte Carlo simulations.

Γ	A [TeV cm^{-2} sec^{-1} sr^{-1}]	E_B [TeV]	N_{evt} for 78 bursts before cuts	N_{evt} for 78 bursts after quality cuts
100	9.2 10^{-11}	77	2.87	1.1
300	6.1 10^{-12}	700	0.078	0.0234
1000	6.0 10^{-14}	7777	0.00023	0.00006

Table 4.1: Number of events expected in the AMANDA-B10 array for different values of the GRB boost factor, Γ. The parameter A and E_B in Equation 4.1 are choosen to reproduce the results of reference [47]. The last two columns are the actual number of events expected for 78 GRBs (the number in the 1997 AMANDA data set) before and after the angular and quality cuts.

iv. an assumption of the GRB Lorentz factor, Γ, or the distribution of Γ.

The distance and energy distributions can be loosely modeled on observational data. Redshifts have been determined for about 20 GRBs. Some are shown in Table 4.2. The effect of possible GRB distributions is illustrated in Table 4.3. In terms of neutrino flux, the most conservative flux normalization is set by GRBs following the star formation rate of the universe (last column). If GRBs follow a Euclidean distribution, the flux normalization constant is slightly higher (third column). The most optimistic fluxes are generated by GRBs following a cosmological distribution (fourth column).

The energy distribution is modeled such that 10% of GRBs have E>10E_{avg} and 1% of GRBs have E>100E_{avg}, where E_{avg} is the average energy of a GRB. Treating the fluctuations in distance and energy increases the neutrino event rate by an order of magnitude [48].

With 1/3 sky coverage, BATSE observed about 1 GRB per day. So ∼1,000 GRBs would be observed in 4π sr in the energy range of BATSE (20 keV to ∼1 MeV). This number of 1,000 GRBs/year in 4π is the number to which models are typically normalized. Therefore, in the 2π sr viewed by AMANDA, the expected total GRB event rate is half that of the total predicted flux and the flux is based on the possibility of observing 500 GRBs per year. Using average fluxes, i.e., assuming that neutrinos are uniformally emitted by all GRBs, the rate of events per GRB is the same regardless of whether 2π or 4π sr are examined.

However, from the astronomical point of view, we draw attention to the fact that neutrino fluxes are sensitive to the Lorentz boost factor, Γ, which characterizes the expanding fireball [47, 48, 25]. The

GRB Date	Redshift z
980425	0.0085
990712	0.430
970228	0.695
991208	0.706
970508	0.835
990705	0.86
970828	0.958
980703	0.966
980613	1.096
000418	1.118
990506	1.300
010222	1.477
990123	1.600
990510	1.619
000301C	2.03
000926	2.066
971214	3.418
000131	4.5

Table 4.2: The well-known redshifts of some GRBs, in increasing distance.

Γ	E_b(TeV)	A (Euclidean)	A(Cosmological)	A(Star Formation)
100	77	9.2×10^{-11}	1.7×10^{-9}	6.9×10^{-11}
300	700	6.1×10^{-12}	1.2×10^{-10}	4.6×10^{-12}
1000	7777	6.0×10^{-14}	1.2×10^{-12}	4.5×10^{-14}

Table 4.3: The values of the normalization constant, A, for 3 values of Γ and 3 assumptions of GRB evolution. The units are TeV / cm^2 sec sr.

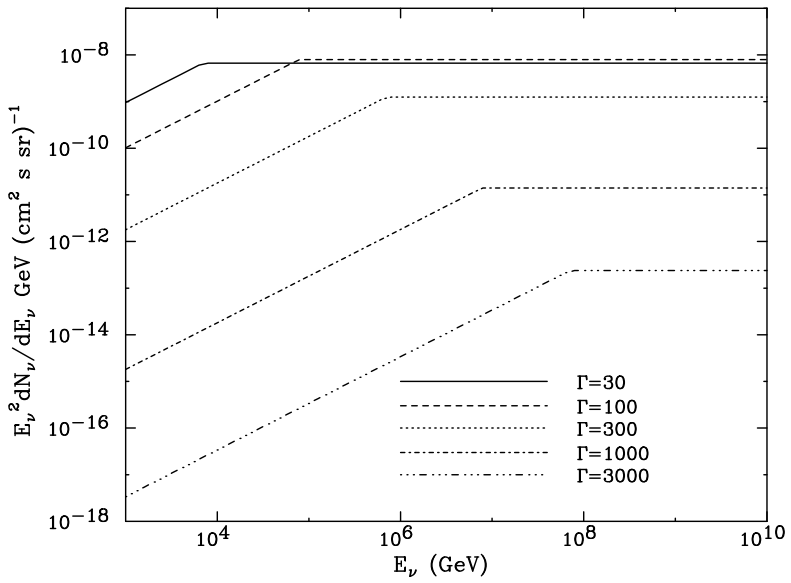

Figure 4.1: The Alvarez-Muñiz, Halzen and Hooper fluxes for 5 values of Γ [47].

boost factor has been only indirectly determined by GRB follow-up observations. The compactness problem sets a lower bound on Γ of $\sim$100. The efficiency for producing pions in the p-γ fireball collisions varies as Γ^{-4} [23] while the neutrino energy varies as Γ^2.

Highly transparent sources with large boost factors will preferentially emit photons. They should be relatively weak neutrino sources though, because the actual photon target density for pion production is diluted by the large Lorentz factor. However, an even moderately reduced value of Γ will create a prolific neutrino source due to a larger effective beam dump. See Figure 4.1. In fact, an ordinary or dim GRB (or a GRB too weak to have been detected by BATSE) may be a brilliant neutrino source.

Here, we make allowance for the problem of unknown fluctuations in the boost factor by assuming that Γ is single-valued and performing all calculations for three typical values (Γ = 100, 300 and 1000). A correction for the absorption of PeV neutrinos in the earth has also been included [47, 52]. Expected event rates are shown in Table 4.1.

An important consequence of fluctuations is that the signal is dominated by a few very bright bursts, which greatly simplifies their detection. Although we expect less than one neutrino event in

Bin	Max. $Cos(\theta)$	Min. $Cos(\theta)$	Avg. $Cos(\theta)$	Min. Zenith	Max. Zenith	Center of Bin
1	0.0	-0.1	-0.05	90.0^o	95.8^o	92.9^o
2	-0.1	-0.2	-0.15	95.8^o	101.3^o	98.6^o
3	-0.2	-0.3	-0.25	101.6^o	107.5^o	104.5^o
4	-0.3	-0.4	-0.35	107.5^o	113.6^o	110.5^o
5	-0.4	-0.5	-0.45	113.6^o	120.1^o	116.7^o
6	-0.5	-0.6	-0.55	120.1^o	126.9^o	123.4^o
7	-0.6	-0.7	-0.65	126.9^o	134.5^o	130.1^o
8	-0.7	-0.8	-0.75	134.5^o	143.2^o	138.6^o
9	-0.8	-0.9	-0.85	143.2^o	154.2^o	148.2^o
10	-0.9	-1.0	-0.95	154.2^o	180.1^o	161.8^o

Table 4.4: Sky binning for determining zenith-dependent cuts.

AMANDA-B10 from an average GRB, a burst with favorable characteristics would produce multiple events in the detector. The observation of neutrinos from GRBs may therefore be possible with detectors too small to observe the average yearly rate shown in Table 4.1. The situation is even better for AMANDA-II (see Figure 3.2 and Table 3.1) which has doubled the number of OMs, and for the future IceCube (see last chapter) detector, which will have fifteen times the number of OMs. Moreover, the spatial and temporal information provided by satellite detection greatly reduces the potential background and permits searches with much larger effective area than for diffuse or point source searches.

Neutrino Monte Carlo was generated uniformly in $\cos(\theta)$ between 80^o and 180^o. The northern hemisphere was sampled in 10 bins, equally spaced in $\cos(\theta)$ as shown in Table 4.4. Muons produced by neutrinos in the rock or in the ice below the detector are tracked [53] until they reach the optical sensors. The modeling of the detector includes the simulation of the muon track, its emission spectrum of Cherenkov photons, their propagation in the ice, the PMT detection, the pulse transfer from the PMT to the surface data acquisition system, and the event trigger. The Monte Carlo events were filtered and reconstructed in the same way as the data.

The event rate at trigger level is shown in Figure 4.2 as a function of neutrino energy. The result represents the convolution of the neutrino flux of Equation 4.1, and the probability of conversion of the neutrinos to muons near the detector. For a boost factor of $\Gamma = 300$, the neutrino energy peaks near 700 TeV.

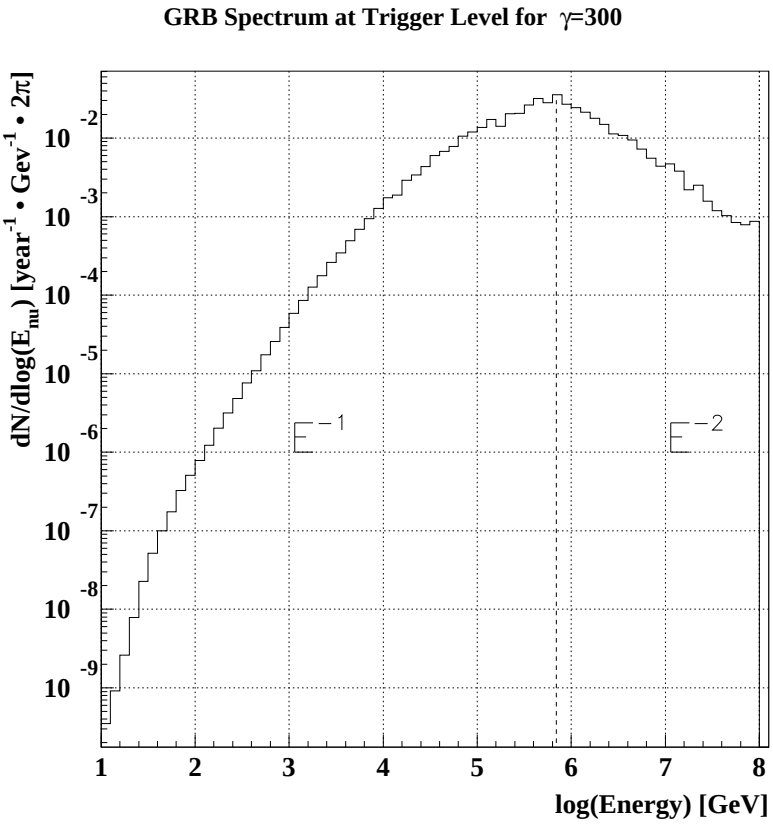

Figure 4.2: GRB spectrum at AMANDA-B10 trigger level. The plot is a convolution of the neutrino flux and the probability of conversion to a muon within the range of the detector. The integral of this curve gives the expected event rate for AMANDA-B10. The result is about 0.1 events for 78 bursts with Γ=300.

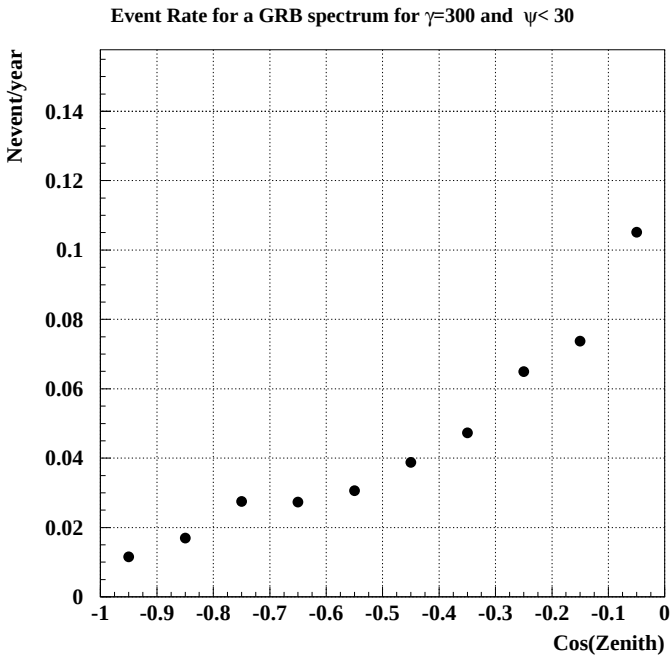

chch

Figure 4.3: Number of events expected at trigger level as a function of zenith angle for $\Gamma = 300$ and a 30^o search bin. Cos(zenith)=1 denotes upgoing events and cos(zenith)=0 denotes horizontal events.

	Expected Number Per Burst	Expected Number Per Year in 2π	Expected Number for 78 GRBs in 1997 Data
Γ=100			
Before Cuts	$1.1\text{x}10^{-1}$	57	8.9
After Cuts	$1.7\text{x}10^{-2}$	8.7	1.4
Γ=300			
Before Cuts	$3.2\text{x}10^{-3}$	1.6	$2.5\text{x}10^{-1}$
After Cuts	$4.1\text{x}10^{-4}$	$2.0\text{x}10^{-1}$	$3.2\text{x}10^{-2}$
Γ=1000			
Before Cuts	$8.4\text{x}10^{-6}$	$4.2\text{x}10^{-3}$	$6.6\text{x}10^{-4}$
After Cuts	$8.3\text{x}10^{-7}$	$4.2\text{x}10^{-4}$	$6.5\text{x}10^{-5}$

Table 4.5: Expected number of events in AMANDA-B10 from Monte Carlo simulations. Here, the cuts are independent of zenith and burst durations. Results are shown for comparison purposes.

One also has to account for the efficiency of the quality cuts in retaining signal events in the final estimate of the number of predicted events. This efficiency is on average 35%. The event rate at trigger level is shown in Figure 4.3 as a function of the zenith angle. We notice that the telescope is 10 times more sensitive to horizontal events relative to vertical ones. This results mostly from the preferential absorption by the earth of the near-vertical high energy neutrinos with typical energy near 700 TeV. The effect is less pronounced for $\Gamma = 100$ because of the softer energy spectrum.

One of the strengths of the GRB analysis is that we use Monte Carlo simulations to model the GRB signal only. We use actual data to characterize the background of our search, thereby avoiding any shortcomings of using computationally-intensive background Monte Carlo at high rejection levels.

Table 4.5 shows the event rates predicted by Monte Carlo in the AMANDA detector, before and after cuts, for 3 values of Γ. Rates are based on a Euclidean distribution of GRBs. Here, the same cuts (ndirc> 10 and $\psi < 10^o$) are used for all GRBs. These rates are shown for comparison purposes. Positive detection of a GRB is more likely than inferred from these numbers because the neutrino events are not spread equally among the bursts; most neutrino events will come from a single GRB. Cuts were later optimized for specific zeniths and T90s.

4.2 Effective Area

The effective volume of AMANDA is much greater than than the geometric volume. Traditionally, the effective area of a particle detector has been calculated by simulating particles directed at the detector from a generation plane. The generation plane must be large enough to account for all particles that may trigger the detector. The effective area of the detector is then calculated as

$$A_{\text{eff}}^{\text{det}} = A^{\text{gen}} \times \frac{N^{\text{det}}}{N^{\text{gen}}} \tag{4.2}$$

where $A_{\text{eff}}^{\text{det}}$ is the calculated effective area of the detector, A^{gen} is the generation plane, N^{det} is the number of events detected, and N^{gen} is the number of events produced at the generation plane.

This method is straightforward for detectors that are not extended in size and for particles that do not exhibit energy losses. Defining an effective area is considerably more complicated for AMANDA. It is not a point-like detector and muons lose energy as they travel. AMANDA can detect muons that do not pass through the fiducial volume of the array. The effective area of AMANDA also depends on the direction from which the muons are traveling.

The effective area of AMANDA is given by

$$N = A_{\text{eff}} \int_{E_\mu^{\text{thresh}}}^{\infty} \int_{E_\nu^{\text{min}}}^{E_\nu^{\text{max}}} P_{\nu\to\mu} \times \frac{dN_\nu}{dE_\nu} dE_\nu$$

where P is the probability that a neutrino of energy E_ν will produce a muon that will be detected by the array. Therefore, P is a function that convolves the column density of matter traversed, the neutrino-nucleon cross section, and the range of the muon. The last two depend on the energy of the muon.

Note, P functions can be defined in different ways. Sometimes, P is defined as the probability of detecting a muon of $E > E_{\text{threshold}}$ that was produced by a neutrino of energy E_ν, where $E_{\text{threshold}}$ is the energy threshold for detecting the muon and is a fixed parameter. Therefore, P would not depend on the energy of individual muons.

Here, $P = \rho \times \sigma_\nu \times R_\mu$ where R_μ is the range of the muon. Then

$$\frac{dN}{dA_{\text{eff}}} = \rho \frac{dN_\nu}{dE_\nu} \sigma_\nu R_\mu \tag{4.3}$$

and

$$\frac{dN}{d(A_{\text{eff}} R_\mu)} = \rho \frac{dN_\nu}{dE_\nu} \sigma_\nu \tag{4.4}$$

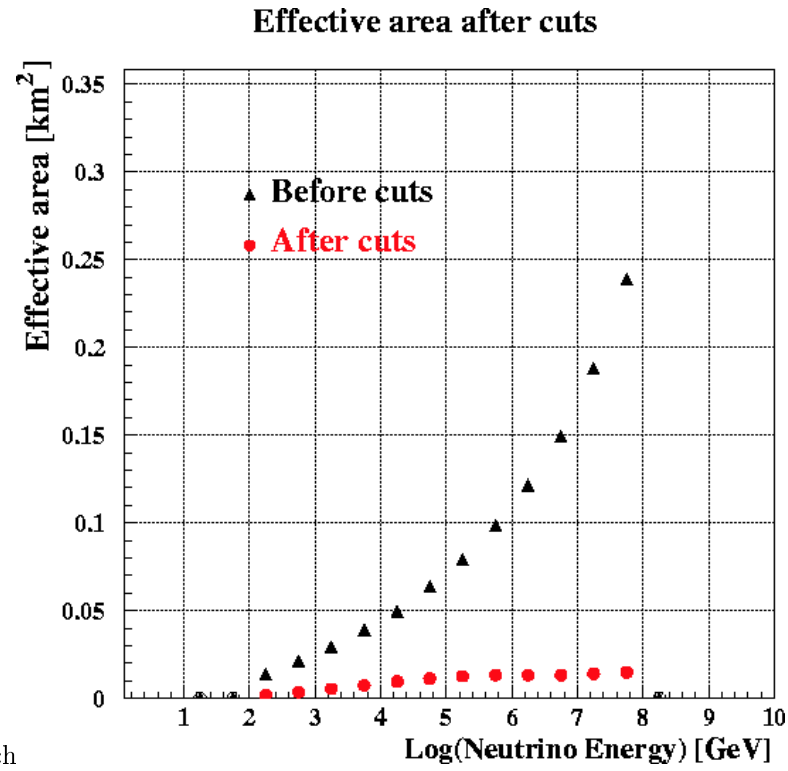

chch

Figure 4.4: Effective area of detector before and after cuts.

where $d(A_{\text{eff}}R_{\mu}) = V_{\text{eff}}$, the effective volume of the detector. See Figure 4.4 for the effective area of AMANDA-B10 as a function of neutrino energy, before and after cuts.

4.3 Background Studies

The duration of a GRB is characterized by its T90 length. T90 is the period of time in which 90% of the burst fluence (ergs/cm^2) was detected. The T90 begins when 5% of the fluence has been collected and ends when 95% of it has been collected. This requires analysis of the complete burst time profile after it has been recorded, hence this data is added later by the BATSE team to its publicly available archives.

In the fireball scenario, GRB neutrino emission is expected to closely coincide with the gamma-ray emission as they are produced in the internal shocks. We therefore search the T90 window plus margins for neutrino candidates. Some times the T90 period actually begins before the trigger time. To ensure that we have the beginning of the burst in our temporal search window, we use the earlier

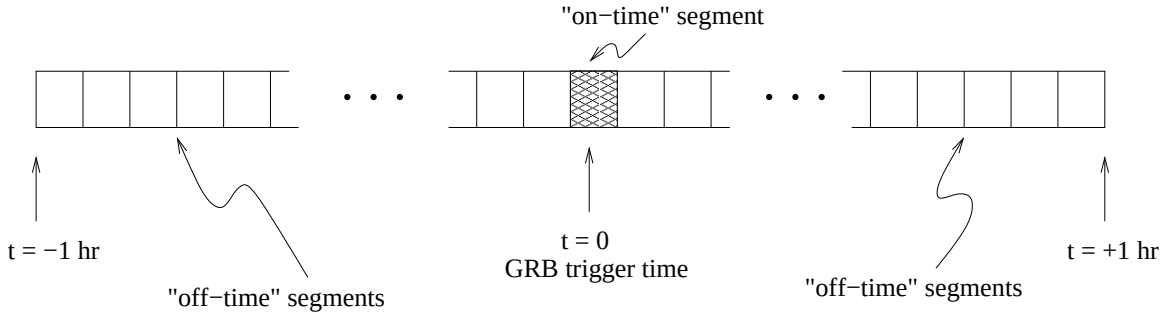

Figure 4.5: Two hours of data are used to characterize the background.

of the trigger time or the T90 beginning and subtract one second. This is the start of the on-time search window in our analysis.

We first estimated the background for each angular bin near a given (θ, ϕ), where θ and ϕ are the local zenith and azimuthal coordinates. See Figure 3.3. The background is dominated by down-going cosmic ray muons that are misreconstructed as upgoing tracks. Although there are upgoing neutrinos created by cosmic rays interacting in the earth's northern hemisphere, their rate is negligible on the time scales of our GRB neutrino search.

Events occurring within a two-hour time interval centered on the time of the burst, but excluding events occurring during the six (-1,+5) minutes around the burst, were used to estimate the background. A two hour interval provides sufficient statistics to parametrize the background and to minimize systematic effects resulting from any time dependence of the detector's efficiency. For our 1997 data set, the total amount of background studied is 859,053 seconds, or almost 10 days. Neutrinos that may be emitted hours or days later [32] are not the focus of this search.

The probability of a background event occuring in the *on-time*, *on-source* bin is:

$$\epsilon(\theta,\phi) = \frac{N^{\mathrm{offtime}}_{\mathrm{searchbin}}}{N^{\mathrm{offtime}}_{\mathrm{allbins}}},$$

where $N^{\mathrm{offtime}}_{\mathrm{searchbin}}$ is the number of events observed in the region of the GRB during an non-GRB time window (i.e., when no signal is expected). $N^{\mathrm{offtime}}_{\mathrm{allbins}}$ is the total number of all events observed during the same *off-time* time window.

Therefore, the number of background events we expect to see when looking in the right place

Year	1997	1998	1999	2000
Detector	B10	B10	B10	II(B19)
Number of BATSE bursts analyzed	78	138	96	44

Table 4.6: The number of triggered BATSE bursts analyzed in each year of AMANDA data.

at the right time for a GRB signal is:

$$< n_{\text{background}} >= \epsilon(\theta, \phi) \times N_{\text{allbins}}^{\text{ontime}},$$

where $N_{\text{allbins}}^{\text{ontime}}$ is the number of all observed events in the sky during the T90 *on-time* search window.

Although the overall trigger rate may vary with time, $\epsilon(\theta,\phi)$ is approximately constant. Therefore our background estimates are robust to overall changes of the trigger rate. Deadtime and downtime are also completely accounted for in this way. The stability of the efficiency $\epsilon(\theta,\phi)$ was studied for each burst and from burst to burst to ensure the stability of the background estimate with time. The 2 hours of background data, excluding the (-1,+5) minutes around the burst, were divided into 4 bins of 1,725 seconds. For each GRB, the standard deviation of ϵ in each bin was compared to the average ϵ_{avg}. The standard deviation is gaussian with mean equal to zero and $\sigma \approx 1$, consistent with statistical fluctuations.

With $\sim 1/3$ sky coverage, BATSE detected 304 GRBs in 1997. Approximately 240 occurred during regular AMANDA detector operation in austral winter. Of these, 105 occurred in the northern hemisphere during reliable data-taking and were more closely examined for data quality. We omit GRBs with data gaps and large fluctuations from the mean rate [54]. AMANDA data for 78 bursts detected on-board the BATSE satellite between April 7 and November 10, 1997, met quality criteria and were examined in this analysis.

From 1998 data, 138 GRB files have been extracted – 81 triggered and 57 non-triggered bursts. The results from this data year will be reported at a later time.

See Appendix F for the distribution of background events for the 1999 GRBs.

From 1999 data, 96 GRBS were examined for quality criteria. The files that required extra attention are shown in Table 4.7. Only one file showed peculiar background rates that required

Data Gaps				
GRB	Date (YYMMDD)	Gap (secs)	Excluded?	Due to Missing Files
7456	990308	614.1	no	no
7594	990603	6628.4	no	yes
7602	990610	472.25	no	no
7735	990824	low, unsteady rate	yes	no
7750	990903	low rate	no	no

Table 4.7: Data gaps found in 96 GRB files.

exclusion from the analysis. This is a significant improvement in stability and data quality from 1997.

The number of GRBs studied with each year of data is shown in Table 4.6. For a complete list of analyzed GRBs, see Appendix E.

4.4 Blindness

Another strength of the GRB analysis is that it constitutes a blind search. Our methods ensure that the data is never biased by the determination of cuts or examination for a signal. For 1997 data, we set cuts by using only 1/2 half of the data set. In doing so, we follow the method of Section 3.3 of [55].

For analyses that search the entire year for a signal that is unknown in time and location (e.g., point sources or atmospheric neutrinos), they may (properly) finalize their search method and cuts on a fraction of the data, say 20%. They then apply those cuts to the unopened box of data, the other 80%. This can prevent the tuning of cuts to unfairly produce a false signal. The reason so much data must be stowed away is that it is not known when (or where) the signal might exist. It is also important to save most data if one concludes that the first sample of data must be excluded in the final analysis.

If one has a data set that is signal free, then one can work with that data without fear of biasing the signal. The GRB search does this. We use a known non-signal set of data to characterize the background, check for detector stability, and determine cuts. That data includes events [-60,-1] minutes before a GRB trigger time and [+5,+60] minutes after a trigger. The data that occurs [-1,+5] minutes around the trigger is never examined before the final analysis is undertaken. Our analysis

searches for neutrinos that are coincident with the gamma-rays of the GRB. We search for neutrino candidates only in events that occur during and very near the T90 (i.e., the duration) of the GRB. This data of interest remains an unopened and unexamined box until the analysis is final, just like the 80% data box of the other analyses. This data of interest can in no way affect the cuts. Cuts are set only on the known non-signal background and on Monte Carlo signal events. Additionally, the cuts are few and straightforward: a cut on the number of unscattered hits in the event and an angular search bin cut.

If there is a signal in the background data – from undetected bursts or because we are looking for neutrinos at the wrong time after all – the result will be an overestimation of our background and, consequently, an upper limit that is too conservative or a detection signifiance that is too low. We use hundreds of time bins for the background estimation though, so such an effect would be very small.

When future AMANDA GRB analyses are undertaken, they may use GRB detections from other satellites to once again reduce the background by telling us where and when to look for neutrinos. It is likely that another AMANDA analysis will be conducted without using satellite detections. This rolling search through all of the data will have to use the more common method of blind analysis – using a fraction of the data to develop cuts while stowing the rest away for the final analysis.

4.5 Data Handling

In the years of 1997-2000, AMANDA data was recorded continuously and recorded onto magnetic tapes. As the South Pole is accessible only during austral summer, a year of data was saved on tapes and then hand-carried out with the first planes arriving for station opening. Annual data sets were filtered for several different scientific goals at Lawrence Berkeley National Laboratory (LBNL) or Deutsches Elektronen Synchrotron (DESY) in Zeuthen, Germany. Reduced data sets were set to individual institutions for analysis. See Appendix B for more details.

4.6 Merging of BATSE and AMANDA Data

The BATSE GRB data – including detections, durations, fluxes and locations and much more – is publicly available at [8]. Two methods were used to merge the BATSE and AMANDA data.

One incorporated BATSE data into the AMANDA standard format; the other maintained separate data streams and accessed information only as needed.

The right ascension and declination used in BATSE data was transformed to local AMANDA θ (zenith) and ϕ (azimuth) coordinates [56]. Both BATSE and AMANDA events are stamped with UTC times. The delay time between the satellite stamp and the AMANDA stamp is negligible[2]. Therefore, no temporal correction is needed.

4.7 Reconstruction

All AMANDA muon events in the two hours surrounding a GRB trigger time and north of a declination of -40° were reconstructed. (The declination cut was performed in the first filtering of the 1997 data and is not specific to this analysis.) An initial line fit was made to all events in this sample. Then the line fit was used to seed a full muon reconstruction. Muon tracks are reconstructed using the timing and topology of OM detections in each event. Scattering and absorption of photons in the ice are accounted for in the maximum likelihood fit. These events were then searched for up-going neutrino-induced events.

4.8 Quality Cuts

Using the simulation and background studies, we designed a search which gives the best significance for the expected signal. This search accounts for:

- The zenith angle dependence of the angular resolution of the AMANDA detector, which is better for vertical than for horizontal muon tracks.
- The low number of signal events expected.
- The number of background events in the search bin, which depends on the zenith angle and duration of each GRB.

Because misreconstructed cosmic ray muons represent the dominant background, we studied the rejection efficiency of a number of our standard quality parameters [46]. We found that, in addition to optimizing the size of the search bin around a GRB position, a cut on the number of

[2]BATSE flew at a maximum altitude of ~500 km. So the time delay is on the order of hundredths of a second.

"direct" hits gives the best search sensitivity. "Direct" hits have a small time delay relative to the expected arrival times derived by calculation. That is, the arrival time of the Cerenkov photons closely match the fitted track hypothesis. They are delayed by less than 75 nsec due to scattering in ice. Well-reconstructed tracks have many direct hits. Requiring more than ~10 direct hits in an event removes essentially all misreconstructed background events. Therefore, we are left with an essentially background-free search with only two cuts: the angular search bin size and the number of direct hits. Minimizing the number of quality cuts increases the efficiency with which we retain the small number of expected signal events.

Cuts were optimized for each GRB based on its zenith position. See Table 4.8. Although the cuts depend on the zenith of the GRB, the way in which we set the cuts does not. The sky was divided into 10 equal bins in zenith angle. For each bin in zenith angle, the cut efficiencies for the signal (from Monte Carlo) and for the background data have been parametrized by a sixth order polynomial. Typically, the cuts we applied lead to a background rejection factor of 500 with a signal efficiency of about 35%.

Generally speaking, cuts can be loosened when the expected background is small. In general, background events of misreconstructed muons increase near the horizon for AMANDA and are minimal near vertical. In this analysis, we search slightly before and during the GRB photon emission, so the chance of observing a background event increases with the duration of the GRB.

4.9 Significance Calculations

For the small statistics of the event samples in this analysis, Poisson statistics is used and therefore the significance is no longer given by $\frac{S}{B}$. The optimal bin size and optimal quality cuts are determined by minimization of the chance probability $log(P_c)$ for a hypothetical neutrino signal N_ν [76]. See Figure 4.6. We assumed $N_\nu = 2$. Note that we chose to optimize on a possible signal, generated for instance by a favorable fluctuation from the average γ, redshift or burst energy (see Table 4.1), and not on obtaining the best limit. The results are however relatively insensitive to the choice of N_ν.

Center of Bin	Optimal Search Bin Ψ	Optimal Ndirc Cut
93	20.5	17.
99	20.5	17.
105	19.0	17.
111	17.5	17.
117	16.5	18.
123	15.5	18.
130	14.5	18.
139	11.5	18.
148	8.5	19.
162	6.5	19.

Table 4.8: Final cut results for AMANDA-B10. (See Table 4.4 for details on the sky binning procedure.)

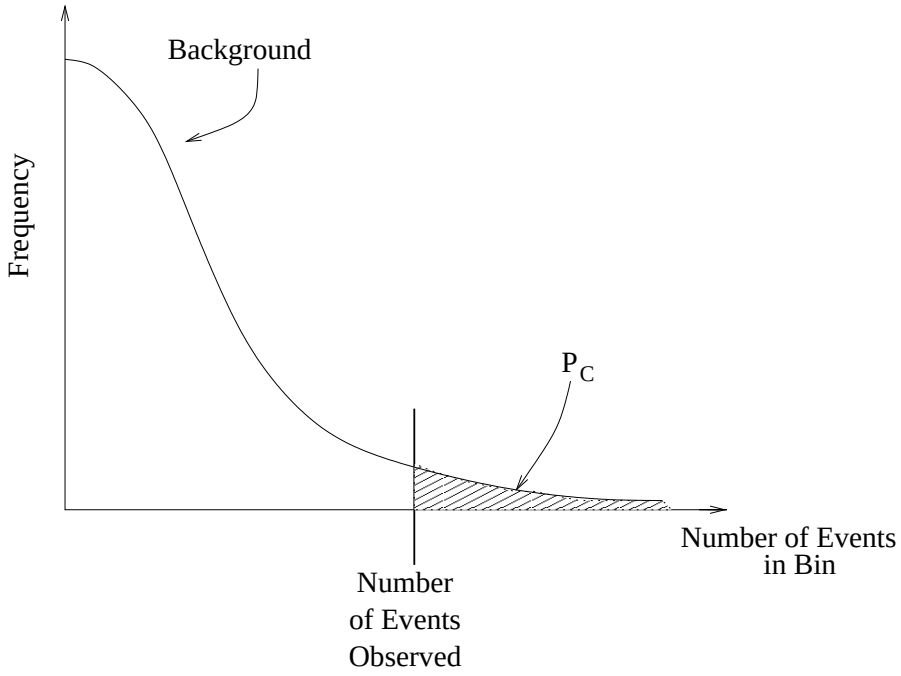

Figure 4.6: P_C is the probability that the observed number of events is due to background. It is the area under the curve greater than the number of events observed.

4.10 Additional Notes for 1998 and 1999

The re-filtered 1998 GRB files are being processed and the stability and quality of those files will be appended soon.

The 1999 GRB data has been treated in the same way as the 1997 (and 2000) GRB data. The background portions of the data have been thoroughly investigated, while maintaining blindness around the GRB time. Stability and data quality have been examined for each of 96 bursts. Again, the data proved to be very stable, with only 5 of 96 bursts requiring extra examination. See Table 4.7.

In order to provide a straightforward result from the 1997-1999 duration of the AMANDA-B10 detector, we apply the same cuts to all three years of GRB data. Only the hits on string 1 to 10 are used in the reconstructions. The B10 detector does not have a uniform response from horizon to vertical. Therefore, we maintain our zenith-dependent cuts. See Table 4.8.

Peter Niessen created some Monte Carlo files that simulated the 1999 detector conditions. We used the Monte Carlo that was created with the Modified Absorption Model (MAM) to check changes to detector response and event rates. Differences were minimal from the 1997 analysis, so the same cuts can be applied and results are presented in Chapter 6.

Chapter 5

Analysis of AMANDA-II GRB Data (2000)

5.1 AMANDA-II

During the austral summer of 1999 and 2000, six additional AMANDA strings were deployed in the south polar ice cap. These strings completed AMANDA-II which consists of 19 strings and 680 optical modules. AMANDA-II represents a significant increase in effective area for the instrument and thus in discovery potential.

5.2 Data Filtering and Stability

The 2000 data set was filtered at Deutsches Elektronen-Synchrontron (DESY), in Zeuthen, Germany. After the data was calibrated, a simple line fit to the space and time coordinates of the hits in each event was made. An initial guess was also made using a "direct walk" track search algorithm [86]. Events with a simple line fit or direct walk track greater than 70^o were selected and kept for further reconstruction. This selection passed 92% of signal events and 9.4% of the data [87].

Full reconstruction methods were applied to the remaining events. A full muon reconstruction using the initial line fit as the first guess and a full muon reconstruction using the direct walk track as a first guess were performed. Events with at least one reconstructed muon track of greater than 80^o were selected and kept for further analysis. This level of data is referred to as Level 1.

In August of 2001, I provided a document to the collaboration that summarized the blindness approach of the UW GRB work [88]. The collaboration approved distribution of data related to

GRB	Date (YYMMDD)	Data Gap (secs)	Excluded from Analysis	Due to Missing File
7989	000217	1439.5	no	yes
8012	000303	161.7	no	no
8079	000418	798.0	no	no (end of run)
11652g	000418	684.6	no	yes
8084	000421	236.6	no	no
8097	000508	many small ones	yes	no
8110	000518	during GRB trigger	yes	no (end of run)

Table 5.1: Data gaps found in 70 GRB files.

the GRB neutrino search on the condition that all searches adhere to the method described in the blindness document.

In October of 2001, I used log files supplied by DESY to create a list of all AMANDA files that recorded data within one hour of a BATSE GRB trigger. Tonio Hauschildt made these 831 Level 1 files available in November of 2001. (A small number of files had not been processed at the time and were therefore not included in the log files. This resulted in a few files missing in the final selection of GRB data, but none were vital to the analysis.)

Data was available for 70 GRBs, 44 bursts triggered on board BATSE and 26 bursts located in BATSE archival records. (See Appendix A for additional information on non-triggered bursts.) Despite BATSE's demise in May of 2002, this number of GRBs was almost as great as the number we studied in the 1997 AMANDA data. This was due to fewer technical problems and greater detector stability.

In general, the data quality in AMANDA-II's first year of data taking was excellent. The AMANDA data files associated with each GRB were combined to produce a single data file for each GRB. Of these 70 files, only seven had unusual data gaps. Five (7989, 8012, 8079, 8084, 11652g) of them had gaps that could be omitted from background studies without adversely affect the analysis. One (8110) had a data gap that included the GRB trigger time and therefore had to be excluded from the analysis. One file (8097) had an abnormal number of small, but uncorrelated, data gaps and is treated with caution. See Table 5.1.

The time between consecutive events in each GRB file was plotted. These plots of the "delta-t" distributions were remarkably uniform and linear for all bursts. See Appendix I for these plots.

Event Selection	Requirement
1	θ(linefit or direct walk)$> 70^o$
2	θ(full reconstruction)$> 80^o$
3	θ(16-fold iterative fit)$> 80^o$

Table 5.2: Stages of event selection.

At Wisconsin, I applied an iterative muon reconstruction to all of the Level 1 GRB data. The reconstruction used Powell's minimization method and performed a 16-fold iterative search around the reconstructed muon track[1]. I then selected events whose best iterative search results was greater than 80^o. See Table 5.2. There were 302,000 events remaining for all 70 GRBs. The best iterative fit was used in the study of potential quality cuts.

The background data was split into consecutive 10-second windows. The distribution of the number of background events in these 10-second windows is shown in Appendix H. The distributions are Poissonian.

5.3 Signal Simulation and Monte Carlo Generation

The AMANDA-II detector, 19 strings in size, required a new Monte Carlo effort from that of the AMANDA-B10 detector. The AMANDA-II simulation incorporated improvements that had been made since the 1997 data analysis. It utilized the MAM (Muon Absorption Model) to describe ice properties. Muons were tracked using mudedx based on the Lohman model and, for high energies, propmu based on the Lipari code. A total of 170,000 neutrinos and 170,000 anti-neutrinos were generated between 10GeV and 100PeV (10^8GeV) and between 80^o and 180^o. The Monte Carlo generation followed the entire simulation chain outlined in [91].

The GRB signal at trigger level as a function of zenith is shown in Figure 5.1. The Waxman-Bahcall flux [24] is used. See Section 5.6 for further comments on this flux.

For a GRB flux in AMANDA-II, 70% of events are reconstructed within 10^o of the true angle. Resolution at large zenith angles (near vertical) is better than near the horizon, but the difference is not large enough to require different search bin sizes. BATSE resolved the location of 93% of GRBs to better than 10^o. See Figure 1.5. Therefore, a 20^o search bin size is appropriate for this analysis.

[1] It used the muon track that had been seeded by the direct walk first guess.

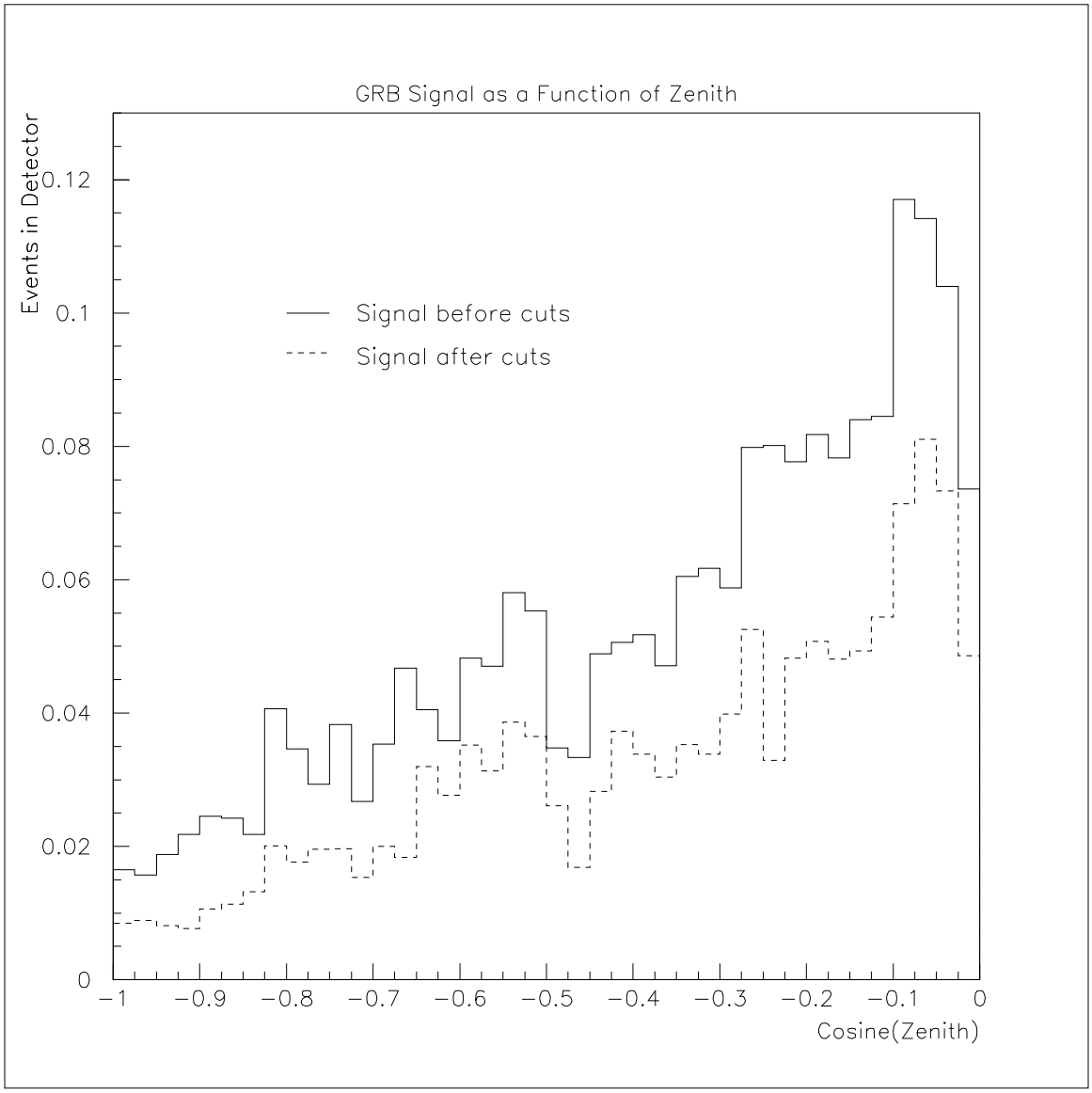

Figure 5.1: The zenith dependence of the GRB signal at trigger level in AMANDA-II.

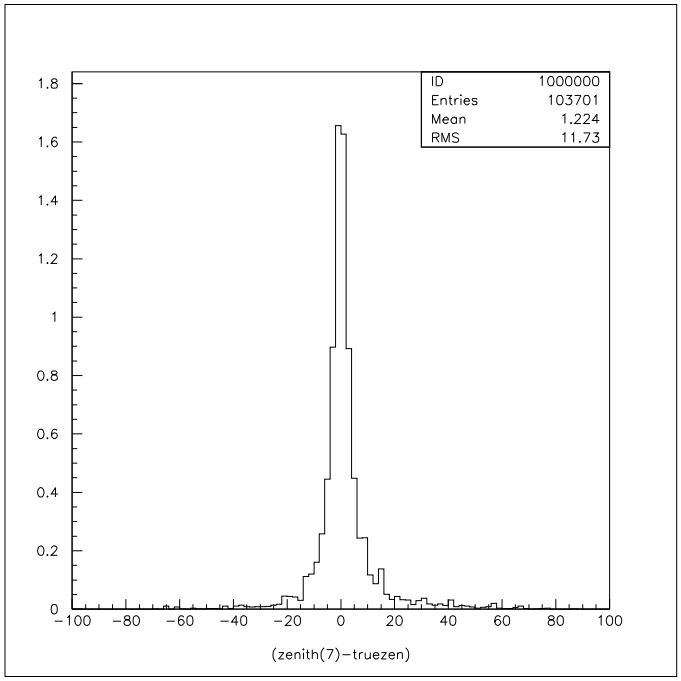

Figure 5.2: Offset between the reconstructed zenith angle and the true zenith angle in AMA-II without any quality cut.

Without quality cuts, there is a $+1.2^o$ offset between the reconstructed zenith angle and the true zenith angle in AMA-II. See Figure 5.2. This means that muons are being reconstructed slightly more vertical than they actually are. This is consistent with what was observed in B10. However, the offset disappears when even soft quality cuts (nch>8) are applied. See Figure 5.3

5.4 Model Rejection Factor

Traditionally, physicists have maximized $\frac{\text{Signal}}{\sqrt{\text{Bkgd}}}$ in order to optimize cuts. This method fails when signal and background are distributed as in Figure 5.4. In such a situation, $\frac{\text{Signal}}{\sqrt{\text{Bkgd}}} \to \infty$.

Another approach to setting cuts is to maximize the potential impact that the results will have on the current state of the field. A positive detection of neutrinos from a GRB will, of course, revolutionize the study of GRBs. In the GRB analysis for B10, we optimize on a potential $N_{\text{event}} = 2$ signal, a positive fluctuation from average expectations, from a single GRB.

In the absence of detection, one seeks to minimize the upper limit that can be placed on

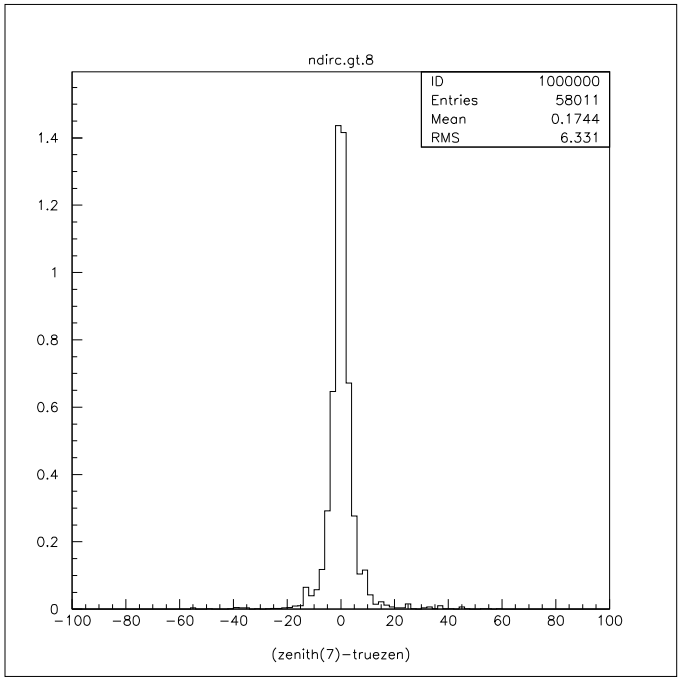

Figure 5.3: There is almost no offset between the reconstructed zenith angle and the true zenith angle in AMA-II when a soft quality cut of nch>8 is applied.

Ψ	Smoothness	Ndird	Nch	Signal	Bkgd	UL_{evt}	MRF
20^o	-0.40<S<0.35	>14	>25	0.12	0.43	2.8	25
22^o	no cut	no cut	no cut	0.20	20	8.9	45

Table 5.3: Calculation of the Model Rejection Factor (MRF) for two sets of cuts. The signal and background rates are for 44 GRBs, the number of triggered bursts examined in this analysis. See text for more details.

current models. This approach is outlined in [89] and is characterized by the Model Rejection Factor (MRF). Because AMANDA-II can set meaningful limits in a short amount of time, we chose this approach for optimizing the cuts in the 2000 GRB analysis. The MRF approach accounts for the spectral shape of the expected signal, as well as the presence of background.

To determine the MRF for a particular set of cuts, the expected signal rate is calculated using the Monte Carlo simulation and the background event rate is determined from examination of the two hours of background data (with the center on-time region removed). Then the average background rate, b, is used to look up the 90% confidence limit interval for the signal mean, μ, from Table XII of Feldman-Cousins [85], in the event that no signal is observed. The Feldman-Cousins tables were interpolated and extrapolated where necessary. This provides the event upper limit, UL_{evt}, that could be placed after an ensemble of experiments with the observed background rate, b, and no true signal. The MRF is defined as the UL_{evt}/(expected signal). It represents the ratio of the upper limit to the simulated signal flux.

An example of two cut sets and the MRF calculation is shown in Table 5.3. The expected signal for the tighter set of cuts (top row) is 0.12 with an average background rate of 0.43. The expected signal rate for the loose set of cuts (bottom row) is greater, 0.20, but so is the background rate of 20 events. Even though the signal is increased by 67%, the background is increased by a factor of 47. Thus, the MRF for the first set of cuts is lower and, hence, ultimately more restrictive in terms of setting the upper limit.

5.5 Quality Cuts

Many cut parameters were studied for their effectiveness in eliminating background events and preserving GRB signal. The ranges of reasonable cuts in each parameter were determined. For example, there is no reason to explore a cut in a region where tightening the cut reduces signal without reducing background, or in a region where loosening the cuts allows an increase in background without increasing signal. These ranges were at first explored in large steps through the parameter space, studying the effects on the MRF and locating the general area of the global minimum. A subset of parameters that looked particularly promising were examined in more detail (nch, ndirc, ndird, smootallphit, ldirb). When near the global minimum, the fineness of the search mesh was increased and smaller steps through the parameter space were taken. Three cuts were found to be most useful (nch, smootallpit and ndird). Others (such as ndirc or ldirb) were found to be redundant or insignifcantly helpful.

Smoothness measures the distribution of hits along the length of a reconstructed track. A smooth event is one in which hits are evenly and consistently spread along the track. A perfectly smooth track would have a smoothness very close to zero[2]. A track that lacks smoothness has hits disproportionately piled up in one or more sections of the reconstructed track. A negative (positive) smoothness indicates that too many hits are located at the end (beginning) of the track. These event profiles are often indicative of electromagnetic showers or events that pass outside the detector. Well-reconstructed muons tend to have very small values of smoothness. Smootallphit is a particular variation of smoothness that accounts for the non-uniformity of the detector. See Figure 5.5. Making a cut on smootallphit is a "free" cut in that we can reject a portion of background events while losing almost no signal.

When using ndird, a hit is considered direct (i.e., unscattered) if it was detected by the OM within 150 ns of the expected Cerenkov arrival time. Making a cut on ndirc (residual <75 ns) is nearly as effective as ndird. Therefore, the choice between using ndirc and ndird is not critical, but as ndird resulted in a slightly lower MRF, we utilized it. See Figure 5.4 for the background and signal distributions of ndird.

[2]Due to the discreteness of the OMs in the detector, a perfect smoothness of 0.0 is unattainable.

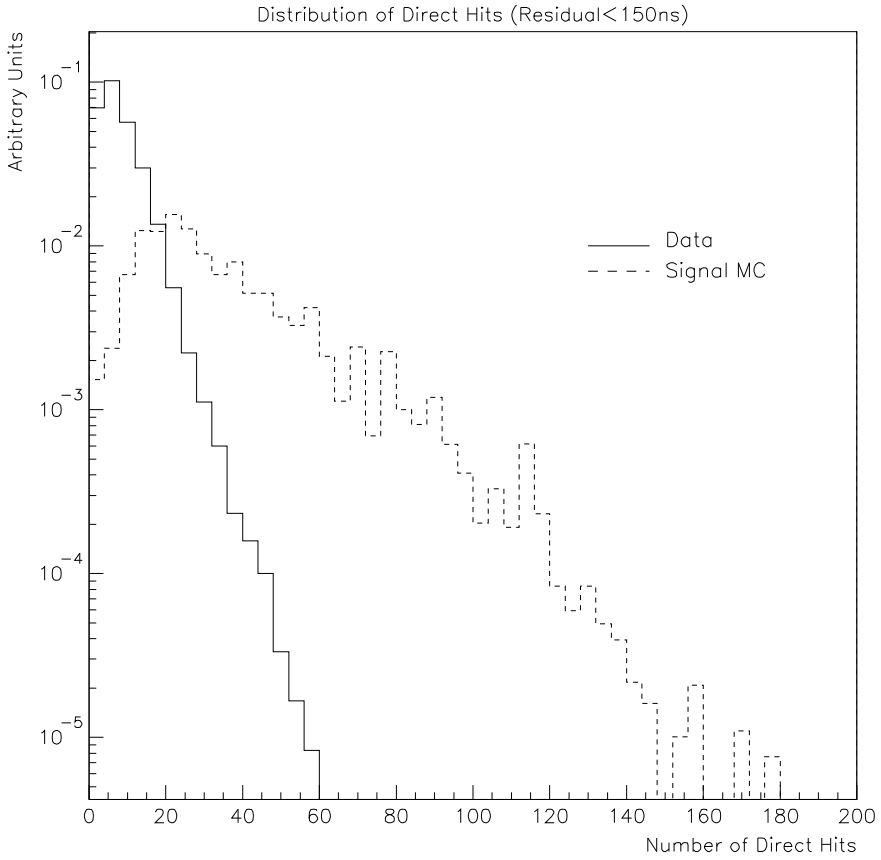

Figure 5.4: The number of ndird direct hits for background data and signal Monte Carlo.

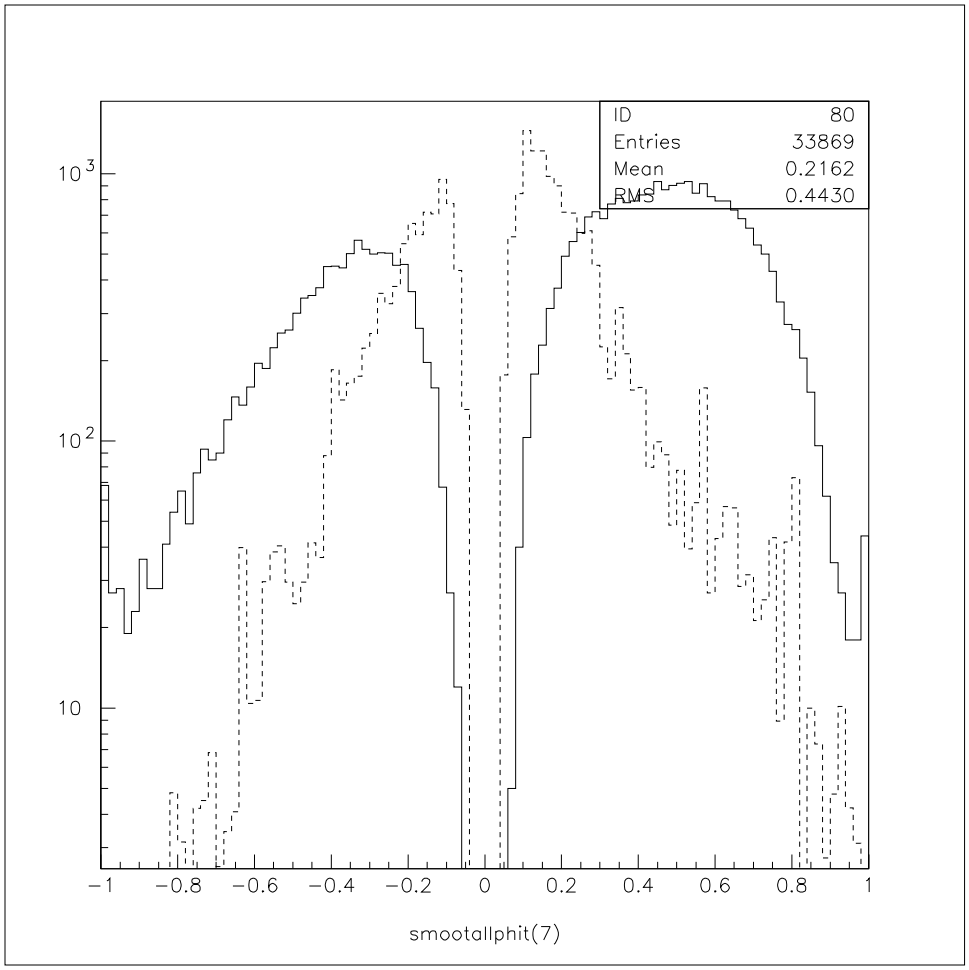

Figure 5.5: The smoothness of the distribution of hits along the reconstructed muon track. Background data is the solid line; signal Monte Carlo is dotted. A high-quality event has a small absolute value of smoothness.

Search Bin Size Ψ	Smoothness smootallphit	Direct Hits ndird	Number of Channels nch
20^o	$-0.40 < S < 0.35$	> 14	> 25

Table 5.4: Final quality cuts for AMANDA-II GRB data.

The data used in this analysis was the first Level 1 data available from the filtering process at DESY. This data was not reprocessed with software that creates new triggering requirements. Therefore, a cut on multiplicity, i.e., the number of channels involved in each event, was very useful for eliminating small, unpromising events. The re-triggering software eliminated 17.44% of such events [19].

Final cuts for the 2000 GRB analysis are shown in Table 5.4. These cuts minimize the Model Rejection Factor. The MRF as a function of nchannel and ndird is shown in Figure 5.7 and Figure 5.8. See the previous section for more details on MRF.

For the final cuts, MRF = 25, or 25 times the Waxman-Bahcall 1999 flux. Due to the more symmetric geometry of AMANDA-II, optimal cuts did not vary strongly with zenith. Therefore, a single cut set is used for all GRBs.

The effectiveness and appropriateness of a particular cut can be evidenced by looking at its "n-1" plot. In "n-1" plots, all cuts except the one being studied are applied. The result is a comparison of the distributions of background and signal in the parameter of interest, but with the other cuts already applied. See Figures 5.9 through 5.11.

The Waxman-Bahcall signal flux is shown in Figure 5.12, before and after the final quality cuts are applied. The cuts retain 62% of the signal. (Although the cuts were optimized for the Waxman-Bahcall flux, they were nearly as efficient for the Alvarez-Muñiz, Halzen and Hooper flux, maintaining 55% of signal events.) The signal events as a function of zenith, before and after cuts, is shown in Figure 5.13.

5.6 Evolution of "Waxman-Bahcall" and "Halzen-Hooper" Fluxes

Some confusion currently exists about what is meant by the Waxman-Bahcall and Halzen fluxes. In 1995, Waxman [20, 21] and Vietri [22] independently proposed a connection between the

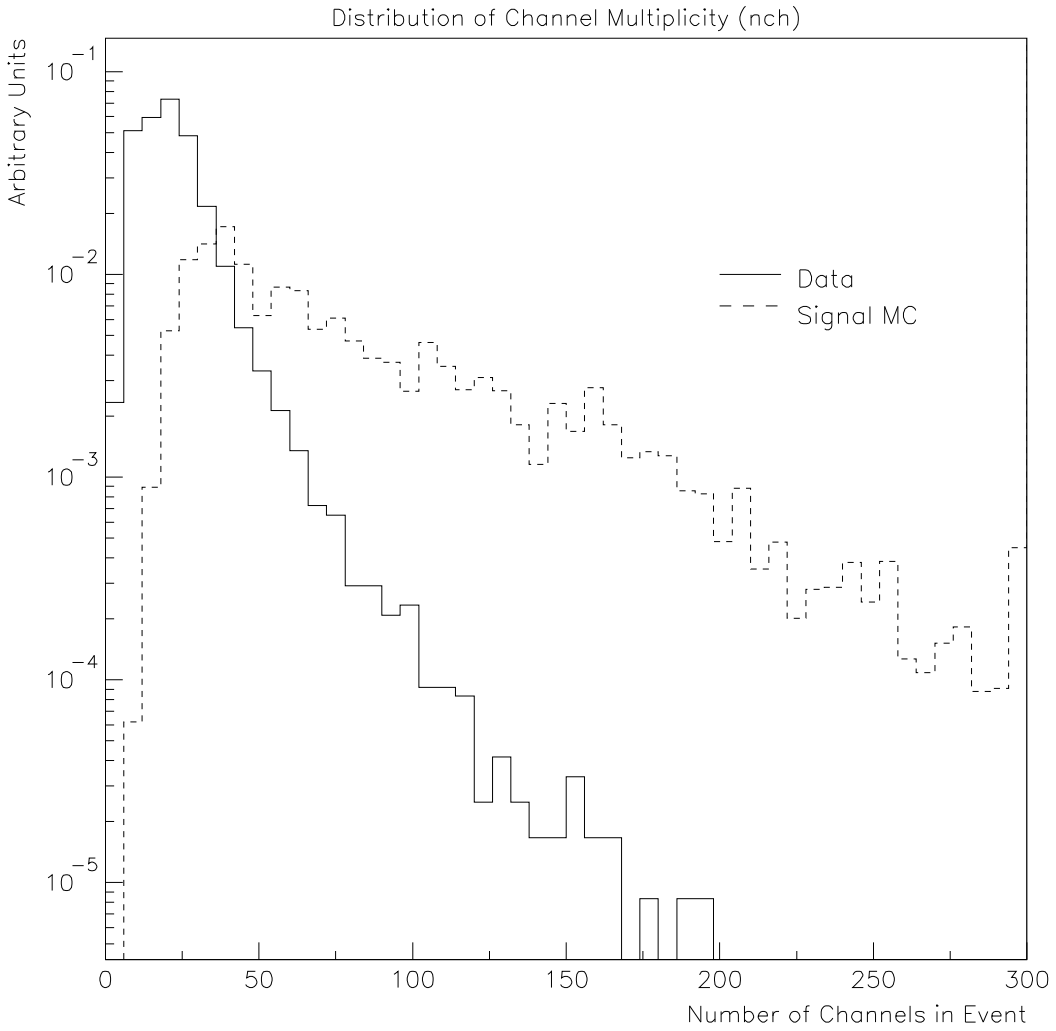

Figure 5.6: The number of channels involved in background and signal events.

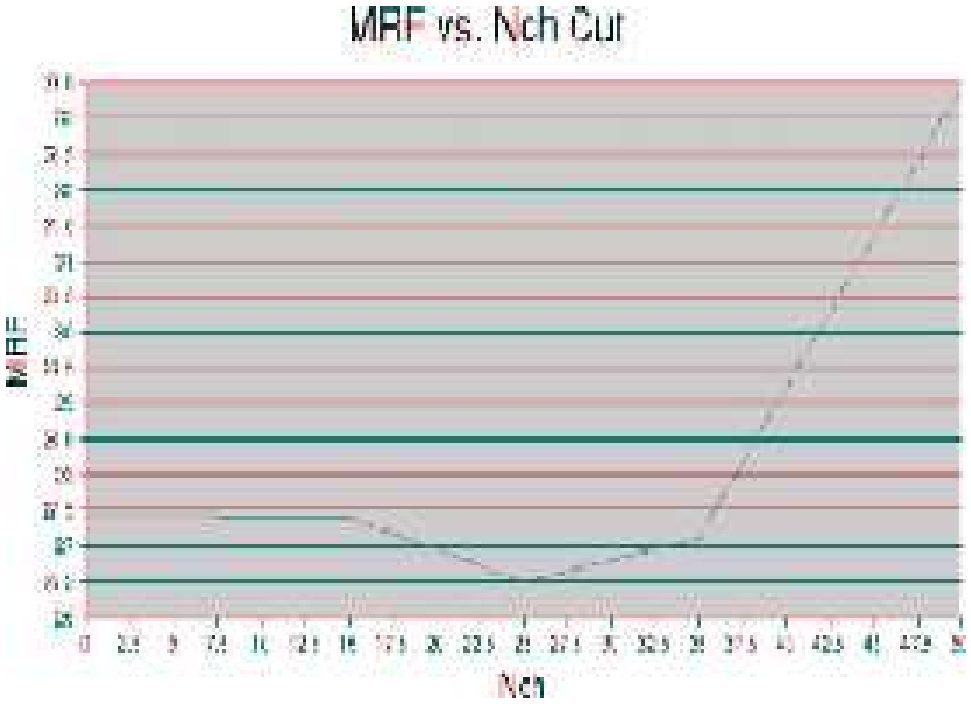

Figure 5.7: The MRF as a function of nch.

generation of the highest energy cosmic rays (those above the "ankle" – see Figure 2.1), and GRBs. They noted that energy production rates are similar in both and that both originate at cosmological distances. If protons are Fermi accelerated [94] in the fireball model (see Chapter 2), a significant fraction of the fireball explosion will be converted to high energy neutrinos [23]. Waxman and Bahcall [23] also derived the broken power law that describes the energies of neutrinos emitted by the fireball. The neutrino spectrum is a convolution of the gamma-ray and proton energy spectrums. The gamma-ray spectrum is a broken power law of E^{-1} below, and E^{-2} above, the break at 1 MeV. The protons will be Fermi accelerated to a power law distribution of E^{-2}. The resulting neutrino spectrum is:

$$\frac{dN_\nu}{dE_\nu} = \frac{A}{E_b E_\nu} \text{ for } \mathrm{E}_\nu < \mathrm{E}_\mathrm{b} \tag{5.1}$$

and

$$\frac{dN_\nu}{dE_\nu} = \frac{A}{E_\nu^2} \text{ for } \mathrm{E}_\nu > \mathrm{E}_\mathrm{b}. \tag{5.2}$$

A, with units of $\frac{\mathrm{TeV}}{\mathrm{cm}^2 \text{ sec sr}}$, is the normalization constant. The value of A depends on the efficiency of pion production, among other things. E_b is the energy at which the differential flux

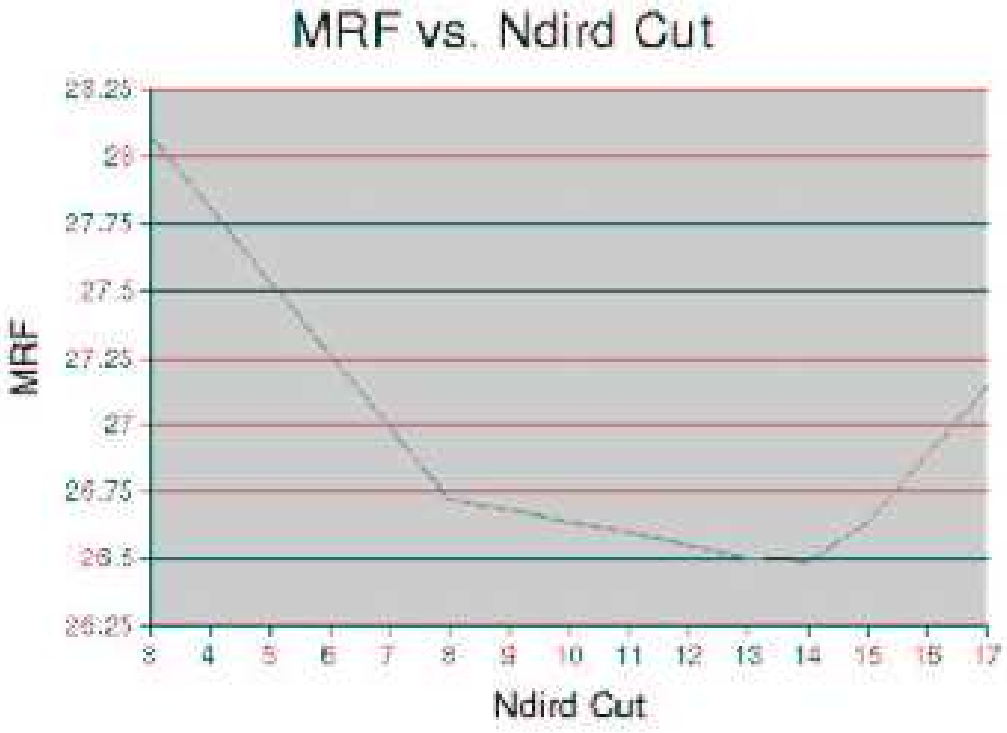

Figure 5.8: The MRF as a function of ndird.

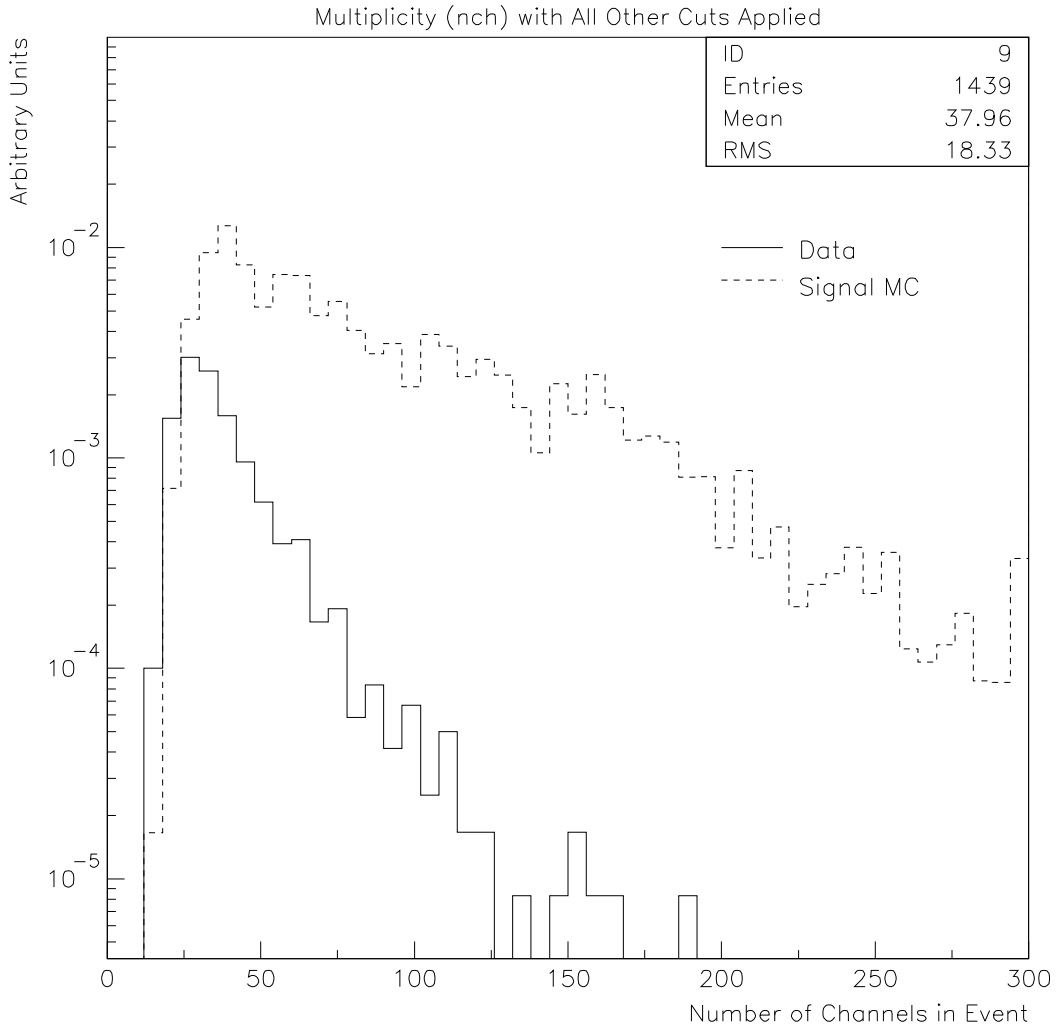

Figure 5.9: The background and signal distribution of nch with all cuts except nch>25 applied.

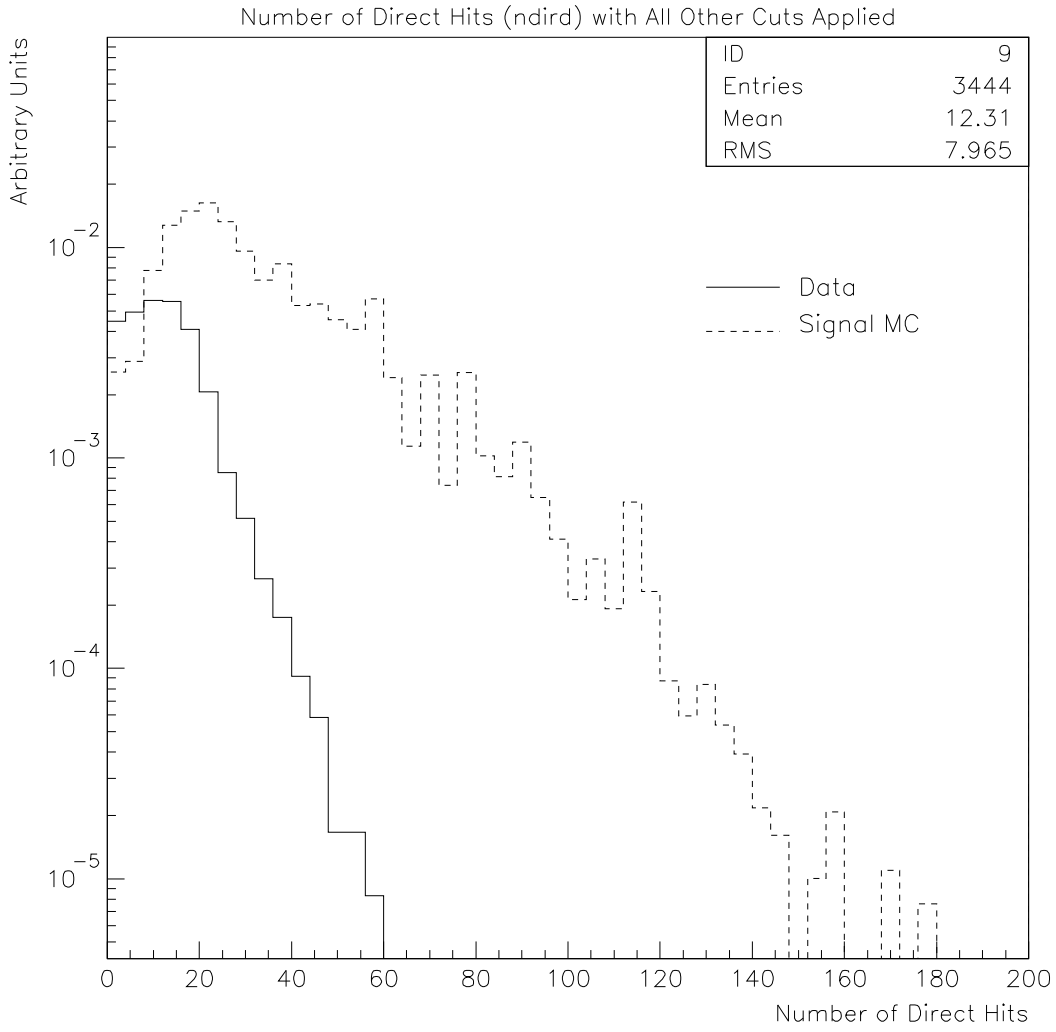

Figure 5.10: The background and signal distribution of ndird with all cuts except ndird>14 applied.

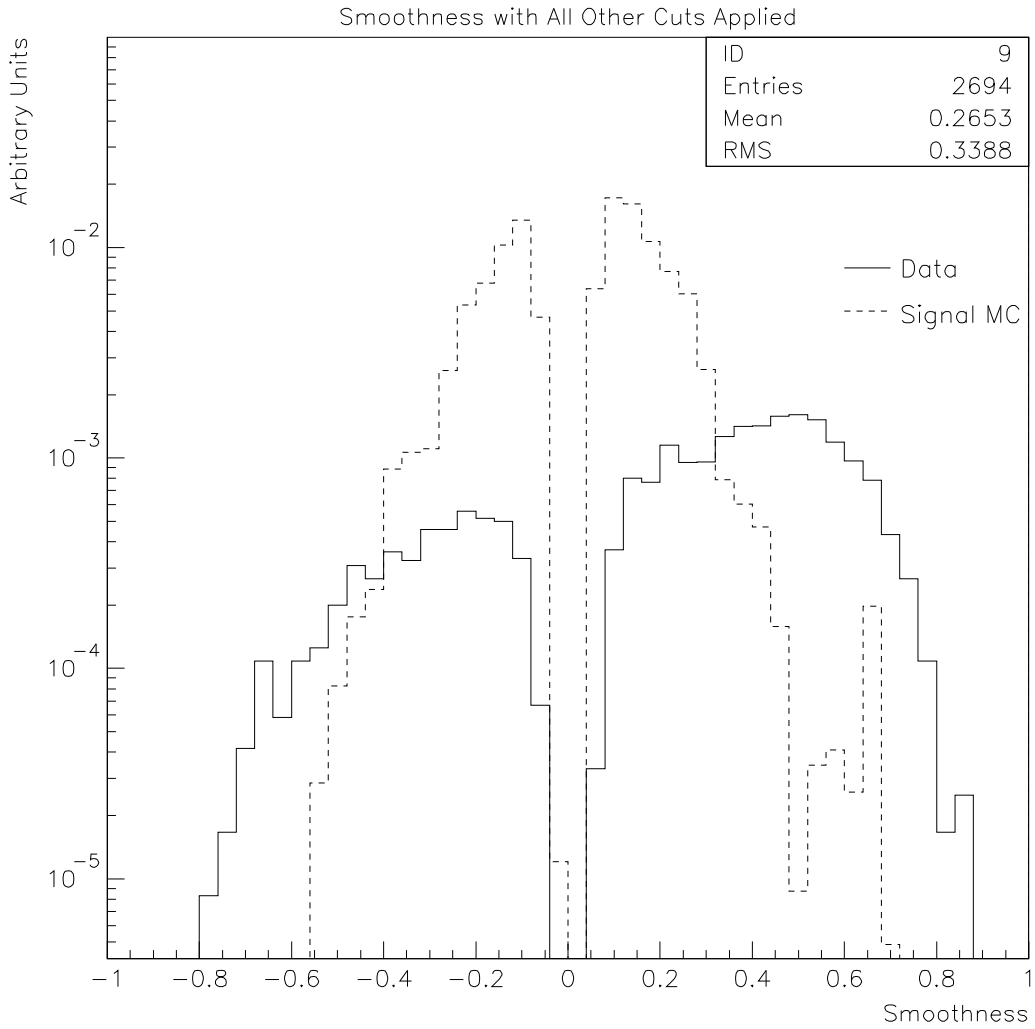

Figure 5.11: The background and signal distribution of smootallphit with all cuts except smoothness applied.

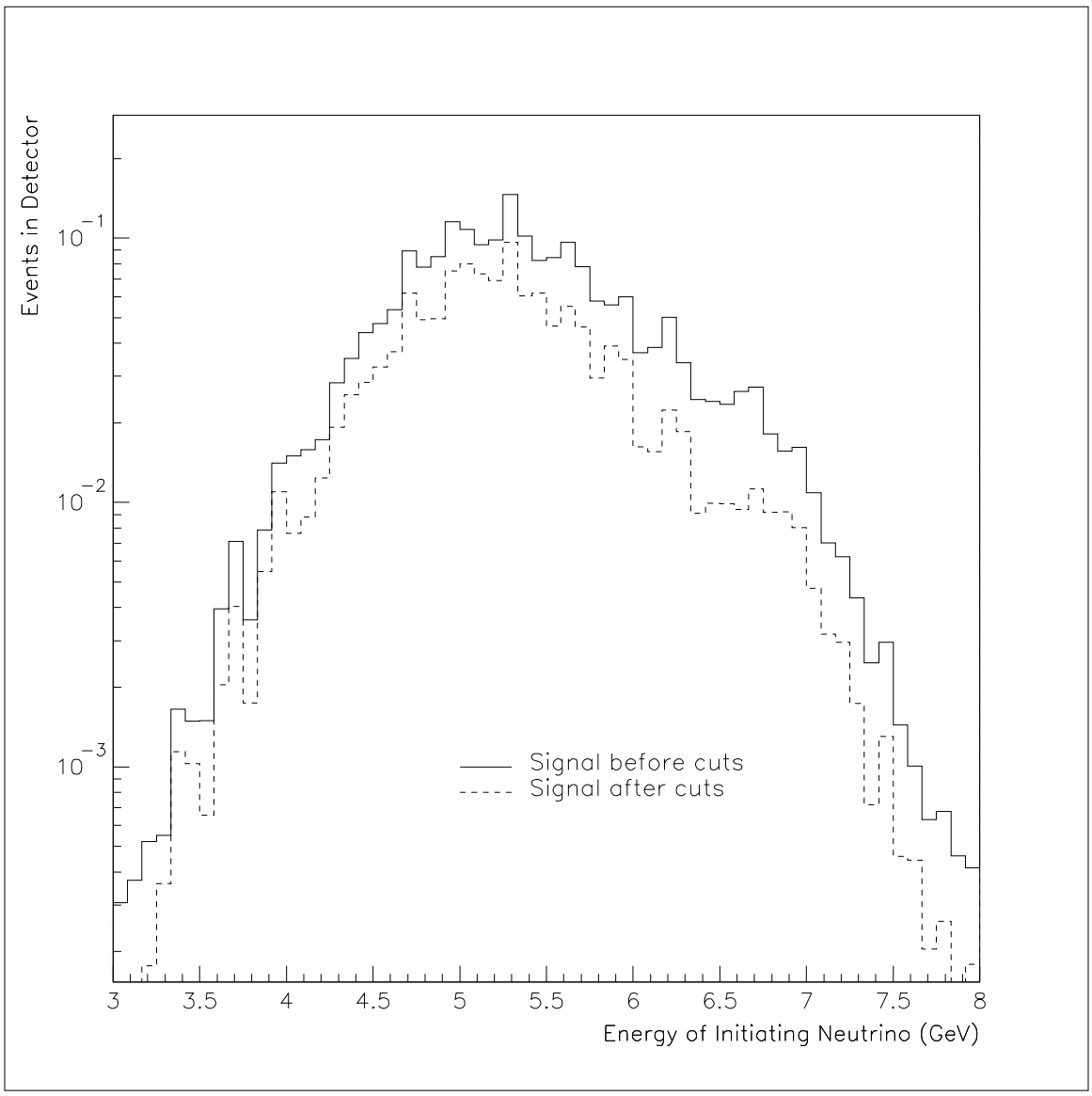

Figure 5.12: The Waxman-Bahcall flux [24] before and after the final quality cuts.

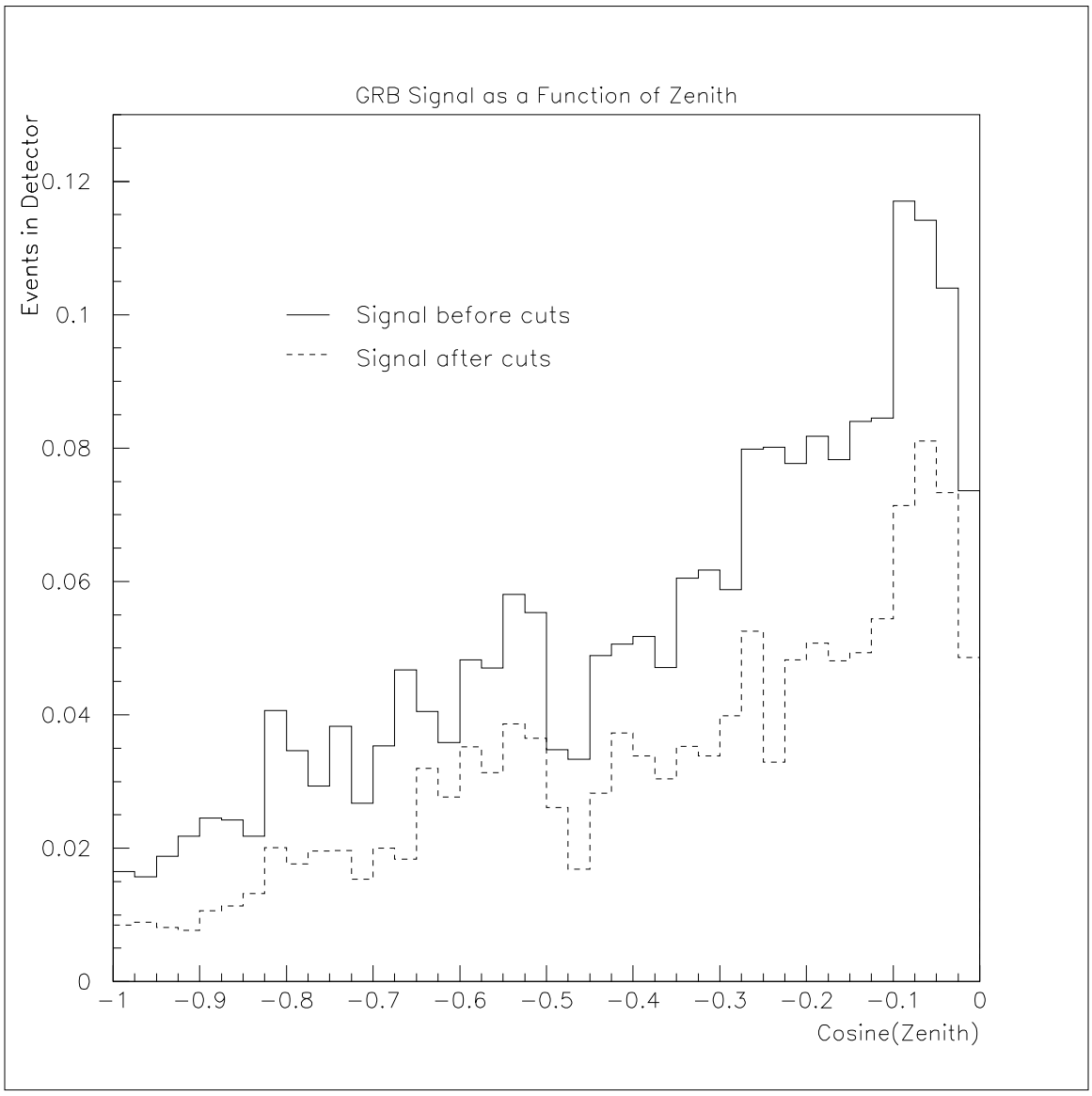

Figure 5.13: The Waxman-Bahcall flux [24] as a function of cosine(zenith) before and after the final quality cuts. Horizontal events have a cos(zenith)=0.0 and vertical upgoing events have a cos(zenith)=-1.0.

spectrum breaks from power $\alpha = -1$ to $\alpha = -2$. Waxman and Bahcall put the break energy at 100 TeV. This is based on their estimation that protons will be accelerated to ~ 10 PeV [3] and on particle physics calculations that show each neutrino produced in the pion decay will carry about 5% of the energy of the initiating proton [26].

In [24] of 1999, Waxman and Bahcall corrected the flux they derived in [23] of 1997 because a logarithmic term had been omitted. When corrected, the Waxman-Bahcall flux was reduced by a factor of 5. [24] also provided more details about the predicted neutrino spectrum and introduced a second break in the spectrum, from E^{-2} to E^{-3}, at 10PeV. See Figure 5.14 and Section V-B of [24]. The second break is induced by the strong suppression of the neutrino flux at these energies due to synchrotron losses.

All of our AMANDA-II simulations so far are based on this neutrino flux. The second break is included, but expected event rates are affected little because the earth becomes opaque to neutrinos at these extremely high energies anyway. When the W-B flux is folded with the detector efficiency, most events are produced by 100 TeV neutrinos. Waxman predicts on the order of "tens" of 100 TeV neutrinos in a km^2 detector [26, 25]. In a later paper [27], Waxman predicts the break energy to be slightly larger, near 500 TeV.

Waxman and Bahcall referred to this flux as an upper bound on high energy neutrinos [24, 28]. They argue that neutrino fluxes above the W-B limit would require additional sources to be accelerating protons to very high energies. This would violate observations of cosmic ray fluxes. Their limit does not apply to neutrino-only sources that are opaque to protons but from which neutrinos can escape.

When referring to the Halzen flux, there are also some iterations that need to be differentiated. In [34], Halzen showed that the break energy is closer to 700 TeV. Then Halzen and Hooper [48] calculated the total energy in GRB neutrinos and determined the normalization constant, A, to be 1.20x10^{-12}Tev/(cm^2 s sr). This flux would produce $\sim$10 events in a km^2 detector per year. This is

[3] This energy is required to produce neutrinos from pion decay because the typical photon energy is 1 MeV. Waxman and Bahcall also point out that protons may be accelerated to energies in excess of 10^{20}eV, resulting in neutrinos of 10^{18}eV that arrive up to 10 seconds after the burst of gamma-rays. These neutrinos would require a different AMANDA search.

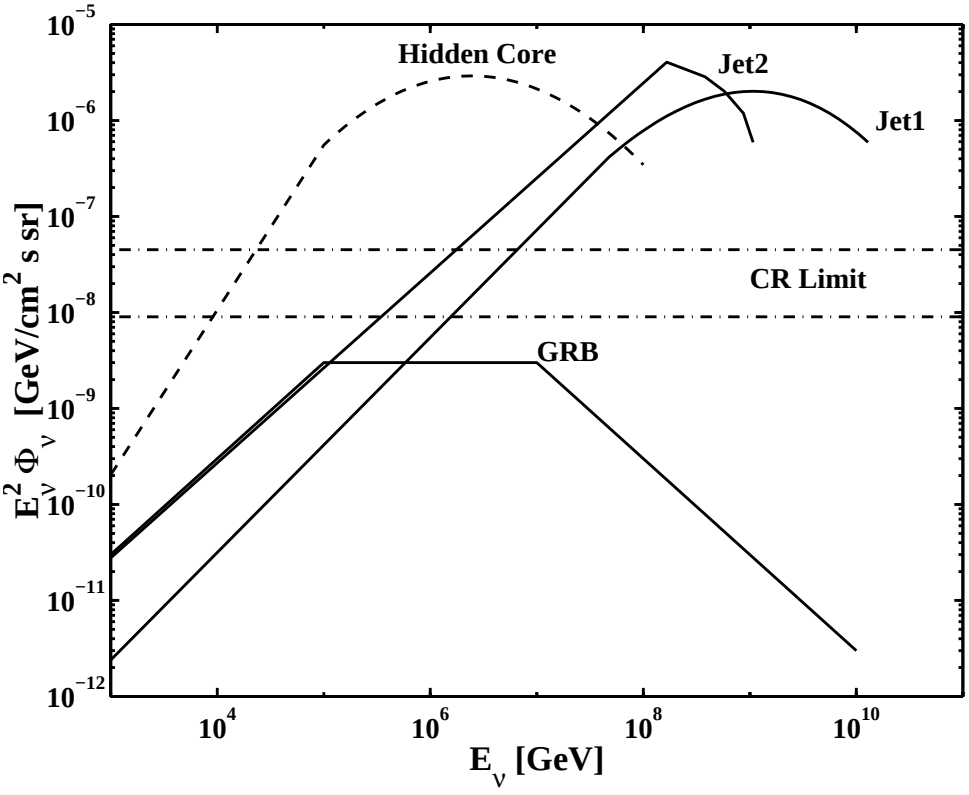

Figure 5.14: The Waxman-Bahcall flux of [24].

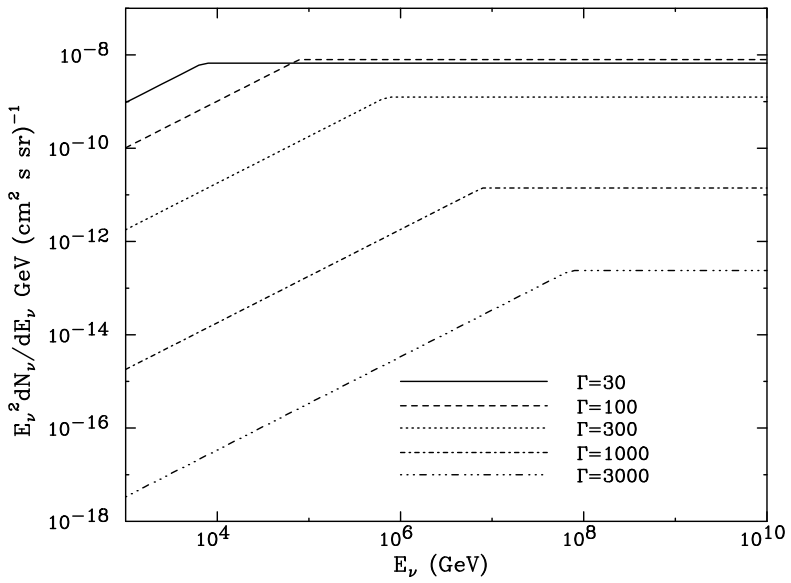

Figure 5.15: The Alvarez-Muñiz, Halzen and Hooper fluxes for 5 values of Γ [47].

somewhat lower than, but consistent, with the Waxman-Bahcall flux of a few 10's of events in a km^2 per year.

Halzen and Hooper go on to show that fluctuations in GRB energy and distance increases the expected event rate by a factor of 3 to 10, depending on the location distribution of GRBs. In general, assuming that GRBs trace the star formation rate, and thus peak at a distance of z=1∼2, produces the smallest and most conservative event rates. Assuming a Euclidean distribution results in a slightly less conservative event rate. A cosmological distribution produces the most optimistic event rates. This relationship is illustrated in Table 4.3.

Halzen and Hooper also examine fluctuations in the Lorentz boost factor of the fireball, Γ. Fluctuations in Γ affect the fraction of energy that goes into pion production and the position of the break energy. Pion (and thus neutrino) production increases strongly (as Γ^{-4}) with decreases in Γ. For small values of Γ, more protons and photons will have the chance to interact to produce pions. This is some times referred to as a "greater effective beam dump". The break energy increases with Γ as Γ^2. These relationships are illustrated in Figure 5.15.

These differences in Γ and GRB evolution can be implemented by appropriately altering the

normalization constant, A. This work was being conducted at UW at the same time as the 1997 GRB analysis and preliminary adjustments to A were made to reflect these developments. They are shown in Table 4.3.

It is apropos here to point out that the work of Halzen and Hooper makes the generally weaker non-triggered bursts (see Appendix A) excellent candidates for larger-than-average numbers of neutrinos. Though they cannot be used to set limits on the Waxman-Bahcall flux (see Section 5.8), they are most interesting candidates.

Alvarez-Muñiz, Halzen and Hooper further treat fluctuations in [47] and model the absorption of high energy neutrinos in the earth. They point out that the Waxman-Bahcall flux may not really be an upper bound. It is possible that additional sources of accelerated protons exist without affecting the observed cosmic ray spectrum because distant high energy cosmic rays will lose energy to the cosmic microwave background.

For Γ=300, [47] predicts $\sim$75 events per year in a km^2 detector before consideration of absorption effects. Absorption in the earth reduces the event number to $\sim$25 events per year in km^2. At $\sim$100 PeV, the earth becomes opaque to muon neutrinos.

Figure 5.15 from [47] does not include fluctuations in energy and distance. Fluctuations in energy and distance are simulated via Monte Carlo. The event rate after including these two fluctuations and absoption in the earth is 14 upgoing events in 2π sr per km^2 per year for Γ=300. A Euclidean distribution of GRBs is used. Using the star formation rate reduces the events rate by about 20%. A cosmological distribution increases the event rate by a factor of 20.

The Waxman-Bahcall flux of [wax-bah2] and the Alvarez-Muñiz, Halzen and Hooper flux of [47], with and without fluctuations is shown in Figure 5.16.

In the absence of a signal detection, limits will be placed on both the Waxman-Bahcall and Alvarez-Muñiz, Halzen and Hooper fluxes. The same Monte Carlo will be used, as the Monte Carlo weighting system easily allows for the modeling of different spectra.

5.7 Search

The fireball may be opaque to photons longer than it is opaque to neutrinos. This would permit the arrival of neutrinos before the beginning of the gamma ray detection. Theorists [95]

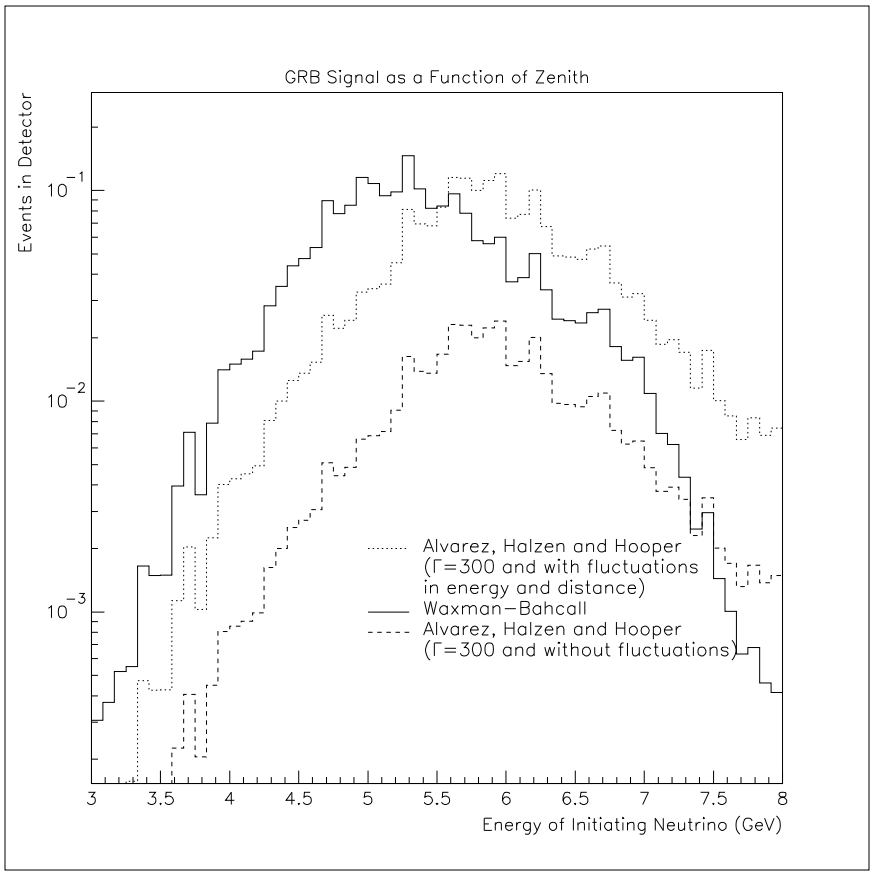

Figure 5.16: The Waxman-Bahcall flux of [wax-bah2] and the Alvarez-Muñiz, Halzen and Hooper flux, with and without fluctuations in energy and distance, for Γ=300.

predict that neutrinos may arrive up to 10 seconds (and pehaps up to 100 seconds) before the initial gamma rays. We want to ensure that our search allows for this early arrival. Therefore, to set the beginning of the temporal search window, we use the earlier of the T90 start time or the trigger time (t_0 = minimum{T90 start,trigger time}) and then subtract 10 seconds. The temporal search window will extend to the end of the T90 duration..

Some GRBs do not have durations catalogued. This occurred, for example, when there were data gaps in the BATSE record. Based on comprehensive distributions, most GRBs lasted no longer than 100 seconds. See Figure 1.6. Therefore, 100 seconds will be used as the T90 duration for the eight GRBs lacking this information (7991, 8002, 8005, 8031, 8056, 8057, 8074, 8109).

5.8 Note on Setting Upper Limit

The Waxman-Bahcall flux, and related fluxes, are explicitly based on GRB observations made by BATSE. (See Section V-A of [24].) BATSE observed 1/3 of the sky at a time, and saw about 1 GRB per day. Therefore, the nominal number of bursts frequently used in GRB models, including Waxman-Bahcall, is 365 x 3 $\approx$ 1000 bursts per year. Waxman and Bahcall also used the energy distribution of BATSE GRBs in their model.

However, we now know that BATSE was not entirely efficient in detecting GRBs even in the 1/3 of the sky it was observing. From studies of archival data [78, 81], about 50% more GRBs occurred in BATSE's view than were detected by the on-board triggers. See Appendix A for more details. In general, these bursts are weaker than the main BATSE sample. Therefore, current models should be altered to account for these additional bursts. If a model does not include these non-triggered bursts, then the non-triggered bursts can not be used to place upper limits on that model. Only the GRBs modeled by the theory can be used to set limits. Therefore, as we did in 1997, we will use only the triggered bursts to place limits on the Waxman-Bahcall and similar fluxes. The non-triggered bursts will be searched for detections only. Any analysis that uses the non-triggered bursts to set limits must alter the tested model to account for these bursts. They can not be used to constrain models based on the triggered GRB subset.

5.9 Summary

From the beginning, I increased the "blind spot" around a GRB trigger time from (-1,+5) minutes to (-5,+5) minutes in order to better account for the possible early arrival neutrinos. All studies on the 2000 GRB data at UW have maintained this 600-second blind spot, as shown in Appendix J.

The background portions of the 2000 GRB data have been thoroughly investigated. Stability and data quality have been examined for each of 70 bursts. Final cuts were set my optimizing the Model Rejection Factor for the Waxman-Bahcall GRB flux. The final cut set retains 62% of signal events. The expected background rate is 0.01 events per burst.

Chapter 6

Results

6.1 Comment on Neutrino Oscillations

If current results from Super-K bear out, muon neutrinos oscillate to tau neutrinos near the maximal mixing angle. We therefore expect that the number of muon neutrinos from GRBs will be halved, with half of the neutrinos being tau neutrinos at the detector. If so, future analyses and enlargements of the AMANDA detector will be able to study the first ever tau neutrino appearance experiment. Tau neutrinos would penetrate the earth at energies where muon neutrinos are absorbed in the earth [50]. However, in this analysis, which searches for muon neutrinos only, the expected signal rates would be 1/2 of the listed numbers.

6.2 Results

After extensive studies of the background data regions, the on-time regions of the 1997, 1999 and 2000 data were un-blinded and the number of events in the GRB region at the time of a GRB were studied. The number of events in the on-time region (i.e., during the burst) is shown in Appendix G for year 1999 bursts and in Appendix K for year 2000 bursts.

The expected number of signal events in the AMANDA-II detector from 2π sr are shown in Table 6.1 for several fluxes.

Alvarez-Muñiz, Halzen and Hooper predict 14 events in 2π sr in a km^2 detector. Therefore, the effective area before cuts is approximately 100,000 m^2 and after cuts it is 75,000 m^2.

Flux	500 bursts no cuts	500 bursts with cuts	44 bursts after cuts
WB1999	2.102	1.29	0.114
AHH (no flucs.)	0.40	0.30	0.026
AHH (with flucs.)	1.4	1.1	0.092

Table 6.1: The expected number of signal events in 2π sr for three fluxes: Waxman-Bahcall [24], Alvarez-Muñiz, Halzen and Hooper [47] with and without fluctuations in energy and distance.

In most cases, the optimization procedure yields optimal bin sizes with no on-source, on-time events as all background events have been removed by the quality cuts. Because the search did not yield statistically significant bursts we derive a combined upper limit for the AMANDA-B10 and AMANDA-II searches. It is calculated by summing the average number of background events, $< n_{\rm bg}^{\rm tot} >$, and by summing the observed number of events in the GRB search bin, $\rm n_{counted}$, over all bursts. Then,

$$\frac{d\phi_\nu^{\rm uplim}}{E} \leq \frac{n^{\rm uplim}}{n_{\rm signal}} \frac{d\phi_\nu}{dE},$$

where $\frac{d\phi}{dE}$ is the GRB flux, $\rm n_{signal}$ is the expected number of events from GRB neutrinos after cuts, and $\rm n^{uplim}$ is the event upper limit calculated according to [85] at 90% from $< n_{\rm bg}^{\rm tot} >$ and $\rm n_{counted}$.

For the search on 78 triggered bursts in 1997, with the window opened to -10 seconds before the beginning of the gamma-ray burst and the strong cuts in place, the expected background is $< n_{bg}^{tot} >= 0.06$ events. We observed 0 events. Therefore, the Feldman-Cousin 90% upper limit for the signal mean is 2.41. Our expected signal is 0.043. Therefore, from the one year of 1997 data, we obtain an flux upper limit that is $2.41/0.043 = 56$x the Waxman-Bahcall flux prediction.

For the search on 96 bursts in 1999, $< n_{bg}^{tot} >= 0.2$ and $\rm n_{counted}$=0. Therefore, the Feldman-Cousin 90% upper limit for the signal mean is 2.24. Our expected signal rate is 0.053. Therefore, from one year of 1999 data, we obtain an flux upper limit that is $2.24/0.053 = 42$x the Waxman-Bahcall flux prediction.

For the search on 44 triggered bursts in 2000, $< n_{bg}^{tot} >= 0.833$ events. We observed $\rm n_{counted}$=0. Therefore, the Feldman-Cousin 90% upper limit for the signal mean is 1.72. Our expected signal rate

Data Year	Average Background	Detected Detected	Expected Signal	Event Upper Limit	Upper Limit on Waxman-Bahcall
1997	0.06	0	0.043	2.41	56x
1999	0.20	0	0.053	2.24	42x
2000	0.83	0	0.114	1.72	15x
Overall	1.14	0	0.22	1.153	7x

Table 6.2: Summary of search results.

is 0.114. Therefore, from one year of 2000 data, we obtain an flux upper limit that is $1.72/0.114 =$ 15x the Waxman-Bahcall flux prediction.

Over the three years of data, We have an expected background of 1.14events. We observe 0 events. Therefore the combined event upper limit is 1.53 from [85]. The total expected signal is 0.22. Therefore the combine upper limit is $1.153/.22 =$ 7x Waxman Bahcall.

The AMANDA-II bursts dominate and greatly improve the upper limit. Although it is most unfortunate that BATSE was decommisioned in May of 2000, the results show the promise of using other satellite detections for study in the AMANDA-II years.

6.3 Theoretical Impact

At 7x the Waxman-Bahcall flux, the AMANDA GRB neutrino search can not rule out the leading model of GRB production. But AMANDA-II will be able to rule out (or confirm) the model in the next few years.

Chapter 7

Future

7.1 Other Satellite Detectors

BATSE was a prolific GRB detector, discovering about one burst per day. Other satellites have, and will, detect gamma-ray bursts.

The Third Interplanetary Network (IPN3) consists of several satellites, including Ulysses, the Near Earth Asteroid Rendevouz (NEAR), WIND, Mars Odyssey, RXTE and BeppoSAX. These satellites have primary science missions other than the detection of gamma-ray bursts, but in addition to their primary work, these satellites occasionally detect GRBs. Under the direction of Kevin Hurley at the Space Science Laboratory in Berkeley, California, data from this network of satellites is combined to produce approximate positions of GRBs. IPN3 detects $\sim$1 GRB per week. Some of these satellites, such as NEAR (which landed on an asteroid in 2001) are no longer contributing to this effort.

The High-Energy Transient Explorer II (HETE2) was launched in October of 2000 and is a follow-up to the first ill-fated HETE satellite, which failed to separate from its third stage rocket. Predictions were that HETE2 would detect about one burst per week. Some components of HETE2 have experienced technological difficulties. The first year of the HETE2 mission was celebrated and discussed at a Woods Hole conference in November of 2001.

In summary, the current rate of GRB detections is much reduced from the days of BATSE. The situation will improve in the future with additional satellite deployments. The European spacecraft

INTEGRAL [67] is scheduled for an October 2002 launch. Although it is not strictly a GRB mission, INTEGRAL will likely detect and precisely locate several GRBs per month. The U.S. SWIFT mission [68] is scheduled for launch in July 2003. The detection and precise location of GRBs is its main objective. It is expected to locate 100-300 GRBs per year.

NASA's Gamma-Ray Large Area Space Telescope (GLAST) is is scheduled for launch in 2006. Its main instrument, the Large Area Telescope (LAT), will provide unprecedented sensitivity to gamma rays in the energy range of about 20 MeV to about 300 GeV. The GLAST Burst Monitor (GBM) is a complementary instrument and will be sensitive to X-rays and gamma rays in the 5 keV - 25 MeV range. GLAST is expected to detect about 200 GRBs per year.

Many of the current and future detectors are designed to better resolve the position of GRBs so that other instruments can locate and study the GRBs in longer wavelengths for additional days and weeks. As the resolution of AMANDA and IceCube for GRB searches is on the order of a few degrees, this additional resolution is not critical to AMANDA searches. With the type of analysis detailed in this thesis, the critical parameter for the discovery potential (or placement of theoretical upper limits) of AMANDA and IceCube[96] is the number of bursts detected by satellites. More specifically, the science potential of AMANDA/IceCube GRB searches is proportional to the number of northern hemisphere GRBs that can be examined by AMANDA/IceCube after satellite detection.

This thesis presents the results of incorporating the BATSE data from 1997 through 2000 with AMANDA-B10 and -B19 data. GRBs that were discovered and located by detectors other than BATSE can be examined, but these are a small number compared to the productivity of BATSE.

7.2 Current Data Extraction

Gamma-ray satellites rapidly release their findings via the Global Coordinates Network (GCN), formerly called BACODINE. AMANDA now buffers enough data at the South Pole such that two hours of data can be extracted around a GRB time announced by GCN email alerts. This will allow future GRB analyses to proceed immediately following a burst detection. This is a significant improvement over the system in place between 1997 and 2000 when data was stored at the South Pole until the end of austral winter and then hand-carried out on data tapes, uploaded and filtered at LBNL, and then distributed to collaboration scientists. (See Appendix B on data processing.) This

process often took many months to complete.

7.3 Other Types of Searches

Another method for AMANDA/IceCube GRB searches that will likely be employed in the future is a "rolling" search through all the available AMANDA/IceCube data. This method does not rely on detection of GRBs by other instruments, but rather rolls through the entire AMANDA/IceCube data set, searching for an excessive number of neutrinos from a given location at any time. These neutrinos could then be compared to the expected energy distribution of GRB neutrinos. A point-source search for very high energy neutrinos using all available AMANDA data is underway[64].

Rolling searches will be particularly important to AMANDA/IceCube GRB neutrino searches during the time between the end of BATSE (May, 2000) and the launching of SWIFT (scheduled for 2003). This type of search will also be critical to the potential detection of GRBs that were too weak to trigger the BATSE detector. There may be a class of such GRBs and these GRBs may indeed be more prolific neutrino sources. AMANDA/IceCube has the potential to discover GRBs that have not been previously detected by other instruments.

7.4 IceCube

Initial funding has been approved for the construction of IceCube [96], a project that will instrument a km^3 of ice. IceCube is based on the AMANDA-B10 and AMANDA-II prototypes. It will consist of 80 strings and nearly 5,000 OMs. IceCube will be deployed over six years, beginning in 2005-06.

Bibliography

[1] Klebesadel, et al., Ap. J. Lett. (1973).

[2] S. White, Astrophys. Space Sci., 208, 301 (1993).

[3] B. Luchkov, Astron. Letters, 20, 253 (1994).

[4] J. Higdon and R. Ligenfelter, Ann. Rev. Astron. Astrophys. 28, 401 (1990).

[5] A. K. Harding, Phys. Reports, 206, 327 (1991).

[6] D. Hartmann, et al Ap. J. Suppl., 90, 893 (1994).

[7] C. A. Meegan, et al., Nature **355**, 143 (1992).

[8] http://gammaray.msfc.nasa.gov/batse

[9] K. Hurley, *Gamma Ray Bursts and their Afterglows*, Institute for Theoretical Physics, UC-Santa Barbara GRB Workshop, March 15-19, 1999.

[10] S. R. Kulkarni, et al., Nature 393, 35 (1999).

[11] F. A. Harrison, et al., astro-ph/9905306 (1999).

[12] J. P. Halpern, et al., Ap. J. Lett. **517**, 105 (1999)

[13] J. N. Reeves, et al. (2002)

[14] Wang and Wheeler (1998).

[15] Kippen (1998).

[16] Bloom (1998).

[17] B. Paczynski Ap. J. Lett. 1986

[18] J. Goodman Ap. J., 1986.

[19] M. Ribordy, http://www-zeuthen.desy.de/ ribordy/AIInumbers.html

[20] E. Waxman, Phys. Rev. Lett. **75**, 386 (1995).

[21] E. Waxman, Astrophys. J. **452** L1 (1995).

[22] M.Vietri, Astrophys. J. **453**, 883 (1995).

[23] E. Waxman and J.N. Bahcall, Phys. Rev. Lett. **78**, 2292 (1997).

[24] E. Waxman and J.N. Bahcall, Phys. Rev. D **59**, 023002 (1999).

[25] E. Waxman, TAUP99, Nucl. Phys. B Proc.Suppl. **87**, 345 (2000).

[26] E. Waxman, Nucl. Phys. Proc. Suppl. 91, 494-500 (2000).

[27] E. Waxman, 7th Internl. Symp. on Particles, Strings and Cosmology (2000).

[28] J. Bahcall and E. Waxman, Phys. Rev. D **64**, 023002 (2001).

[29] E. Waxman

[30] Rachen and Meszaros (1998).

[31] Totani (1998).

[32] C.D. Dermer, astro-ph/0005440.

[33] Dar and De Rujula+

[34] F. Halzen, TASI 1998: Neutrinos in Physics and Astrophysics(2000).

[35] J.D. Jackson, chapter 13.

[36] E. Andres, et al., Nature **410**, 441-443 (2001).

[37] L. B. Price and L. Bergstrom, Applied Optics 36, 4181 (1997).

[38] Y.D. He and P.B. Price, J. of Geophys. Res. 103, 17041 (1998).

[39] P. Askebjer, et al., Applied Optics 36, 4168 (1997).

[40] J. Ahrens, et al. Physical Review D66, 032006 (2002).

[41] AMANDA Collaboration, Astropart. Phys. **16** 4 355-369.

[42] J. Ahrens, et al., accepted for publication by Astrophys. J. (2002).

[43] J. Ahrens, et al., submitted to Phys. Rev. D (2002).

[44] J. Ahrens, et al., accepted for publication by Phys. Rev. D (2002).

[45] K. Rawlins, Ph.D. thesis, University of Wisconsin (2001).

[46] E. Andres *et al.*, Astropart. Phys. **13**, 1-20 (2000).

[47] J. Alvarez-Muñiz, F. Halzen and D.W. Hooper, Phys. Rev. D **62**, 093015 (2000).

[48] F. Halzen and D.W. Hooper, Astrophys. J. Lett. **527**, L93 (1999).

[49] T. Gaisser, F. Halzen and T. Stanev, Phys. Rep. 258(3), 173 (1995).

[50] F. Halzen and D. Saltzberg, Phy. Rev. Lett. 81, 4305 (1998).

[51] Vernetto, Astropart. Phys. **13**, 75-86 (2000).

[52] Reno and Quigg, HE neutrino absorption in the earth

[53] P. Lipari, T. Stanev, Phys. Rev. D **44**, 11 (1991).

[54] R. Bay, Ph.D. thesis, University of California-Berkeley (2000), astro-ph/0008255.

[55] D. Cowen, "Blindness: Using Known Non-Signal Data", AMANDA internal report 20010803.

[56] P. Duffet-Smith, "Practical Astronomy with your Calculator", 2nd ed., Cambridge University Press (1981).

[57] INTEGRAL

[58] E. Costa, et al., Nature **387**, 783 (1997).

[59] J. P. Rachen, et al., astro-ph/9908031.

[60] K. Mannheim, et al., astro-ph/9812398.

[61] Hurley, et al., astro-ph/9912061

[62] Hurley, et al., Astrop. J. 510:L111-114 (1999).

[63] Hurley, et al., Astrop. J. 510:L107-L109 (1999).

[64] Point Source paper from UC-Irvine, in preparation or submitted (2002).

[65] Halzen and Hooper review paper, Rept. Prog. Phys. 65:1025-1078 (2002).

[66] AMANDA Collaboration, *The IceCube Paper*, in preparation.

[67] http://astro.estec.esa.nl/SA-general/Projects/Integral/integral.html

[68] http://swift.sonoma.edu/; http://www.swift.psu.edu/

[69] T. Piran, Phys. Rep. **333** – **334**, 529-553 (2000).

[70] B.E. Stern & Y. Tikhomirova http://www.astro.su.se/groups/head/grb_archive.html

[71] J. Lamoureux and J. Jacobsen, internal AMANDA report (1999).

[72] AMANDA collaboration meeting, Brussels, Belgium (2000).

[73] P. Ekstrom, Ph.D. thesis, Stockholm University (2002).

[74] J. Lamoureux, personal communication.

[75] D. Cherkin, MMC internal report (2001).

[76] H. Krawczynski, HH-HEGRA/97-01.

[77] B.C. Rubin *et al.*, AIP Conf Proc. **280**, 719 ed. M. Friedlander *et al.* (1992).

[78] B.E. Stern *et al.*, A&AS **138**, 413 (1999)

[79] B.E. Stern *et al.* ASP Conf. Ser. **190** 253, ed. J. Poutanen and R. Svensson (1999).

[80] B.E. Stern *et al.*, Astrophys. J. Lett. **540** L21 (2000); B.E. Stern *et al.*, astro-ph/0009447.

[81] J.M. Kommers *et al.*, Astrophys. J. **491**, 704 (1997).

[82] J.M. Kommers *et al.*, http://space.mit.edu/BATSE

[83] J.M. Kommers *et al.*, Astrophys. J. **533**, 696 (2000).

[84] K. Hurley, private communication.

[85] G. F. Feldman and R.B. Cousins, Phys. Rev. D, **57**, 3873-3889 (1998).

[86] P. Steffen, Direct-Walk II, AMANDA Internal Report 20020201.

[87] P. Steffen, email to amanda-c, 26July01.

[88] R. Hardtke, http://amanda.physics.wisc.edu/rellen/grb_blindness.html, Aug01.

[89] G. Hill and K. Rawlins, submitted to Astropart. Physics (2002) and AMANDA Internal Report 20000902.

[90] http://www-zeuthen.desy.de/ niessen/ana99/mc99/mc99.html

[91] http://amanda.physics.wisc.edu/simulation/

[92] http://www.ps.uci.edu/ kuehn/00/00.html

[93] T. Piran, review paper, Phys. Rep. 314, 575 (1999).

[94] E. Fermi, Phys. Rev., 75, 1169 (1949)

[95] E. Waxman and P. Meszaros, personal communication (2002).

[96] http://icecube.wisc.edu

Appendix A

Non-Triggered Bursts

A.1 BATSE Archived Data

BATSE recorded all data on a 1.024 second time scale in each of its eight detectors. Jeff Kommers and Boris Stern searched this archived data for GRBs that were missed by BATSE's onboard trigger. GRBs may have not met the BATSE onboard trigger conditions because they were too weak or their fluence rose too slowly. Candidates may not have been successfully recorded because the trigger or recording device was disabled. At times, the BATE trigger was set for optimal detection of phenomena other than GRBs, such as Galactic soft gamma repeaters or terrestrial gamma flashes. (The last was not true in years 1997-1999.)

GRB candidates discovered in this way are called "non-triggered bursts". The light curves of these bursts are convincing. (See Figure A.1 for an example. The Ulysses satellite has confirmed >50 of these bursts [84]. The triggers are similar to the BATSE onboard trigger, but with different estimations of background rates. The Kommers and Stern samples have signicant overlap of candidates in 1997. (Kommers' list ends in 1997.) Stern estimated the efficiency of his search by adding test bursts to the data.

In general, the non-triggered bursts are weaker than the triggered ones. See Figure A.2. As explained in [47], GRBs that are weak in gamma production may be copious neutrino emitters. Therefore, the non-triggered busts are desirable subjects of investigation.

Because they are weaker, the non-triggered bursts are not as well localized. See Figure A.3.

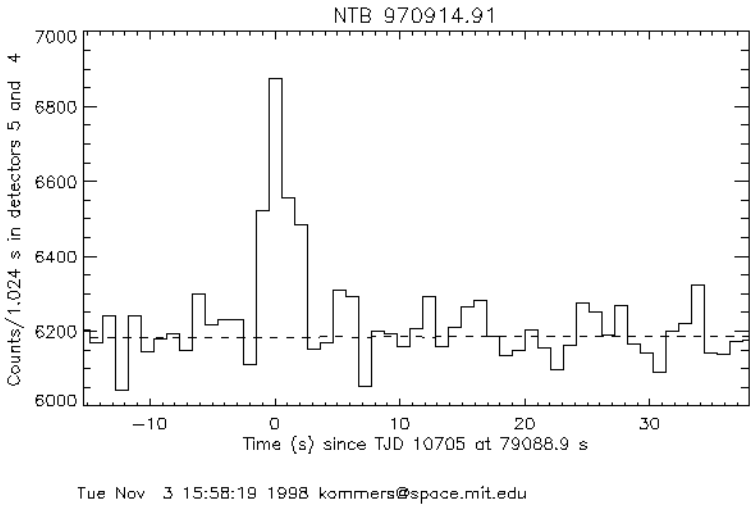

Figure A.1: Light curve from non-triggered burst 970914.91 found by Kommers [82].

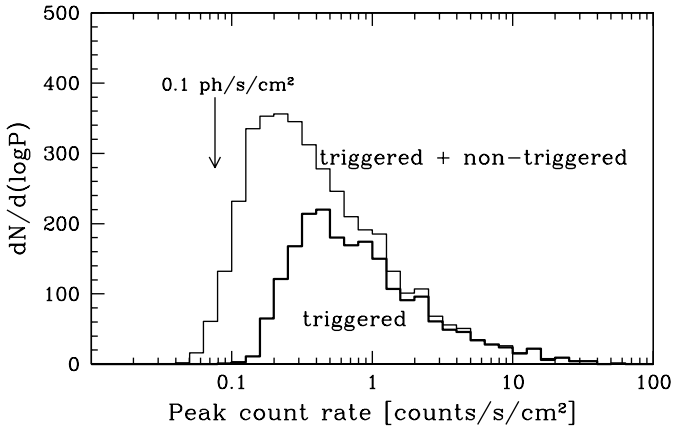

Figure A.2: Distribution of peak fluxes for bursts triggered on-board BATSE and for non-triggered bursts found in archived data by [70].

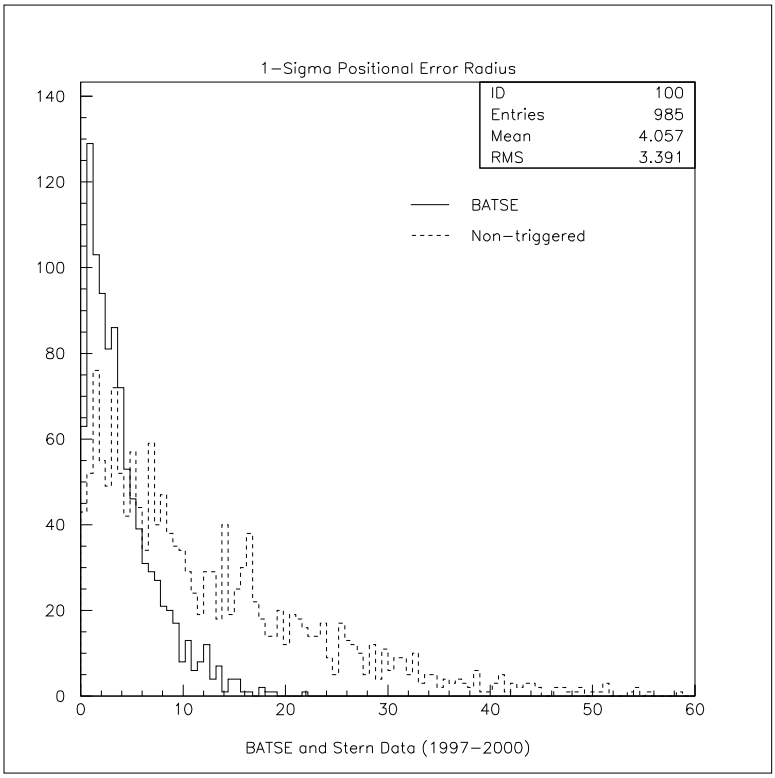

Figure A.3: Distribution of 1σ error boxes for triggered and non-triggered bursts.

In 1997, we examined the union of candidates from Kommers and Stern. Sixty-four non-triggered bursts occurred between April 5 and November 15, the period of stable data-taking. Eight occurred during AMANDA data gaps. Three could not be extracted because the log file of the initial filtering process was incomplete. Five were removed due to unstable trigger rates. Therefore, 48 bursts were added to the sample of 78 triggered bursts examined in that analysis. This in creased the GRB sample size 61

In 2000, 26 non-triggered bursts occurred during AMANDA-II data taking. Representative of the increased reliability and performance of the AMANDA array, none of these bursts had to be omitted due to data gaps or data quality concerns. These bursts augmented the 44 analyzed triggered bursts for a total of 70 bursts in the AMANDA sample.

Appendix B

Computation and Data Processing

B.1 1997-1999

After being recorded on magnetic tape during the austral winter data-taking season, the 1997 AMANDA-B10 data set was filtered at LBNL. The data was first filtered with a T3E supercomputer. After refinements to the filter, it was re-filtered on an alpha cluster. The data for the first AMANDA GRB analysis was initially extracted by Ryan Bay [54].

The Monte Carlo used in the GRB analysis needed to be updated. Several major changes occurred, including corrections of (1) a noise bug in recoos and (2) a photon flight time bug in the Photon Transportation and Detection (PTD) tables. PTD is a software package that tracks photons through ice. It records the arrival time of a photon at an AMANDA optical module of arbitrary orientation and the probability of detection. Tables of probability distributions for detecting photons are produced for starting and stopping muons, for differential muons (i.e., infinitesimal muon tracks of 1 cm), and for showers. Also in the new Monte Carlo, new layered ice models have been implemented. Changes in reconstruction and detector simulation have also been made. The new simplex minimizer by Kael Hanson was also used.

We ran signal Monte Carlo using the mass00v005 version of the mass production software written and organized by Stephan Hundertmark.

The GRB analysis uses MC at Level 1. The only cut placed on events is that the initial line fit must have a zenith angle $\theta > 50^o$. This is also how the data was processed for GRBs. In the 1997

data, 22the Level 1 filter [71].

So we removed the cuts of ndirb> 3 and $\theta > 80^o$ in mass production reco.script. These two cuts were called Level 2. Only Level 2 Monte Carlo was saved in the mass production, hence our need to run separate signal MC for the GRB analysis.

We selected the nusim generator in the master script master.qsub. We produced neutrinos in the zenith range from 80^o to 180^o. Neutrinos were produced uniformly in $\cos(\theta)$. We set the minimum neutrino generation energy at 1 GeV and increased the maximum neutrino generation energy to 10 PeV. Above 1 PeV, the earth becomes opaque to vertically upgoing neutrinos. We created an additional set of Monte Carlo for energies bewteen 10 PeV and 100 PeV. Energies up to 100 PeV are needed for horizontal events because there is less absorption at shallow angles due to less matter being traversed by the neutrino.

We used the Lipari-Stanev (L-S) code called muprop, integrated into mudedx by Gilles, to model the muon propagation. The L-S code works at energies above $10^{5.5}$ GeV whereas the Lohman code does not. The L-S code uses fewer vertices for energy dissipation than mudedx, allowing it to calculate the propagation of high energy muons in reasonable CPU time. In the future, Dima's MMC code will used as the muon propagator.

In mudedx, the active cylinder is the volume around the detector in which mudedx will actually track energy losses. Outside the active volume, the muon is propagated but the energy losses are not recorded. The height of the active cylinder is 800m and the radius is 400m. (The AMANDA-B10 detector is a cylinder of 302 OMs with an outer radius of 60m and 400m of ice instrumented vertically.)

We used the layered ice model from Kurt Woschnagg and Stephan Hundertmark. Kurt measured the depth profile of scattering in the ice at 532nm. Four sets of parameters are used to describe the ice properties in 16 layers of ice around the detector. The ice layers have geometric scattering lengths ranging from 19m to 31m. The H2 ice hole model and the Bergstroem-Price absorption model are used. The critical parameter of the absorption model is F which defines the maximum absorption length near 400nm. The value of F ranges from 133m to 58m in this ice model.

We used amacalib to calibrate the data. OM cleaning and hit cleaning were performed following

Component	Number of Events	Time Req'd (secs)	File Size (Mb)	Time Per Evt (secs)
Script	500,000			
Nusim	435,000	50,000	130	0.11
Mudedx	435,000	700	143	0.002
Amasim (triggered)	110,000	49,000	210	0.45
Recoos (line fit)	109,000	22,600*	204*	0.2-0.3*
Muff (line fit $\theta > 50^o$)	89,000			
Recoos (upandel)	89,000			
Total		122,300	687	

Table B.1: Monte Carlo production statistics. The number of events, time required, and file sizes are per file per CPU for $E_\nu < 10$ PeV. *Line fit results are piped directly to muff and then to recoos again for the full reconstruction.

the standard set of cuts in the mass production scripts. Thirty-seven OMs were omitted entirely. An initial line fit that ignores the time structure of the event was made. Then we used muff to keep only the events with a line fit $\theta > 50^o$. A upandel reconstruction was done using the line fit as a first guess.

Nusim files were piped through the nusim mass00v002 fix script so that the nusim generated event weights can be parsed properly into the rdmc structure as there was a problem with long US line IDs in the rdmc structure.

The UW AMANDA group now has a cluster of 14 Dual Pentium III 1GHz PCs with 512Mb RAM. The production and reconstruction of 500,000 events at energies below 10PeV took about 1.4 days on 1 machine of our new cluster. Neutrinos with energy between 10 PeV and 100 PeV took significantly longer and were produced in smaller files distributed over many machines. CPU time is not a limiting factor in the GRB MC production. See Table B.1 for details of the production.

Eleven files of neutrinos and 11 files of anti-neutrinos were produced for E_ν ¡ 10PeV. In total, 9.6x10^6 neutrino events were produced by nusim. 2.0x10^6 events remain after the line fit $\theta > 50^o$ cut and were fully reoconstructed for further analysis. The new simplex minimizer was used. The siegmund version used is the stable release of v3.1 000719. For energies between 10PeV and 100PeV, 830,000 neutrinos were produced and likewise processed.

The 1998 GRB data was filtered and extracted at LBNL. The data was calibrated using the

most recent data base then currently available, 'omdb-19991020.db.txt'. This data base was later found to be less than optimal as new calibration work had not yet been included. The data has been recently re-filtered and is currently being analyzed.

Four chronically noisy channels, responsible for 30% of the raw data size, were removed from the data stream (OM 40, 190, 234 and 258). The reformatting, calibration, removal of undesirable channels, as well as gathering of statistics, creating of minimum-bias events files (every 500th event), and writing of SPASE triggers required approximately 354 CPU days for the 3 billion events in the raw data [74].

'Recoos' was then applied to these events and performed 3 fits: (1) a moment of inertia tensor (2) a line fit and (3) plane wave fit. The 66% of events which had hits recorded in 10 or more channels were retained. Application of recoos and this filtering stage required approximately 207 CPU days.

The upgoing events that bracketed a northern hemisphere BATSE trigger time by (+1,-1) hours was extracted for this analysis. This resulted in 21 Gigabytes of data, 0.7% of the raw data set.

The 1999 AMANDA data was again filtered at LBNL after I uploaded it to the NERSC mass storage system in the summer of 2000 during my fellowship practicum.

B.2 2000

The 2000 AMANDA-II data was filtered at DESY-Zeuthen. Again, two hours of data surrounding BATSE trigger times were extracted. The 2000 GRB data set was 4.8 Gb in size when zipped. Though the detector was much larger than in previous years, the data set was smaller because BATSE was de-orbited at the end of May. Forty-five triggered GRBs and 26 non-triggered GRBs occurred during operation. Only one GRB had to be excluded from analysis due to a gap in AMANDA data.

Updates and improvements were made in the AMANDA-II simulations. A new propagator was used that ably tracked muons in the ice up to energies of 100PeV [75].

Appendix C

Soft Gamma Repeater 1900+14

C.1 Soft Gamma Repeaters

Soft Gamma Repeaters (SGR) are short bursts of soft gamma rays ($\leq$100keV). They exhibit periods of intense activity for days or weeks and then are quiescent for years or decades. SGR are a fundamentally different phenomenon than GRBs. They likely result from magnetic quakes on highly magnetized neutron stars in our galaxy.

C.2 Neutrino Search

On August 27, 1998, a huge burst from SGR 1900+14 was detected[61, 62, 63]. I searched AMANDA data for neutrinos associated with this burst, but none were detected.

Appendix D

Atmospheric Neutrino Overlap Analysis

D.1 Atmospheric Neutrinos

The 1997 AMANDA-B10 data was searched for atmospheric neutrinos from cosmic rays interacting with the earth's atmosphere in the northern hemisphere[44]. Some of the neutrinos in this sample have ~TeV energies.

D.2 GRB Search

I searched the atmospheric neutrino sample from 1997 to see if any of the sample was correlated with known satellite detections. The sample was compared to all BATSE triggered and non-triggered (see Appendix A) GRBs. There was no statistically significant correlation in time or location between the atmospheric sample and GRBs.

Appendix E

GRBs Studied in Analysis

E.1 1997 BATSE GRBs

A total of 126 GRBs from 1997 were analyzed: 78 triggered and 48 non-triggered bursts. BATSE identification numbers are provided for triggered bursts. Stern's ID numbers include the truncated Julian date (TJD) and are provided for non-triggered bursts. For non-triggered bursts found only by Kommers, his ID number, which includes the date of the burst, is shown.

6162
6163
6165
6166
6167
6168
6176
6188
6189
6190
6204
6209
6212
6213
6214
6215
6219
6222
6223
6225
6226
6227
6229
6234
6237
6240
6241
6242
6255
6260
6265

6266
6267
6268
6270
6272
6273
6276
6279
6280
6295
6300
6304
6305
6306
6319
6321
6322
6325
6334
6335
6336
6337
6339
6341
6343
6344
6345
6350
6354
6358
6366
6368
6370
6376
6385
6408
6412
6414
6427
6428
6435
6436
6439
6443
6453
6455
6472
10545g
10547a
10552c
970427.86
10569b
10570c
10574a
10579e
10581b

970518.41

10593c

10603c

10606b

10610d

10616c

10618b

10636a

10638b

10648c

10651a

10668a

10676c

10677c

10689b

10697c

970906.24

970909.79

10703b

10705a

10705b

10705d

10708a

10708c

10734c

10734e

10738a

10739d

10747a

10748c

10748f

10753a

10754a

10755a

10757a

10760b

10760d

10762a

10762c

E.2 1998 BATSE GRBs

A total of 138 GRBs from 1998 will be analyzed: 81 triggered and 57 non-triggered bursts. BATSE identification numbers are provided for triggered bursts. Stern's ID numbers include the truncated Julian date (TJD) and are provided for non-triggered bursts.

10866c

10868c

10868d

10870d

10873b

10876a

10876b

10878h

10901d

10916a

10932a

10933b

109376

10941d

10946c

10957c

10958b

10966b

10969a

10971a

10975d

10977a

10977c

10979c

10980b

10981d

10982c

10983a

10987a

10990b

10993e

10993f

10997a

10997g

10999b

10999b

11000d

11002a

11006a

11006d

11014b

11019c

11021b

11025b

11030f

11033c

11035a

11036a

11036e

11037a

11037b

11039a

11044c

11051a

11061a

11072a

11073b

6610

6613

6615

6617

6618

6619

6620

6622

6631

6658
6662
6665
6666
6672
6676
6677
6679
6680
6681
6682
6683
6686
6689
6690
6693
6694
6698
6699
6702
6709
6716
6718
6720
6744
6753
6763
6764
6786
6787
6788
6789
6800
6812
6815
6816
6817
6828
6831
6853
6867
6882
6884
6886
6891
6892
6897
6903
6904
6911
6914
6916
6922
6927
6931
6935

6938
6953
6963
6978
6985
6986
6987
6989
7000
7009
7023
7028
7059
7078
7087
7093

E.3 1999 BATSE GRBs

Ninety-six triggered bursts were extracted from the 1999 data.

7379
7387
7403
7429
7434
7448
7451
7452
7455
7456
7457
7460
7464
7470
7481
7484
7485
7486
7487
7489
7494
7495
7497
7498
7504
7513
7514
7523
7528
7529
7539
7541
7550
7552
7554
7561
7567

7573
7578
7581
7582
7587
7594
7598
7599
7602
7604
7608
7615
7625
7626
7630
7632
7633
7648
7652
7654
7655
7660
7662
7665
7671
7674
7683
7688
7693
7703
7705
7706
7707
7735
7737
7749
7750
7753
7754
7764
7766
7769
7770
7774
7775
7776
7781
7784
7790
7791
7792
7800
7802
7811
7822
7835

7838

7840

7849

E.4 2000 BATSE GRBs

A total of 70 GRBs from 1997 were analyzed: 44 triggered and 26 non-triggered bursts. BATSE identification numbers are provided for triggered bursts. Stern's ID numbers are provided for non-triggered bursts.

7988

7989

7991

7992

7994

7995

7997

7998

7999

8002

8004

8005

8008

8009

8012

8019

8022

8030

8031

8035

8036

8039

8045

8047

8049

8056

8057

8061

8063

8064

8069

8071

8074

8075

8077

8079

8084

8085

8086

8097

8099

8109

8110

8111

11591c

11597b

11599b

11600b

11602b

11608a

11609b

11625b

11633b

11633f

11634g

11637c

11637e

11638b

11642d

11644b

11644f

11646c

11650a

11652g

11654b

11663b

11663f

11668c

11672h

11675e

Appendix F

Blinded Event Rates for 1999

Here are the background distributions for some 1999 GRBs. The number of events as a function of time is shown. The 10-minute blind spot is the region of interest and remained unexamined until final cuts had been set.

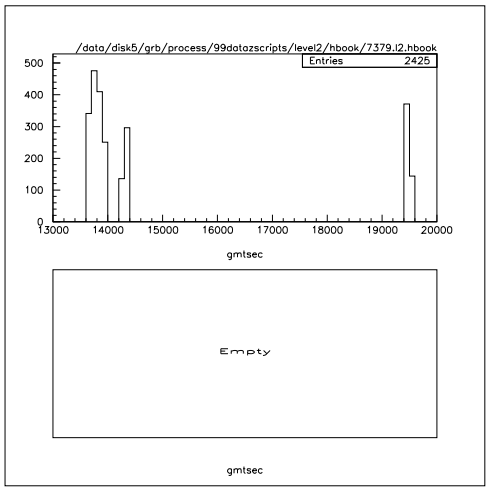

Figure F.1: The background distribution of events for grb7379, except for the 10 minute blind spot around the trigger time, before (top) and after (bottom) cuts.

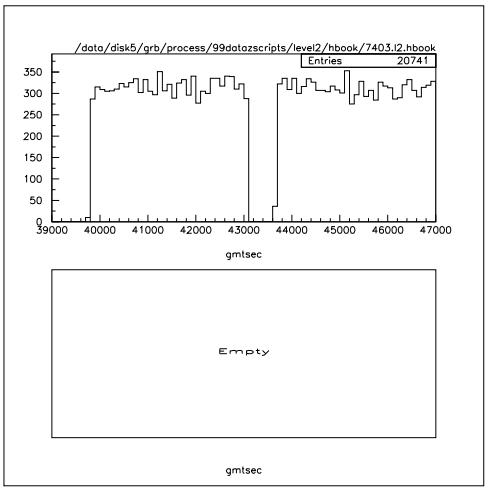

Figure F.3: The background distribution of events for grb7403, except for the 10 minute blind spot around the trigger time, before (top) and after (bottom) cuts.

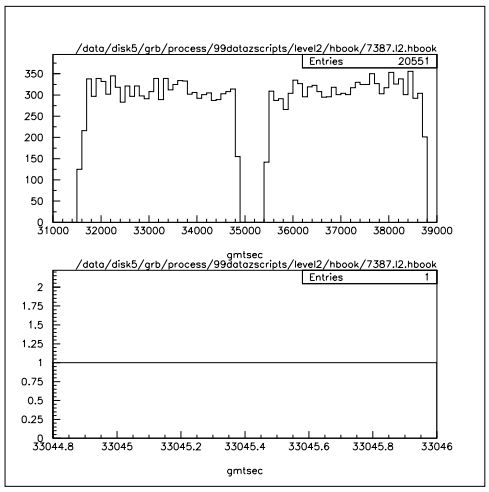

Figure F.2: The background distribution of events for grb7387, except for the 10 minute blind spot around the trigger time, before (top) and after (bottom) cuts.

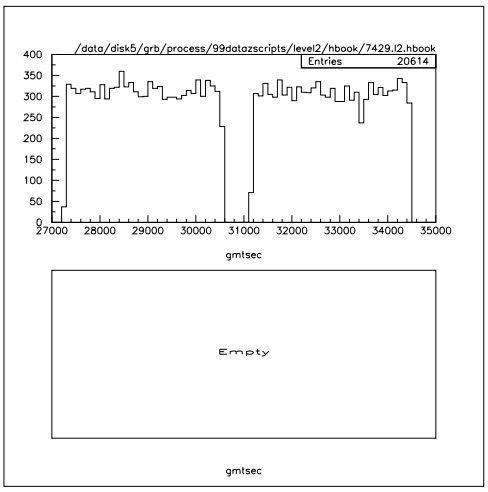

Figure F.4: The background distribution of events for grb7429, except for the 10 minute blind spot around the trigger time, before (top) and after (bottom) cuts.

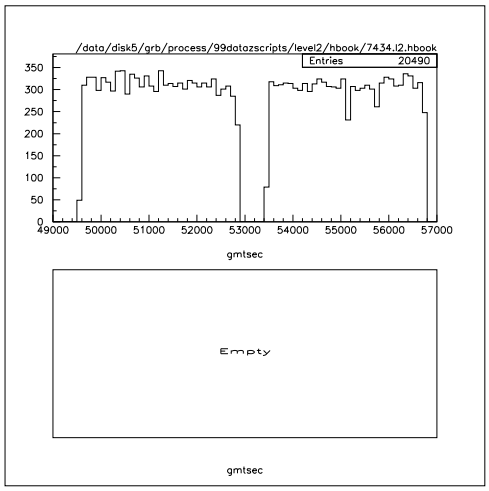

Figure F.5: The background distribution of events for grb7434, except for the 10 minute blind spot around the trigger time, before (top) and after (bottom) cuts.

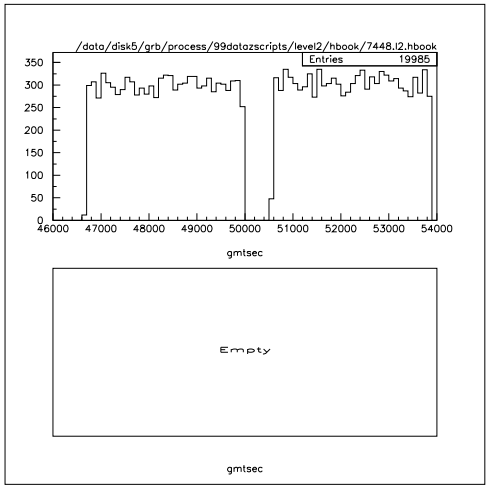

Figure F.6: The background distribution of events for grb7448, except for the 10 minute blind spot around the trigger time, before (top) and after (bottom) cuts.

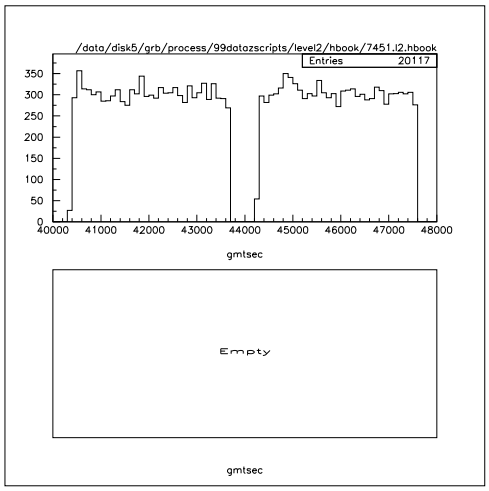

Figure F.7: The background distribution of events for grb7451, except for the 10 minute blind spot around the trigger time, before (top) and after (bottom) cuts.

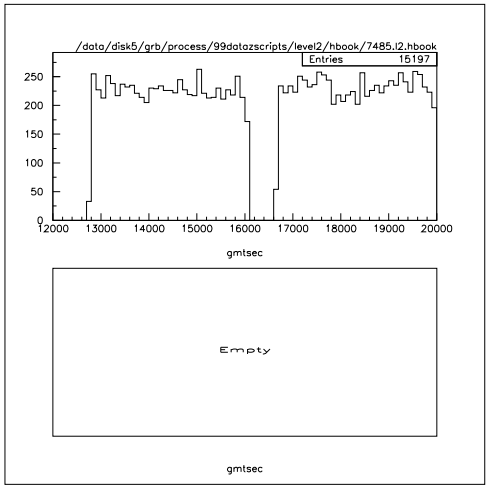

Figure F.8: The background distribution of events for grb7452, except for the 10 minute blind spot around the trigger time, before (top) and after (bottom) cuts.

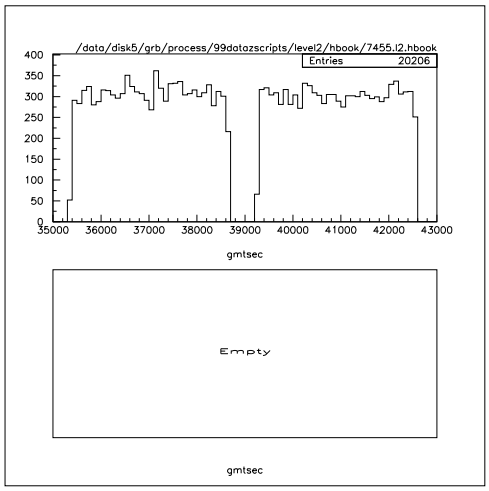

Figure F.9: The background distribution of events for grb7455, except for the 10 minute blind spot around the trigger time, before (top) and after (bottom) cuts.

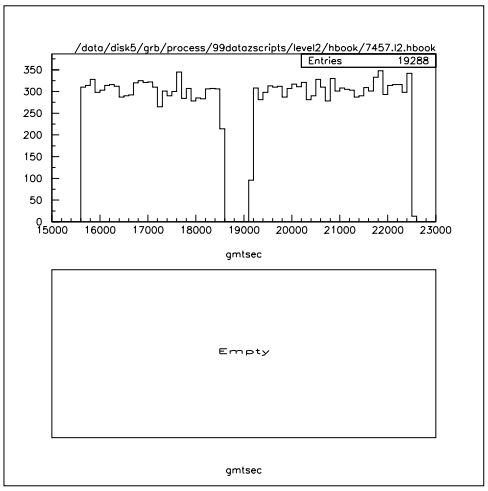

Figure F.11: The background distribution of events for grb7457, except for the 10 minute blind spot around the trigger time, before (top) and after (bottom) cuts.

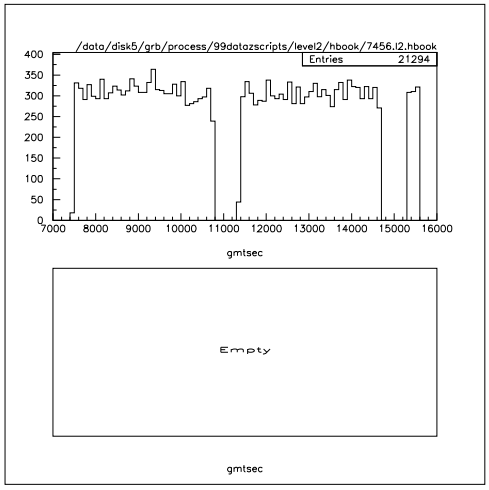

Figure F.10: The background distribution of events for grb7456, except for the 10 minute blind spot around the trigger time, before (top) and after (bottom) cuts.

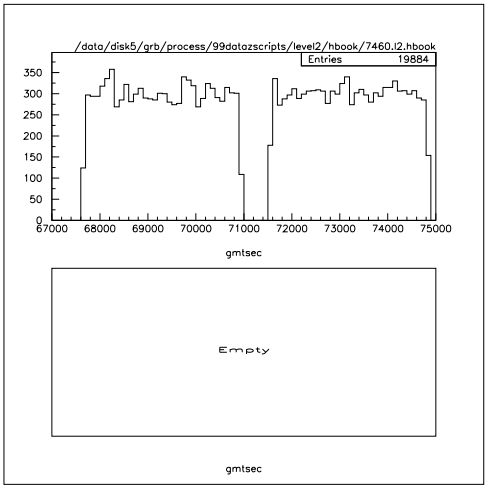

Figure F.12: The background distribution of events for grb7460, except for the 10 minute blind spot around the trigger time, before (top) and after (bottom) cuts.

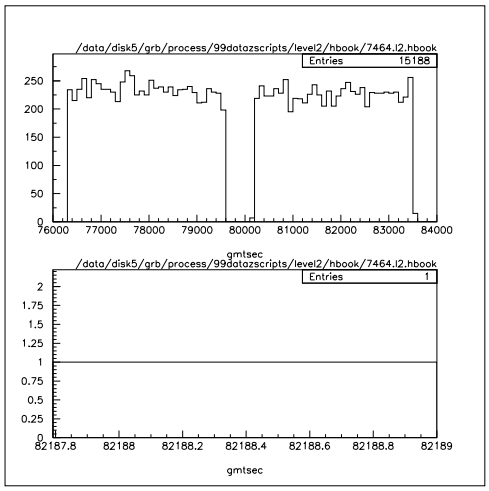

Figure F.13: The background distribution of events for grb7464, except for the 10 minute blind spot around the trigger time, before (top) and after (bottom) cuts.

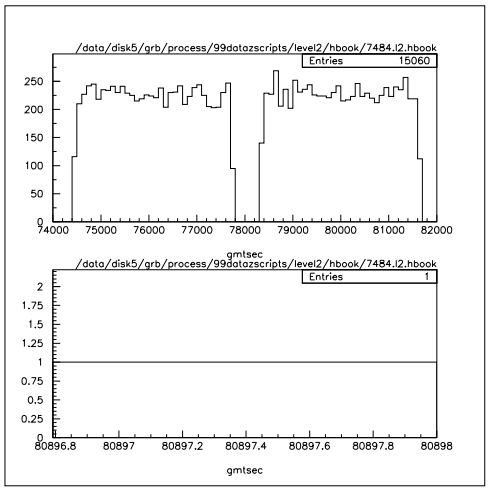

Figure F.15: The background distribution of events for grb7484, except for the 10 minute blind spot around the trigger time, before (top) and after (bottom) cuts.

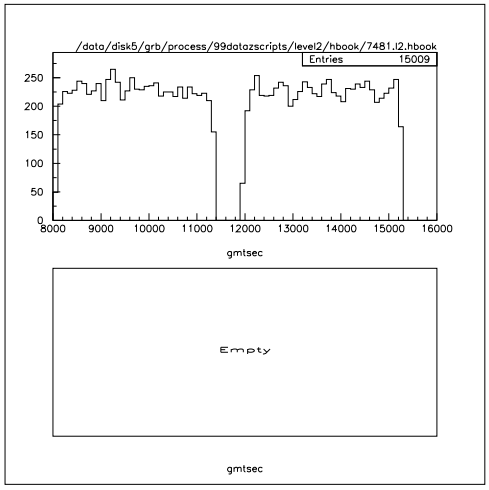

Figure F.14: The background distribution of events for grb7481, except for the 10 minute blind spot around the trigger time, before (top) and after (bottom) cuts.

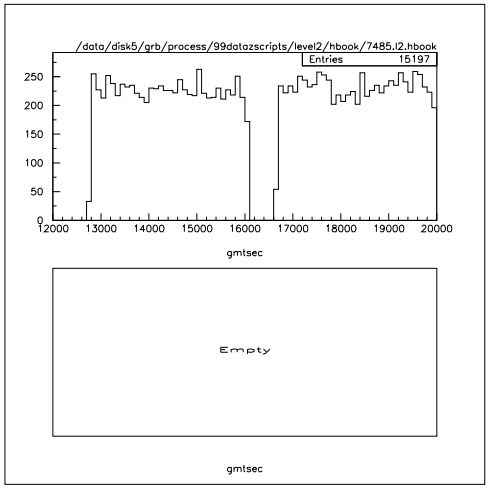

Figure F.16: The background distribution of events for grb7485, except for the 10 minute blind spot around the trigger time, before (top) and after (bottom) cuts.

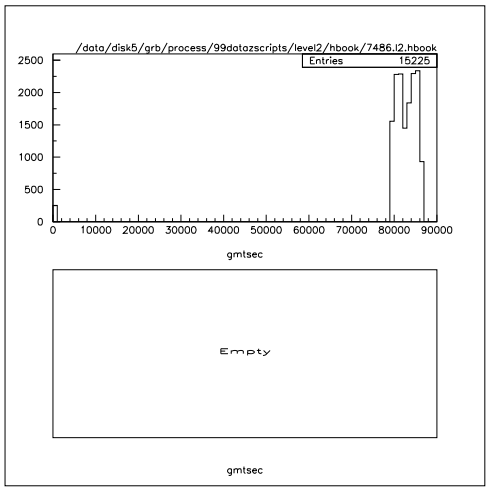

Figure F.17: The background distribution of events for grb7486, except for the 10 minute blind spot around the trigger time, before (top) and after (bottom) cuts.

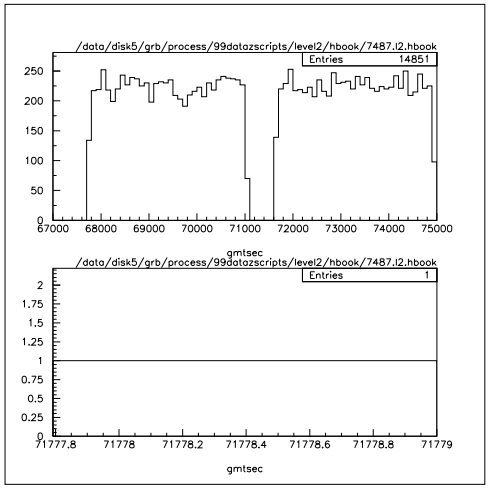

Figure F.18: The background distribution of events for grb7487, except for the 10 minute blind spot around the trigger time, before (top) and after (bottom) cuts.

Appendix G

Unblinded Event Rates for 1999

These plots show the number of events during the GRB before and after cuts. The search was begun 10 seconds before the earliest gamma-rays and finished at the end of the T90 time.

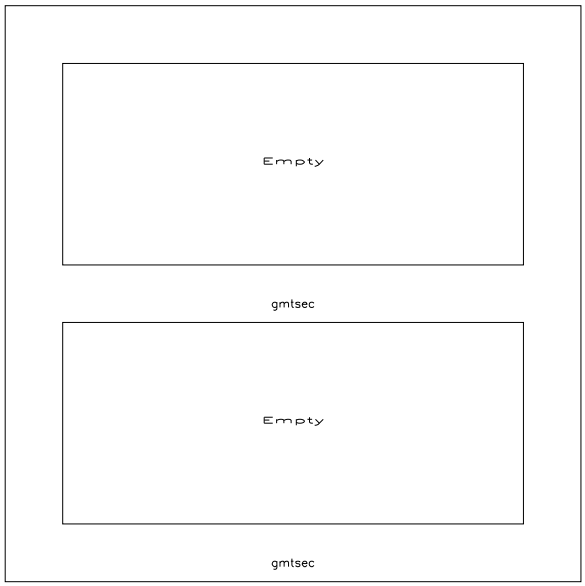

Figure G.1: The number of events for grb7379 during the burst, before (top) and after (bottom) cuts.

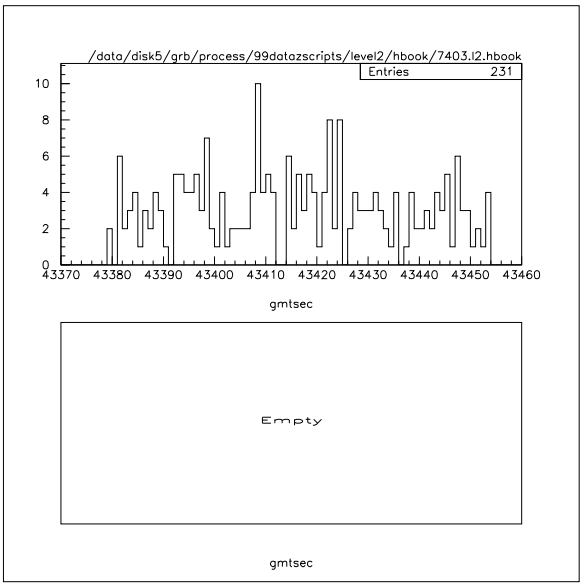

Figure G.3: The number of events for grb7403 during the burst, before (top) and after (bottom) cuts.

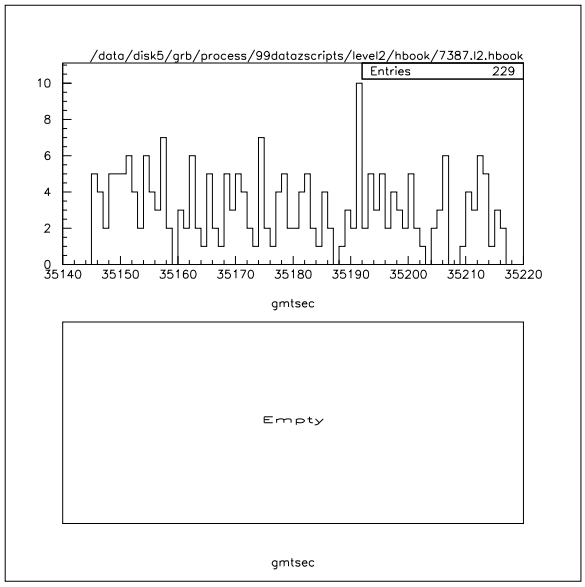

Figure G.2: The number of events for grb7387 during the burst, before (top) and after (bottom) cuts.

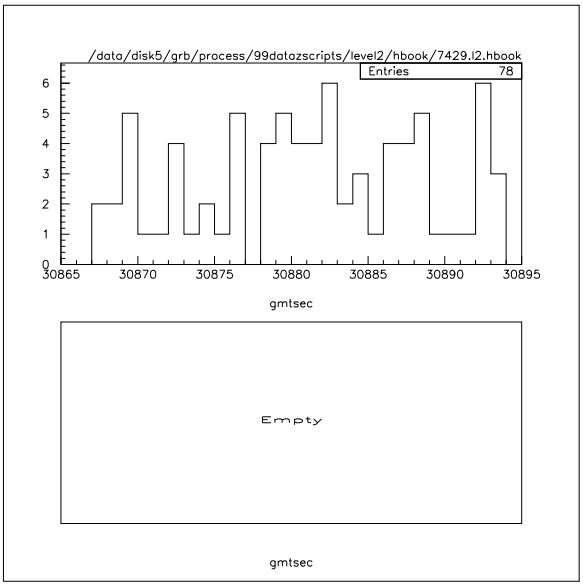

Figure G.4: The number of events for grb7429 during the burst, before (top) and after (bottom) cuts.

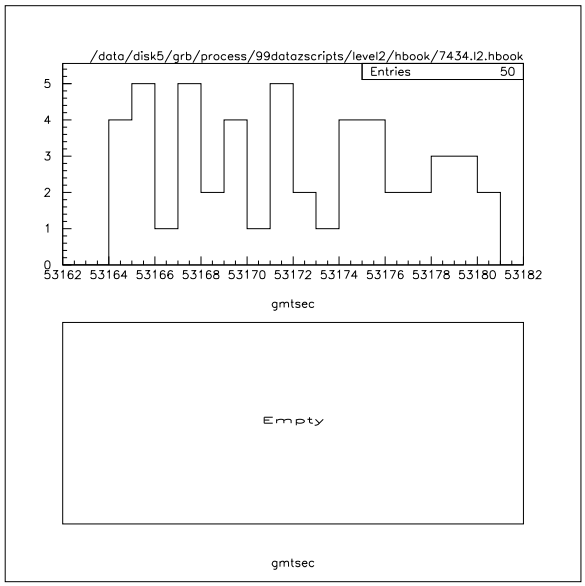

Figure G.5: The number of events for grb7434 during the burst, before (top) and after (bottom) cuts.

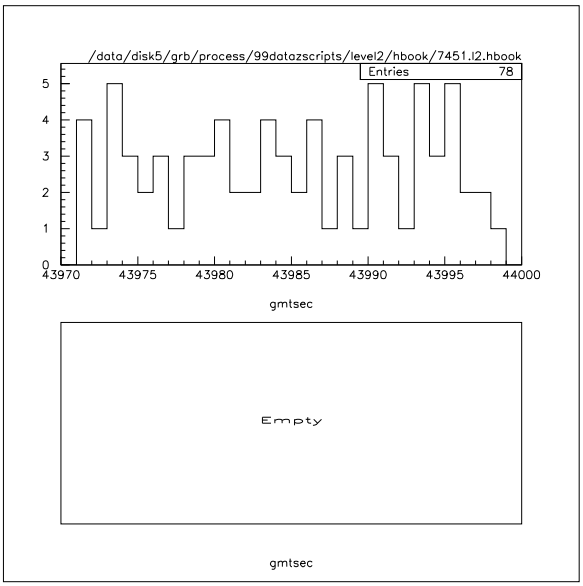

Figure G.7: The number of events for grb7451 during the burst, before (top) and after (bottom) cuts.

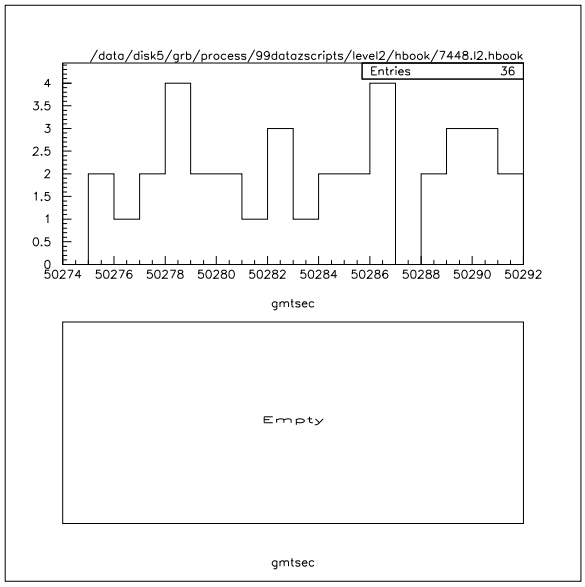

Figure G.6: The number of events for grb7448 during the burst, before (top) and after (bottom) cuts.

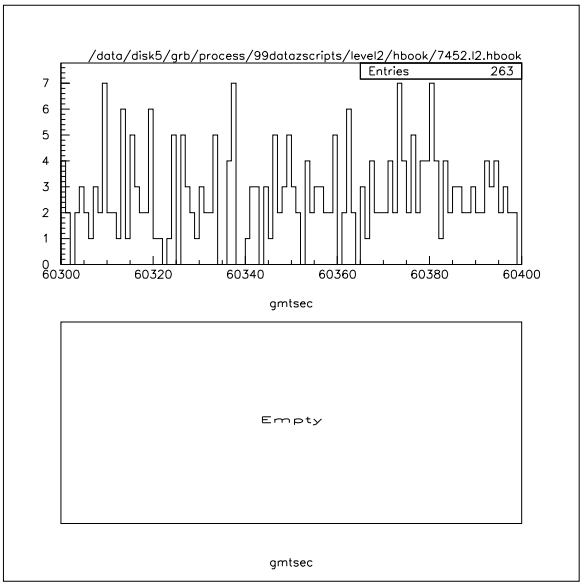

Figure G.8: The number of events for grb7452 during the burst, before (top) and after (bottom) cuts.

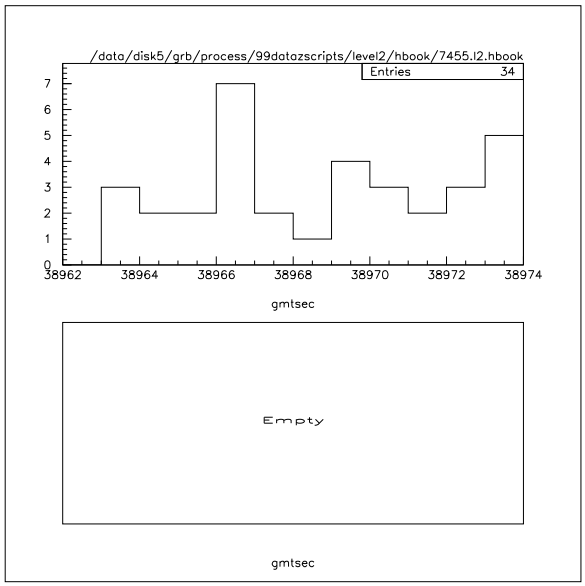

Figure G.9: The number of events for grb7455 during the burst, before (top) and after (bottom) cuts.

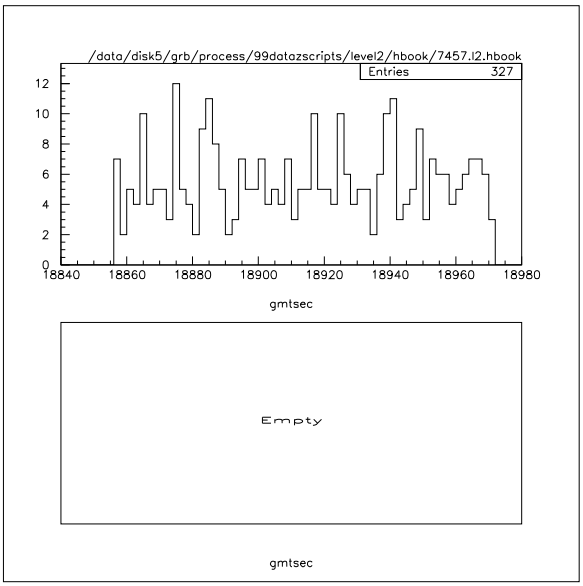

Figure G.11: The number of events for grb7457 during the burst, before (top) and after (bottom) cuts.

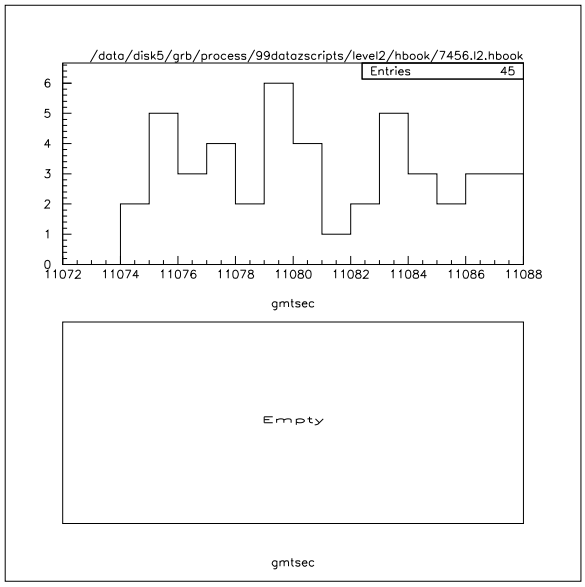

Figure G.10: The number of events for grb7456 during the burst, before (top) and after (bottom) cuts.

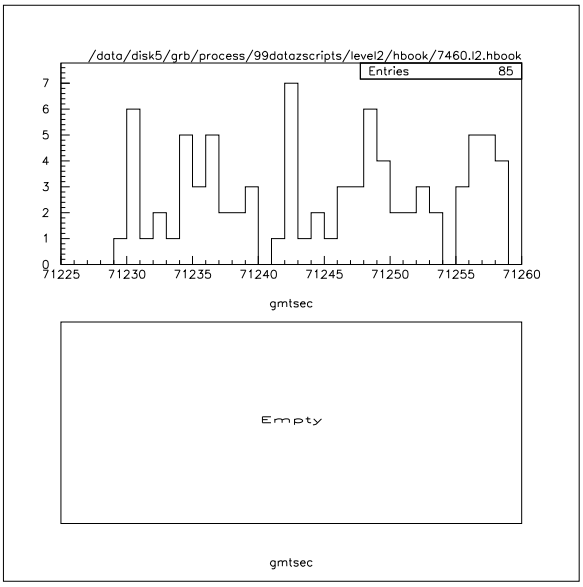

Figure G.12: The number of events for grb7460 during the burst, before (top) and after (bottom) cuts.

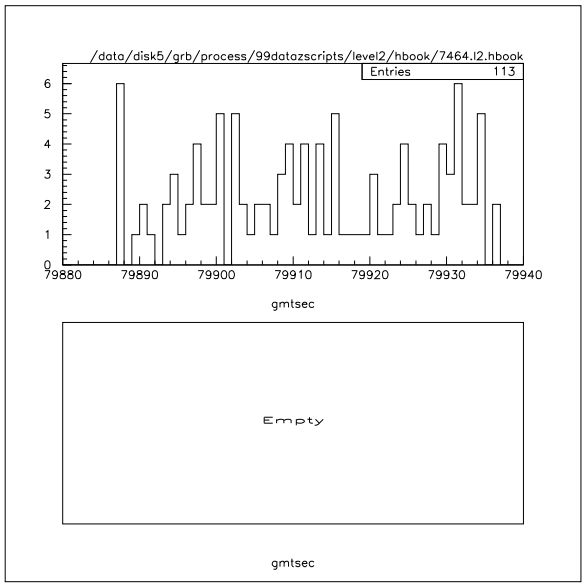

Figure G.13: The number of events for grb7464 during the burst, before (top) and after (bottom) cuts.

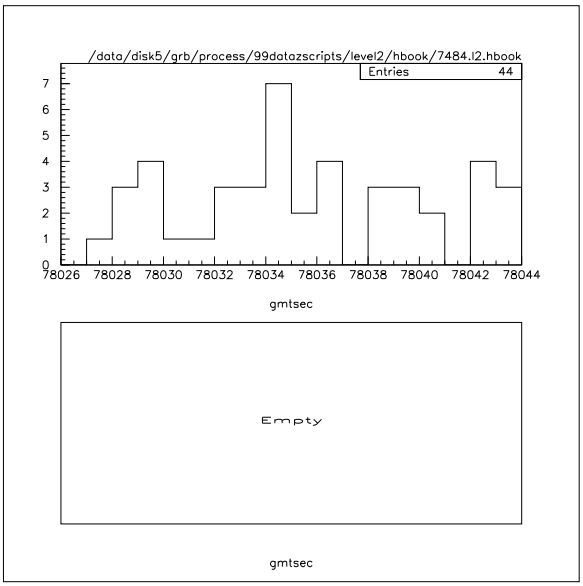

Figure G.15: The number of events for grb7484 during the burst, before (top) and after (bottom) cuts.

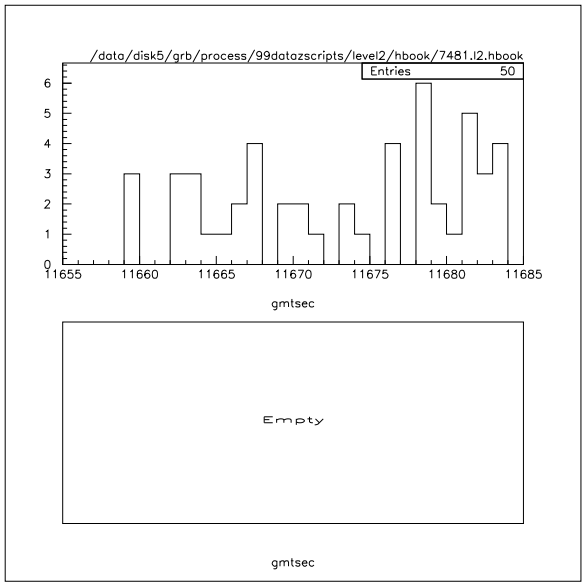

Figure G.14: The number of events for grb7481 during the burst, before (top) and after (bottom) cuts.

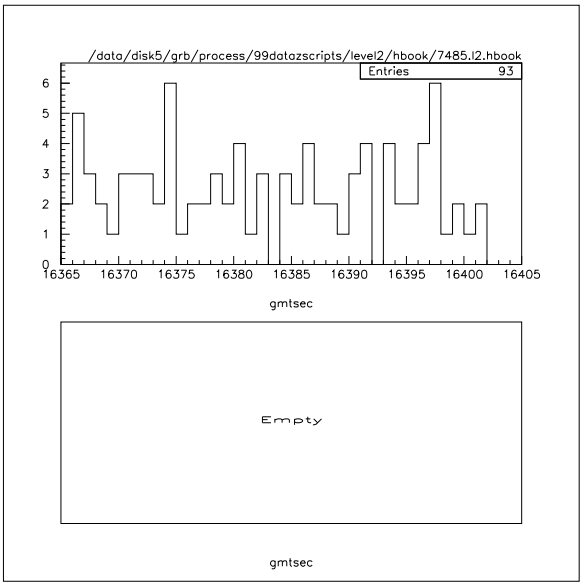

Figure G.16: The number of events for grb7485 during the burst, before (top) and after (bottom) cuts.

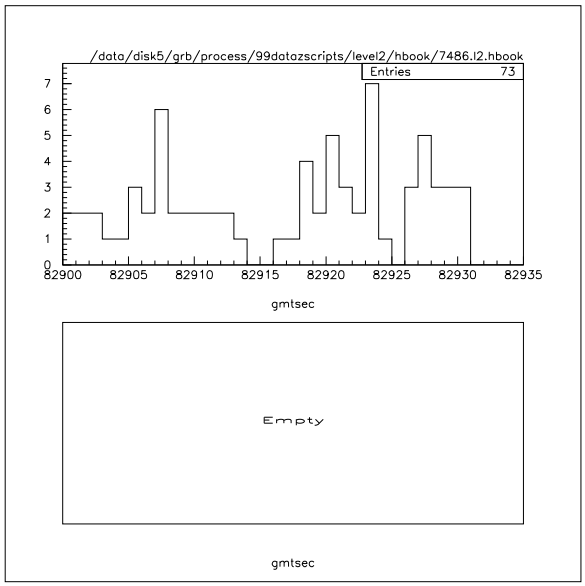

Figure G.17: The number of events for grb7486 during the burst, before (top) and after (bottom) cuts.

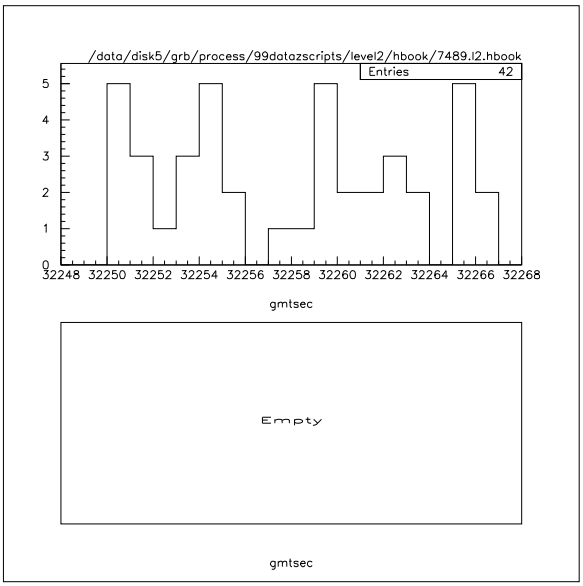

Figure G.19: The number of events for grb7489 during the burst, before (top) and after (bottom) cuts.

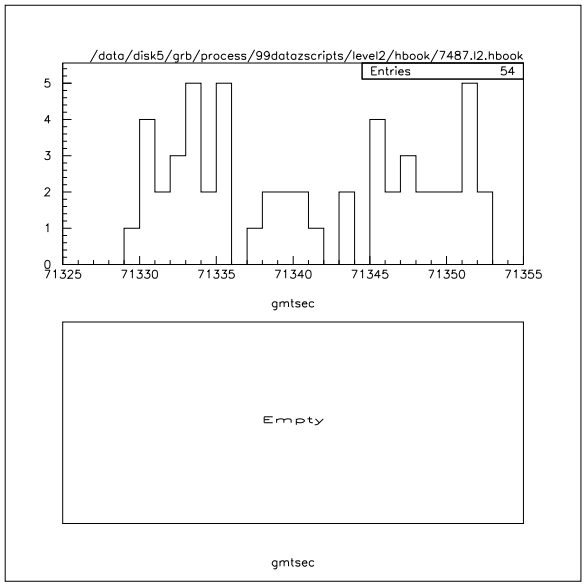

Figure G.18: The number of events for grb7487 during the burst, before (top) and after (bottom) cuts.

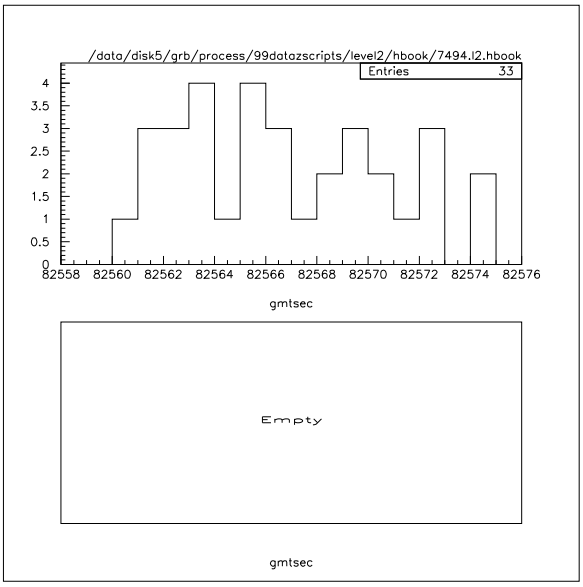

Figure G.20: The number of events for grb7494 during the burst, before (top) and after (bottom) cuts.

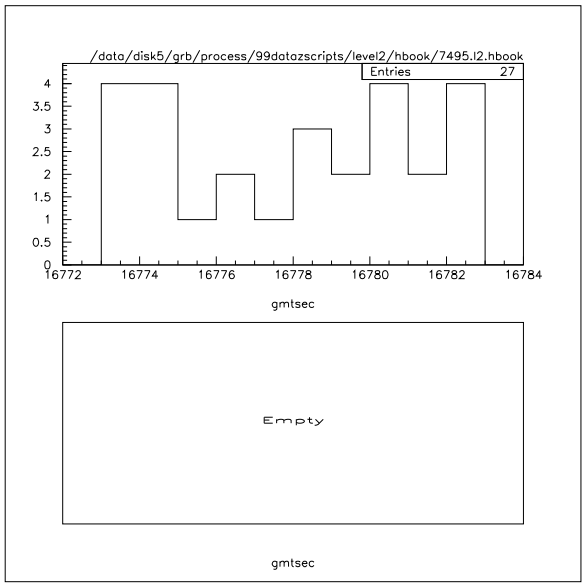

Figure G.21: The number of events for grb7495 during the burst, before (top) and after (bottom) cuts.

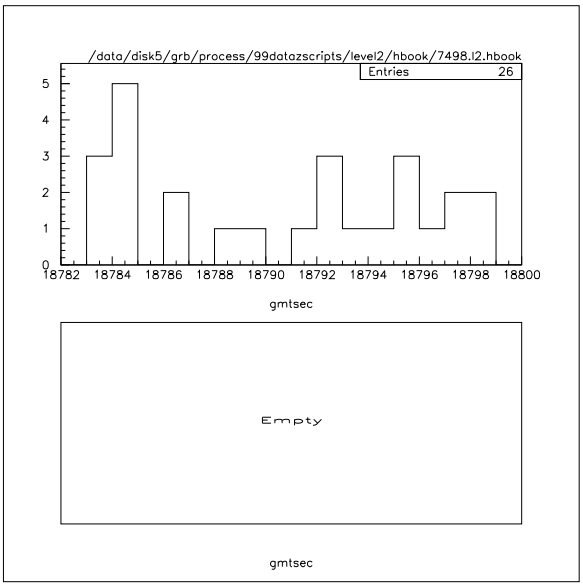

Figure G.23: The number of events for grb7498 during the burst, before (top) and after (bottom) cuts.

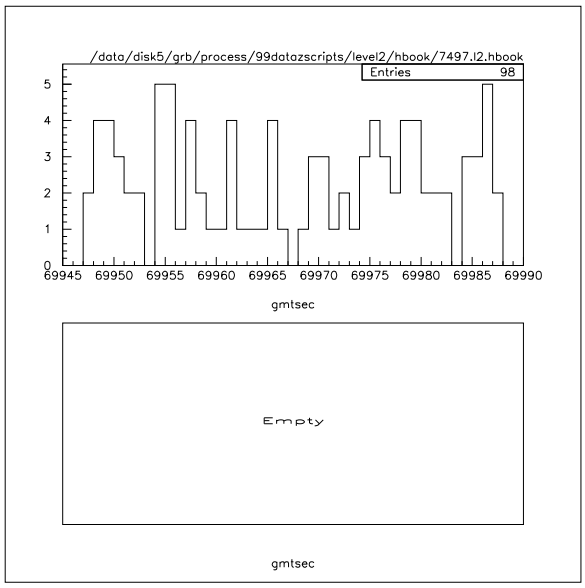

Figure G.22: The number of events for grb7497 during the burst, before (top) and after (bottom) cuts.

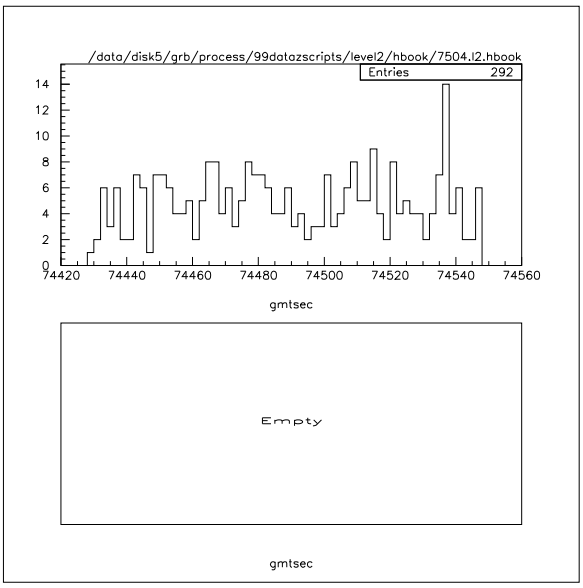

Figure G.24: The number of events for grb7504 during the burst, before (top) and after (bottom) cuts.

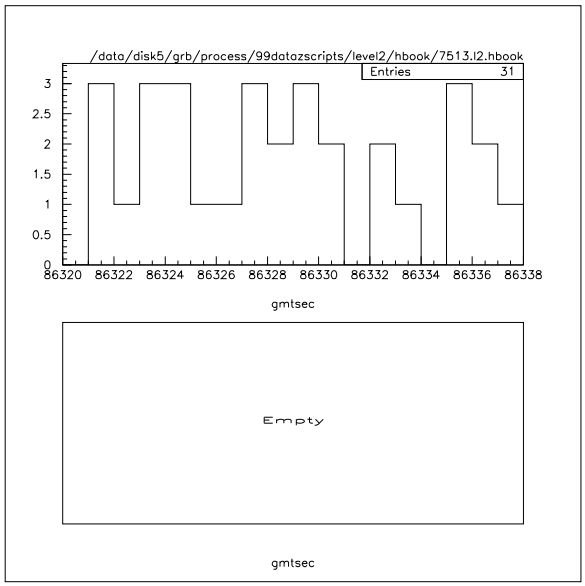

Figure G.25: The number of events for grb7513 during the burst, before (top) and after (bottom) cuts.

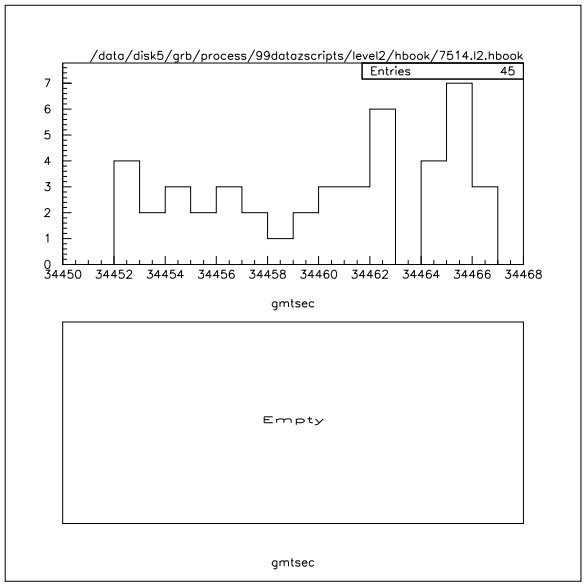

Figure G.26: The number of events for grb7514 during the burst, before (top) and after (bottom) cuts.

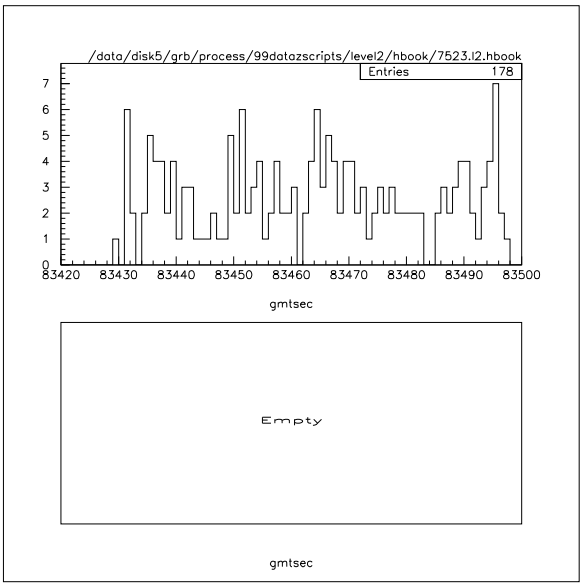

Figure G.27: The number of events for grb7523 during the burst, before (top) and after (bottom) cuts.

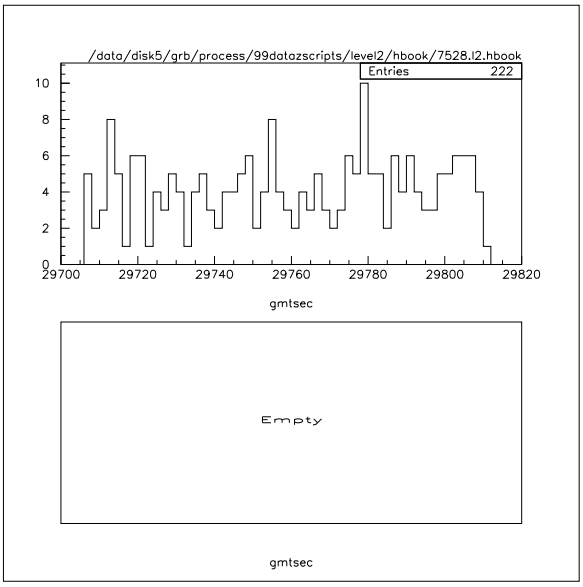

Figure G.28: The number of events for grb7528 during the burst, before (top) and after (bottom) cuts.

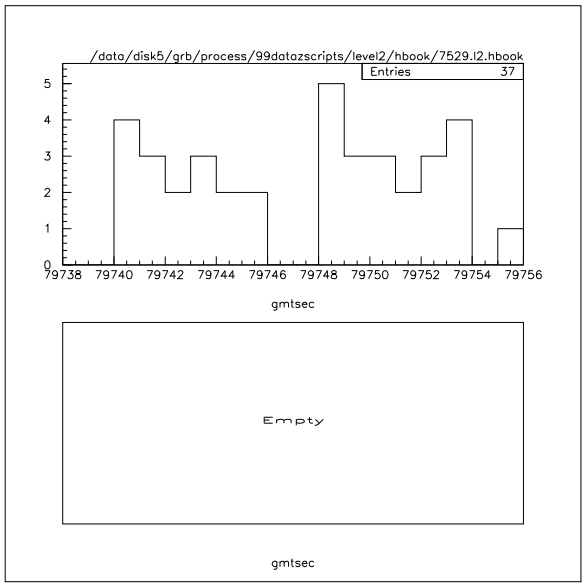

Figure G.29: The number of events for grb7529 during the burst, before (top) and after (bottom) cuts.

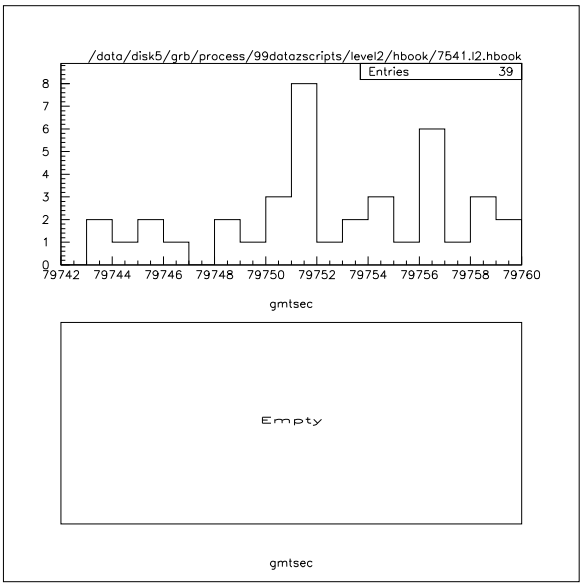

Figure G.31: The number of events for grb7541 during the burst, before (top) and after (bottom) cuts.

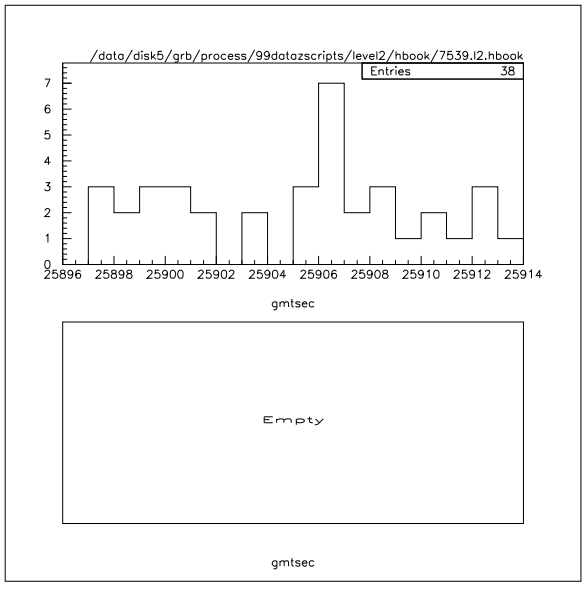

Figure G.30: The number of events for grb7539 during the burst, before (top) and after (bottom) cuts.

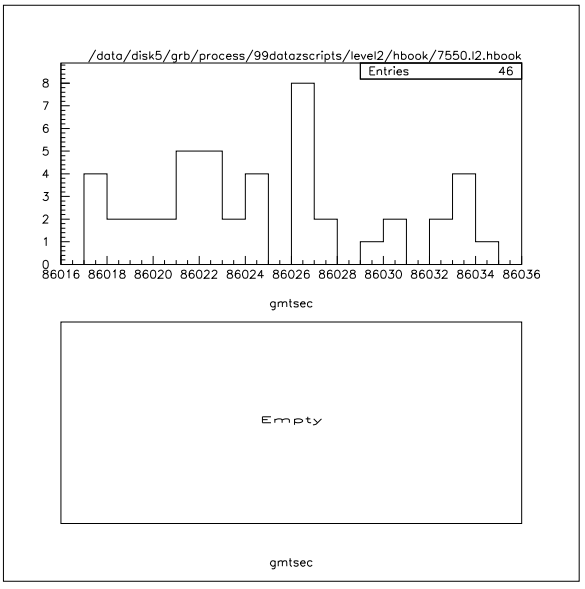

Figure G.32: The number of events for grb7550 during the burst, before (top) and after (bottom) cuts.

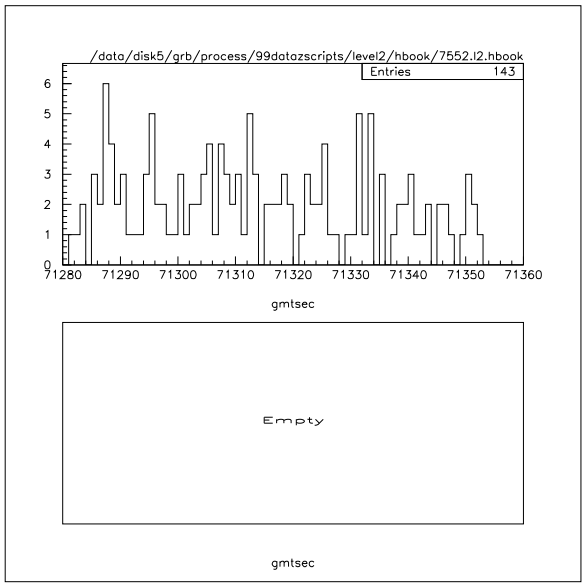

Figure G.33: The number of events for grb7552 during the burst, before (top) and after (bottom) cuts.

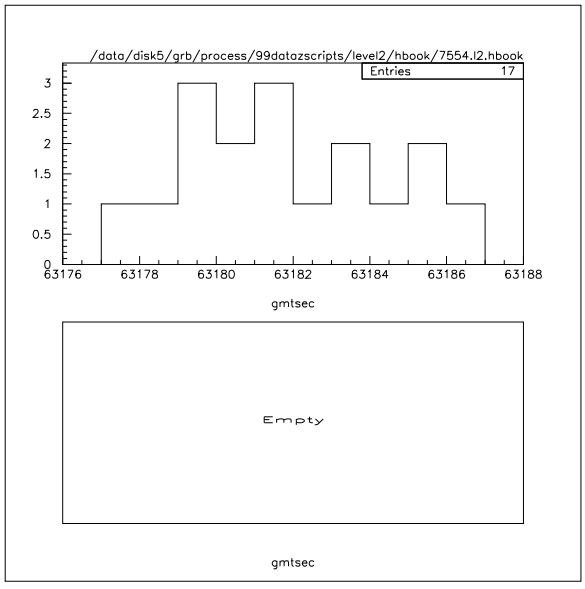

Figure G.34: The number of events for grb7554 during the burst, before (top) and after (bottom) cuts.

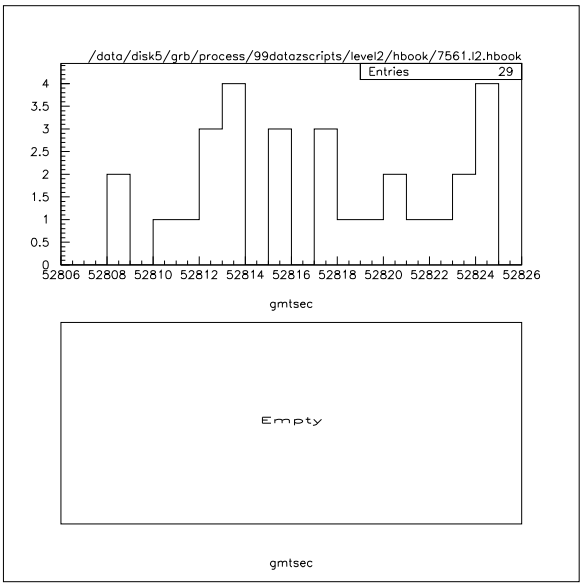

Figure G.35: The number of events for grb7561 during the burst, before (top) and after (bottom) cuts.

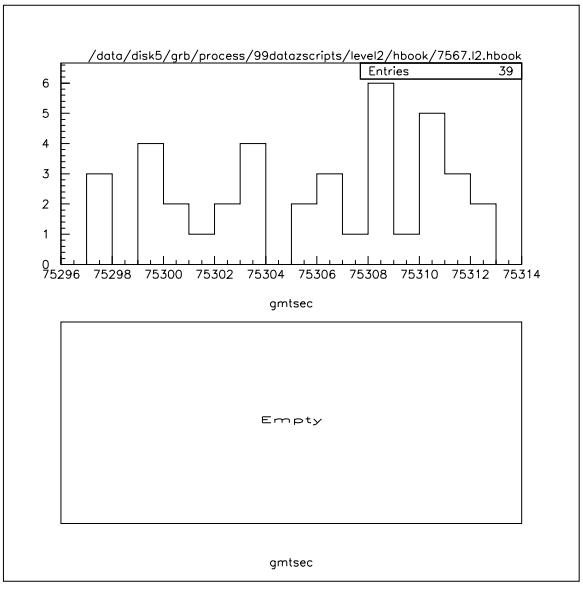

Figure G.36: The number of events for grb7567 during the burst, before (top) and after (bottom) cuts.

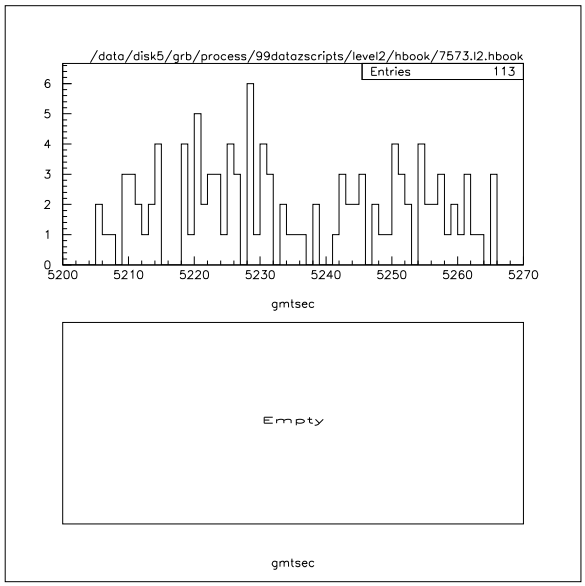

Figure G.37: The number of events for grb7573 during the burst, before (top) and after (bottom) cuts.

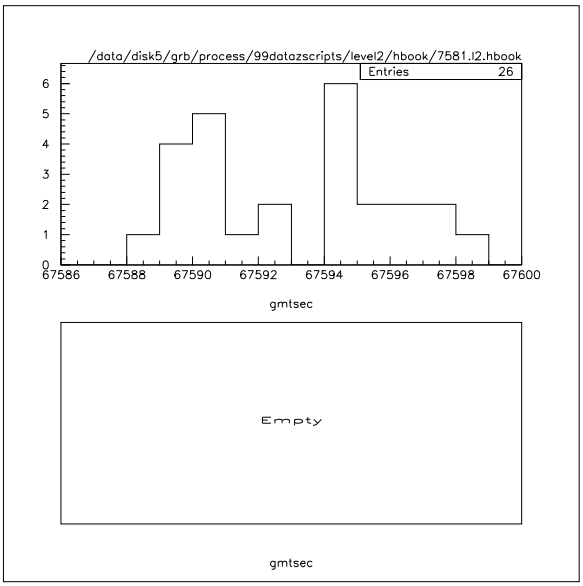

Figure G.39: The number of events for grb7581 during the burst, before (top) and after (bottom) cuts.

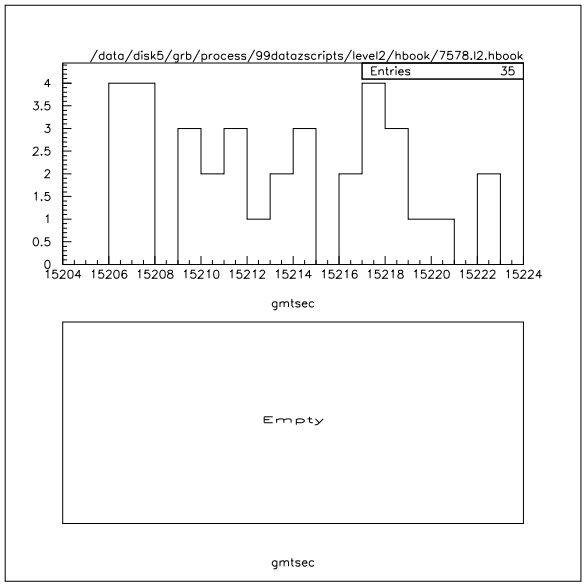

Figure G.38: The number of events for grb7578 during the burst, before (top) and after (bottom) cuts.

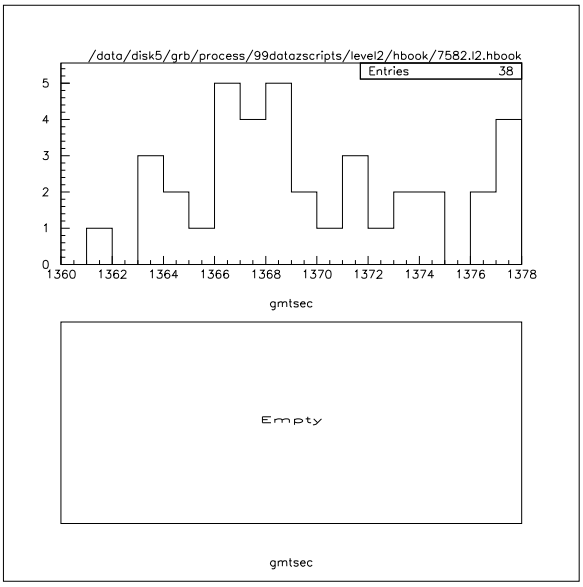

Figure G.40: The number of events for grb7582 during the burst, before (top) and after (bottom) cuts.

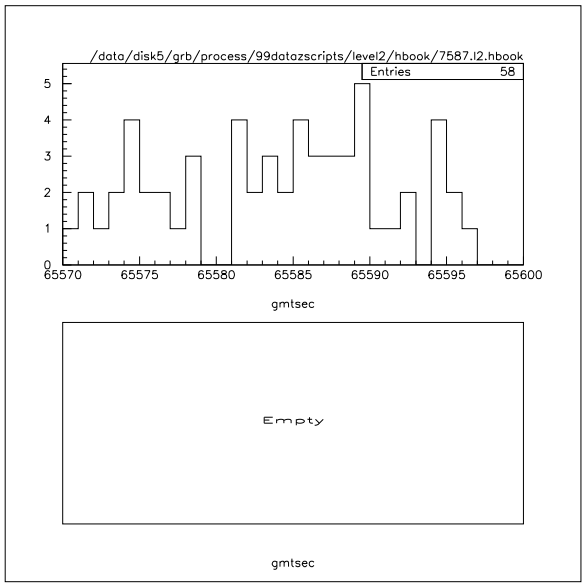

Figure G.41: The number of events for grb7587 during the burst, before (top) and after (bottom) cuts.

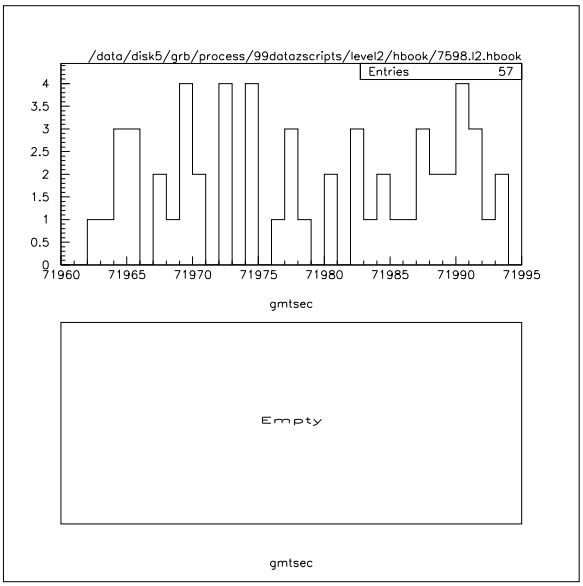

Figure G.43: The number of events for grb7598 during the burst, before (top) and after (bottom) cuts.

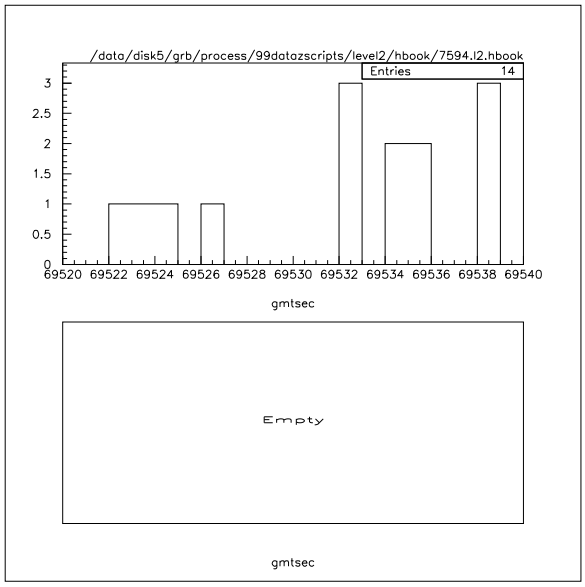

Figure G.42: The number of events for grb7594 during the burst, before (top) and after (bottom) cuts.

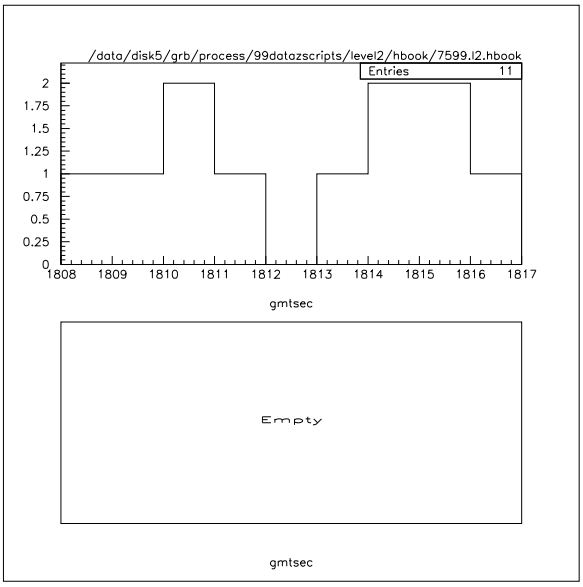

Figure G.44: The number of events for grb7599 during the burst, before (top) and after (bottom) cuts.

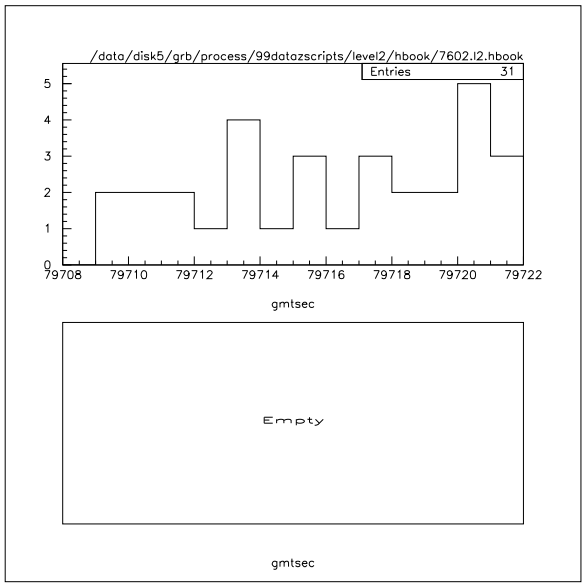

Figure G.45: The number of events for grb7602 during the burst, before (top) and after (bottom) cuts.

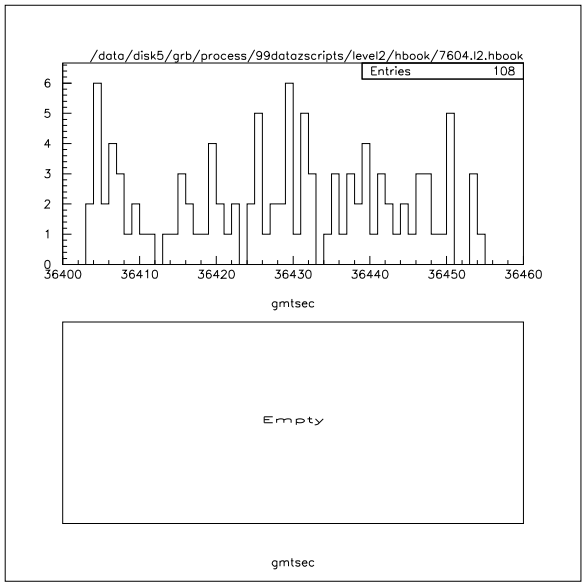

Figure G.46: The number of events for grb7604 during the burst, before (top) and after (bottom) cuts.

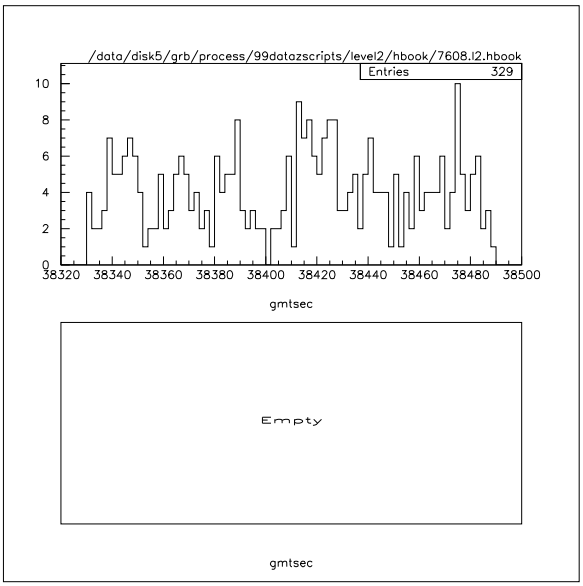

Figure G.47: The number of events for grb7608 during the burst, before (top) and after (bottom) cuts.

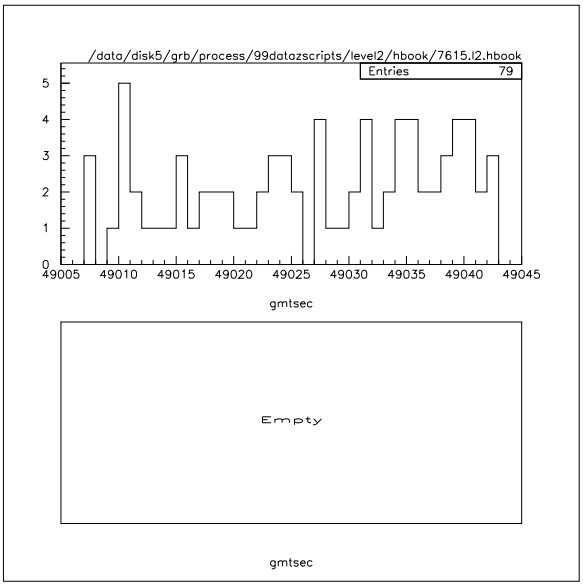

Figure G.48: The number of events for grb7615 during the burst, before (top) and after (bottom) cuts.

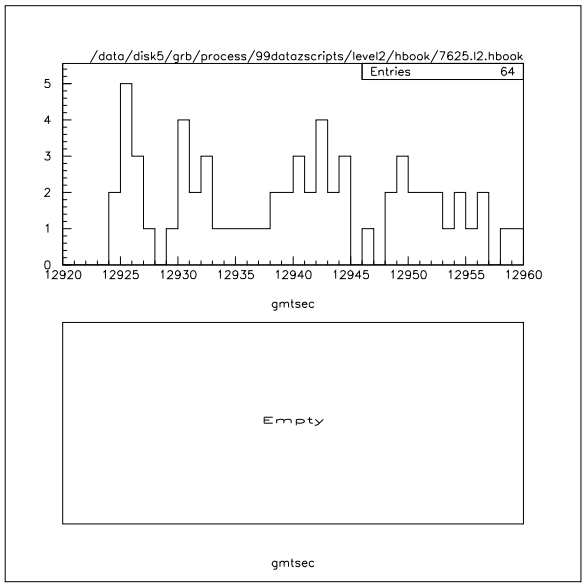

Figure G.49: The number of events for grb7625 during the burst, before (top) and after (bottom) cuts.

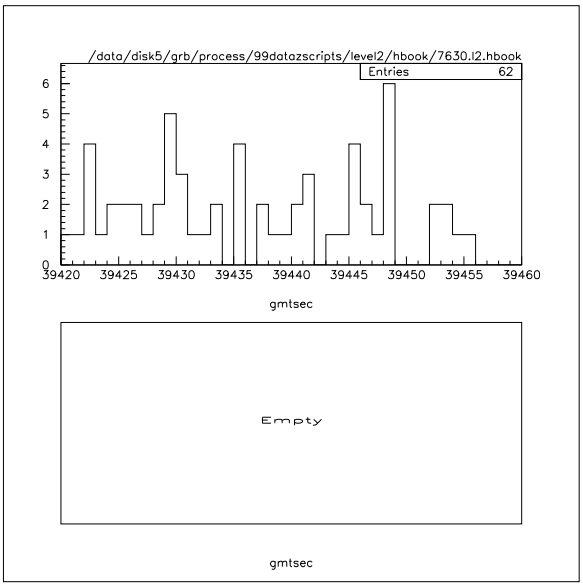

Figure G.51: The number of events for grb7630 during the burst, before (top) and after (bottom) cuts.

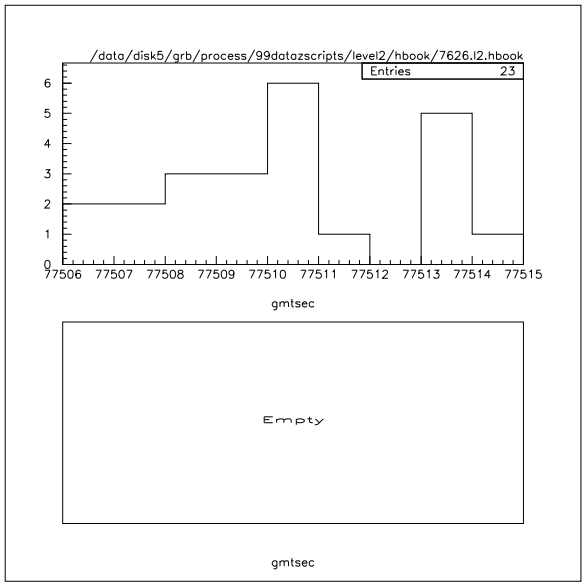

Figure G.50: The number of events for grb7626 during the burst, before (top) and after (bottom) cuts.

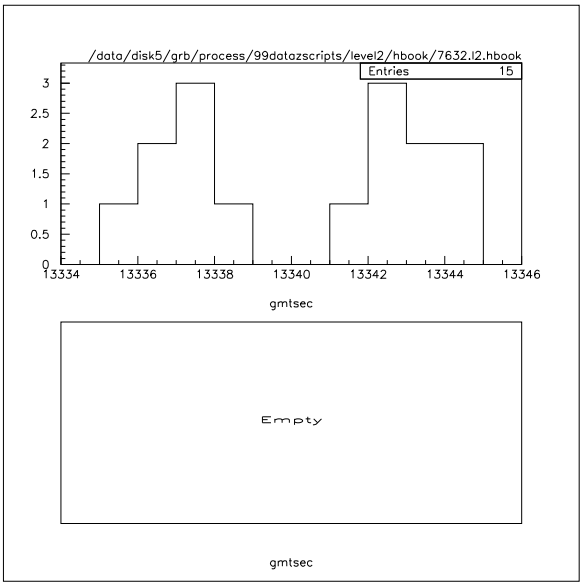

Figure G.52: The number of events for grb7632 during the burst, before (top) and after (bottom) cuts.

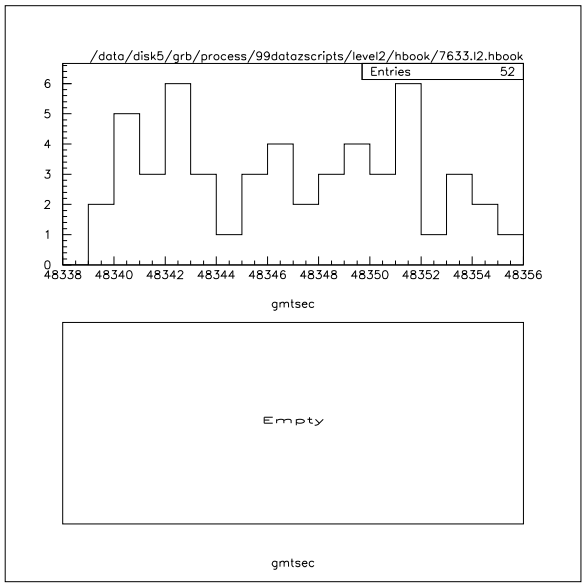

Figure G.53: The number of events for grb7633 during the burst, before (top) and after (bottom) cuts.

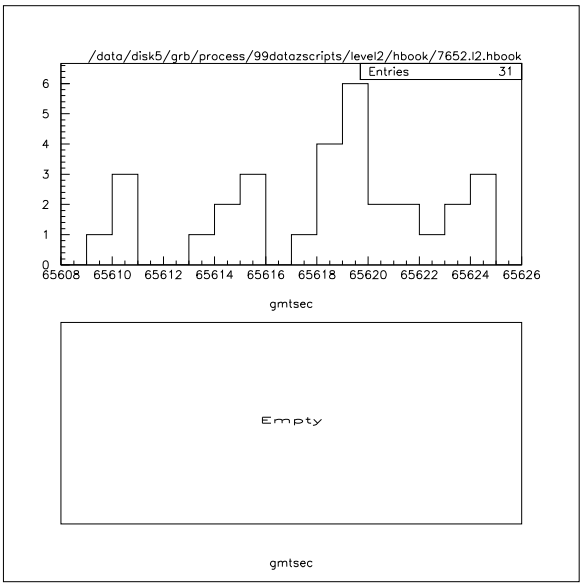

Figure G.55: The number of events for grb7652 during the burst, before (top) and after (bottom) cuts.

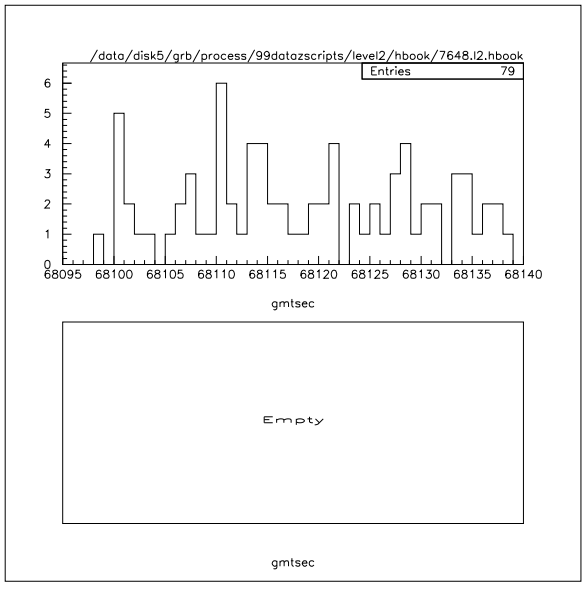

Figure G.54: The number of events for grb7648 during the burst, before (top) and after (bottom) cuts.

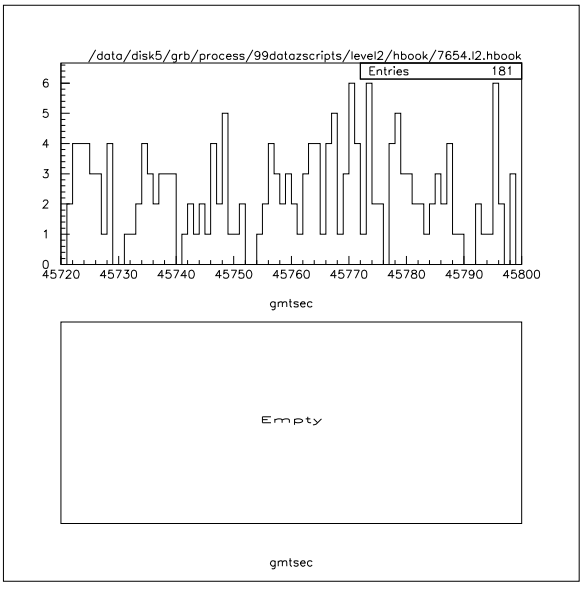

Figure G.56: The number of events for grb7654 during the burst, before (top) and after (bottom) cuts.

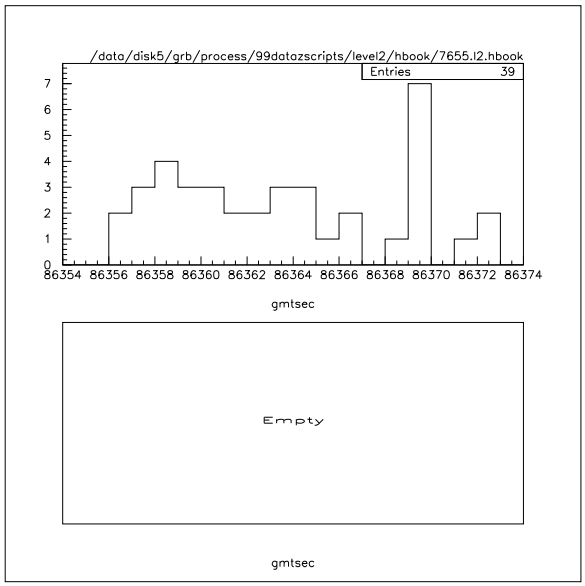

Figure G.57: The number of events for grb7655 during the burst, before (top) and after (bottom) cuts.

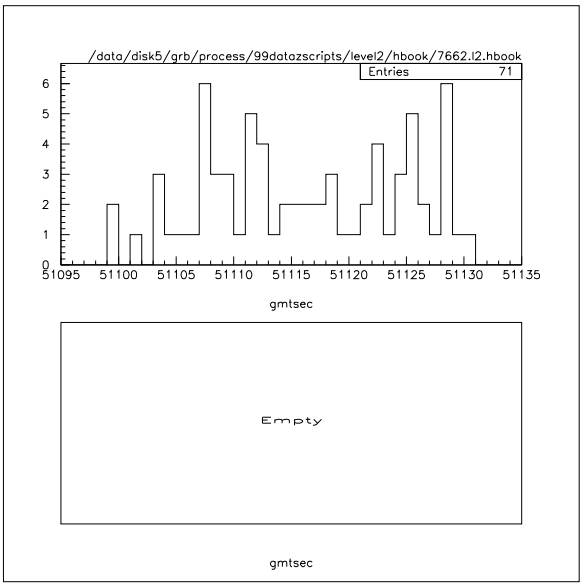

Figure G.59: The number of events for grb7662 during the burst, before (top) and after (bottom) cuts.

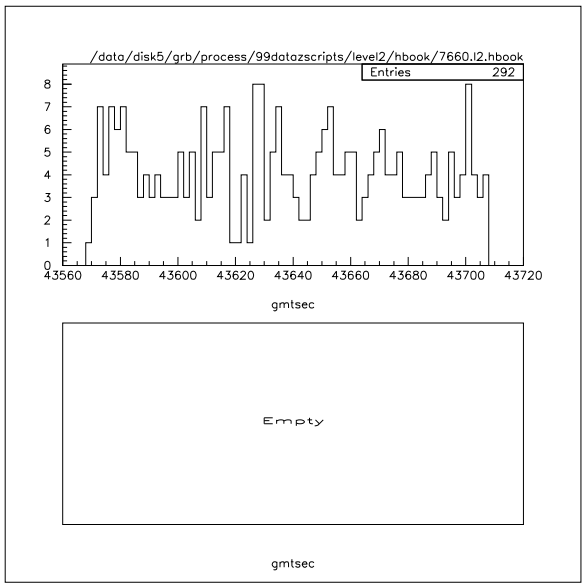

Figure G.58: The number of events for grb7660 during the burst, before (top) and after (bottom) cuts.

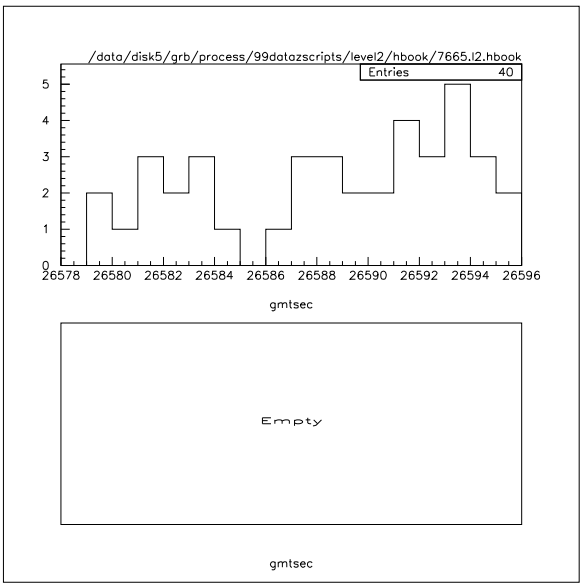

Figure G.60: The number of events for grb7665 during the burst, before (top) and after (bottom) cuts.

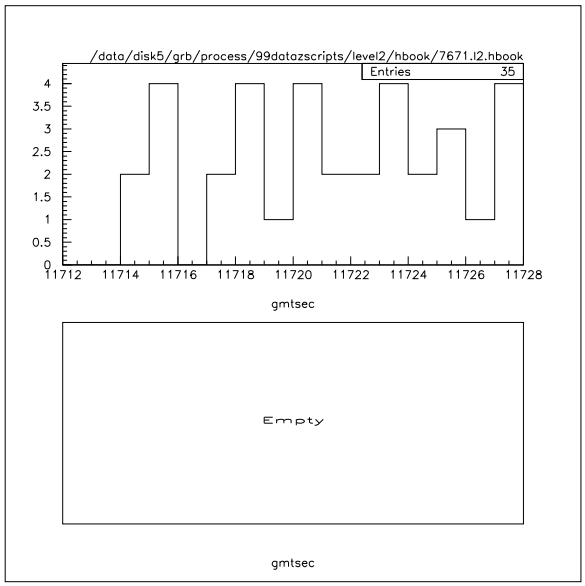

Figure G.61: The number of events for grb7671 during the burst, before (top) and after (bottom) cuts.

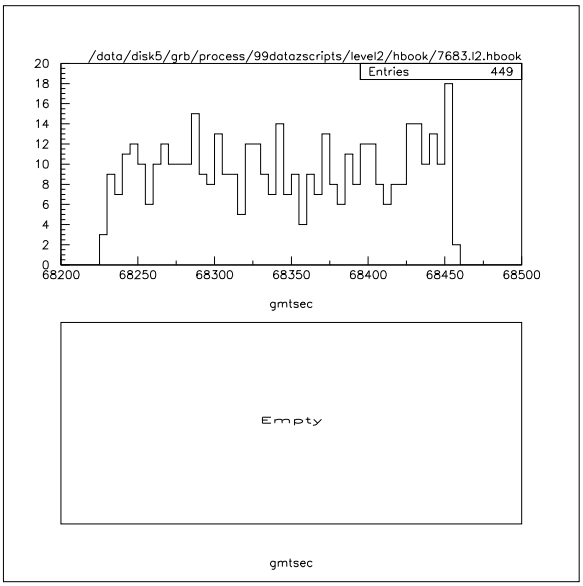

Figure G.63: The number of events for grb7683 during the burst, before (top) and after (bottom) cuts.

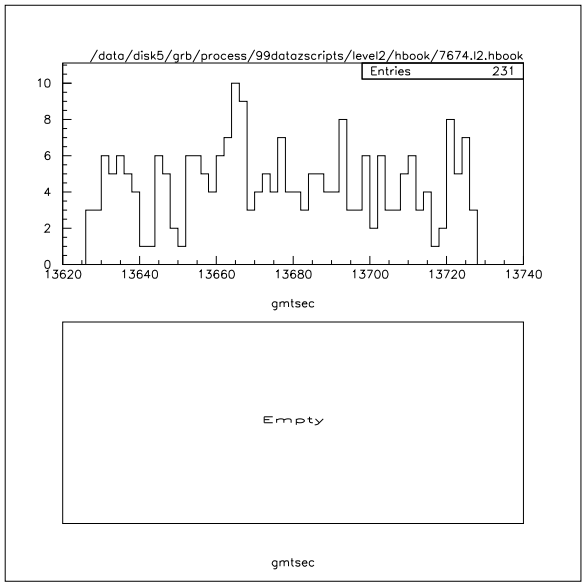

Figure G.62: The number of events for grb7674 during the burst, before (top) and after (bottom) cuts.

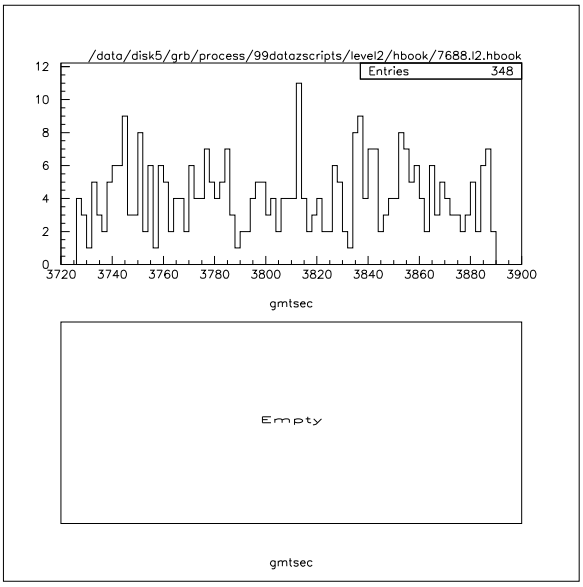

Figure G.64: The number of events for grb7688 during the burst, before (top) and after (bottom) cuts.

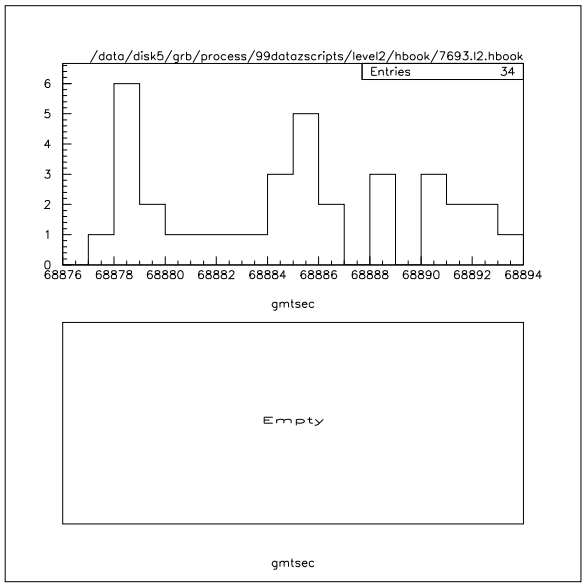

Figure G.65: The number of events for grb7693 during the burst, before (top) and after (bottom) cuts.

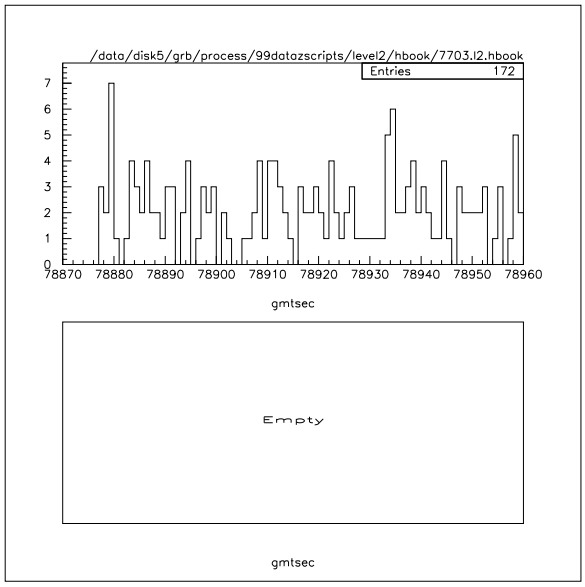

Figure G.66: The number of events for grb7703 during the burst, before (top) and after (bottom) cuts.

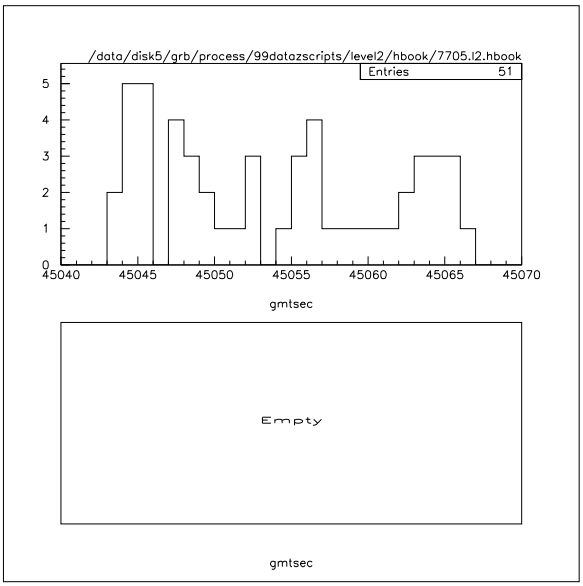

Figure G.67: The number of events for grb7705 during the burst, before (top) and after (bottom) cuts.

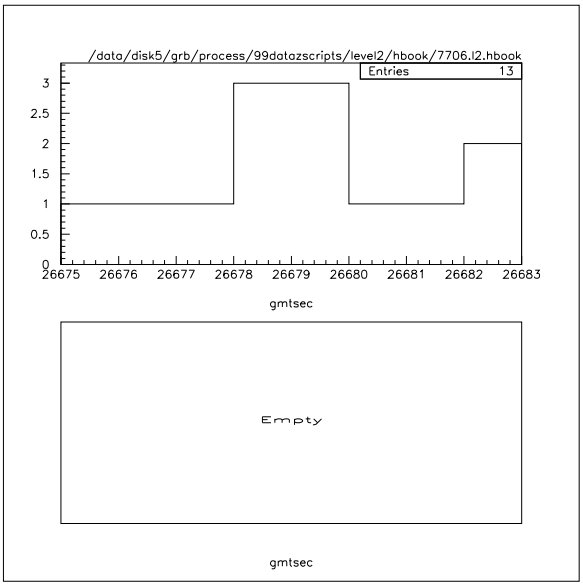

Figure G.68: The number of events for grb7706 during the burst, before (top) and after (bottom) cuts.

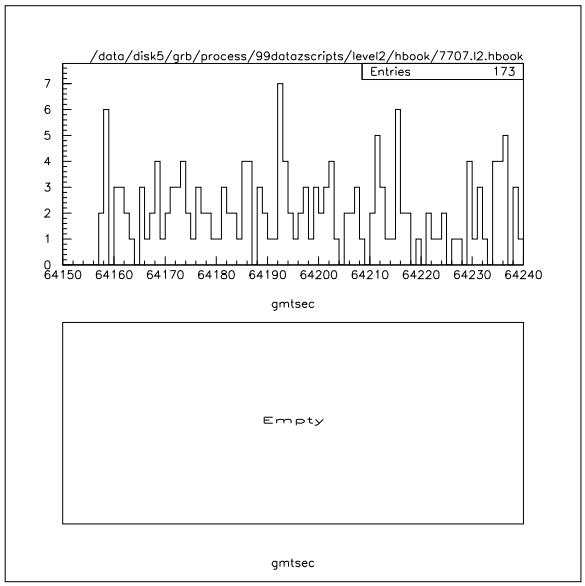

Figure G.69: The number of events for grb7707 during the burst, before (top) and after (bottom) cuts.

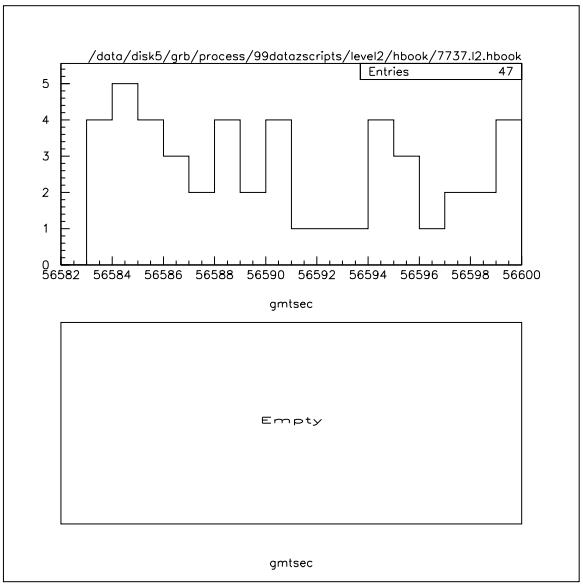

Figure G.71: The number of events for grb7737 during the burst, before (top) and after (bottom) cuts.

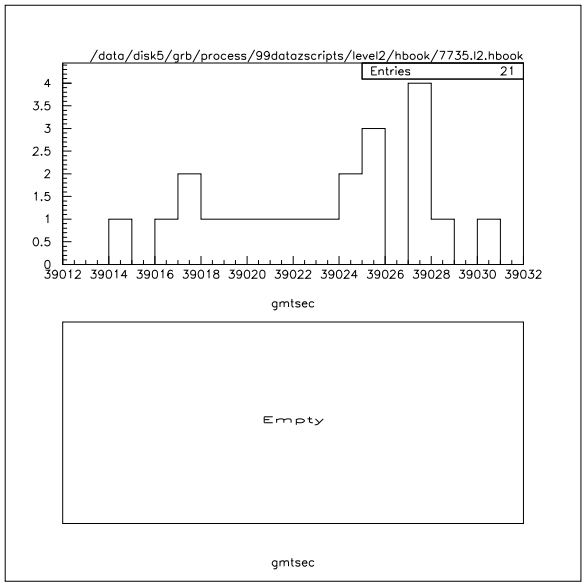

Figure G.70: The number of events for grb7735 during the burst, before (top) and after (bottom) cuts.

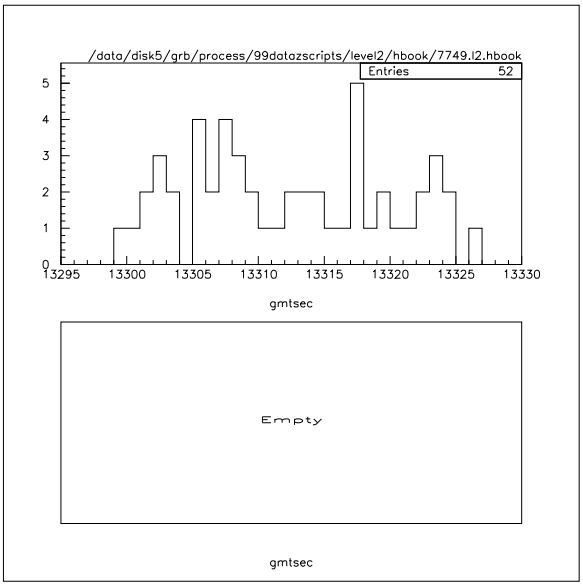

Figure G.72: The number of events for grb7749 during the burst, before (top) and after (bottom) cuts.

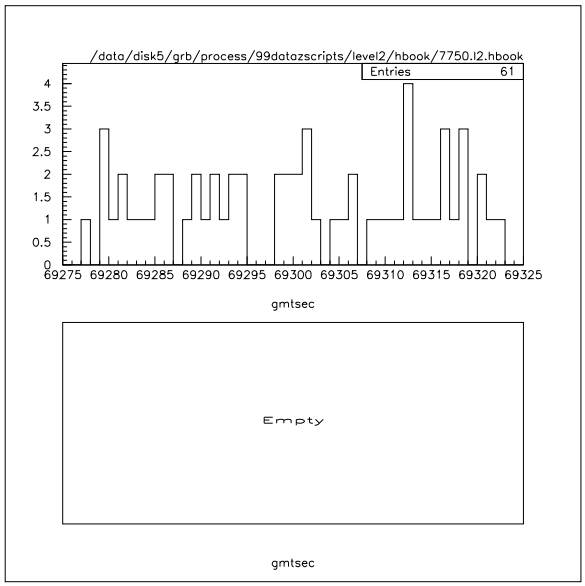

Figure G.73: The number of events for grb7750 during the burst, before (top) and after (bottom) cuts.

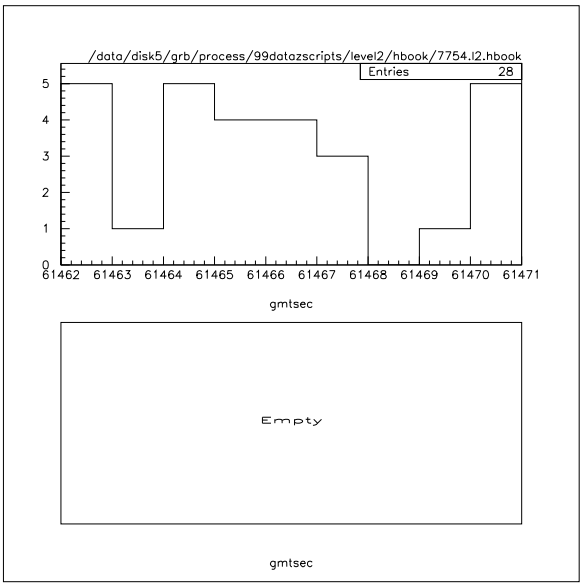

Figure G.75: The number of events for grb7754 during the burst, before (top) and after (bottom) cuts.

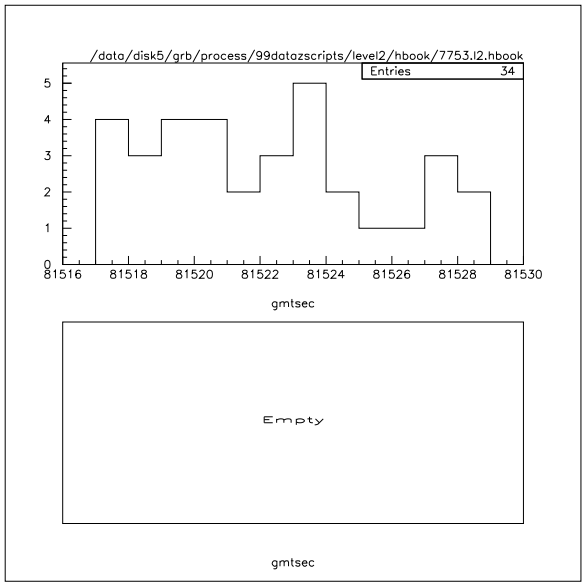

Figure G.74: The number of events for grb7753 during the burst, before (top) and after (bottom) cuts.

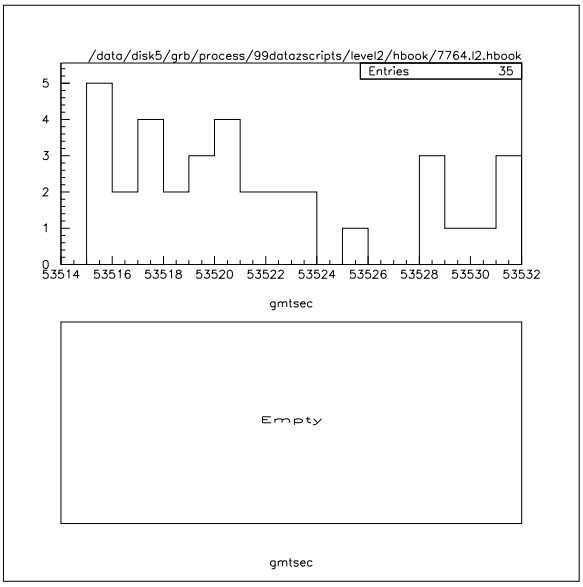

Figure G.76: The number of events for grb7764 during the burst, before (top) and after (bottom) cuts.

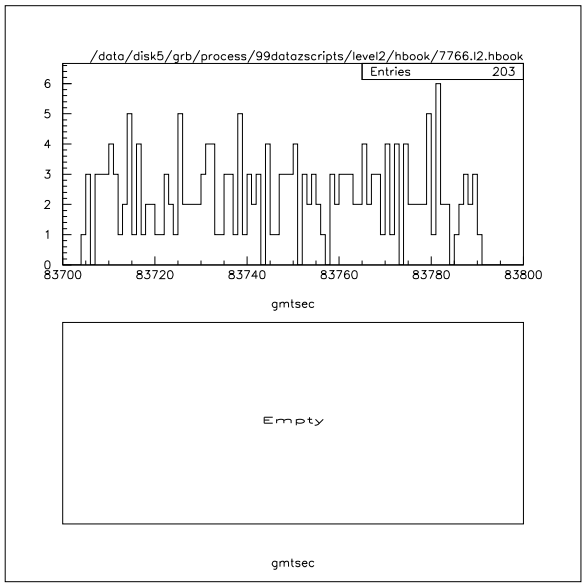

Figure G.77: The number of events for grb7766 during the burst, before (top) and after (bottom) cuts.

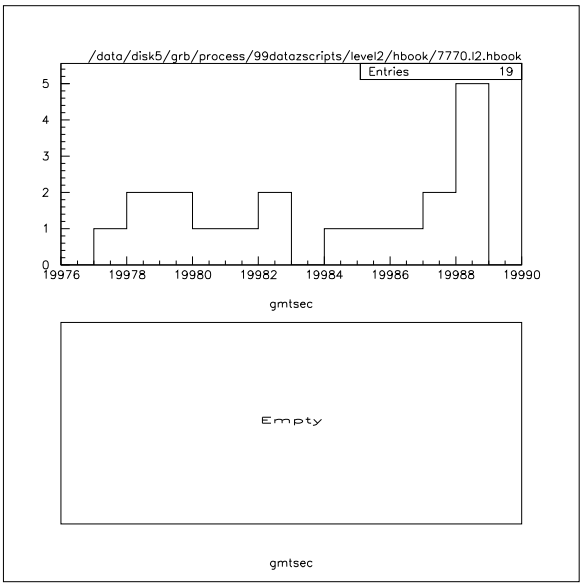

Figure G.79: The number of events for grb7770 during the burst, before (top) and after (bottom) cuts.

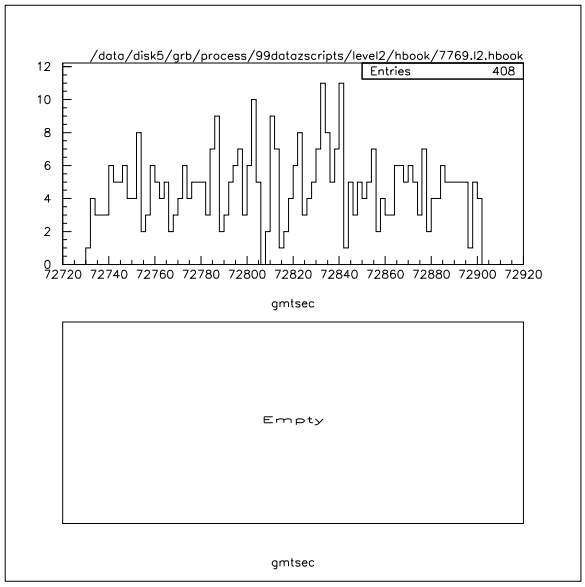

Figure G.78: The number of events for grb7769 during the burst, before (top) and after (bottom) cuts.

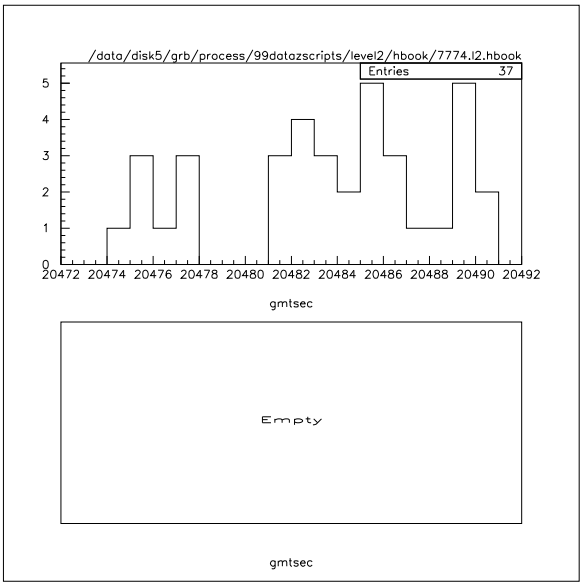

Figure G.80: The number of events for grb7774 during the burst, before (top) and after (bottom) cuts.

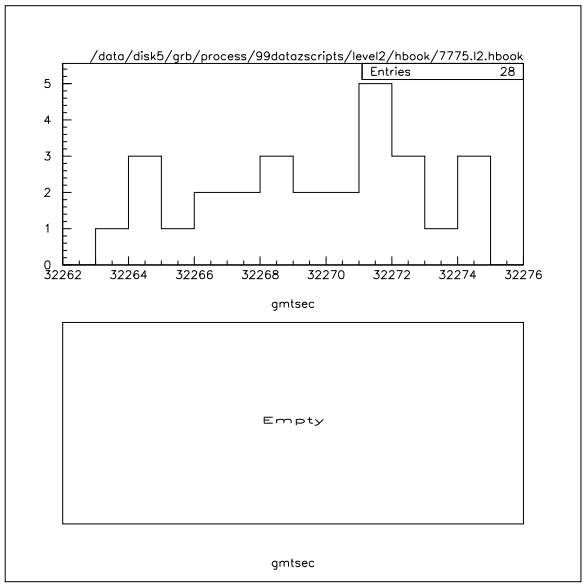

Figure G.81: The number of events for grb7775 during the burst, before (top) and after (bottom) cuts.

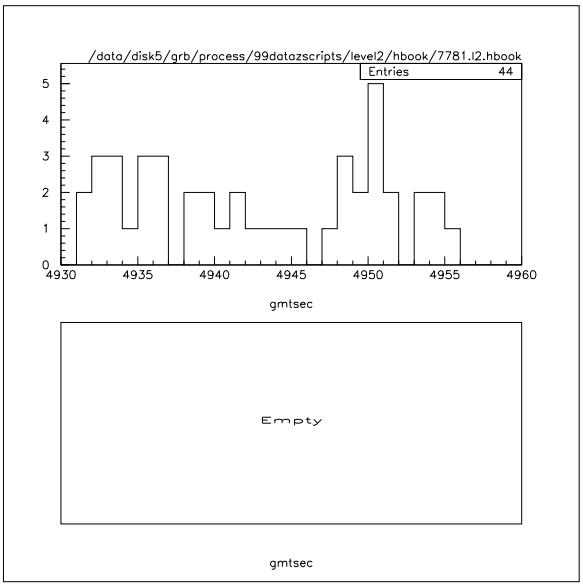

Figure G.83: The number of events for grb7781 during the burst, before (top) and after (bottom) cuts.

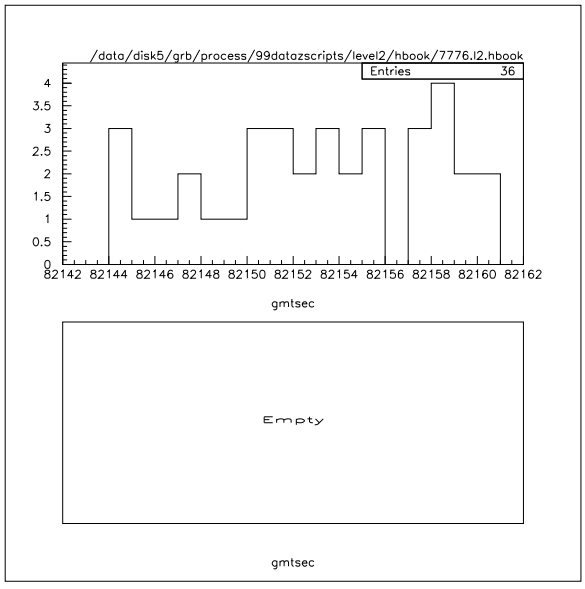

Figure G.82: The number of events for grb7776 during the burst, before (top) and after (bottom) cuts.

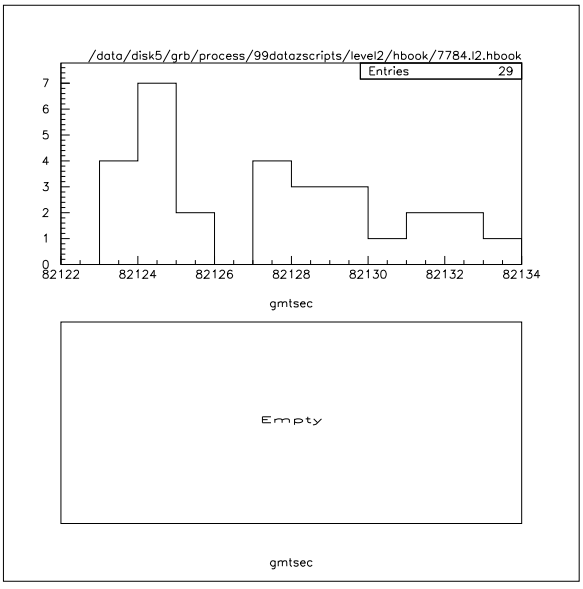

Figure G.84: The number of events for grb7784 during the burst, before (top) and after (bottom) cuts.

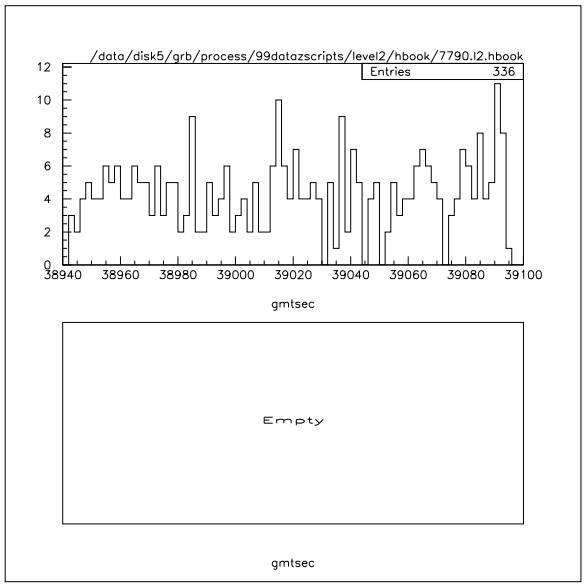

Figure G.85: The number of events for grb7790 during the burst, before (top) and after (bottom) cuts.

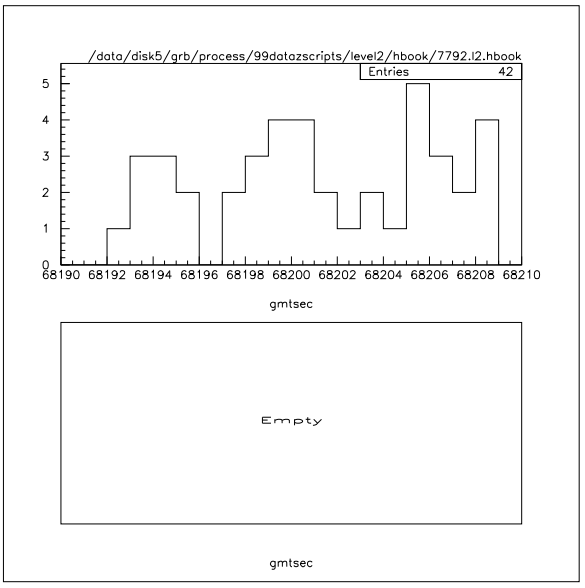

Figure G.87: The number of events for grb7792 during the burst, before (top) and after (bottom) cuts.

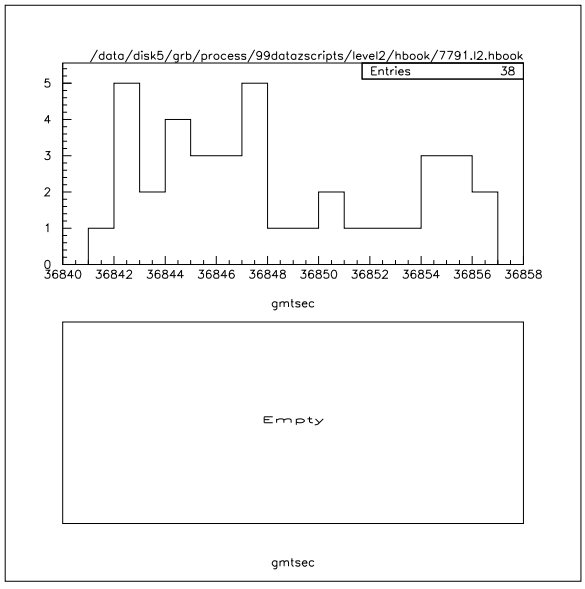

Figure G.86: The number of events for grb7791 during the burst, before (top) and after (bottom) cuts.

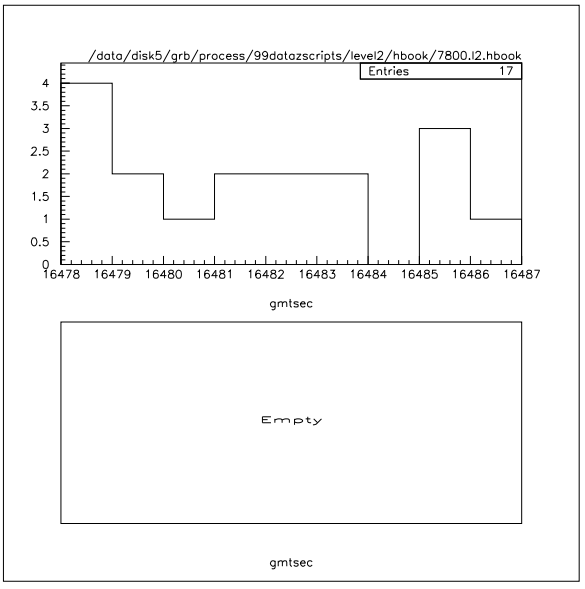

Figure G.88: The number of events for grb7800 during the burst, before (top) and after (bottom) cuts.

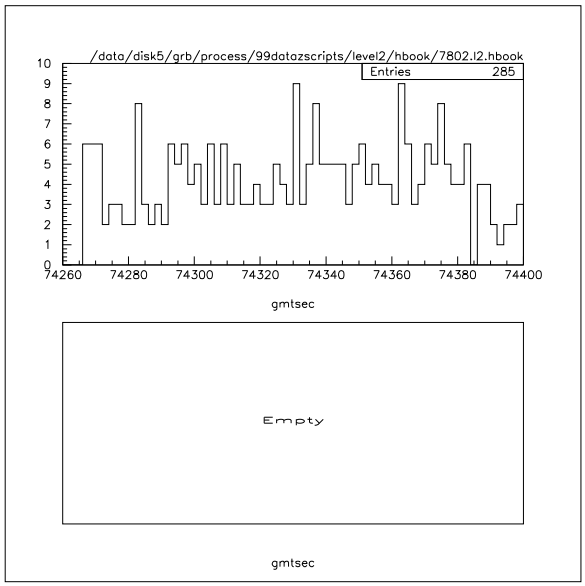

Figure G.89: The number of events for grb7802 during the burst, before (top) and after (bottom) cuts.

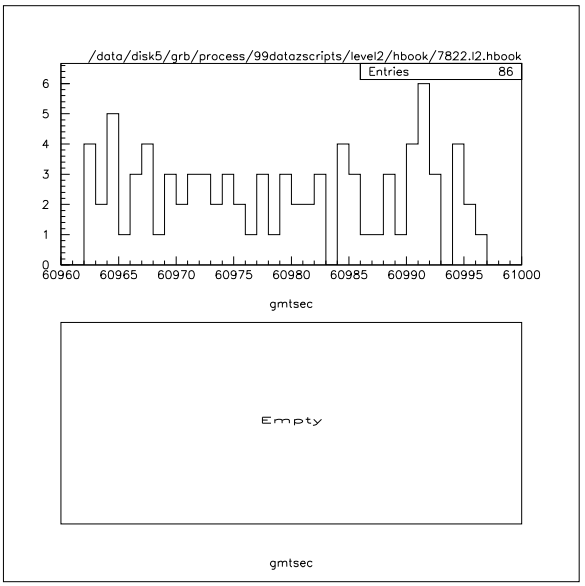

Figure G.91: The number of events for grb7822 during the burst, before (top) and after (bottom) cuts.

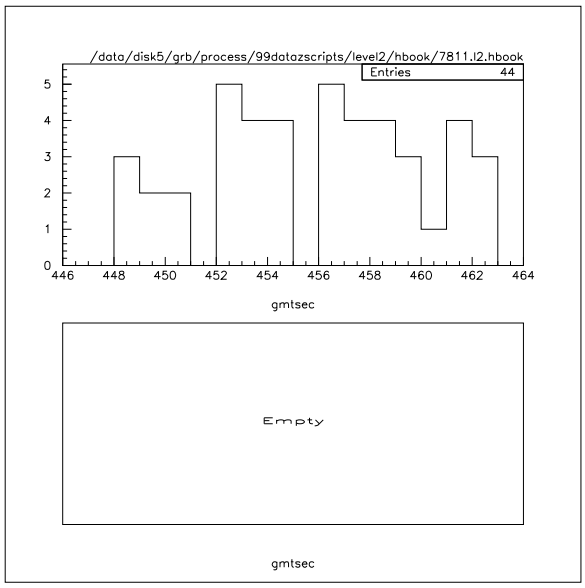

Figure G.90: The number of events for grb7811 during the burst, before (top) and after (bottom) cuts.

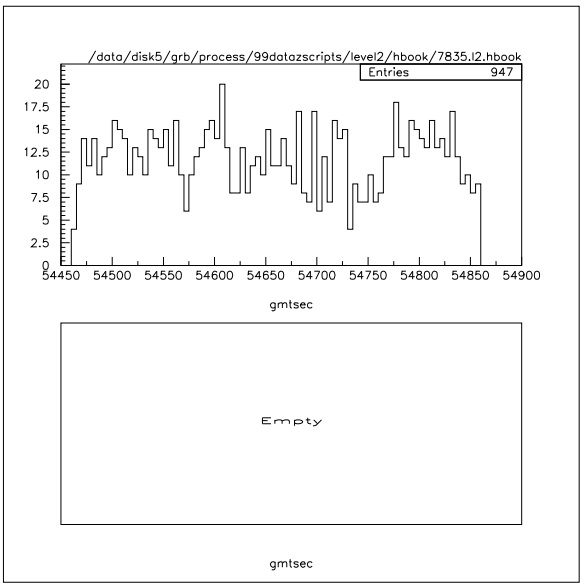

Figure G.92: The number of events for grb7835 during the burst, before (top) and after (bottom) cuts.

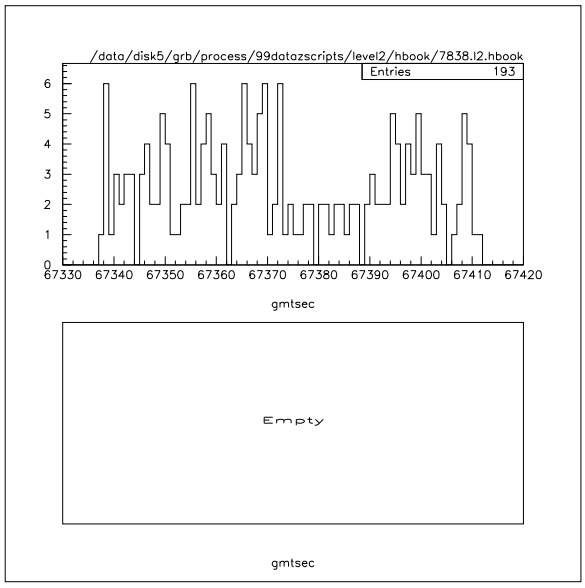

Figure G.93: The number of events for grb7838 during the burst, before (top) and after (bottom) cuts.

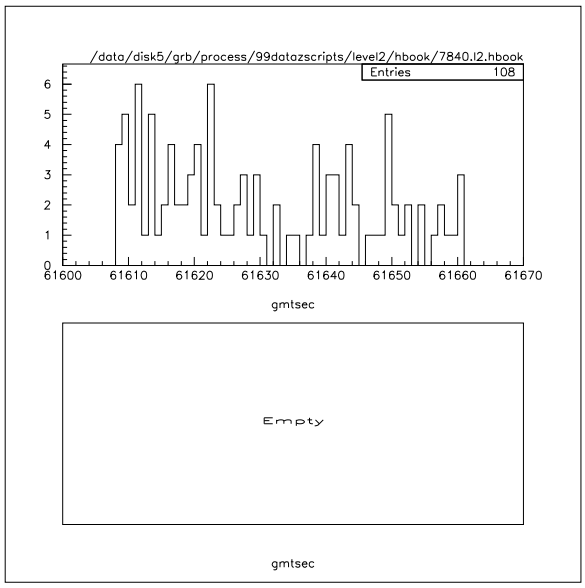

Figure G.94: The number of events for grb7840 during the burst, before (top) and after (bottom) cuts.

Appendix H

Distribution of Background Events in 10-Second Windows

The distribution of the number of background events in 10-second windows are shown here for some 2000 GRBs. The distributions are nice Poissonian in most cases. Where there are an abnormal number of intervals with zero events, the file was examined in detail for data gaps.

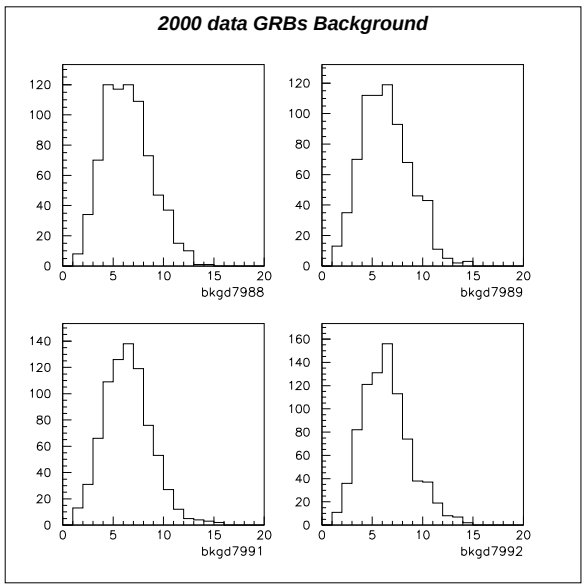

Figure H.1: Number of background events in 10-second intervals for GRB 7988, 7989, 7991 and 7992.

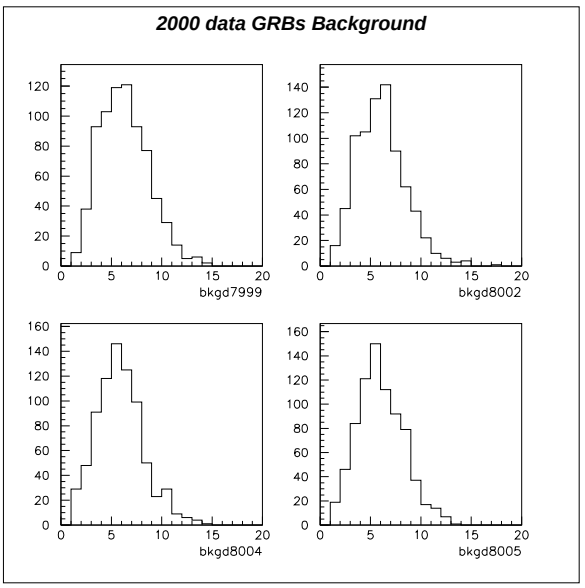

Figure H.3: Number of background events in 10-second intervals for GRB 7999, 8002, 8004 and 8005.

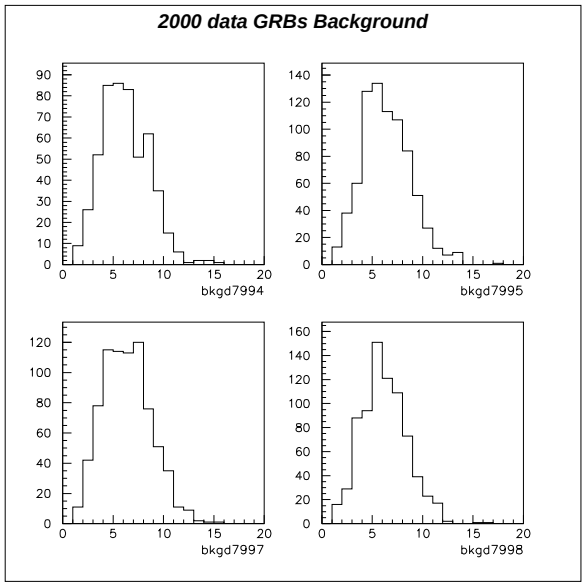

Figure H.2: Number of background events in 10-second intervals for GRB 7994, 7995, 7997 and 7998.

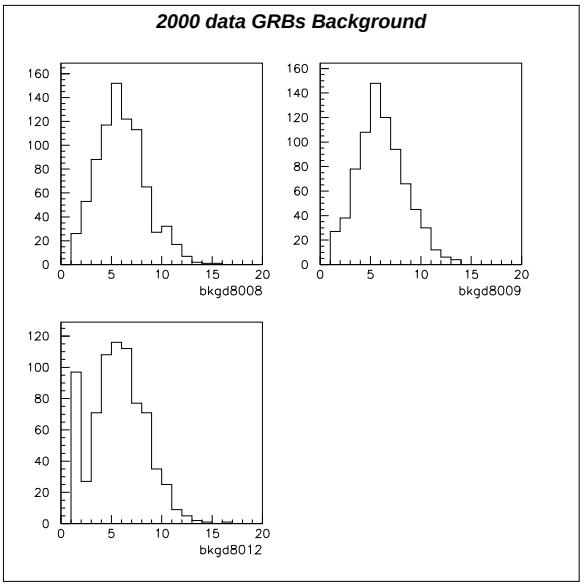

Figure H.4: Number of background events in 10-second intervals for GRB 8008, 8009 and 8012.

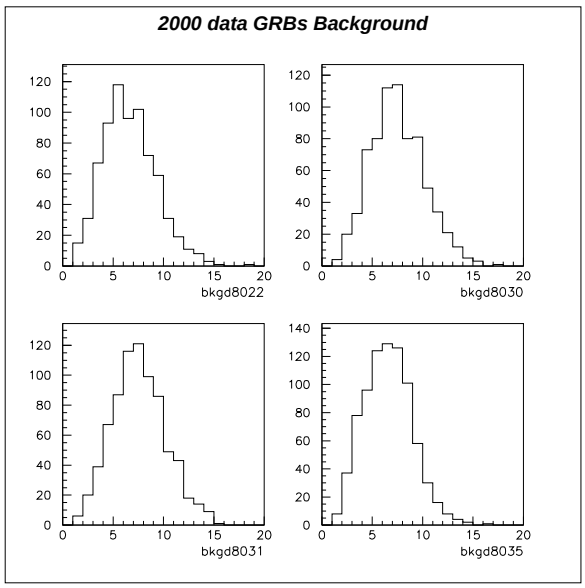

Figure H.5: Number of background events in 10-second intervals for GRB 8022, 8030, 8031 and 8035.

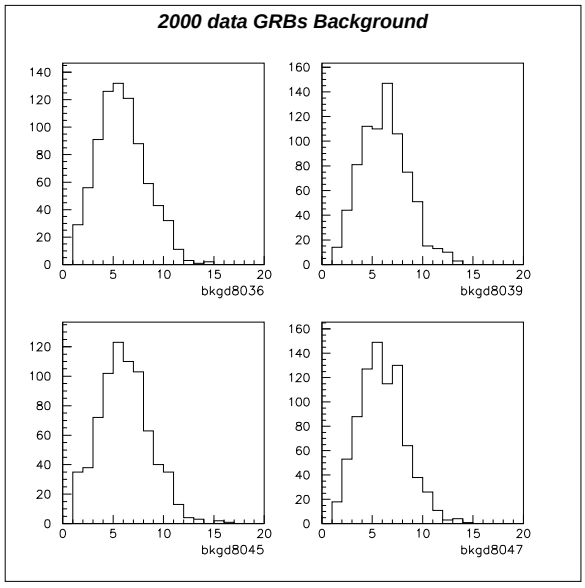

Figure H.6: Number of background events in 10-second intervals for GRB 8036, 8039, 8045, 8047.

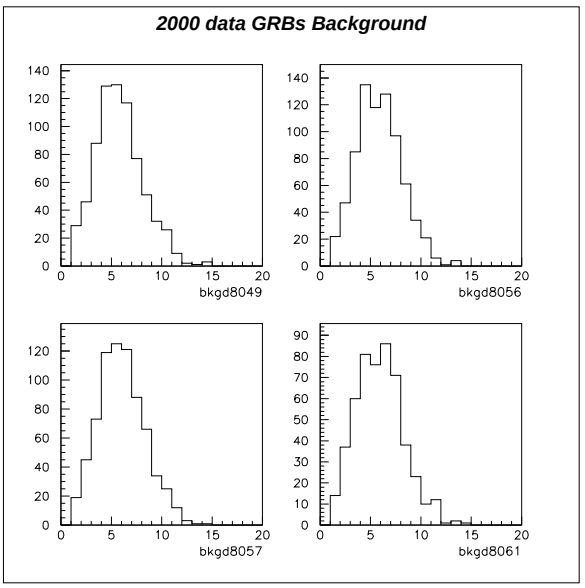

Figure H.7: Number of background events in 10-second intervals for GRB 8049, 8056, 8057 and 8061.

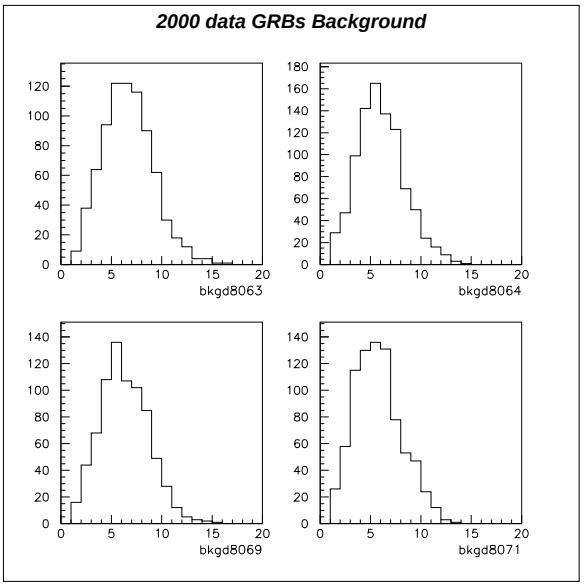

Figure H.8: Number of background events in 10-second intervals for GRB 8063, 8064, 8069 and 8071.

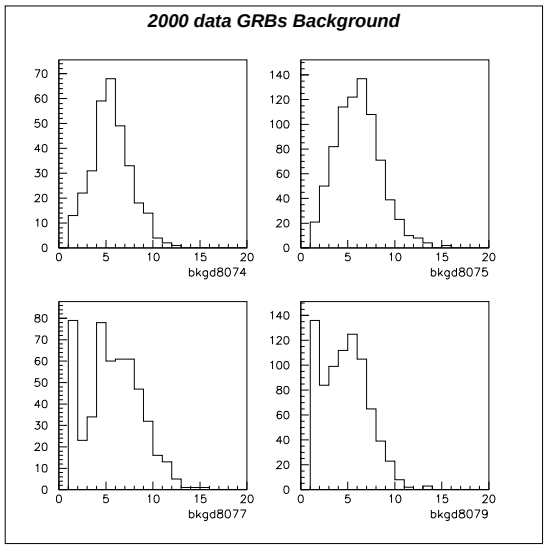

Figure H.9: Number of background events in 10-second intervals for GRB 8074. 8075, 8077 and 8079.

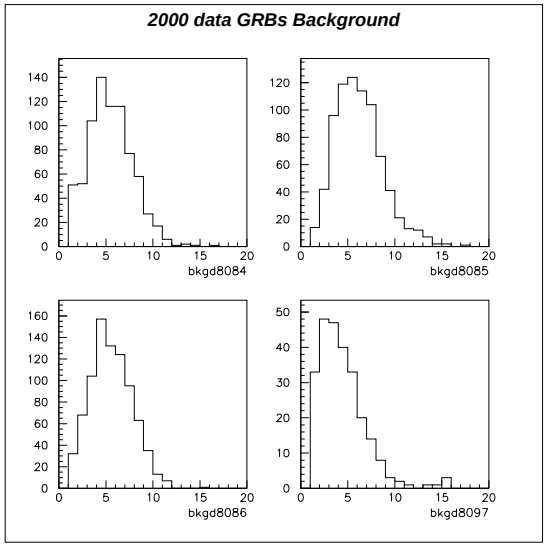

Figure H.10: Number of background events in 10-second intervals for GRB 8084, 8085, 8086 and 8097.

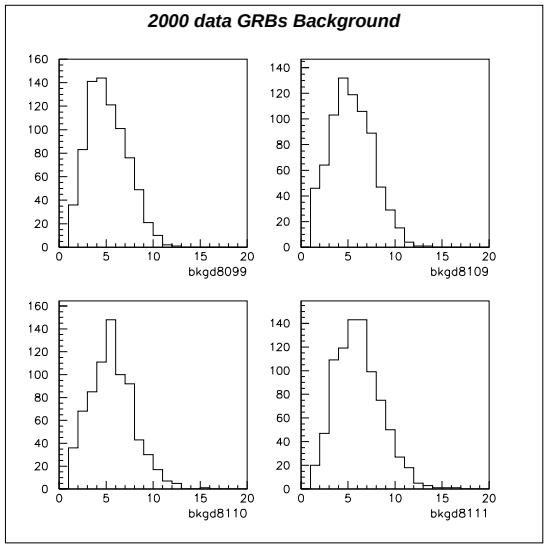

Figure H.11: Number of background events in 10-second intervals for GRB 8099, 8109, 8110 and 8111.

Appendix I

Some δ-t Plots for 2000

These examples show the distribution of the time between consecutive events in the detector. On average, the detector has a dead time of 17out events. Large δ-t's were examined as potential data gaps.

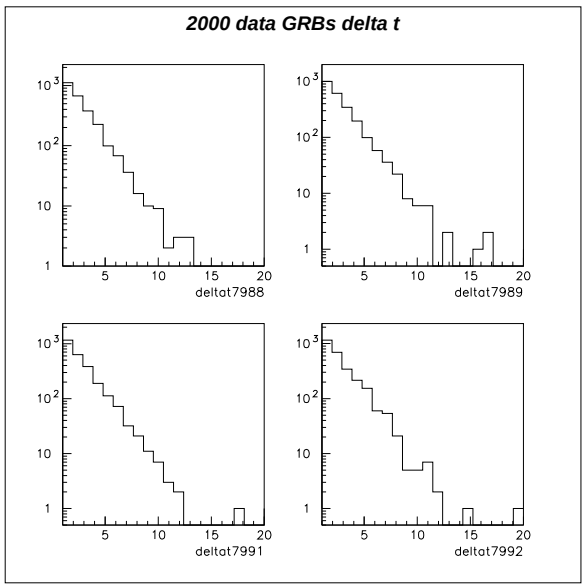

Figure I.1: Time between consecutive events, δt, plots for GRB 7988, 7989, 7991 and 7992.

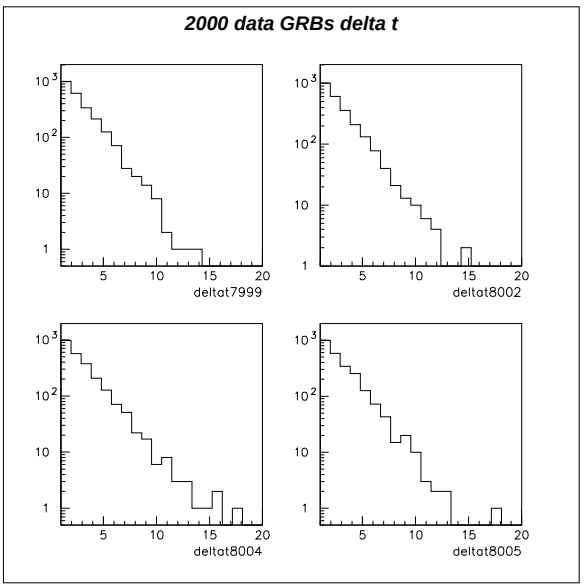

Figure I.3: Time between consecutive events, δt, plots for GRB 7999, 8002, 8004 and 8005.

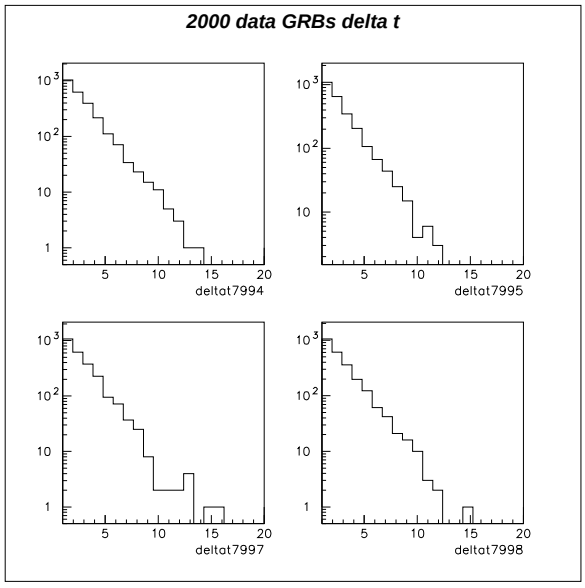

Figure I.2: Time between consecutive events, δt, plots for GRB 7994, 7995, 7997 and7998.

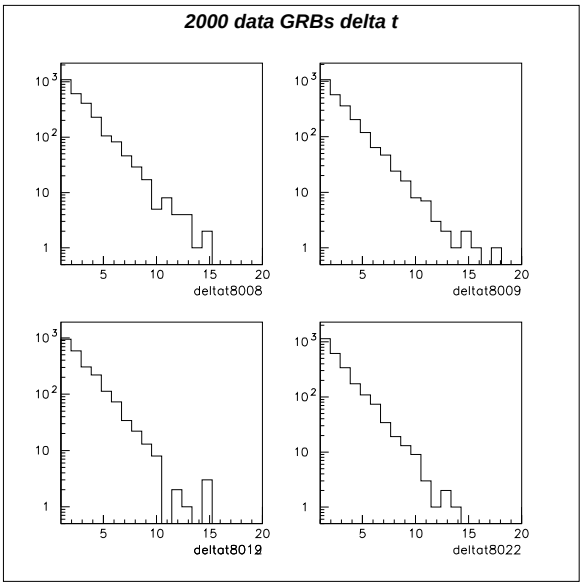

Figure I.4: Time between consecutive events, δt, plots for GRB 8008, 8009, 8012 and 8022.

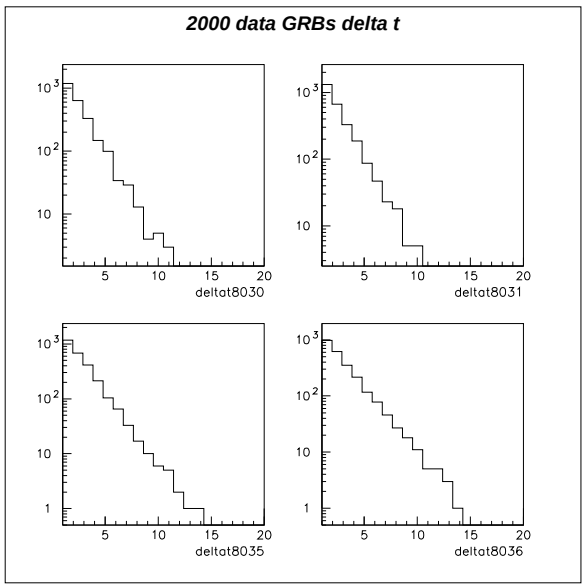

Figure I.5: Time between consecutive events, δt, plots for GRB 8030, 8031, 8035 and 8036.

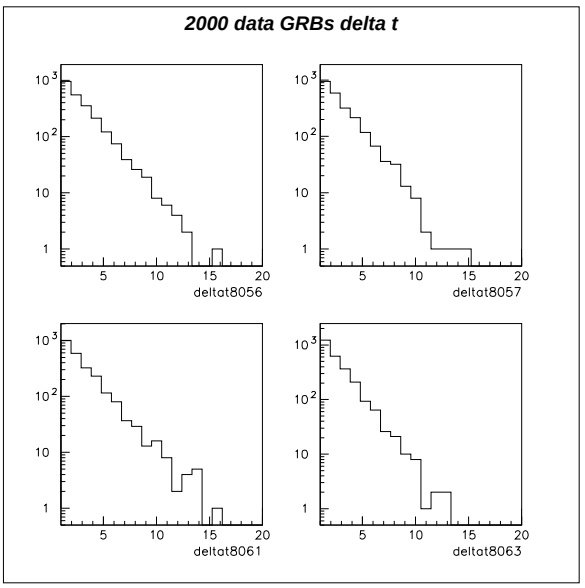

Figure I.7: Time between consecutive events, δt, plots for GRB 8056, 8057, 8061 and 8063.

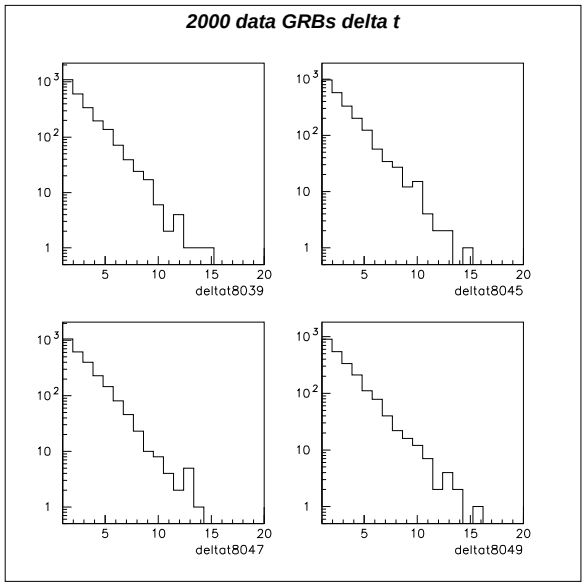

Figure I.6: Time between consecutive events, δt, plots for GRB 8039, 8045, 8047 and 8049.

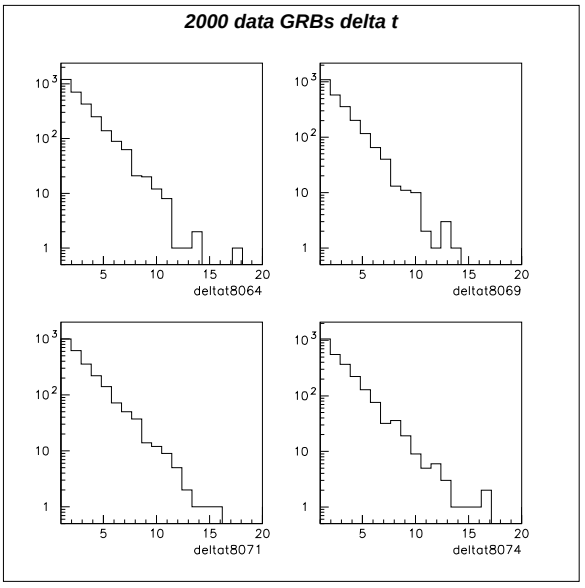

Figure I.8: Time between consecutive events, δt, plots for GRB 8064, 8069, 8071 and 8074.

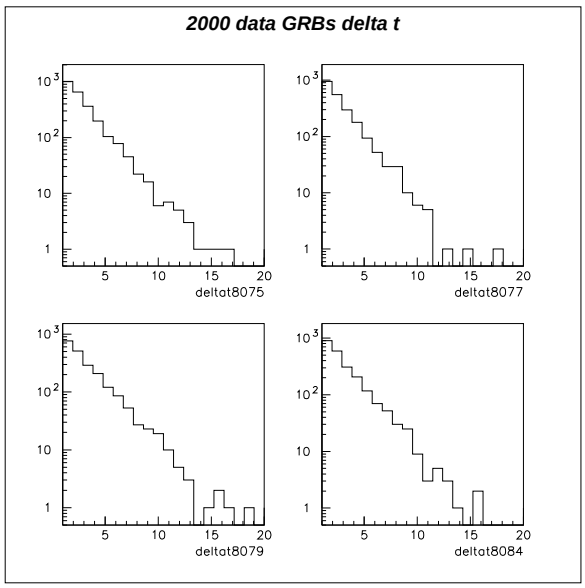

Figure I.9: Time between consecutive events, δt, plots for GRB 8075, 8077, 8079 and 8084.

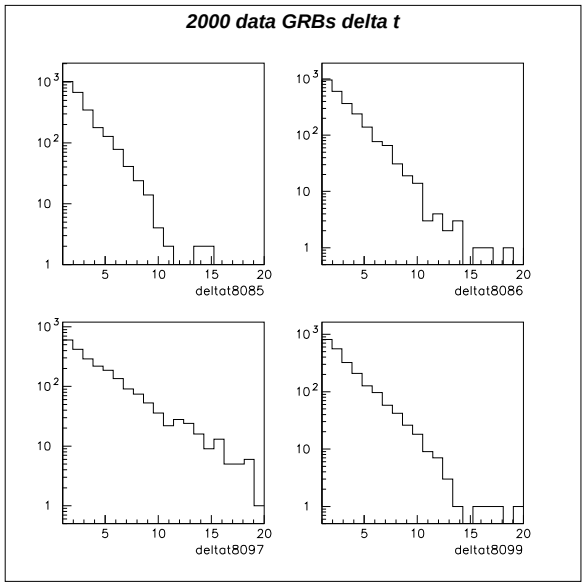

Figure I.10: Time between consecutive events, δt, plots for GRB 8085, 8086, 8097 and 8099.

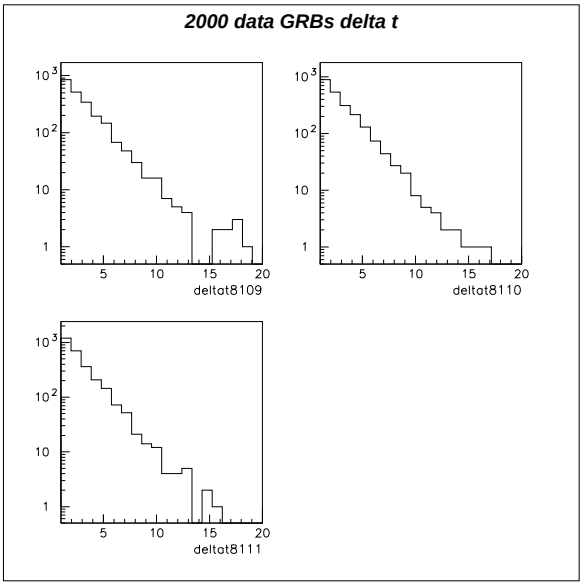

Figure I.11: Time between consecutive events, δt, plots for GRB 8109, 8110 and 8111.

Appendix J

Blinded Event Rates for 2000

Here are the background distributions for some 2000 GRBs. The number of events as a function of time is shown. The 10-minute blind spot is the region of interest and remained unexamined until final cuts had been set.

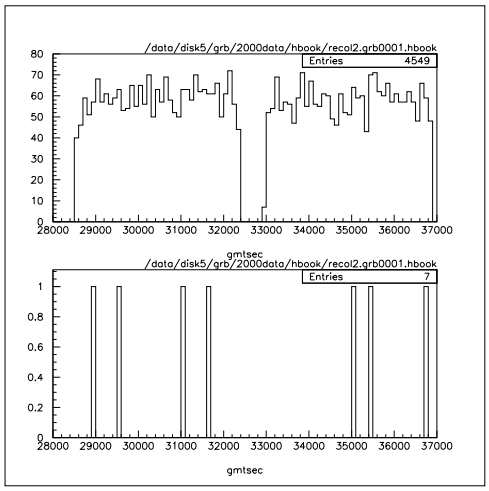

Figure J.1: The background distribution of events for grb11591c, except for the 10 minute blind spot around the trigger time, before (top) and after (bottom) cuts.

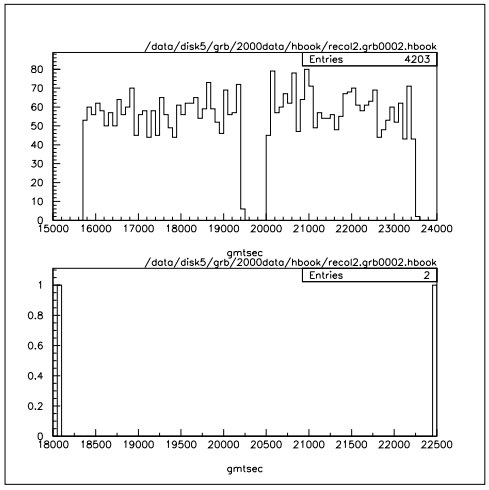

Figure J.2: The background distribution of events for grb11597b, except for the 10 minute blind spot around the trigger time, before (top) and after (bottom) cuts.

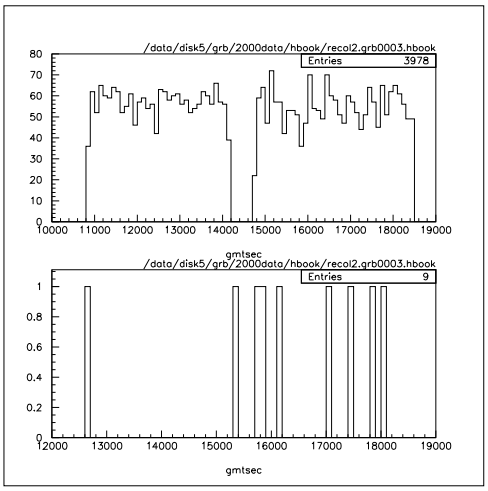

Figure J.3: The background distribution of events for grb11599b, except for the 10 minute blind spot around the trigger time, before (top) and after (bottom) cuts.

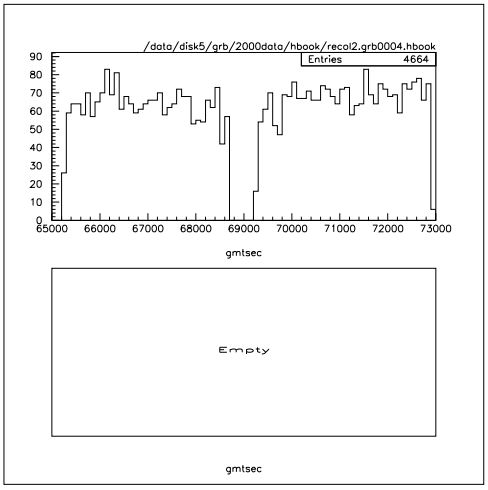

Figure J.4: The background distribution of events for grb11600b, except for the 10 minute blind spot around the trigger time, before (top) and after (bottom) cuts.

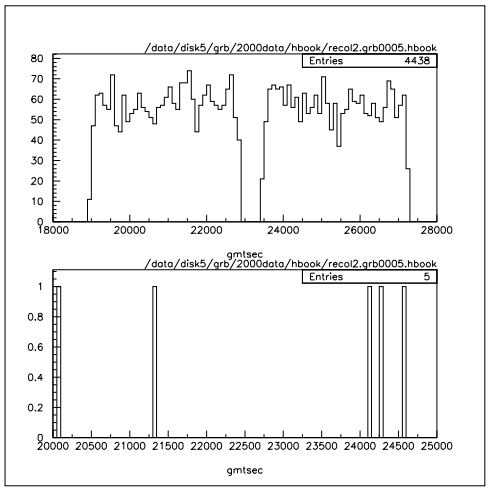

Figure J.5: The background distribution of events for grb11602b, except for the 10 minute blind spot around the trigger time, before (top) and after (bottom) cuts.

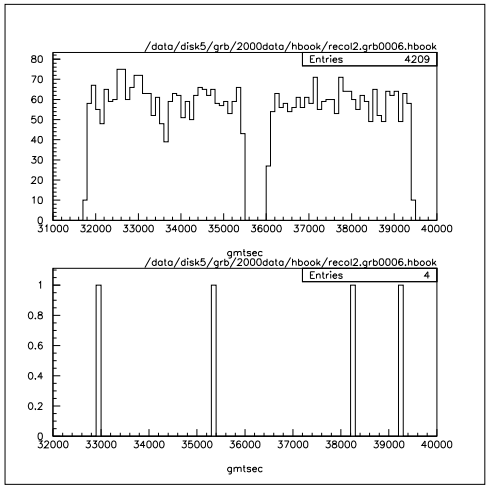

Figure J.6: The background distribution of events for grb11608a, except for the 10 minute blind spot around the trigger time, before (top) and after (bottom) cuts.

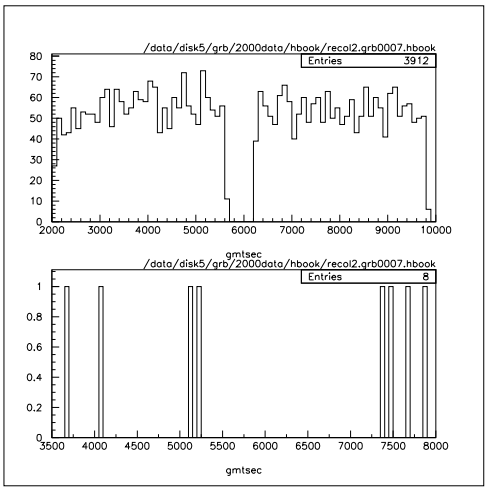

Figure J.7: The background distribution of events for grb11609b, except for the 10 minute blind spot around the trigger time, before (top) and after (bottom) cuts.

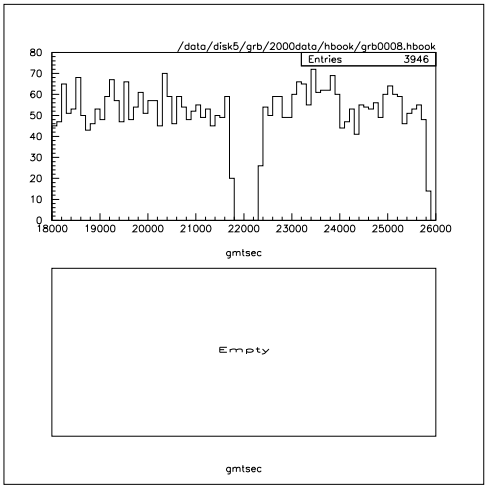

Figure J.8: The background distribution of events for grb11625b, except for the 10 minute blind spot around the trigger time, before (top) and after (bottom) cuts.

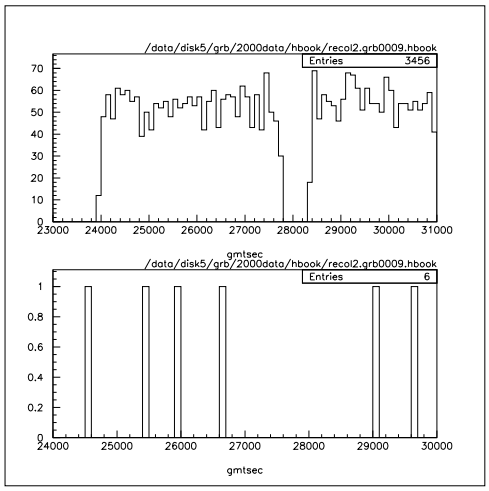

Figure J.9: The background distribution of events for grb11633b, except for the 10 minute blind spot around the trigger time, before (top) and after (bottom) cuts.

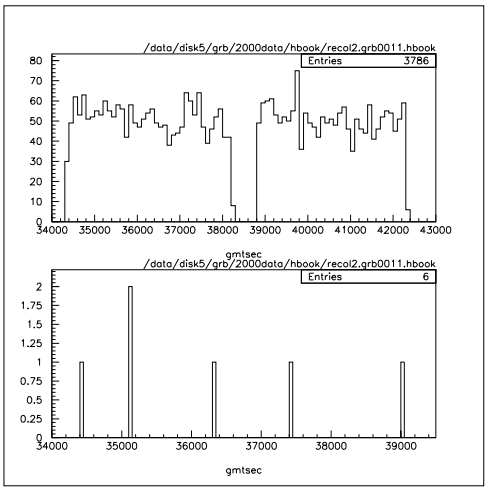

Figure J.11: The background distribution of events for grb11634g, except for the 10 minute blind spot around the trigger time, before (top) and after (bottom) cuts.

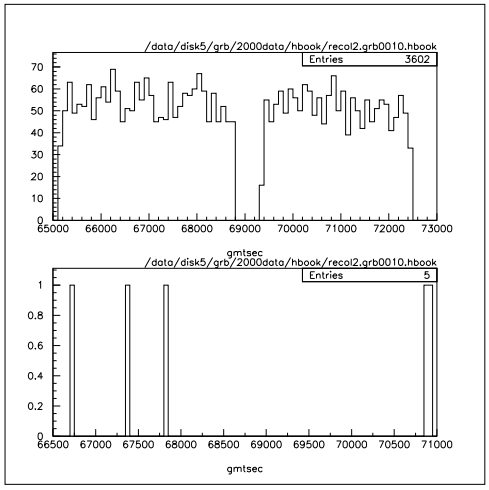

Figure J.10: The background distribution of events for grb11633f, except for the 10 minute blind spot around the trigger time, before (top) and after (bottom) cuts.

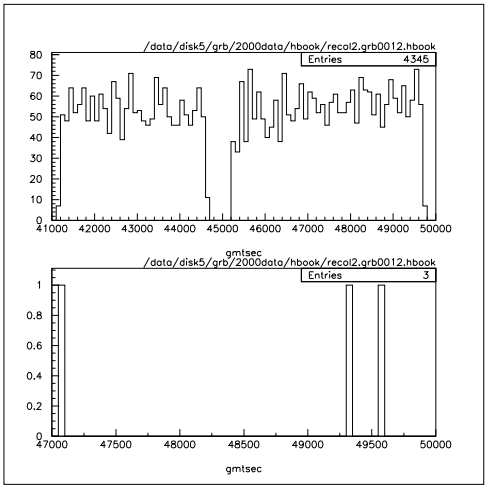

Figure J.12: The background distribution of events for grb11637c, except for the 10 minute blind spot around the trigger time, before (top) and after (bottom) cuts.

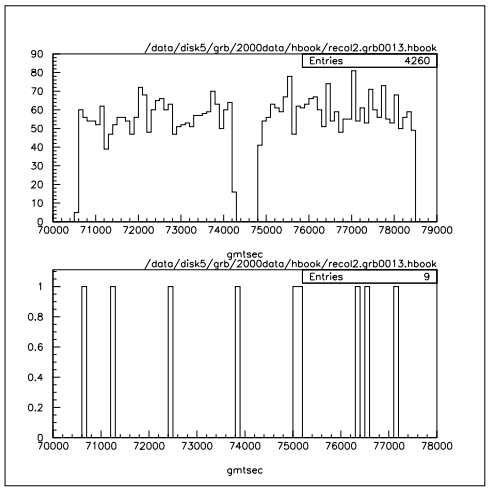

Figure J.13: The background distribution of events for grb11637e, except for the 10 minute blind spot around the trigger time, before (top) and after (bottom) cuts.

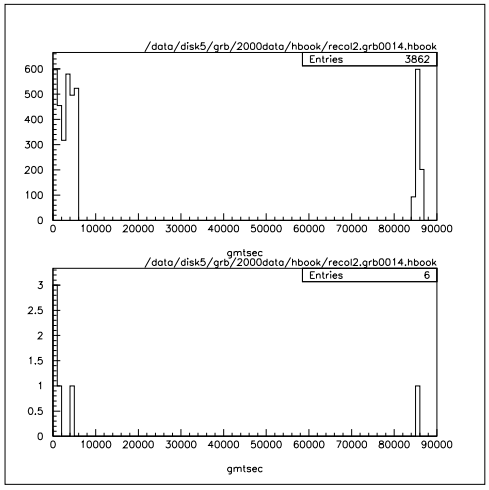

Figure J.14: The background distribution of events for grb11638b, except for the 10 minute blind spot around the trigger time, before (top) and after (bottom) cuts.

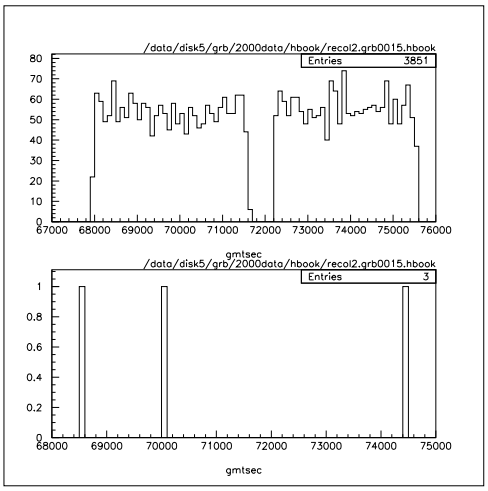

Figure J.15: The background distribution of events for grb11642d, except for the 10 minute blind spot around the trigger time, before (top) and after (bottom) cuts.

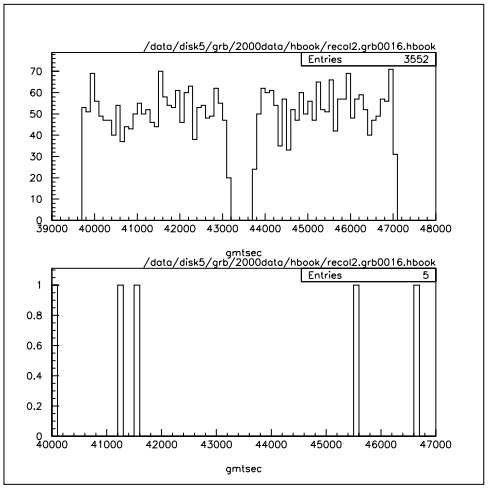

Figure J.16: The background distribution of events for grb11644b, except for the 10 minute blind spot around the trigger time, before (top) and after (bottom) cuts.

Appendix K

Unblinded Event Rates for 2000

These plots show the number of events during the GRB before and after cuts. The search was begun 10 seconds before the earliest gamma-rays and finished at the end of the T90 time.

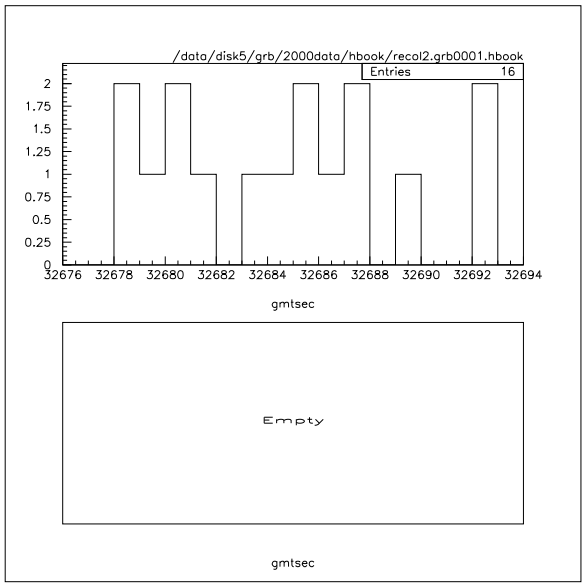

Figure K.1: The number of events for grb11591c during the burst, before (top) and after (bottom) cuts.

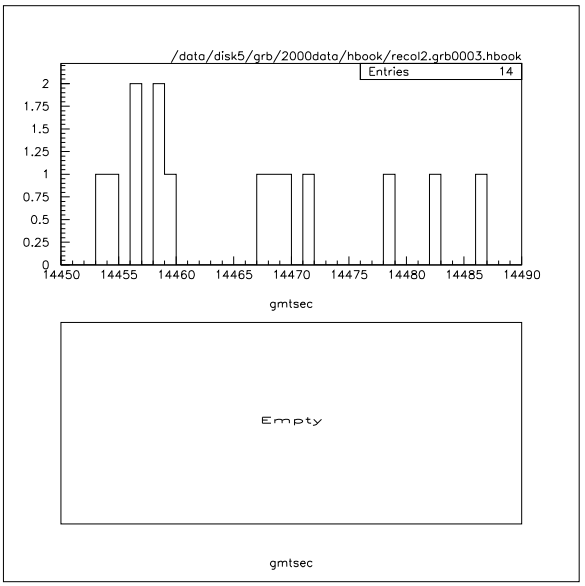

Figure K.3: The number of events for grb11599b during the burst, before (top) and after (bottom) cuts.

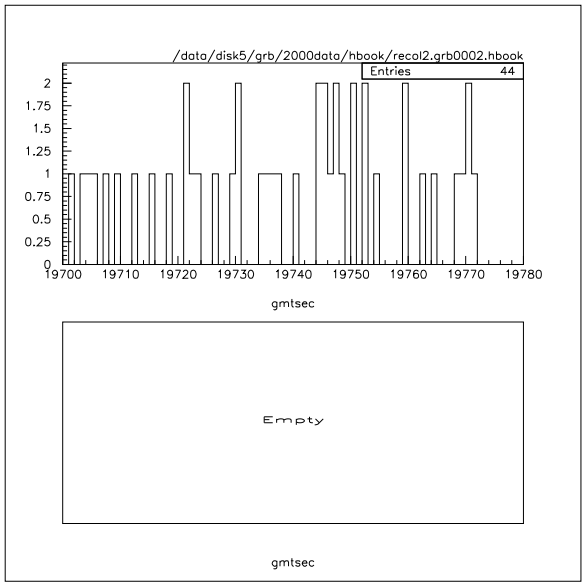

Figure K.2: The number of events for grb11597b during the burst, before (top) and after (bottom) cuts.

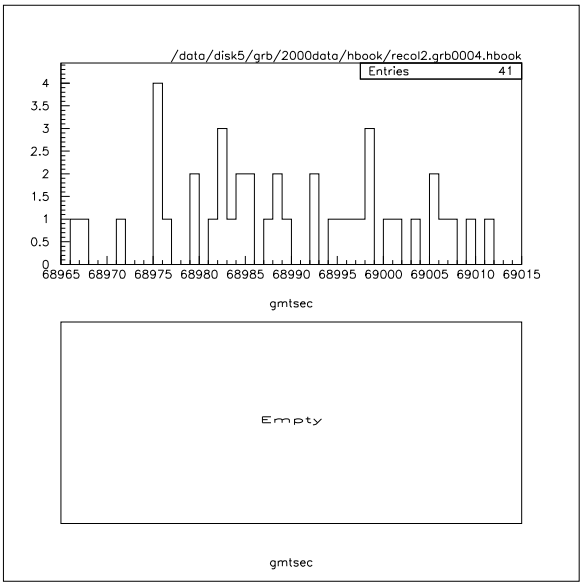

Figure K.4: The number of events for grb11599b during the burst, before (top) and after (bottom) cuts.

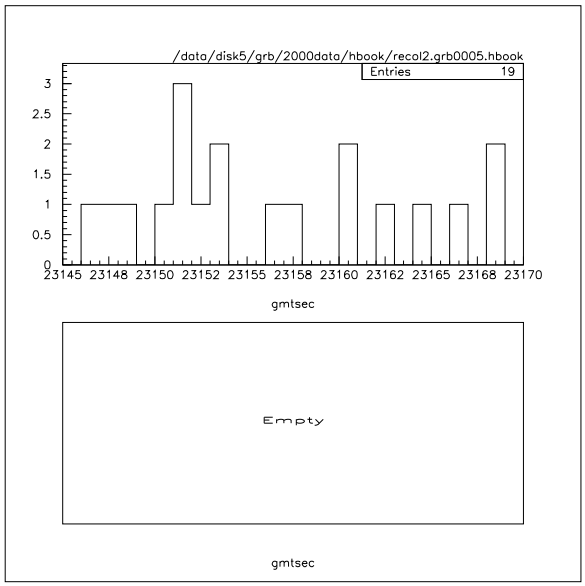

Figure K.5: The number of events for grb11602b during the burst, before (top) and after (bottom) cuts.

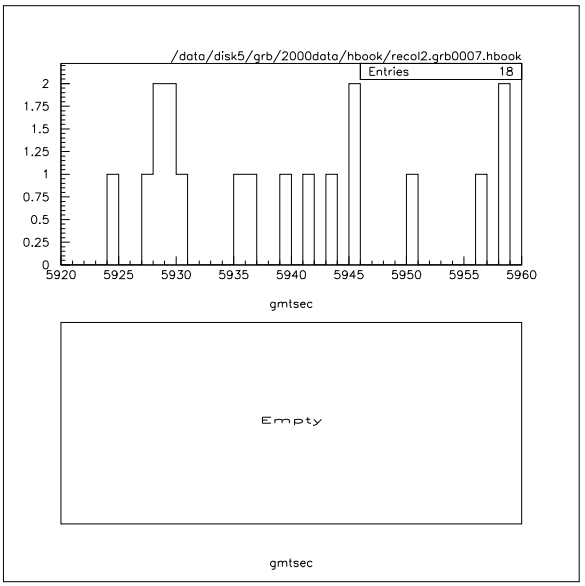

Figure K.7: The number of events for grb11609b during the burst, before (top) and after (bottom) cuts.

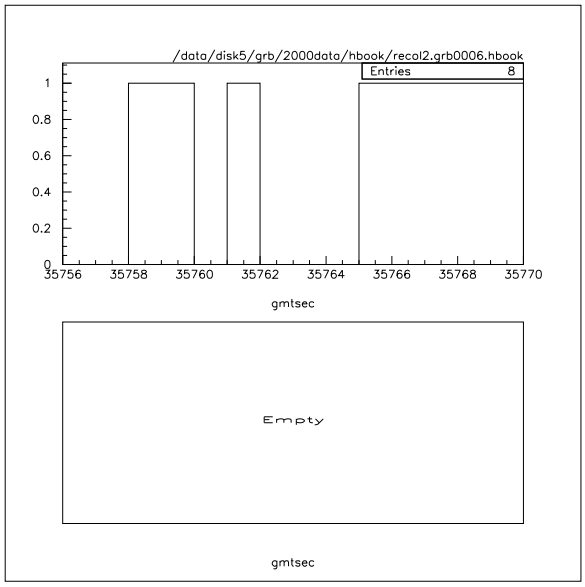

Figure K.6: The number of events for grb11608a during the burst, before (top) and after (bottom) cuts.

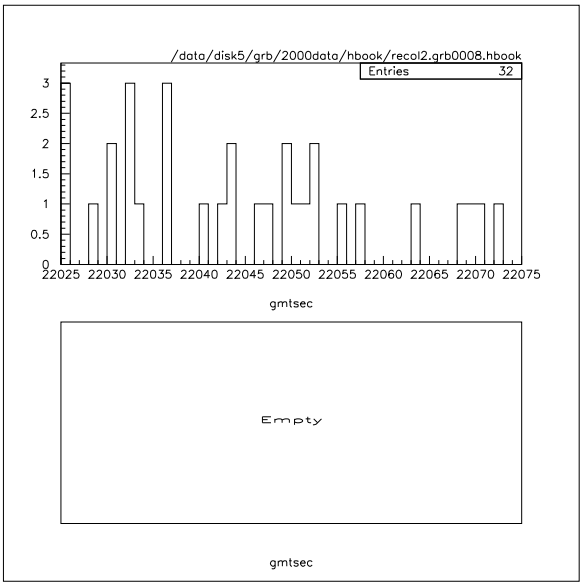

Figure K.8: The number of events for grb11625b during the burst, before (top) and after (bottom) cuts.

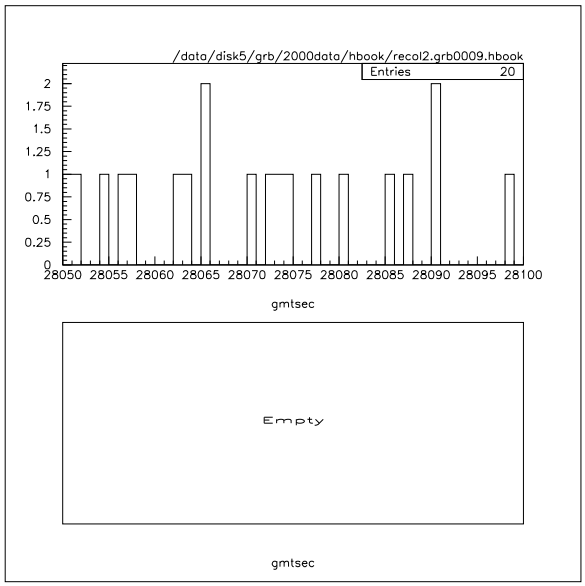

Figure K.9: The number of events for grb11633b during the burst, before (top) and after (bottom) cuts.

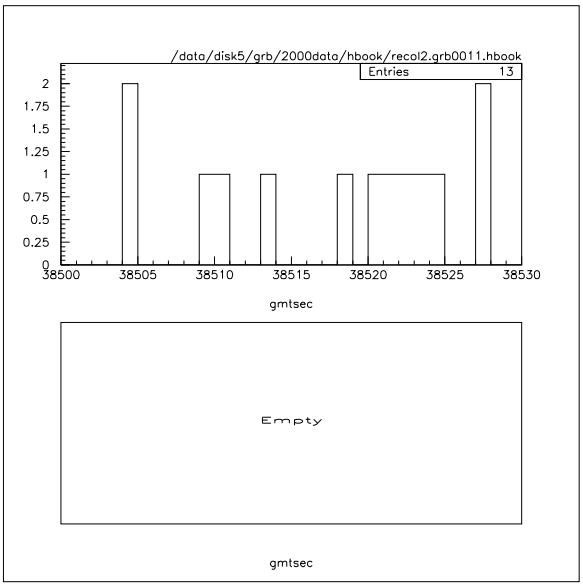

Figure K.11: The number of events for grb11634g during the burst, before (top) and after (bottom) cuts.

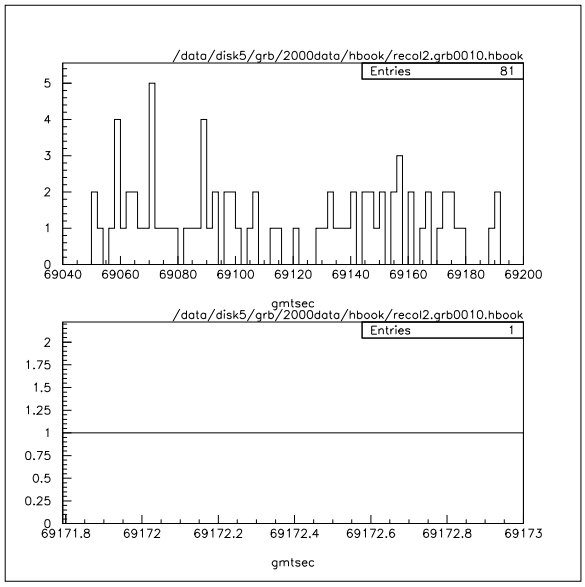

Figure K.10: The number of events for grb11633f during the burst, before (top) and after (bottom) cuts.

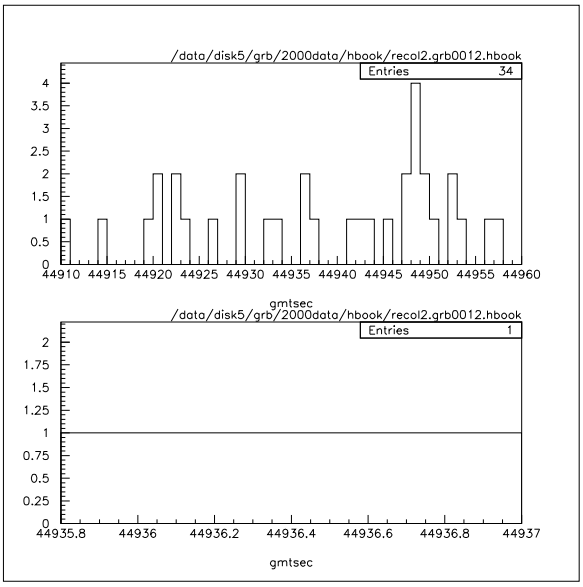

Figure K.12: The number of events for grb11637c during the burst, before (top) and after (bottom) cuts.

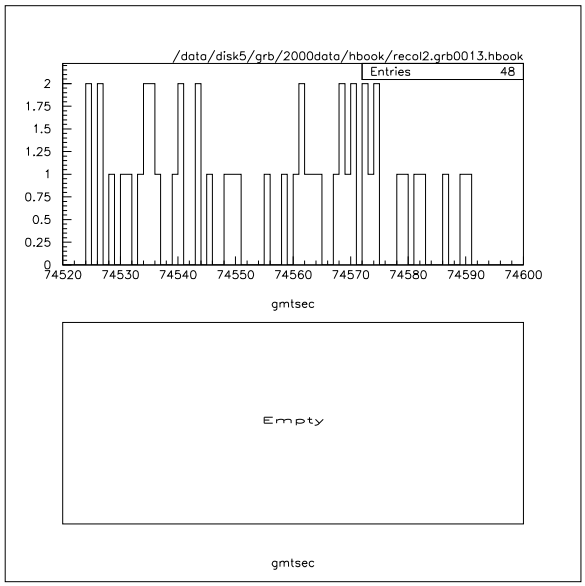

Figure K.13: The number of events for grb11637e during the burst, before (top) and after (bottom) cuts.

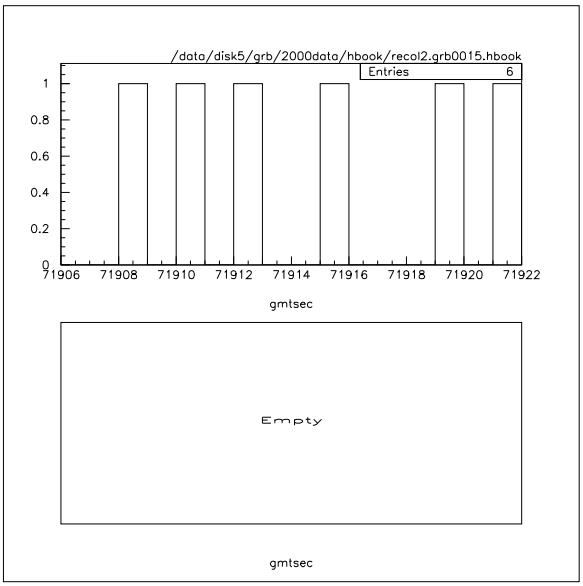

Figure K.15: The number of events for grb11642d during the burst, before (top) and after (bottom) cuts.

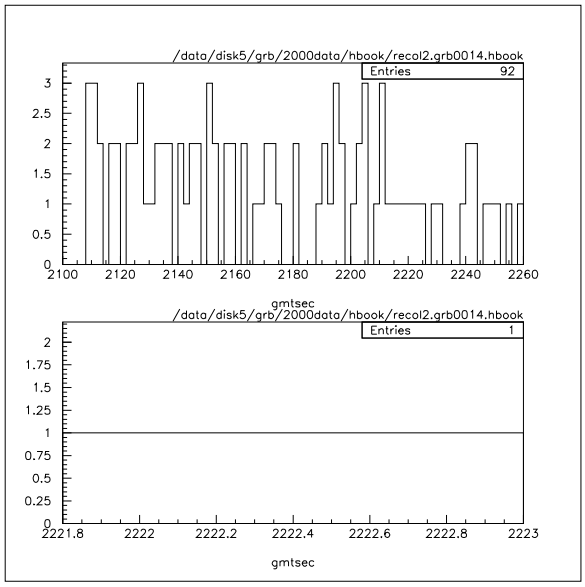

Figure K.14: The number of events for grb11638b during the burst, before (top) and after (bottom) cuts.

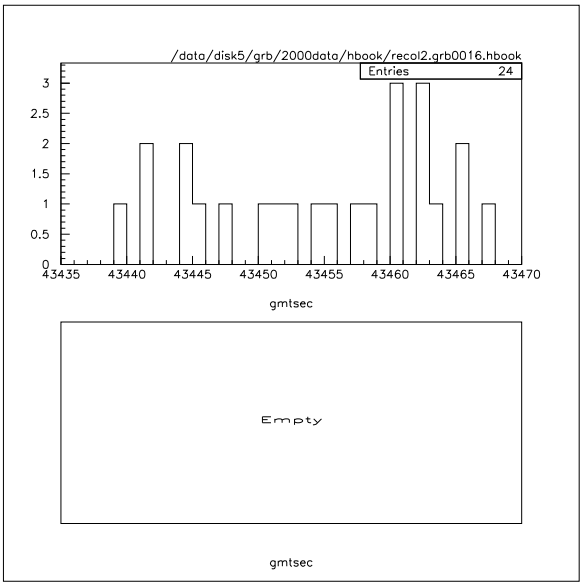

Figure K.16: The number of events for grb11644b during the burst, before (top) and after (bottom) cuts.

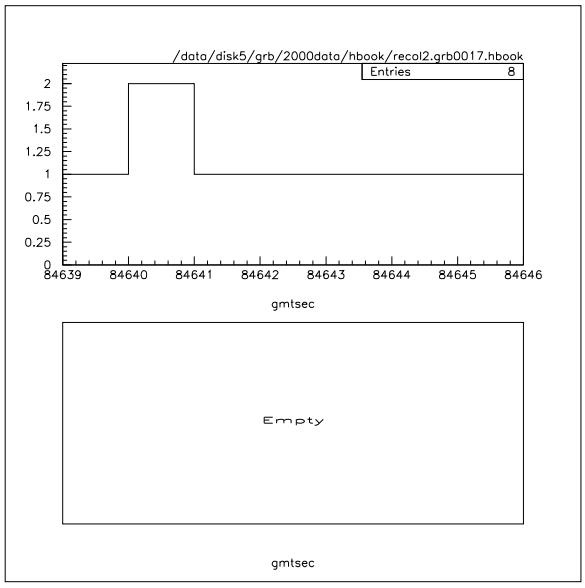

Figure K.17: The number of events for grb11644f during the burst, before (top) and after (bottom) cuts.

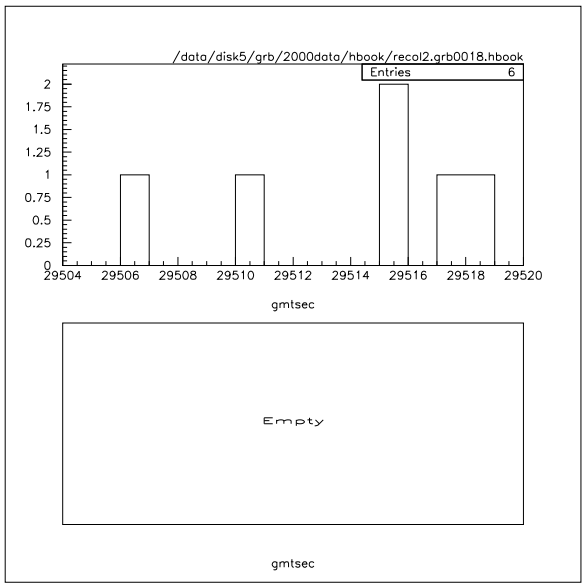

Figure K.18: The number of events for grb11646c during the burst, before (top) and after (bottom) cuts.

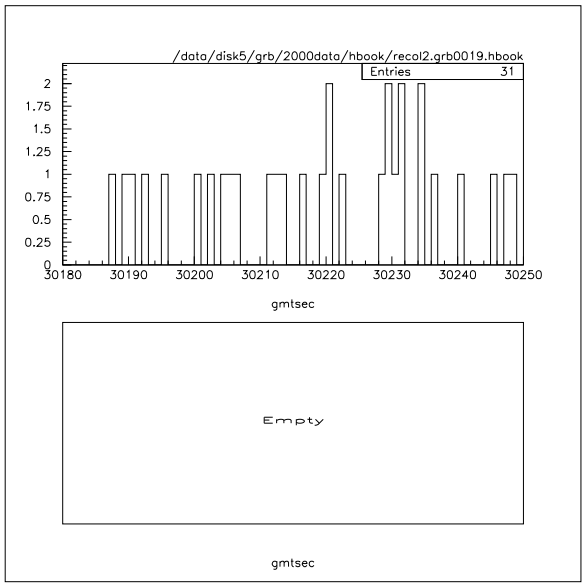

Figure K.19: The number of events for grb11650a during the burst, before (top) and after (bottom) cuts.

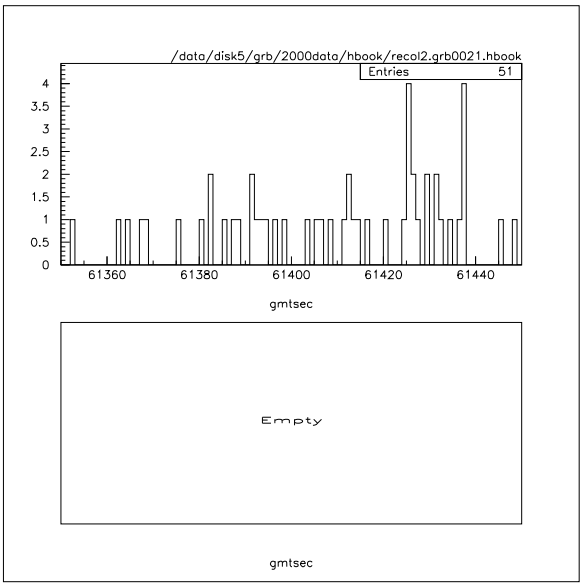

Figure K.21: The number of events for grb11654b during the burst, before (top) and after (bottom) cuts.

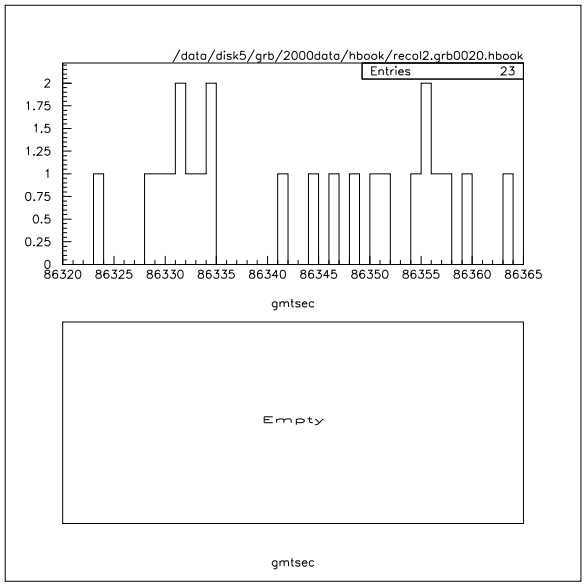

Figure K.20: The number of events for grb11652g during the burst, before (top) and after (bottom) cuts.

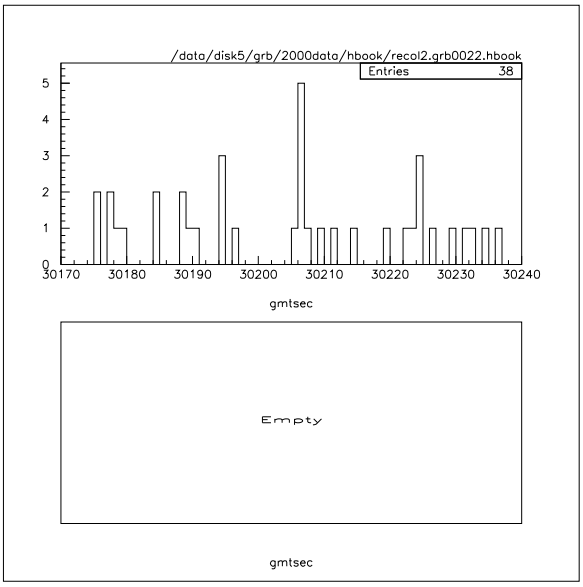

Figure K.22: The number of events for grb11663b during the burst, before (top) and after (bottom) cuts.

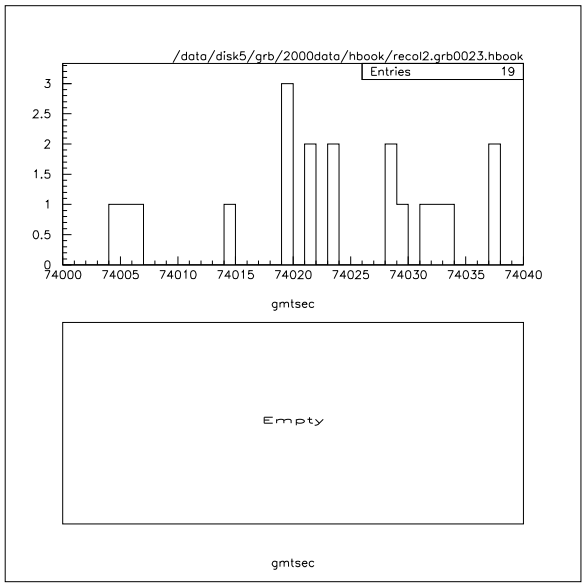

Figure K.23: The number of events for grb11663f during the burst, before (top) and after (bottom) cuts.

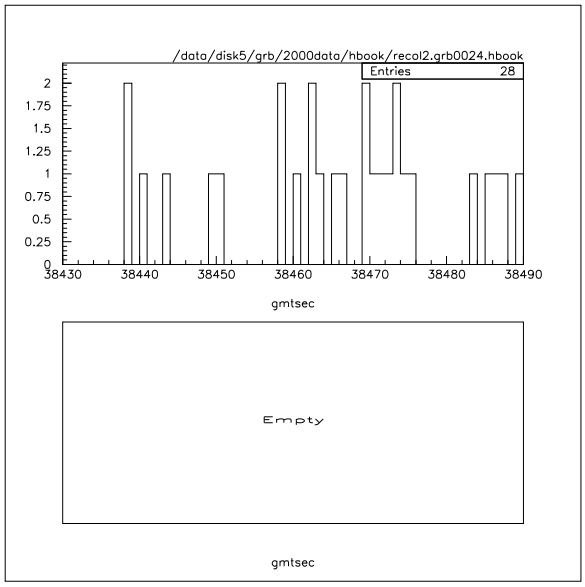

Figure K.24: The number of events for grb11668c during the burst, before (top) and after (bottom) cuts.

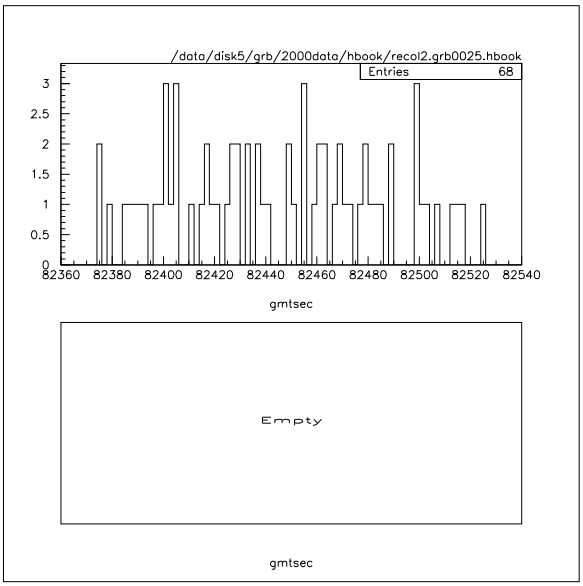

Figure K.25: The number of events for grb11672h during the burst, before (top) and after (bottom) cuts.

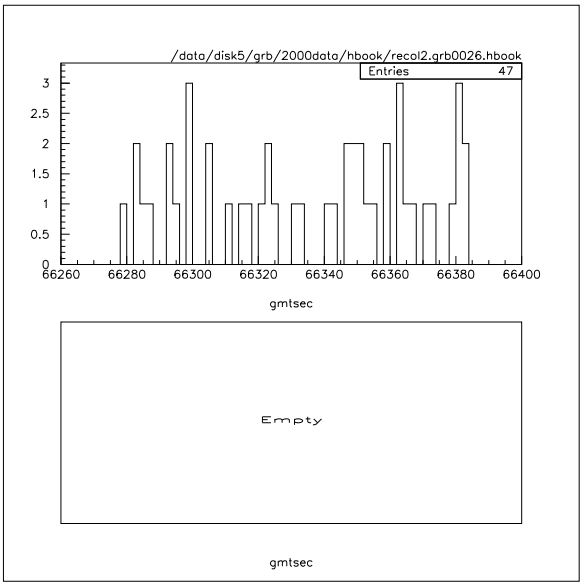

Figure K.26: The number of events for grb11675e during the burst, before (top) and after (bottom) cuts.

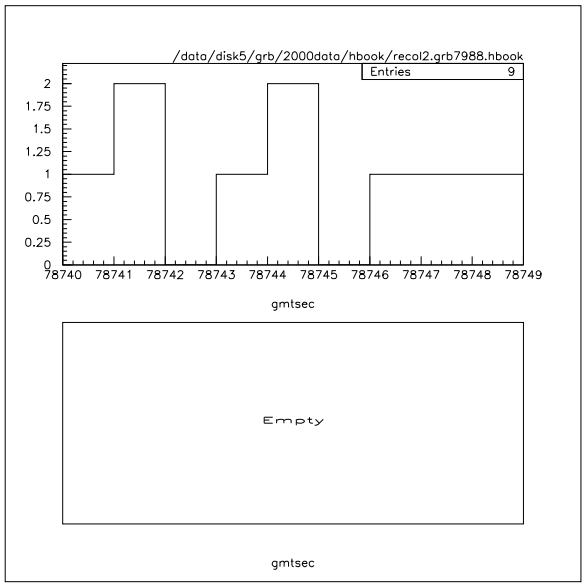

Figure K.27: The number of events for grb7988 during the burst, before (top) and after (bottom) cuts.

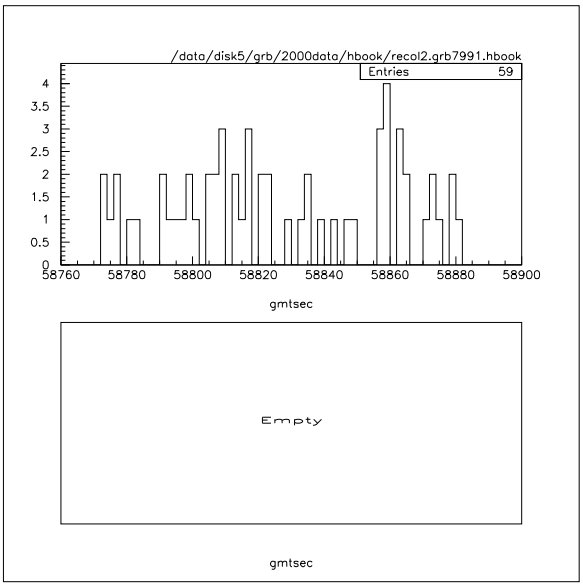

Figure K.29: The number of events for grb7991 during the burst, before (top) and after (bottom) cuts.

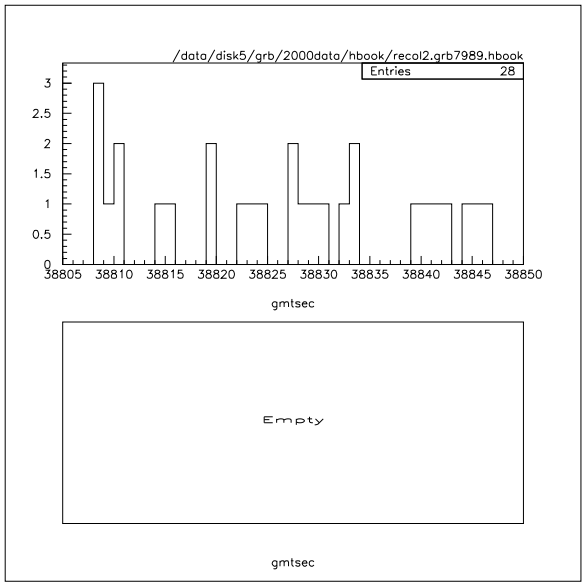

Figure K.28: The number of events for grb7989 during the burst, before (top) and after (bottom) cuts.

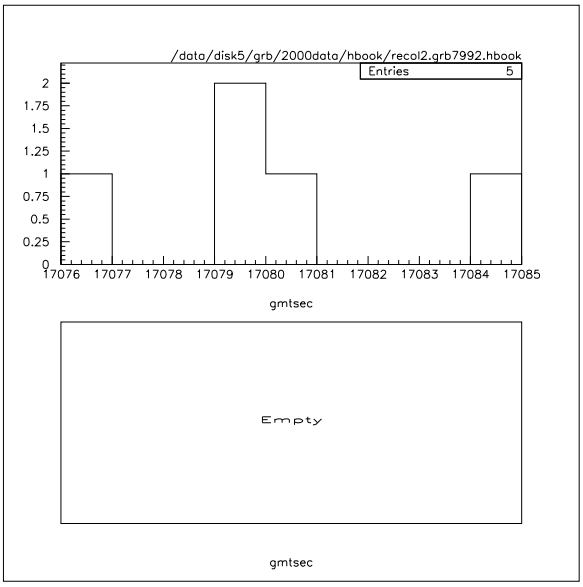

Figure K.30: The number of events for grb7992 during the burst, before (top) and after (bottom) cuts.

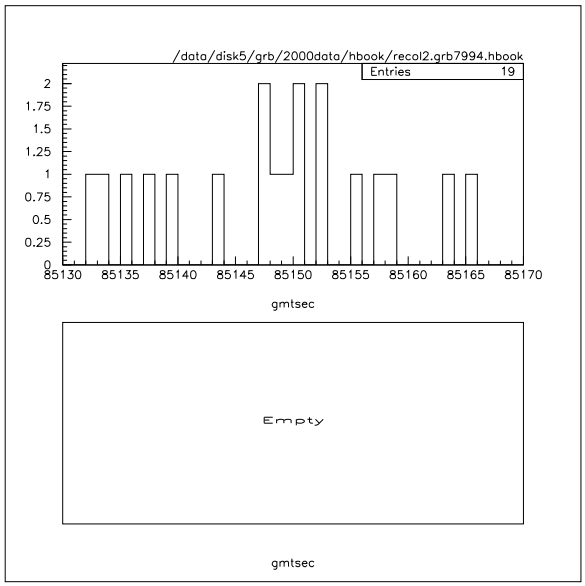

Figure K.31: The number of events for grb7994 during the burst, before (top) and after (bottom) cuts.

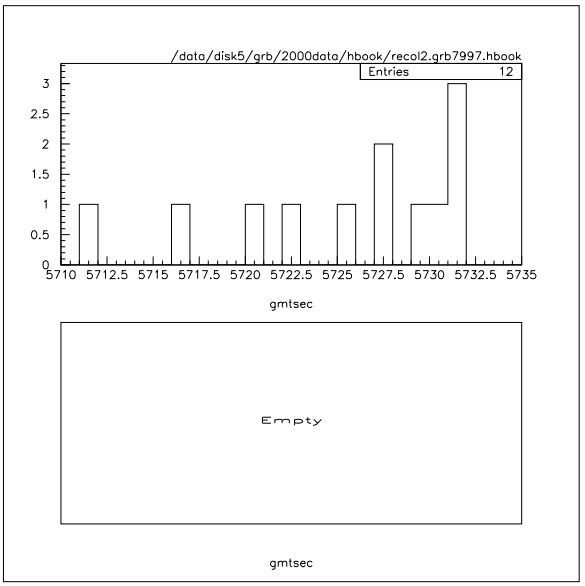

Figure K.33: The number of events for grb7997 during the burst, before (top) and after (bottom) cuts.

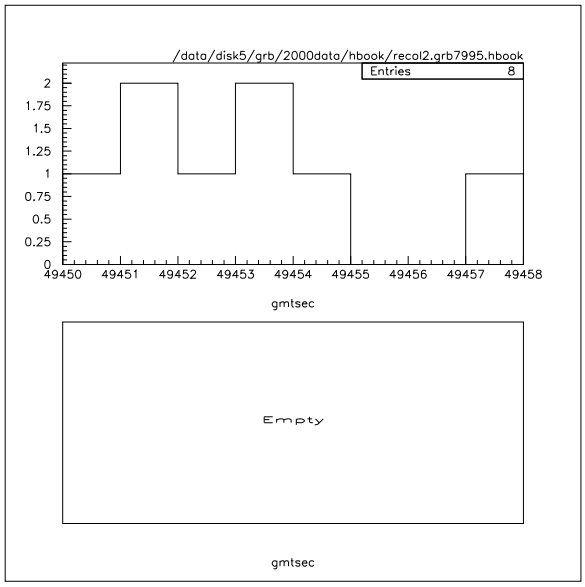

Figure K.32: The number of events for grb7995 during the burst, before (top) and after (bottom) cuts.

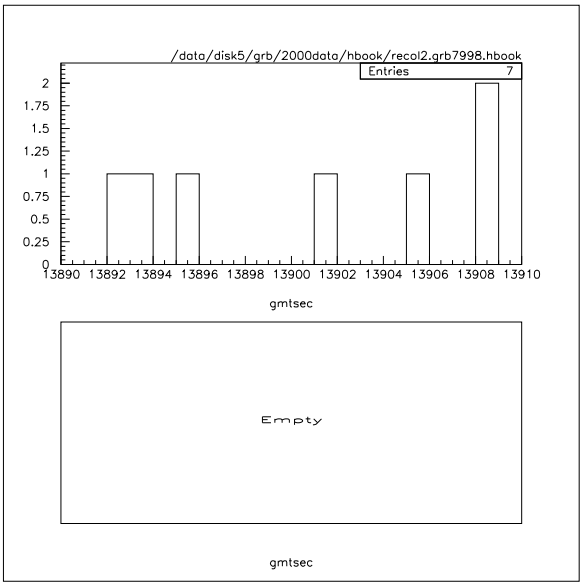

Figure K.34: The number of events for grb7998 during the burst, before (top) and after (bottom) cuts.

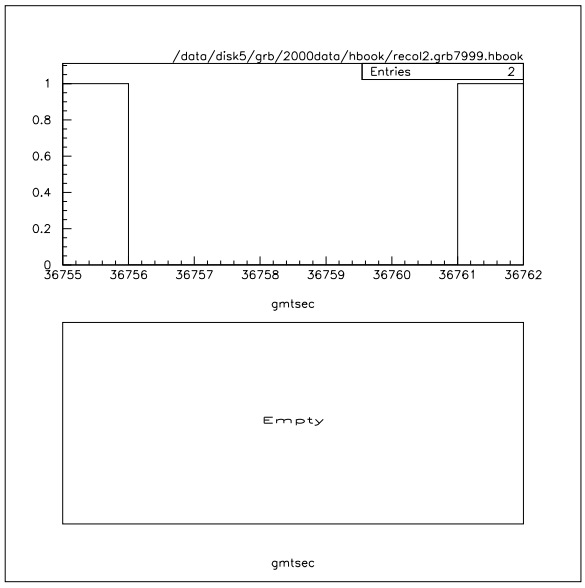

Figure K.35: The number of events for grb7999 during the burst, before (top) and after (bottom) cuts.

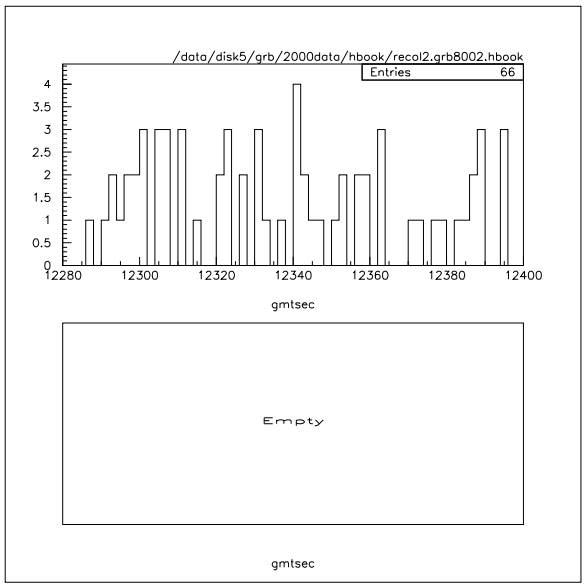

Figure K.36: The number of events for grb8002 during the burst, before (top) and after (bottom) cuts.

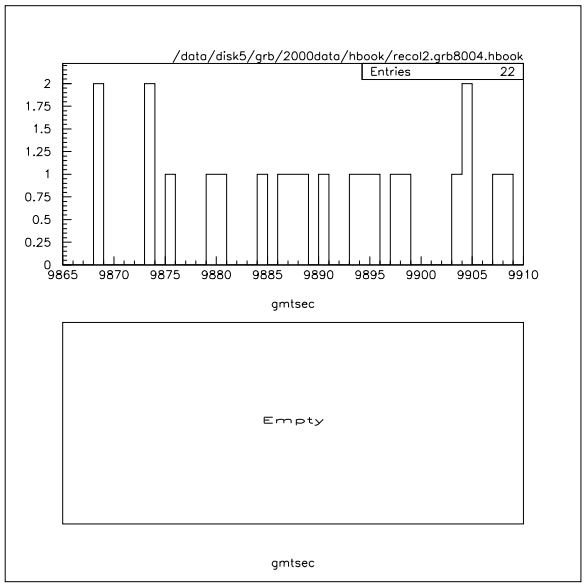

Figure K.37: The number of events for grb8004 during the burst, before (top) and after (bottom) cuts.

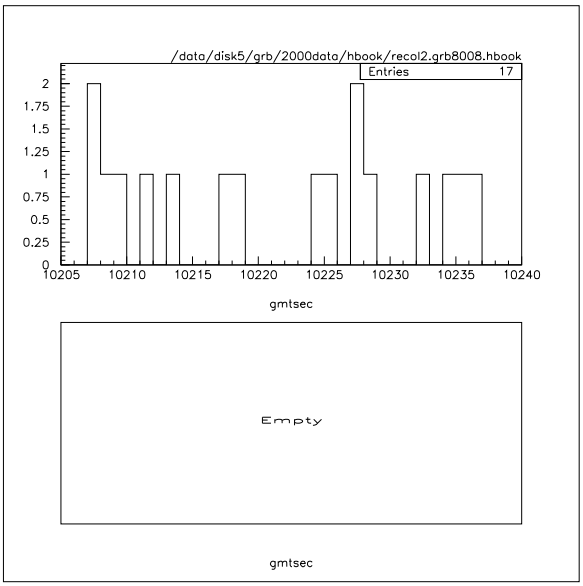

Figure K.39: The number of events for grb8008 during the burst, before (top) and after (bottom) cuts.

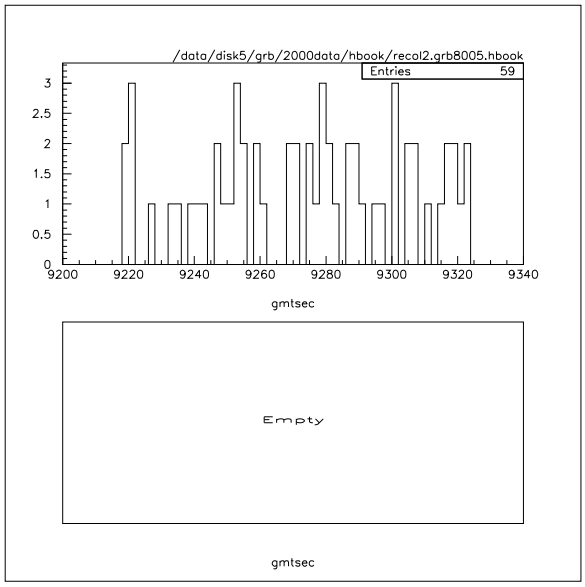

Figure K.38: The number of events for grb8005 during the burst, before (top) and after (bottom) cuts.

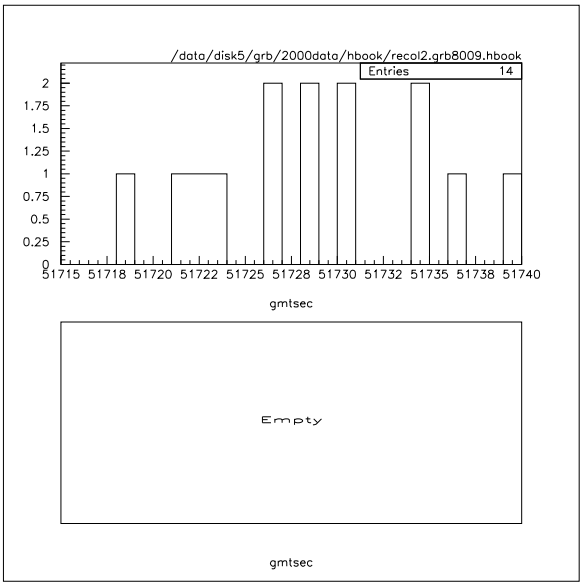

Figure K.40: The number of events for grb8009 during the burst, before (top) and after (bottom) cuts.

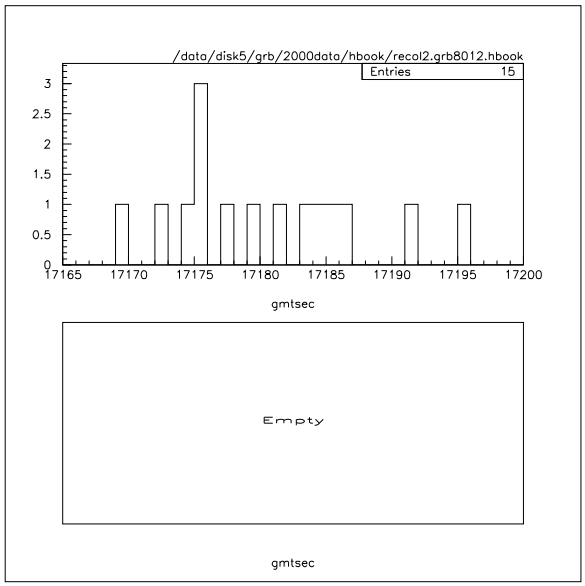

Figure K.41: The number of events for grb8012 during the burst, before (top) and after (bottom) cuts.

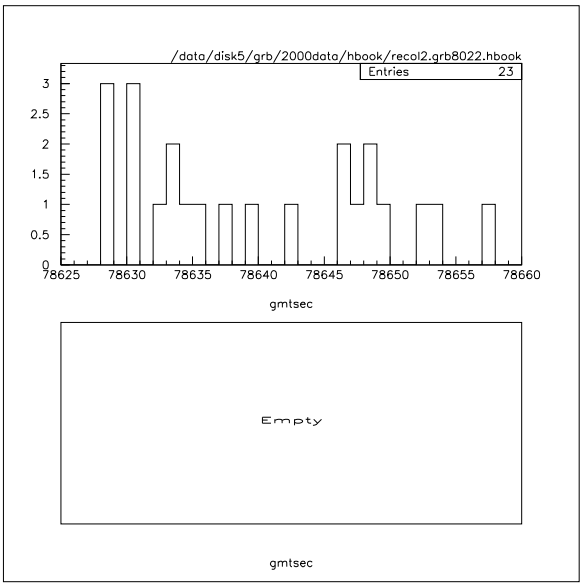

Figure K.43: The number of events for grb8022 during the burst, before (top) and after (bottom) cuts.

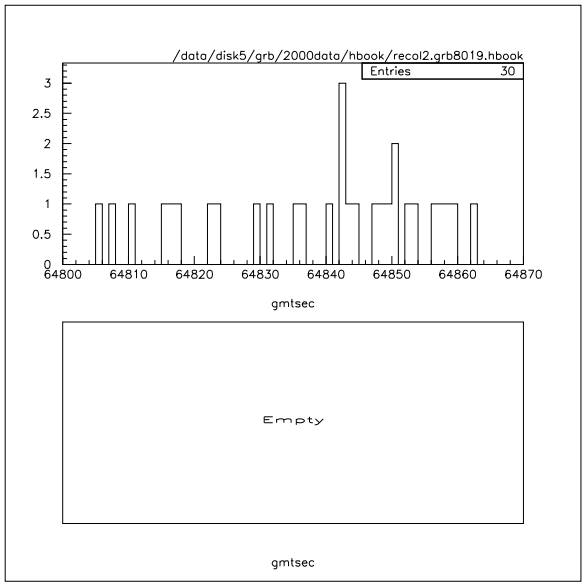

Figure K.42: The number of events for grb8019 during the burst, before (top) and after (bottom) cuts.

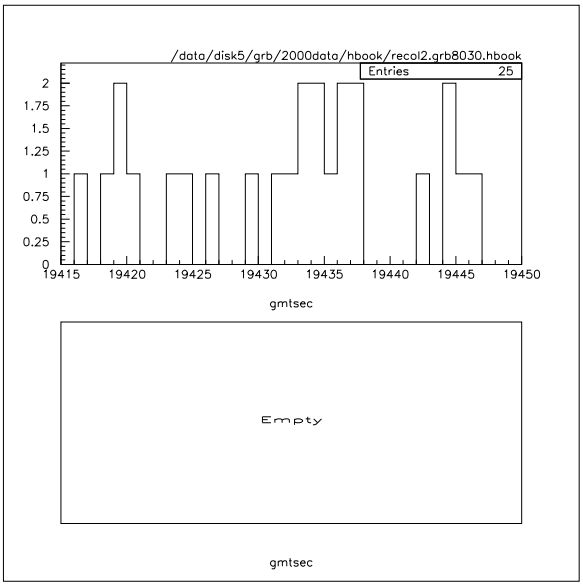

Figure K.44: The number of events for grb8030 during the burst, before (top) and after (bottom) cuts.

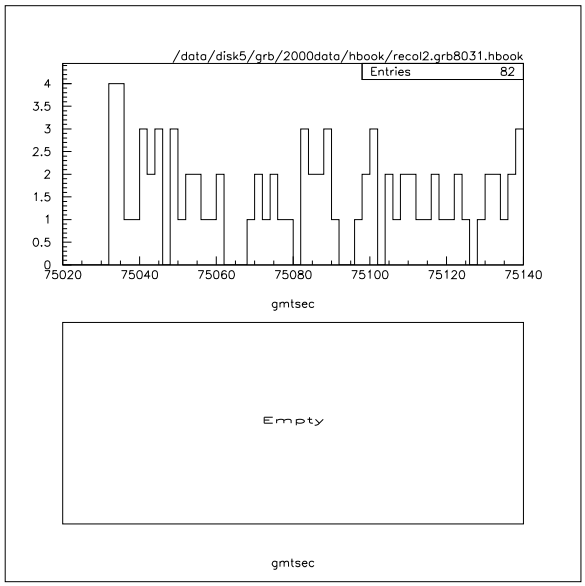

Figure K.45: The number of events for grb8031 during the burst, before (top) and after (bottom) cuts.

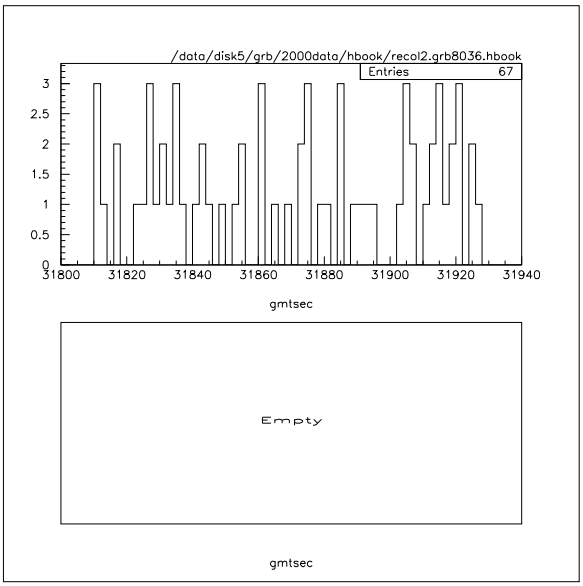

Figure K.47: The number of events for grb8036 during the burst, before (top) and after (bottom) cuts.

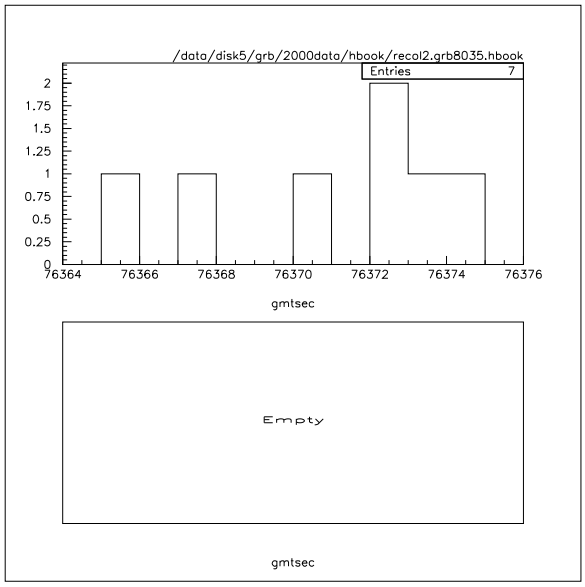

Figure K.46: The number of events for grb8035 during the burst, before (top) and after (bottom) cuts.

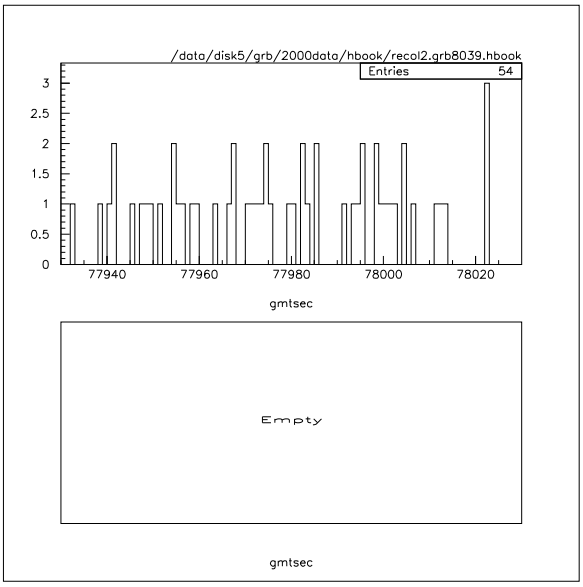

Figure K.48: The number of events for grb8039 during the burst, before (top) and after (bottom) cuts.

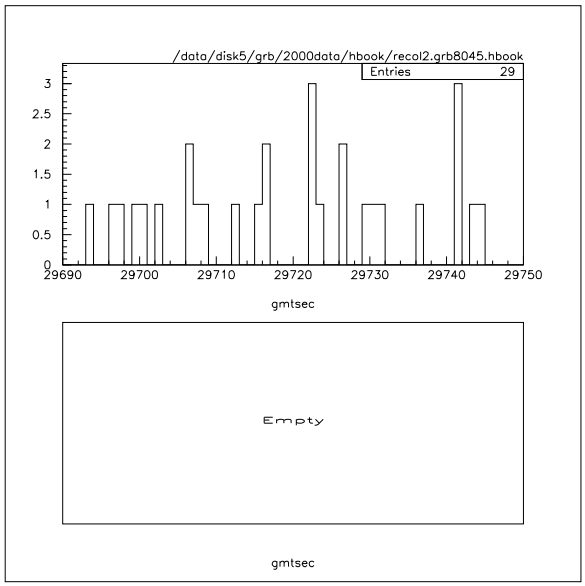

Figure K.49: The number of events for grb8045 during the burst, before (top) and after (bottom) cuts.

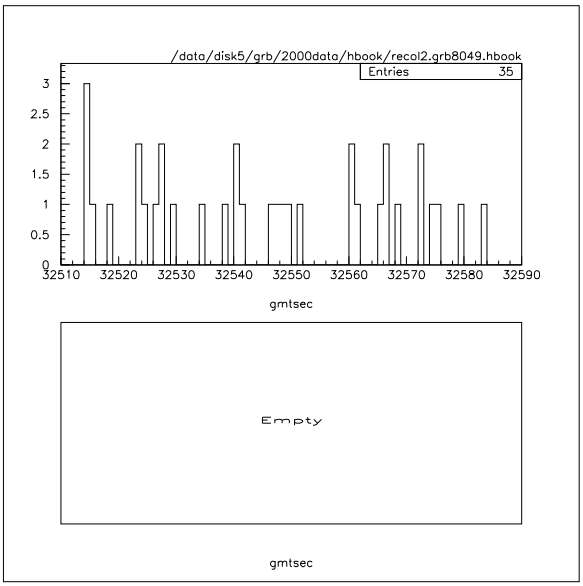

Figure K.51: The number of events for grb8049 during the burst, before (top) and after (bottom) cuts.

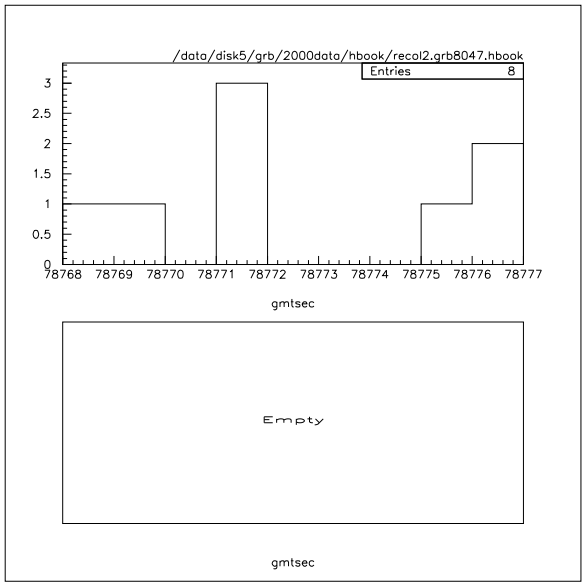

Figure K.50: The number of events for grb8047 during the burst, before (top) and after (bottom) cuts.

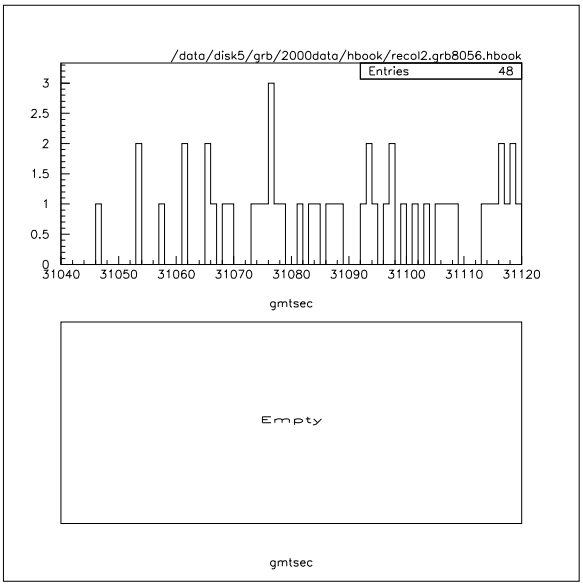

Figure K.52: The number of events for grb8056 during the burst, before (top) and after (bottom) cuts.

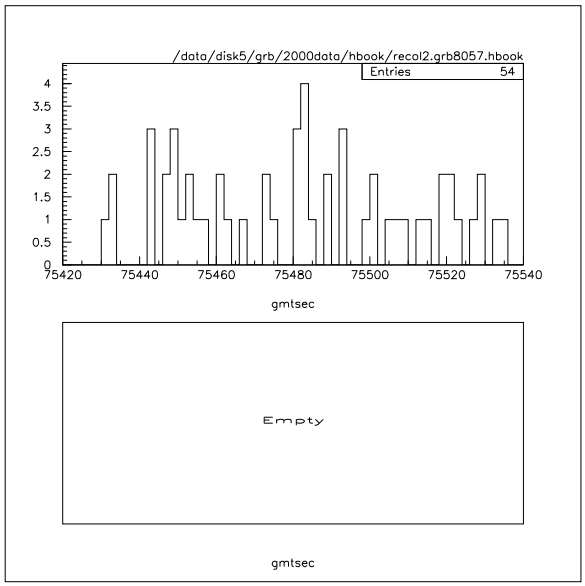

Figure K.53: The number of events for grb8057 during the burst, before (top) and after (bottom) cuts.

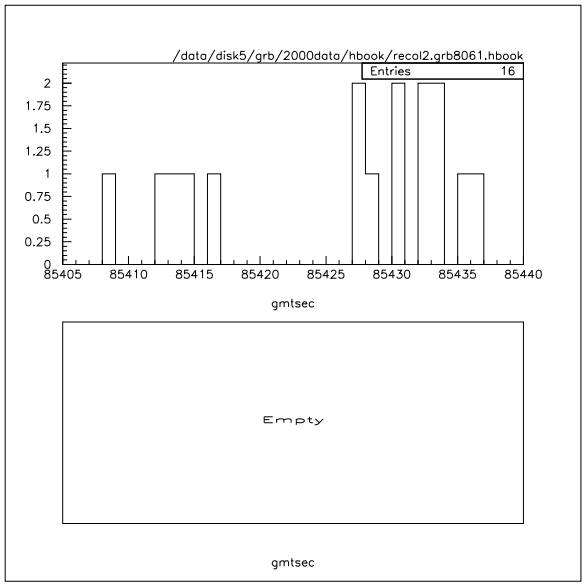

Figure K.54: The number of events for grb8061 during the burst, before (top) and after (bottom) cuts.

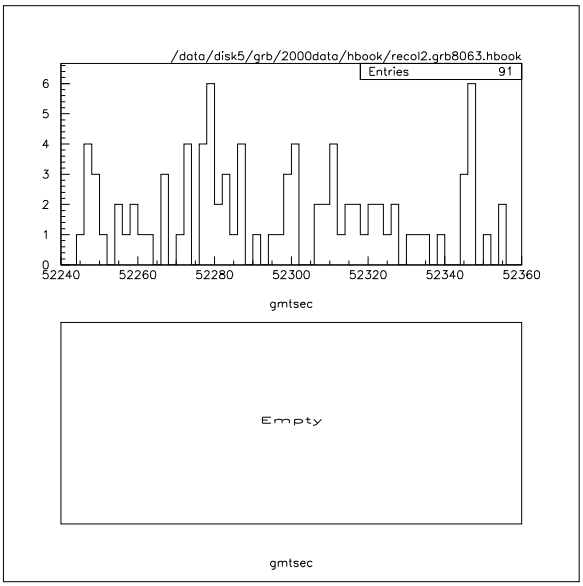

Figure K.55: The number of events for grb8063 during the burst, before (top) and after (bottom) cuts.

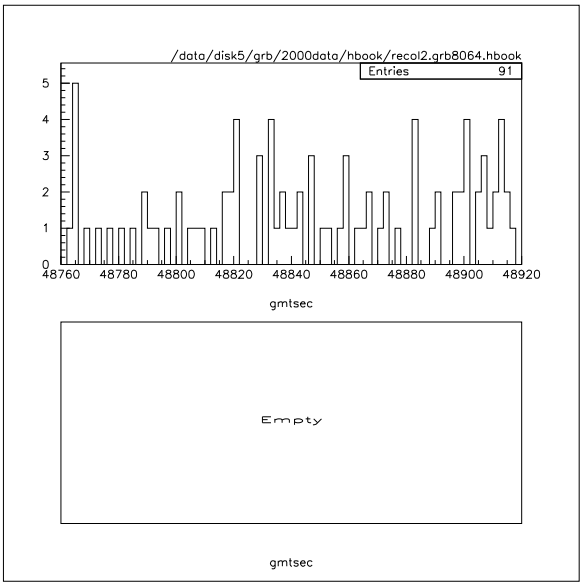

Figure K.56: The number of events for grb8064 during the burst, before (top) and after (bottom) cuts.

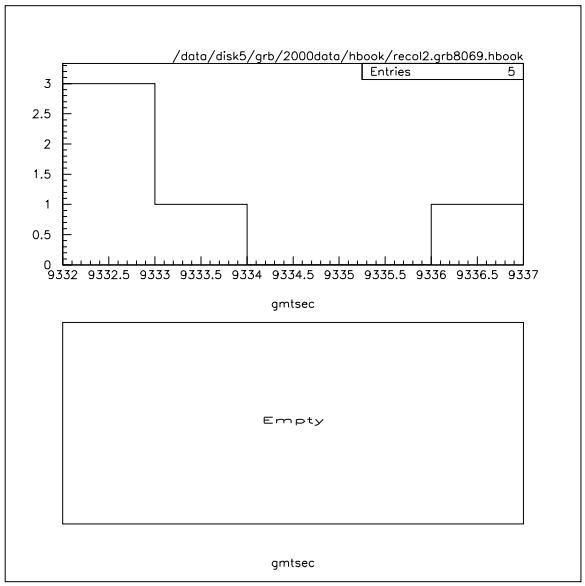

Figure K.57: The number of events for grb8069 during the burst, before (top) and after (bottom) cuts.

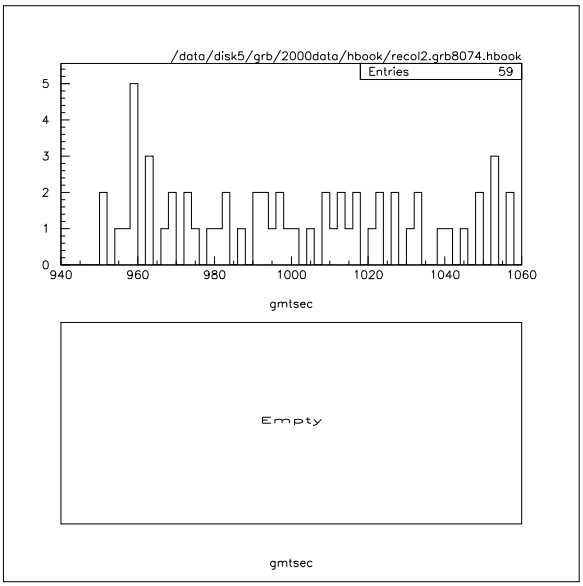

Figure K.59: The number of events for grb8074 during the burst, before (top) and after (bottom) cuts.

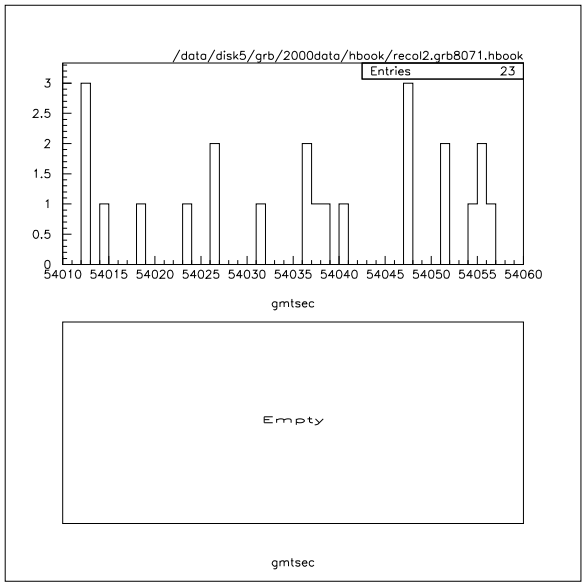

Figure K.58: The number of events for grb8071 during the burst, before (top) and after (bottom) cuts.

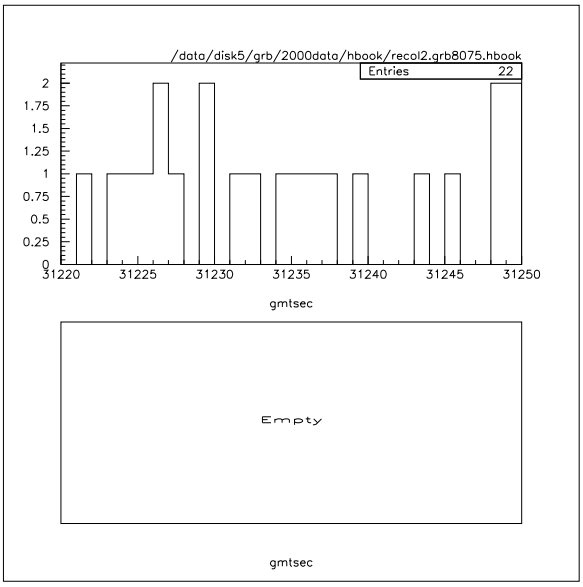

Figure K.60: The number of events for grb8075 during the burst, before (top) and after (bottom) cuts.

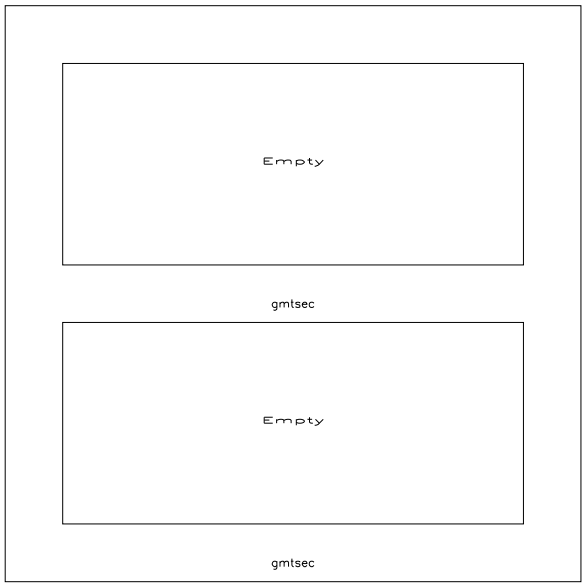

Figure K.61: The number of events for grb8077 during the burst, before (top) and after (bottom) cuts.

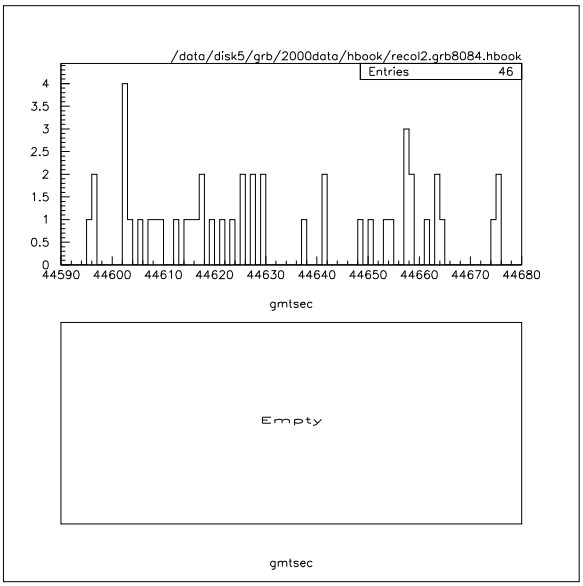

Figure K.63: The number of events for grb8084 during the burst, before (top) and after (bottom) cuts.

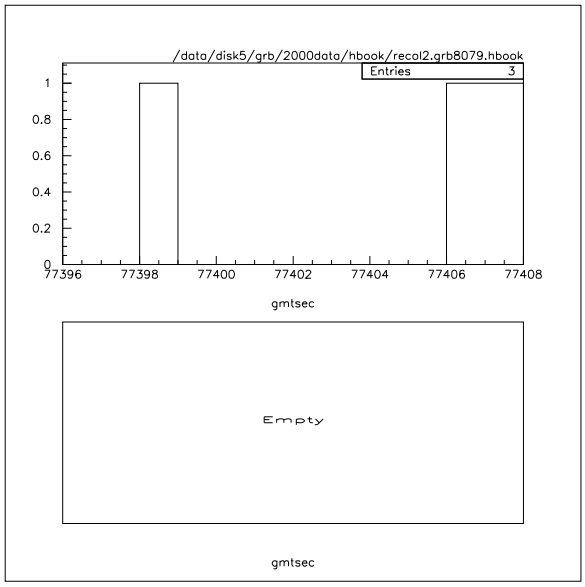

Figure K.62: The number of events for grb8079 during the burst, before (top) and after (bottom) cuts.

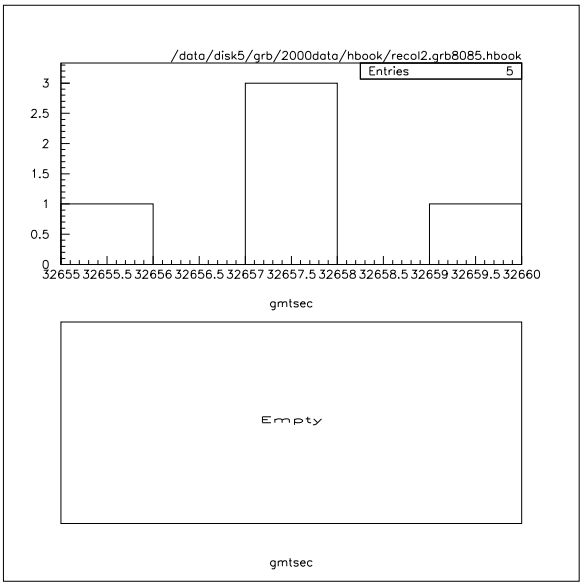

Figure K.64: The number of events for grb8085 during the burst, before (top) and after (bottom) cuts.

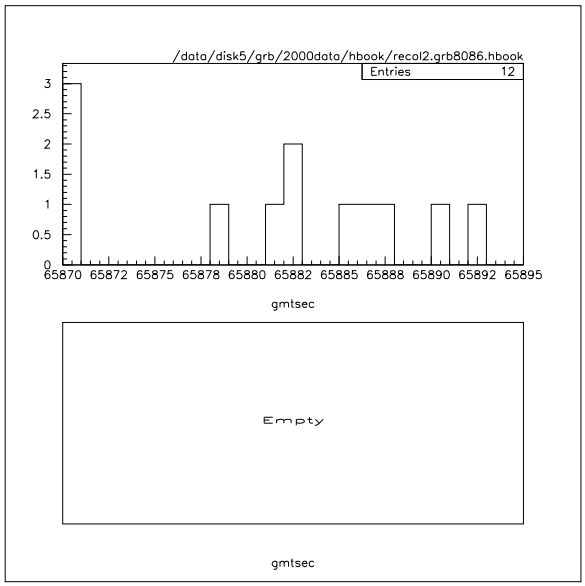

Figure K.65: The number of events for grb8086 during the burst, before (top) and after (bottom) cuts.

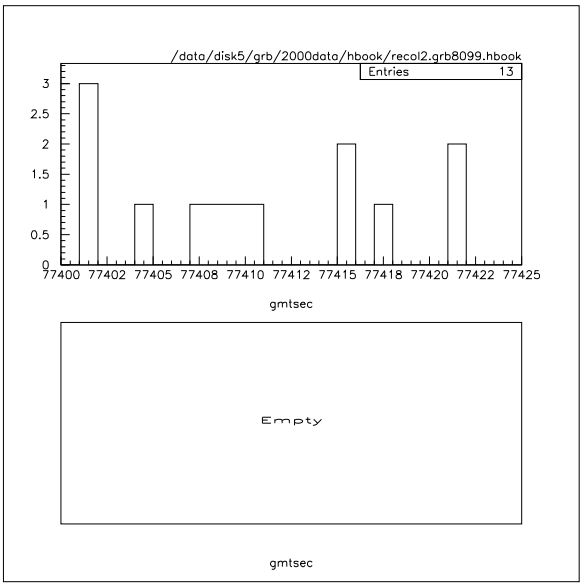

Figure K.67: The number of events for grb8099 during the burst, before (top) and after (bottom) cuts.

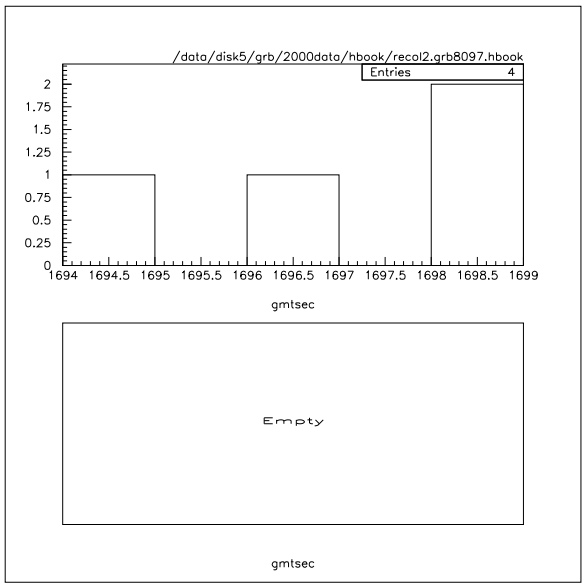

Figure K.66: The number of events for grb8097 during the burst, before (top) and after (bottom) cuts.

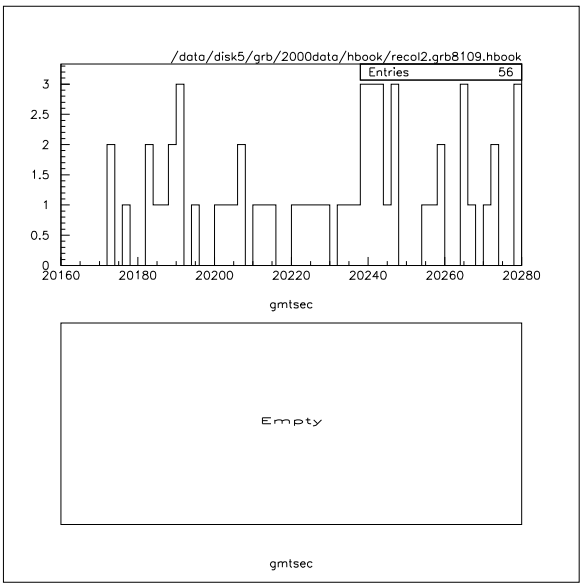

Figure K.68: The number of events for grb8109 during the burst, before (top) and after (bottom) cuts.

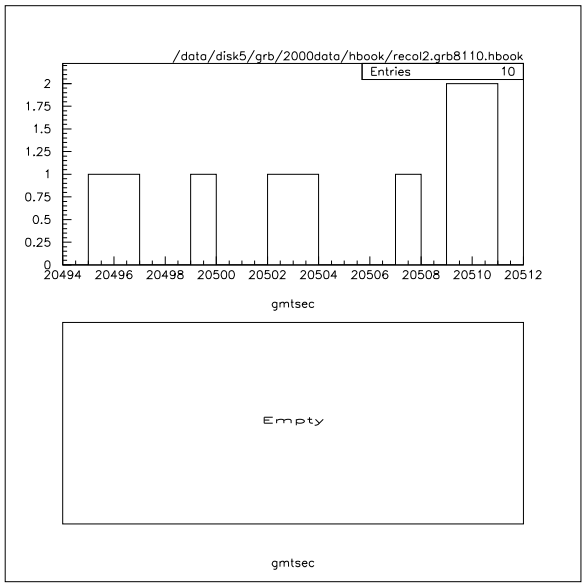

Figure K.69: The number of events for grb8110 during the burst, before (top) and after (bottom) cuts.

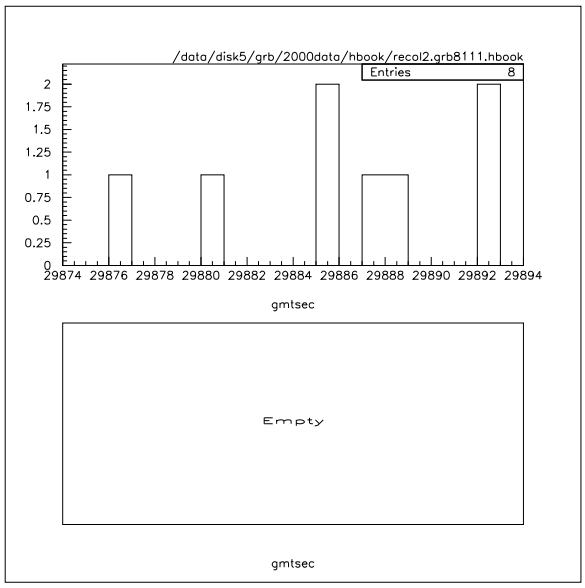

Figure K.70: The number of events for grb8111 during the burst, before (top) and after (bottom) cuts.